Neuro-musculoskeletal Models: A Tool to Study the Contribution of Muscle Dynamics to Biological Motor Control

Dissertation

der Mathematisch-Naturwissenschaftlichen Fakultät
der Eberhard Karls Universität Tübingen
zur Erlangung des Grades eines
Doktors der Naturwissenschaften
(Dr. rer. nat.)

vorgelegt von
Katrin Stollenmaier
aus Mutlangen

Tübingen
2020

Gedruckt mit Genehmigung der Mathematisch-Naturwissenschaftlichen Fakultät der Eberhard Karls Universität Tübingen.

Tag der mündlichen Qualifikation: 25.02.2021

Stellvertretender Dekan: Prof. Dr. József Fortágh
1. Berichterstatter: Dr. Daniel Häufle
2. Berichterstatter: Prof. Dr. Martin Butz

Abstract

Understanding the principles underlying human movement is the basis for investigating the generation of healthy movements and, more importantly, the origins of motor disorders due to neurodegenerative diseases or other pathological conditions. However, gaining this understanding is challenging since human motion is the result of a complex, dynamic interplay of biochemical and biophysical processes in the musculoskeletal system and the hierarchically organized neuronal control structures. To study the interactions of these structures, computer simulations that combine mathematical models of the musculoskeletal system with models of its neuronal control provide a useful tool. In these simulations, single processes or whole functional units can be disabled or perturbed to study the effects of these changes on the predicted movements. The plausibility of the underlying models can be assessed by comparing the simulations with data from human experiments and biologically inspired robotic models.

The purpose of this work was to use neuro-musculoskeletal models as tools to study concepts of biological motor control. Of particular interest was the contribution of muscle dynamics to the control, i.e. how the intrinsic musculoskeletal properties simplify motor control without compromising motor accuracy. Additionally, the influence of proprioceptive reflex mechanisms was tested in different scenarios. The neuro-musculoskeletal models that were used are a combination of multibody musculoskeletal models of the arm or the whole body with a biologically inspired hybrid equilibrium-point controller.

In a simulation study, we found that our arm model predicts realistic reactions to external mechanical perturbations while performing one-degree-of-freedom goal-directed movements. Based on this, we simulated the application of wearable assistive devices to compensate for unwanted hypermetria, i.e. an overshooting response in goal-directed movements associated with cerebellar ataxia and other neurodegenerative disorders. We found that simple mechanical devices may be sufficient to reduce the hypermetria to a normal level. However, we also observed that the magnitude of torque and power that is required to compensate for the disorder may be significantly underestimated if muscle-tendon characteristics are not considered in the computational model. The results of these two studies confirmed the hypothesis from literature that the morphology of musculoskeletal systems significantly contributes to the movement and thus simplifies its control. Therefore, we made use of the information-theoretic approach of quantifying morphological computation to characterize this contribution for goal-directed and oscillatory arm movements with two degrees of freedom. The results asserted that the lower levels of control, including the muscles and their activation dynamics, make important contributions to the overall control hierarchy. For example, a simple piecewise constant muscle stimulation signal that contains only little information results in a smooth movement.

The level of physiological detail that is included in our musculoskeletal models does not only allow for the examination of motor control theories but also makes it possible to study

quantities like internal forces in muscles and joints, usually not experimentally accessible. These quantities are relevant, for example, in ergonomics and for the development of assistive devices. In a whole-body simulation study, we investigated the contribution of the stretch reflex to the resulting muscle forces during active external repositioning of the hip joint for a large range of movement velocities. We found that, depending on the modeled cognitive state, the relative force contribution of the feedback mechanism is not negligible, especially for high repositioning velocities.

The entirety of our results shows that the properties of the musculoskeletal system significantly contribute to the generation and control of movement and, thus, it is important to take them into account when modeling human movement. Therefore, the results advocate the combination of a physiologically well-founded biomechanical and biochemical model of the musculoskeletal system with biologically inspired concepts of motor control. These computer simulations have proven to be a useful tool towards the comprehension of the processes underlying the generation of healthy and pathologically impaired human movements.

Kurzfassung

Das Verständnis der Prinzipien, die menschlichen Bewegungen zugrunde liegen, ist die Basis für die Untersuchung der Entstehung gesunder Bewegungen und, was noch wichtiger ist, der Entstehung motorischer Störungen aufgrund neurodegenerativer Erkrankungen oder anderer pathologischer Zustände. Dieses Verständnis zu erlangen ist jedoch herausfordernd, da menschliche Bewegung das Ergebnis eines komplexen, dynamischen Zusammenspiels von biochemischen und biophysikalischen Prozessen im Bewegungsapparat und den hierarchisch organisierten neuronalen Kontrollstrukturen ist. Um die Wechselwirkungen dieser Strukturen zu untersuchen, bieten Computersimulationen, die mathematische Modelle des muskuloskelettalen Systems mit Modellen seiner neuronalen Kontrolle kombinieren, ein nützliches Werkzeug. In diesen Simulationen können einzelne Prozesse oder ganze Funktionseinheiten deaktiviert oder gestört werden, um die Auswirkungen dieser Veränderungen auf die vorhergesagten Bewegungen zu untersuchen. Die Plausibilität der zugrundeliegenden Modelle kann durch den Vergleich der Simulationen mit Daten aus Humanexperimenten und biologisch inspirierten Robotermodellen beurteilt werden.

Das Ziel dieser Arbeit war es, neuro-muskuloskelettale Modelle als Hilfsmittel zur Untersuchung von Konzepten der biologischen Bewegungskontrolle zu verwenden. Von besonderem Interesse war der Beitrag der Muskeldynamik zur Kontrolle, d.h. wie die intrinsischen muskuloskelettalen Eigenschaften die motorische Kontrolle vereinfachen, ohne die motorische Genauigkeit zu beeinträchtigen. Zusätzlich wurde der Einfluss propriozeptiver Reflexmechanismen in verschiedenen Szenarien getestet. Die verwendeten neuro-muskuloskelettalen Modelle sind eine Kombination von Mehrkörpermodellen der Muskel-Skelett-Struktur des Armes oder des ganzen Körpers mit einem biologisch inspirierten hybriden Gleichgewichtspunkt-Kontrollmodell.

In einer Simulationsstudie stellten wir fest, dass unser Armmodell realistische Reaktionen auf externe mechanische Störungen für zielgerichtete Bewegungen mit einem Freiheitsgrad vorhersagt. Auf dieser Grundlage simulierten wir die Anwendung von tragbaren Assistenzgeräten zur Kompensation unerwünschter Hypermetrie, d.h. einer überschießenden Reaktion bei zielgerichteten Bewegungen im Zusammenhang mit zerebellärer Ataxie und anderen neurodegenerativen Erkrankungen. Wir fanden heraus, dass einfache mechanische Hilfsmittel ausreichend sein können, um die Hypermetrien auf ein normales Niveau zu reduzieren. Wir stellten jedoch auch fest, dass die Größe des Drehmoments und der Kraft, die zur Kompensation der Störung erforderlich sind, möglicherweise deutlich unterschätzt wird, wenn die Muskel-Sehnen-Eigenschaften im Modell nicht berücksichtigt werden. Die Ergebnisse dieser beiden Studien bestätigten die Hypothese aus der Literatur, dass die Morphologie des Muskel-Skelett-Systems signifikant zur Bewegung beiträgt und somit deren Kontrolle vereinfacht. Deshalb haben wir einen informationstheoretischen Ansatz verwendet, um diesen Beitrag für zielgerichtete und oszillatorische Armbewegungen mit zwei Freiheitsgraden zu charakterisieren. Die Ergebnisse bestätigten, dass

die unteren Kontrollebenen, einschließlich der Muskeln und ihrer Aktivierungsdynamik, wichtige Beiträge zur gesamten Kontrollhierarchie leisten. Beispielsweise führt ein einfaches, stückweise konstantes Muskelstimulationssignal, das nur wenig Information enthält, zu einer geschmeidigen Bewegung.

Der physiologische Detailgrad, der in unseren Muskel-Skelett-Modellen enthalten ist, ermöglicht nicht nur die Untersuchung von Theorien zur motorischen Kontrolle, sondern auch die Untersuchung von Größen wie inneren Kräften in Muskeln und Gelenken, die experimentell normalerweise nicht zugänglich sind. Diese Größen sind zum Beispiel in der Ergonomie und für die Entwicklung von Assistenzgeräten von Bedeutung. In einer Ganzkörpersimulationsstudie untersuchten wir den Beitrag des Dehnungsreflexes zu den resultierenden Muskelkräften bei einer aktiven externen Repositionierung des Hüftgelenkes für einen großen Bereich von Bewegungsgeschwindigkeiten. Wir fanden heraus, dass der relative Kraftbeitrag des Feedback-Mechanismus vom modellierten kognitiven Zustand abhängig ist und einen nicht vernachlässigbaren Beitrag leistet, insbesondere bei hohen Repositionsgeschwindigkeiten.

Die Gesamtheit unserer Ergebnisse zeigt, dass die Eigenschaften des Bewegungsapparates signifikant zur Erzeugung und Kontrolle von Bewegung beitragen und es daher wichtig ist, sie bei der Modellierung der menschlichen Bewegung zu berücksichtigen. Daher sprechen die Ergebnisse für die Kombination eines physiologisch fundierten biomechanischen und biochemischen Modells des Bewegungsapparates mit biologisch inspirierten Konzepten der motorischen Kontrolle. Diese Computersimulationen haben sich als ein nützliches Werkzeug zum Verständnis der Prozesse erwiesen, die der Erzeugung gesunder und pathologisch beeinträchtigter menschlicher Bewegungen zugrunde liegen.

Acknowledgments

First of all, I am sincerely and heartily grateful to my advisor Daniel Häufle for the fantastic support and thoughtful professional and personal guidance he granted me throughout the past years. I had the privilege of close supervision and interaction with Daniel in a small, young, and flexible group that allowed me to grow and develop my own working strategies. In this group, I am grateful to have worked with my colleagues Christina, Jonathan, Fabio, and Christian as well as the students that were part of our group and worked with me for some time: Alexander, Svenja, Ariane, Chryso, Cen-You, Junya, Isabelle, and Ilka. All of you contributed to this thesis to some extent and also you have made my everyday work life more colorful. Further, I would like to thank Martin Giese, Martin Butz and Tobias Siebert for supervising and/or examining my PhD project. Also, I am grateful to Winfried Ilg who always opened up a different perspective on things in our discussions. He and the students he supervised over the years were always welcomed lunch partners.

Besides my colleagues in Tübingen, I was lucky to be welcomed as part of a second group: the group around Syn Schmitt in Stuttgart. I would like to thank Syn for his supervision and advice on our common projects. To me, he was like a bonus advisor and the work with him allowed me to learn new methods and, thus, get a better view of the bigger picture around my topic. Also, I am grateful for those members of his group who have worked with me along the path, like Carola, Dan, Fabian, Johannes, Julia, Lennart, Marc, Maria, Michael, Oleksandr, Patrick, Simon, and Tobias. I would particularly like to thank Isabell for the great collaboration and for proofreading this thesis.

Further, I would like to thank the Hertie Institute for Clinical Brain Research and the Ministry of Science, Research and the Arts Baden-Württemberg who funded my work as part of the "Forschungsallianz System Mensch" (Az: 33-7533.-30-20/7/2).

In addition to that, I would like to thank my parents who always believed in me and made it possible for me to go to university and finally reach this goal. Last but not least, I am deeply grateful to Frank for his valuable advice and ideas as well as his never-ending patience and support.

Table of contents

List of important symbols, mathematical notations and abbreviations

List of Symbols

F	muscle force [N]
m	mass [kg]
a	muscle activity
t	time [s]
q	state variable in generalized coordinates
$\mathbf{M}$	mass matrix
$\mathbf{C}$	vector of gravitational, centrifugal and Coriolis forces
$\mathbb{R}$	set of real numbers
u	muscle stimulation
ψ	shoulder angle [rad]
φ	elbow angle [rad]
l	length [m]
λ	reference length in the feedback loop [m]
k_p	feedback gain based on lengths
δ	time delay in the feedback loop [s]
k_d	feedback gain based on velocities
MC	morphological computation
$S_{\text{abs.}}$	absolute sensitivity
$S_{\text{rel.}}$	relative sensitivity
M	torque applied by an assistive device
W	world state
A	actuator state
S	sensor state

Mathematical notation

x	scalar
$\mathbf{x}$	vector or matrix
$\boldsymbol{x}$	scalar x in generalized coordinates
$\boldsymbol{x}$	vector or matrix $\mathbf{x}$ in generalized coordinates
$\frac{df}{dx}$	total derivative of f with respect to x
$\frac{\partial f}{\partial x}$	partial derivative of f with respect to x
$\dot{x}$	first time derivation of x
$\ddot{x}$	second time derivation of x
x_i	i-th element of vector x
$\{x\}_0^1$	sets values $x < 0$ to 0 and $x > 1$ to 1

Control scheme symbols

- block that transforms the input signal to an output signal
- addition or subtraction of the input signals, depending on the signs at its input
- multiplication with the factor specified in the triangle

List of abbreviations

AAS agonistic-antagonistic setup

BEESR Biarticular Elbow Extension Shoulder Retroversion

BEFSA Biarticular Elbow Flexion Shoulder Anteversion

BE Biarticular Extension

BF Biarticular Flexion

CE contractile element

CPG central pattern generator

CSE Cervical Spine Extension

CSF Cervical Spine Flexion

CSSBL Cervical Spine Side Bend Left

CSSBR Cervical Spine Side Bend Right

DHM digital human model

DoF degree of freedom

EBD elementary biological drive

EE Elbow Extension

EF Elbow Flexion

EMG electromyogram or electromyography

EP equilibrium position

FEM finite element method

FE Foot Extension or finite element

FF Foot Flexion

HAbd Hip Abduction

HAdd Hip Adduction

HE Hip Extension

HF Hip Flexion

KE Knee Extension

KF Knee Flexion

LSE Lumbar Spine Extension

LSF Lumbar Spine Flexion

LSSBL Lumbar Spine Side Bend Left

LSSBR Lumbar Spine Side Bend Right

MBS multibody simulation

MC morphological computation

MEE Monarticular Elbow Extension

MEF Monarticular Elbow Flexion

MSA Monoarticular Shoulder Anteversion

MSR Monoarticular Shoulder Retroversion

MTU muscle-tendon unit

PD proportional-differential

PEE parallel elastic element

RoM range of motion

SAbd Shoulder Abduction

SAdd Shoulder Adduction

SDE serial damping element

SEE serial elastic element

SE Shoulder Extension

SF Shoulder Flexion

1 Introduction

1.1 Motivation

How are human movements generated and what happens if the neuronal control is impaired?

The coordinated movement of humans and other animals is a fascinating result of a dynamic interplay between the nervous system, the biomechanical structures (muscles, skeleton, and passive tissue), and the environment. Herein, an output descending from the central nervous system is combined with sensory feedback from the body. The resulting motor command leads to a stimulation of the muscles that drive the movement (Wise and Shadmehr, 2002). This structure allows the human to perform dynamic, but precise and robust movements. Neurodegenerative diseases or other pathological conditions can, however, impair this well-matched interplay by affecting neuronal structures that are involved in motor control, leading to movement disorders. One example of such a neurodegenerative disease is cerebellar ataxia. Due to atrophy in the cerebellum that can have different causes, patients suffering from cerebellar ataxia experience motor dysfunction, balance problems, and ataxia in limbs and gait (Smeets and Verbeek, 2014). For example, dysmetric voluntary movements lead to numerous difficulties in their everyday life (Topka et al., 1998b). Herein, the term *ataxia* describes unspecified movement incoordination typically due to dysfunction in or injury to the cerebellum, while *dysmetria* stands for movements over incorrect distances (hypermetria: overshoot, hypometria: undershoot) (Latash, 2012). Another example of impairment due to neurodegeneration is multiple sclerosis (MS) that can lead to tremor, dysmetria, or other ataxic conditions (Koch et al., 2007; Stadelmann, 2011). To find out more about possible causes and consequences of such movement disorders, the healthy and impaired generation of movement needs to be understood. For example, in the case of cerebellar ataxia, the role of the cerebellum in the movement generation and motor control needs to be identified to investigate the origins of the disorders that result from its dysfunction.

Due to the complexity of the human organism, many studies investigating human movements concentrate on the neuronal control, neglecting or simplifying the dynamics of the musculoskeletal system. In torque-driven models, for example, the outputs of the controller are torques that are directly applied to the joints. The benefit of these models is that the joint torques for a given desired trajectory can be calculated with standard inverse-dynamics algorithms. However, they do not consider the contribution of the viscoelastic properties of the muscle and activation dynamics. Thus, the conclusions drawn from torque-driven models about motor control might be unreliable, depending on the research question (Pinter et al., 2012). To account for this, additional negative feedback controllers (e.g., PD controller) can approximate

the net muscular, biochemical and low-level neuronal reflex response to external perturbations (e.g., Bhanpuri et al., 2014; Kalveram and Seyfarth, 2009). However, internal perturbations on the neuronal or muscular level can not be reproduced as the contribution of these components is not resolved separately. For the same reason, these models do not provide the possibility to investigate proprioceptive feedback that is based on muscle fiber lengths like the stretch reflex.

On the other hand, there are advanced and detailed musculoskeletal models that often use optimal control (Kistemaker et al., 2014; Pandy et al., 1990; Sharifi et al., 2016) or EMG based muscle stimulation signals (Lloyd and Besier, 2003; Sartori et al., 2011) to drive forward-dynamic simulations instead of including models of the neuronal control. However, there is evidence suggesting that especially the interaction of the mechanical properties of the human body with the neuronal control structures is key to understanding human motor control in its entirety (Pinter et al., 2012; Todorov and Jordan, 2002). The complex high-dimensional, nonlinear and redundant hierarchical structure of the human body may even simplify the task of movement control as the intrinsic characteristics of the musculoskeletal system can be exploited (Al Borno et al., 2020; Berniker et al., 2009; Haeufle et al., 2010a, 2020b; Koditschek et al., 2004; Loeb et al., 1999; Ting and Macpherson, 2005). Therefore, an interdisciplinary approach combining neuroscience, natural science, and engineering promises to provide a useful tool for gaining new insights into the generation of biological movement. This integrative method that investigates the coupling between the processing of neural information and the mechanical behavior of the human body has been termed as *neuromechanics* (Nishikawa et al., 2007).

To investigate concepts of motor control, human experiments are usually the first choice. Motion capture systems can measure the kinematics of human movements, force contact sensors can measure the force transmitted to the environment and with the aid of electromyography (EMG), the electric activity generated by muscle cells during a movement can be detected. However, the neuroscientific deductions from these experimental approaches are restricted due to their inherent ethical and practical limitations. For example, it is not possible to remove or add specific control structures to investigate their function. Therefore, computational neuro-musculoskeletal models provide a valuable framework to investigate concepts of motor control as they enable the testing of hypotheses to an extent that is not possible in human experiments (Pandy, 2001). On this basis, the hierarchical composition of motor control and the contribution of muscle-tendon dynamics and reflexes can be evaluated (Berniker et al., 2009; Campos and Calado, 2009; Kistemaker et al., 2013; Latash, 2010). Also, it can be investigated how the movement generation process has to be disturbed to reproduce the movement of patients with neurodegenerative movement disorders (Elias et al., 2018). This newly acquired knowledge about possible causes of these disorders might, for example, help to treat their symptoms in neuro-rehabilitation. Also, the design of assistive devices and (neuro-)prostheses can profit from models that make it possible to predict the behavior of humans in the interaction with the device and to study quantities like internal muscular and joint forces that are not experimentally accessible (Holzbaur et al., 2005; Pennestrì et al., 2007). Another possible benefit of the presented approach lies in ergonomic research: Using neuro-musculoskeletal models, the internal load due to external mechanical loads or repetitive movements (Glenday et al., 2020; Papachrysostomou, 2018) can be predicted. Additionally, the biological control concepts that are developed this way can be used to design new control mechanisms for technical devices (Nishikawa et al., 2007).

1.2 Objectives of the doctoral research

The overall goal of this work was to investigate biological motor control concepts and thus contribute to the understanding of the processes underlying the generation of healthy and impaired movements. Also, the roles of muscles and proprioceptive reflexes in the neuro-musculoskeletal interplay are to be investigated.

To this end, a computational neuro-musculoskeletal model of the arm is implemented to perform forward-dynamic computer simulations of human movements. The model should include the necessary level of physiological detail to allow for the investigation of motor control hypotheses that rely on the viscoelastic properties of the muscles and feedback mechanisms. At the same time, its implementation was supposed to be easy to use to allow for fast proofs of concept, rapid prototyping, and an easy entry for student projects. Using this model in combination with bio-inspired control concepts should make the reproduction of experimental data gained from human test subjects possible. The successful prediction of human behavior in these computer simulations can then indicate whether the suggested control hypothesis is plausible. This framework also allows for the investigation of the contribution of the characteristics of muscles and their activation dynamics to the observed behavior. In particular, the question of whether the control can be simplified due to the stabilizing characteristics of the musculoskeletal system should be addressed. In addition to that, the contribution of an implemented stretch reflex to the movement is tested in different scenarios.

Besides the reproduction of healthy human movements in computer simulations, a future goal would be to simulate pathological movements as well. For the investigation of the origins of these impaired movements, the neuronal control model can be disturbed and the effects can be compared to the behavior observed in patients with neurological motor disorders. Also, technical assistive devices to compensate for the disorders can be designed and tested in computer simulations. First steps in these directions are taken in this project.

1.3 Overview of the project

The doctoral project that is presented in this thesis resulted in five manuscripts that are described below (see Figure 1.1 and Chapter 2). For a better understanding, a summary of the used methods is given in Chapter 3. The structure and benefit of musculoskeletal models are explained and the arm model, as well as the whole-body model, that were used in the presented studies, are described. For the stimulation of the muscles, an overview of concepts of human motor control is given and the hybrid equilibrium point controller that was used is explained. In addition to that, Chapter 3 contains an introduction to biologically inspired robotic models and the concept of quantifying morphological computation.

Using the presented arm model, a bio-inspired control concept that includes a model of proprioceptive feedback was implemented. To validate this neuro-musculoskeletal model of the arm, human movements with and without external perturbations were reproduced (Chapter 4, Manuscript 1). To this end, a way to determine or optimize the involved control parameters needed to be found. Herein, the level of detail of the model allowed for the analysis of the internal muscular force response to the perturbations.

As we were not only interested in the movement of healthy subjects, we also took a first

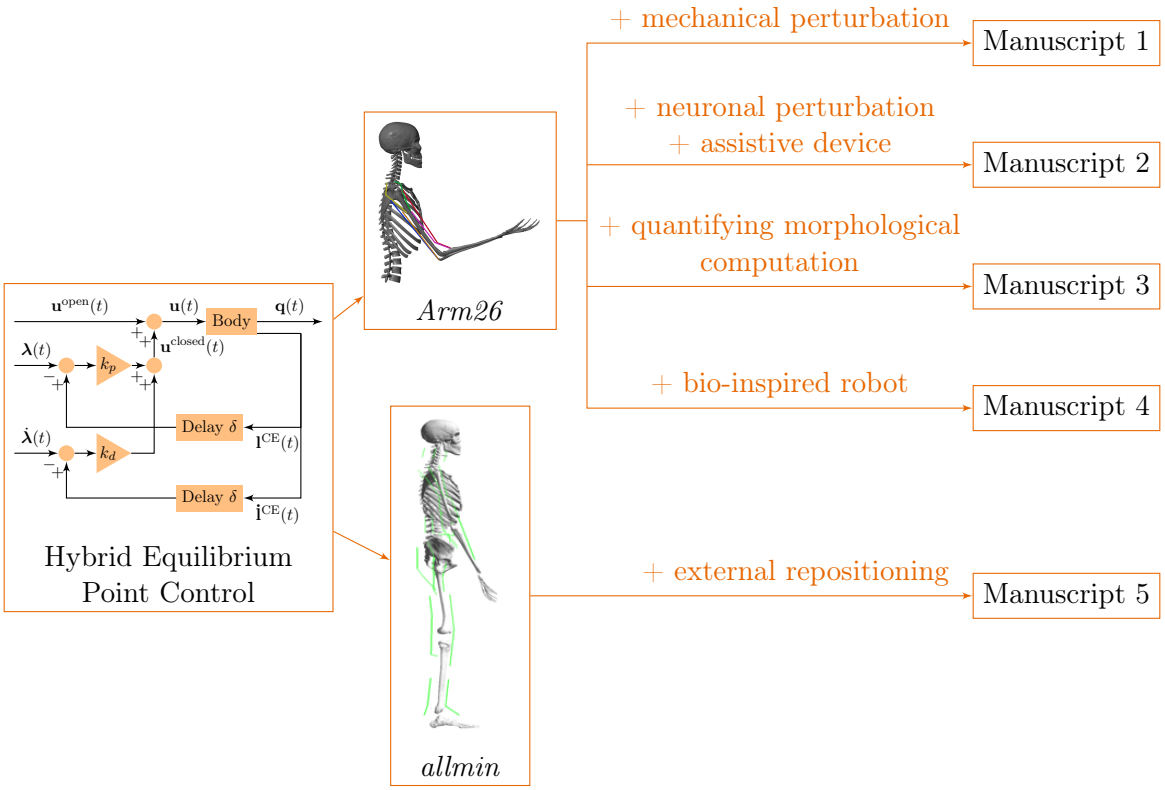

Figure 1.1: **Overview of the manuscripts that resulted from this doctoral project.** A bio-inspired hybrid equilibrium point controller (Section 3.3) was used to determine muscle stimulations for the multibody models of the musculoskeletal structure of the arm *Arm26* (Section 3.2.4) and the whole-body model *allmin* (Section 3.2.5). In the five manuscripts that resulted from this project, different kinds of perturbations were applied to the simulated movements. More details on the manuscripts can be found in Chapter 2.

step in the direction of modeling the motion of patients with neurological impairments and the design of simple assistive devices to compensate for the disorders (Chapter 5, Manuscript 2). Introducing a neuronal perturbation in the controller allowed us to produce an arm movement with an overshooting behavior (hypermetria) that resembled the movement of patients with neurodegenerative movement disorders. Simple assistive torque strategies were tested in the computer simulations with different arm models and possible implications for the design of wearable assistive devices were discussed.

The simulated perturbed movements indicated that the musculoskeletal system significantly contributes to the resulting movement: The mechanical zero-time delay response of the muscle characteristics compensated for the perturbations to a large extend and the influence of the implemented feedback mechanism (with optimized feedback gains) was rather small. To quantify the contribution of the musculoskeletal system to the resulting movement, we applied the concept of quantifying morphological computation on different levels on the biological motor

control hierarchy (Chapter 6, Manuscript 3).

Further, we showed that the control concept that we developed for the simulation model can be transferred to a biologically inspired robot to reproduce human movements (Chapter 7,Manuscript 4). This threefold framework of computer simulation, bio-inspired robot, and data from human experiments can also be used to investigate other bio-inspired control concepts.

To test the same control concept on a more complex model, we implemented it on a whole-body musculoskeletal model (Chapter 8, Manuscript 5). With this model, we looked at the reflex contribution to the muscle forces during an active external repositioning of the hip joint by a technical device.

Finally, to show that our control concept also transfers to other kinds of musculoskeletal models, we applied it to a finite element (FE) model. In comparison to multibody models, FE models consider the deformation of soft tissues and are therefore more suitable for some applications. However, predicting human movements using FE models is much more computationally expensive and, therefore, the determination of control parameters is more difficult. Hence, we investigated whether the control parameters that were optimized for a multibody model can be transferred to its FE equivalent (Chapter 9).

2 | List of publications and personal contributions

The content of this thesis is the product of a close collaboration with my colleagues and large parts have been submitted for peer-reviewed publication in scientific journals or conferences. Therefore, I would like to emphasize my personal contribution to these manuscripts below. All involved co-authors agreed to this listing.

2.1 Accepted publications

Manuscript 1 (Stollenmaier et al., 2020b)

Title:	Predicting perturbed human arm movements in a neuro-musculoskeletal model to investigate the muscular force response
Authors:	Katrin Stollenmaier, Winfried Ilg, and Daniel F.B. Haeufle
Journal:	Frontiers in Bioengineering and Biotechnology
Year:	2020
Link:	https://doi.org/10.3389/fbioe.2020.00308 (see also for electronic supplementary material)
Summary:	Using the musculoskeletal arm model *Arm26*, we simulated static perturbations of the inertia and damping properties of the arm, as well as dynamic torque perturbations for one-degree-of freedom movements around the elbow joint and reproduced experimental data with only one set of basic parameters.
Contribution:	The project was conceptualized in cooperation with Daniel Häufle and with advice from Winfried Ilg. I implemented the arm model and performed and analyzed the numerical experiments under the supervision of Daniel Häufle. I created all the figures for the manuscript and significantly contributed to all parts of the text. I wrote the electronic supplementary material describing the arm model.

Manuscript 2 (Stollenmaier et al., 2020d)

Title:	Simulating the response of a neuro-musculoskeletal model to assistive forces: implications for the design of wearables compensating for motor control deficits
Authors:	Katrin Stollenmaier, Ilka S. Rist, Fabio Izzi, and Daniel F.B. Haeufle
Conference:	IEEE International Conference on Biomedical Robotics and Biomechatronics – BioRob2020
Year:	2020
Summary:	Using the musculoskeletal arm model *Arm26*, we simulated two-degree-of-freedom point-to-point arm movements. By introducing inconsistent neuronal control parameters, we induced hypermetria. We implemented mechanical and low-level assistive torque strategies in simulation which lead to a reduction of hypermetria. We compared the predicted torques and powers to the prediction of a torque-driven model.
Contribution:	The project was conceptualized in cooperation with Daniel Häufle. I performed and analyzed one part of the numerical experiments and the corresponding figures, the rest of the results were created under my supervision by Ilka Rist who did a student project in our group. I drafted the manuscript and significantly contributed to all parts of the text of the manuscript.

Manuscript 3 (Haeufle et al., 2020a)

Title:	Morphological computation increases from lower- to higher-level of biological motor control hierarchy
Authors:	Daniel F.B. Haeufle, Katrin Stollenmaier, Isabelle Heinrich, Syn Schmitt, and Keyan Ghazi-Zahedi
Journal:	Frontiers in Robotics and AI, section Soft Robotics
Year:	2020
Summary:	We simulated point-to-point and oscillatory human arm movements with the neuro-musculoskeletal model *Arm26*. We then quantified morphological computation with an information entropy-based approach on different levels on the neuronal control hierarchy.
Contribution:	I performed the numerical experiments for the goal-directed movements and analyzed the results. I created most of the figures and contributed to the text of the manuscript as well as the electronic supplementary material.

2.2 Submitted manuscripts

Manuscript 5 (Stollenmaier et al., 2020a)

Title:	Active external propulsion of the hip activates internal reflex-based resistance forces depending on movement speed and neuronal preparedness: a full-body computer simulation study
Authors:	Katrin Stollenmaier, Daniel F.B. Haeufle, and Syn Schmitt
Journal:	Computer Methods in Biomechanics and Biomedical Engineering (submitted)
Year:	2020
Summary:	Using the whole-body musculoskeletal model *allmin* in combination with a model of low-level proprioceptive feedback, we investigated an external repositioning of the hip joint by a technical device. For a large range of movement velocities, we investigated the influence of the implemented feedback mechanism and the modeled cognitive state on the resulting internal muscular forces.
Contribution:	The project was conceptualized in cooperation with Syn Schmitt with advice from Daniel Häufle. I performed the numerical experiments and analyzed the results. I drafted and finalized the manuscript and created all the figures within. I significantly contributed to the electronic supplementary material describing the used model.

2.3 Manuscripts ready for submission

Manuscript 4 (Stollenmaier et al., 2020c)

Title:	A coherent numerical and biorobotic framework to investigate neuromuscular interaction in goal-directed arm movements
Authors:	Katrin Stollenmaier, Tobias Nadler, Christina Pley, Winfried Ilg, Simon Wolfen, Syn Schmitt, and Daniel F.B. Haeufle
Year:	2020
Summary:	We developed an integrated framework of data measured in human experiments, the numerical musculoskeletal model *Arm26*, and a bio-inspired robotic system with pneumatic muscles. The framework was designed for the investigation of control concepts for two-degree-of-freedom point-to-point arm movements, a setup commonly used in motor control studies. We demonstrate the relevance of this framework using the example of a bio-inspired intermittent hybrid equilibrium posture control scheme, which has previously been successfully used to reproduce human arm movements in computer simulation.

Contribution: The project was conceptualized in cooperation with Syn Schmitt and Daniel Häufle. I performed the numerical experiments and plotted and analyzed the resulting data from all three methods. I significantly contributed to all parts of the text of the manuscript, in particular the parts describing the computer simulation. I wrote the electronic supplementary material describing the arm model.

3 | Methodological background

3.1 Modeling the interplay of the neuro-musculoskeletal structures

What are computational neuro-musculoskeletal models and why do we use them?

Computational neuro-musculoskeletal models are a combination of mathematical models describing the neuronal and biophysical structures in the human body. They describe the signaling cascade from the nervous system via the musculoskeletal structure to a resulting movement (Figure 3.1). They consist of a musculoskeletal model describing the muscles interacting with the skeleton and a motor control model that describes the neuronal control of these muscles. These components are described in more detail in the following. One of the advantages of the usage of such computational neuro-musculoskeletal models is that they allow for the development and investigation of concepts of motor control. Single structures or whole functional units can be removed or perturbed without practical or ethical limitations and the effects can be analyzed.

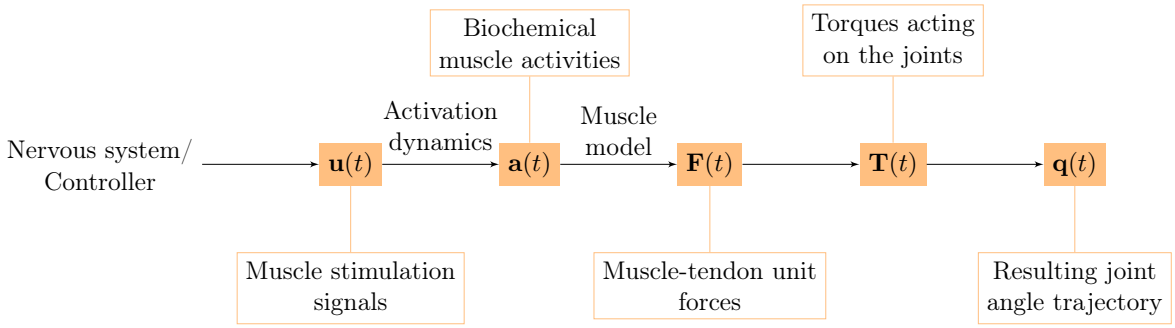

Figure 3.1: **The chain of signals that leads to a movement in the human body and that is represented in neuro-musculoskeletal models.** The nervous system, or in our models the control model that represents the nervous system, generates muscle stimulation signals over time $\mathbf{u}(t)$. Due to biochemical processes, these muscle stimulations lead to muscle activities $\mathbf{a}(t)$. The active muscles contract and thus produce forces $\mathbf{F}(t)$ in the muscle-tendon units. Due to the attachment of the muscles to the skeleton, these forces lead to torques $\mathbf{T}(t)$ acting on the joints resulting in a movement $\mathbf{q}(t)$.

3.2 Models of the musculoskeletal system

How can the interaction between the muscles and the skeleton be described by a mathematical model?

For modeling the musculoskeletal system, there are two main approaches: multibody simulation (MBS) and the finite element method (FEM). At the cost of high computational effort, finite element models allow for the detailed analysis of material stress and deformation and are therefore more suitable for modeling micro-scale mechanics of single body parts than simulating the dynamic behavior of limbs or the whole body (Guess et al., 2010; Lloyd et al., 2012; Navacchia et al., 2019; Stops et al., 2012). In particular, the determination of motor control parameters can be challenging due to the high computational costs of every simulation run (Chapter 9, Martynenko et al. (2019)). In contrast, multibody simulations using rigid bodies coupled via constrained joints and forces are a simplification of the real world that allows the computationally efficient calculation of the course of human movement with several degrees of freedom. Therefore, we chose this multibody approach for most of our musculoskeletal models.

A forward-dynamic multibody model allows for the prediction of kinematics based on given muscle stimulations without the need to invert the underlying set of differential equations. However, the determination of these muscle stimulations for a desired movement is nontrivial, especially due to the non-linearity of the system and the redundant setup of the muscles (see Section 3.3). Due to this complex control task, many models are reduced to single body parts or movement tasks. For example, there are forward-dynamic multibody models of walking (e.g., Anderson and Pandy, 2001; Geyer and Herr, 2010; Günther and Ruder, 2003; John et al., 2013), hopping (e.g., Haeufle et al., 2012a; van Soest et al., 1993b), rising (Shelburne and Pandy, 2002) and standing (e.g., Micheau et al., 2003; Walter et al., 2021) or arm movements (e.g., Huh and Todorov, 2009; Kistemaker et al., 2006; Pinter et al., 2012; Song et al., 2008).

3.2.1 Modeling the skeletal structure

The basis of the multibody approach is that, using Newton's second law ($\mathbf{F} = m\mathbf{a}$), the acceleration of each segment of the body can be determined given that the mass distribution and all forces acting on the body are known. Since the deformations of the body segments are small in comparison to the range of the movements we are interested in, the segments can be approximated by rigid bodies. This means that the position and orientation of a segment can be described by the position and orientation of its center of mass. Therefore, the equations of motion for each degree of freedom can be formulated using the Lagrange approach:

$$\frac{d}{dt}\frac{\partial \mathcal{L}}{\partial \dot{q}_i} - \frac{\partial \mathcal{L}}{\partial q_i} = \mathcal{F}_i\,, \tag{3.1}$$

where $\mathcal{L}(\boldsymbol{q}(t), \dot{\boldsymbol{q}}(t))$ denotes the Lagrange function that is defined as the difference between the kinetic and the potential energy of a system, q are generalized coordinates and $\mathcal{F}$ are generalized forces. The approximation of the joints by simplified joint models (e.g., revolute joints) allows for the calculation of joint forces as constraint forces acting between segments. This approximation is a useful simplification as it leads to a reduction of the degrees of freedom

and thus the number of state variables that are needed to describe the system. The differential equation of motion can then be written as (e.g., Henze, 2002; Legnani et al., 1996; Niku, 2020)

$$\mathbf{M}(\boldsymbol{q})\ddot{\boldsymbol{q}} + \mathbf{C}(\boldsymbol{q}, \dot{\boldsymbol{q}}) = \boldsymbol{\mathcal{F}}\,, \tag{3.2}$$

where $\mathbf{M} \in \mathbb{R}^{n^{\mathrm{DoF}} \times n^{\mathrm{DoF}}}$ is the mass matrix, $\mathbf{C} \in \mathbb{R}^{n^{\mathrm{DoF}}}$ is a vector of gravitational, centrifugal and Coriolis forces and $\boldsymbol{\mathcal{F}} \in \mathbb{R}^{n^{\mathrm{DoF}}}$ is a vector of forces (internal and external) acting on the mechanical part of the system. Herein, n^{DoF} stands for the number of degrees of freedom (DoFs) in the system. Solving these equations for the trajectory $\boldsymbol{q}(t)$ allows for the forward-dynamic prediction of the movement. Besides other software tools, the toolbox Simscape Multibody™ as part of Matlab®/Simulink® provides a graphical tool to set up and then numerically approximate the solution of the underlying equations of a multibody system.

3.2.2 Modeling the muscle-tendon characteristics

To generate movements, the skeletal structure needs to be connected to muscles that drive the movement. These muscles can be represented by mathematical models. However, in order to draw meaningful deductions about concepts of motor control by testing them with musculoskeletal models, these models need to provide the necessary level of physiological detail (Pinter et al., 2012) and – if available – the models should be validated by reproducing experimentally observed data. For validation, the simulation results can, for example, be compared to kinematic data from perturbation experiments (see Chapter 4). The level of detail that is required to investigate motor control concepts depends on the research question and on the control concept that is used.

The criteria on the level of detail that we chose for our models are that they consider

- muscle-fiber characteristics by using Hill-type muscle models (Haeufle et al., 2014a; Millard et al., 2013; Siebert and Rode, 2014),
- non-linear tendon elasticity,
- muscle activation dynamics (Hatze, 1977; Rockenfeller et al., 2015),
- antagonistic muscle setup (Schmitt et al., 2019b) and
- anatomical muscle routing (Hammer et al., 2019; Holzbaur et al., 2005).

The choice of these criteria is justified in the following: It is important to include the viscoelastic properties as well as the force-length and force-velocity relations of the muscle-tendon structures since these relations determine the muscle forces and, for example, elastic energy is stored in the tendons (Biewener and Roberts, 2000). Also, the intrinsic muscle properties provide an immediate response to perturbations which tend to stabilize the system and hence simplify control (Daley et al., 2009; Loeb et al., 1999; Nishikawa et al., 2007). This stabilizing behavior has been termed *preflex* (Brown et al., 1995; Prilutsky and Edwards, 2015) as it acts similar to neural reflexes but without the neuronal delay. These characteristics of the muscle-tendon structures in combination with an antagonistic muscle setup allow for the emergence of stable equilibrium positions (Feldman and Levin, 2009; Kistemaker et al., 2007b) that can

be utilized in motor control (see also Section 3.3). Therefore, both the muscle-fiber characteristics and the non-linear tendon elasticity is included in our models. In addition to that, the biochemistry that transforms muscle stimulations to muscle activities plays an important role in the control of movement as, due to its smoothening properties, it allows for smooth trajectories based on discontinuous muscle stimulation signals. The last criterion that we require our models to fulfill is anatomical muscle routing. It provides realistic moment arms and ensures that the effective direction of the muscle forces is not reverted for extreme joint angles. Also, muscle-bone contact forces can be calculated when the routing of the muscles around the bones is described.

3.2.3 Our musculoskeletal models

The models that are used in most studies presented here are forward-dynamic multibody models of the musculoskeletal system. Additionally, in Chapter 9, a comparison to a finite element (FE) model is drawn. In both kinds of models, a controller (see Section 3.3, Figure 3.7) determines a muscle stimulation pattern over time. Using a model of the muscles' activation dynamics, the muscular activity depending on the current muscle stimulation and the fiber length is predicted (Hatze, 1977; Rockenfeller et al., 2015). The force of each muscle-tendon unit (MTU) is then calculated using a macroscopic Hill-type muscle model that accounts for force-length-velocity characteristics, tendon and parallel tissue elasticity, and damping in the tendon (Haeufle et al., 2014a). To match realistic lever arms, muscle path geometry, i.e., muscle origin, insertion, and deflection, is implemented. To this end, we use a via-ellipse approach, that restricts the muscle path to geometric ellipses that are attached to the rigid bones (Hammer et al., 2019). Using this algorithm, muscle-bone contact forces and internal joint loadings can be predicted.

3.2.4 The arm model *Arm26*

In most of the studies that are described in this thesis, we focused on goal-directed point-to-point movements of the human arm with one or two degrees of freedom. We chose this movement because most voluntary movements of the upper extremity consist of either moving from one pose to another or to hold a pose (Shadmehr, 2017). Also, this movement is the task of many neuroscientific experiments with and without the use of a manipulandum (Campos and Calado, 2009).

Therefore, the forward-dynamic multibody model *Arm26* with two degrees of freedom and six muscles was developed (Figure 3.2). This model has been used in Chapters 4 to 7 (Manuscript 1 to Manuscript 4) and is described in detail in the following. Its implementation was designed to be easy to use to allow for fast proofs of concept, rapid prototyping, or an easy entry for student projects. Large parts of the following model description were published/submitted as electronic supplementary material accompanying Haeufle et al. (2020a); Stollenmaier et al. (2020a,b,c). It was written in collaboration with Daniel Häufle.

The neuro-musculoskeletal model *Arm26* consists of a musculoskeletal model of the arm with two degrees of freedom actuated by six muscles and a controller. The model is implemented using Matlab® R2018a/Simulink® with the Simscape Multibody™ environment. For a better overview, the implementation of the model is divided into three parts: the mechanical part (representing the bone structure and the muscle routing), the actuation of this mechanical part

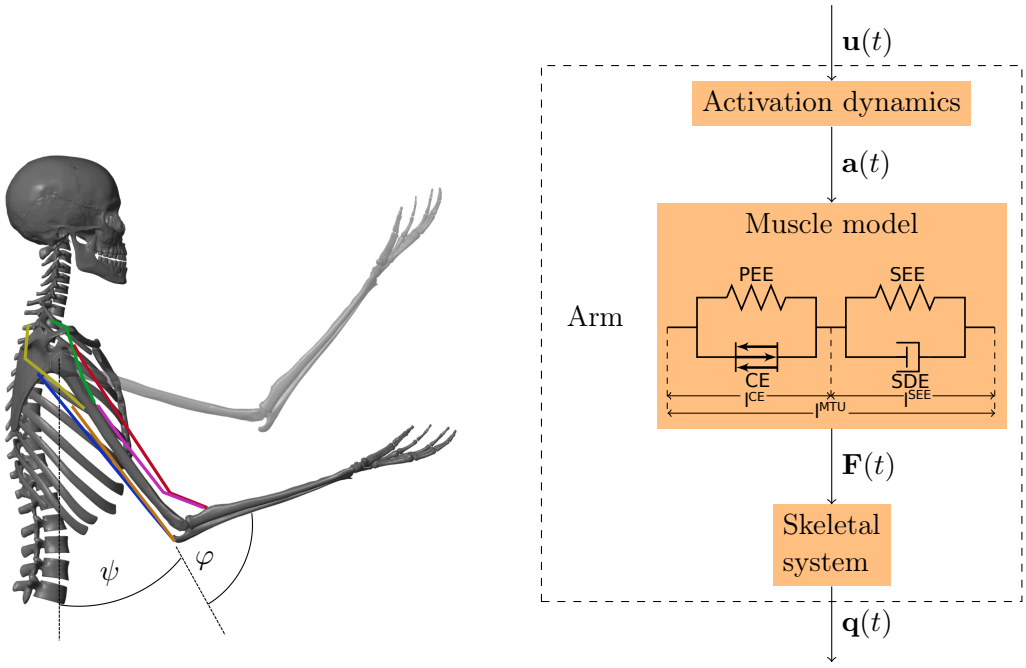

(a) (b)

Figure 3.2: **Visualization of the arm model *Arm26*.** (a) Visualization of the musculoskeletal model of the arm and the definition of the shoulder angle $\psi(t)$ and the elbow angle $\varphi(t)$ and (b) Structure of the arm model: the motor command $\mathbf{u}(t)$ is fed into the model of the activation dynamics of muscles which relates the neuronal stimulation to muscular activity $\mathbf{a}(t)$ that drives the muscle model. The muscles produce forces $\mathbf{F}(t)$ that act on the skeletal system resulting in a simulated movement $\mathbf{q}(t) = [\varphi(t), \psi(t)]$ of the arm.

(muscle-tendon structures) and the controller (nervous system) which provides the input to the actuation part.

3.2.4.1 Musculoskeletal model of the arm: Mechanics and Actuation

The musculoskeletal model *Arm26* of the human arm uses the same geometry and muscle parameters as the simulation model described in Driess et al. (2018) which is based on Bayer et al. (2017). It consists of two rigid bodies (lower and upper arm) that are connected via two one-degree-of-freedom revolute joints that represent the shoulder and elbow joint. This multibody system is actuated by six MTUs, four monoarticular and two biarticular muscles (see Figure 3.2a). The muscles are modeled as lumped muscles, i.e. they represent a multitude of anatomical muscles:

1. Monarticular Elbow Flexion (MEF) (short: Elbow Flexion (EF)):
   m. brachioradialis, m. brachialis, m. pronator teres, m. extensor carpi radialis

2. Monarticular Elbow Extension (MEE) (short: Elbow Extension (EE)):
   m. triceps lateralis, m.triceps medialis, m. an-coneus, m. extensor carpi ulnaris

3. Biarticular Elbow Flexion Shoulder Anteversion (BEFSA) (short: Biarticular Flexion (BF)):
   m. biceps brachii caput longum and caput breve

4. Biarticular Elbow Extension Shoulder Retroversion (BEESR) (short: Biarticular Extension (BE)):
   m. triceps brachii caput longum

5. Monoarticular Shoulder Anteversion (MSA) (short: Shoulder Flexion (SF)):
   m. deltoideus (pars clavicularis, anterior, lateral), m. superior pectoralis major, m. coracobrachialis

6. Monoarticular Shoulder Retroversion (MSR) (short: Shoulder Extension (SE)):
   m. deltoideus (pars spinalis, posterior), m. latissimus dorsi

The MTU structure is modeled using an extended Hill-type muscle model as described in Haeufle et al. (2014b) with muscle activation dynamics as introduced by Hatze (1977). The muscle model is a macroscopic model consisting of four elements: the contractile element (CE), the parallel elastic element (PEE) and the serial elastic element (SEE) and serial damping element (SDE), as illustrated in Figure 3.2b. The inputs to the muscle model are the length of the MTU l^{MTU}, the contraction velocity of the MTU $\dot{l}^{\mathrm{MTU}}$ and the muscular activity a. The output of the muscle model is a one-dimensional muscle force F^{MTU}. This force drives the movement of the skeletal system. For the routing of the muscle path around the joints, deflection ellipses are implemented as described by Hammer et al. (2019) (see Figure 3.3). The muscle path can move within these ellipses and is deflected as soon as it touches the boundary.

All in all, the governing model dependencies for all muscles $i = 1, ..., n$ are:

$$\dot{l}_i^{\mathrm{CE}} = f^{\mathrm{CE}}(l_i^{\mathrm{CE}}, l_i^{\mathrm{MTU}}, \dot{l}_i^{\mathrm{MTU}}, a_i) \tag{3.3}$$

$$\dot{a}_i = f^{a}(a_i, u_i, l_i^{\mathrm{CE}}) \tag{3.4}$$

$$F_i^{\mathrm{MTU}} = f^{F}(l_i^{\mathrm{MTU}}, \dot{l}_i^{\mathrm{MTU}}, l_i^{\mathrm{CE}}, a_i) \tag{3.5}$$

$$\ddot{\mathbf{q}} = f^{q}(\dot{\mathbf{q}}, \mathbf{q}, \mathbf{F}^{\mathrm{MTU}})\,, \tag{3.6}$$

where $\mathbf{q}$ denotes a generalized state vector, in this case it can be defined as $\mathbf{q} = [\varphi, \psi]$ and $\mathbf{F}^{\mathrm{MTU}} = \left\{F_i^{\mathrm{MTU}}\right\}_{i=1}^{n}$.

The mechanical parameters of the arm segments are taken from Kistemaker et al. (2006) and can be found in Table A1.1. The positions and sizes of the deflection ellipses were chosen in order to match moment arms in literature (see Figure 3.4) and can be found in Appendix A1. For more details on this see Suissa (2017). The (non-)muscle-specific parameters can be found in Table A1.3 and Table A1.2.

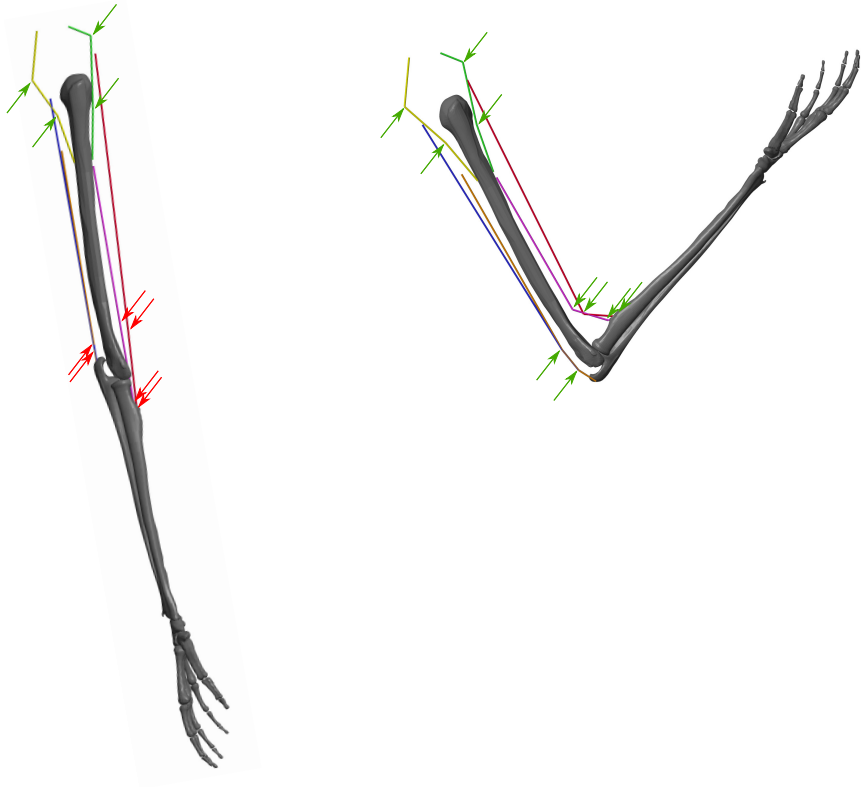

Figure 3.3: **Illustration of the positions of the deflection ellipses that are used for the muscle routing in two different arm positions.** Green arrows indicate active ellipses that deflect the muscle path, while red arrows indicate inactive ellipses that do not change the muscle path.

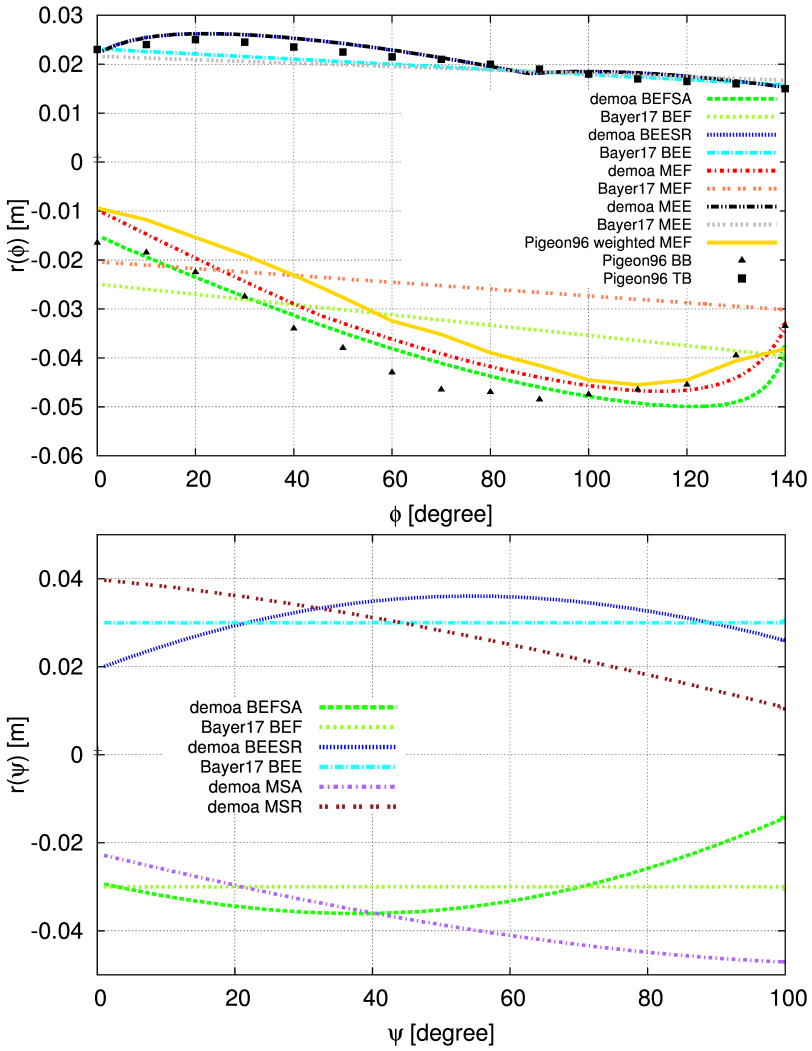

Figure 3.4: **Comparison of the moment arms of the muscles in the model with simulation and experimental data from literature for the elbow muscles (upper plot) and the shoulder muscles (lower plot)**. The lines marked with *demoa* refer to the model by Suissa (2017) on which our model is based (for the naming of the muscles see Table A1.3). We use the same geometry and position and size of the ellipses, so our moment arms are the same as in the *demoa* model. The moment arms are compared to a calculatory model by Bayer et al. (2017) (here M/B stands for mono- and biarticular, E stands for elbow and F/E stands for flexion and extension, respectively) and to experimental data. The black marks show experimental data of the biceps brachii (BB) and the triceps brachii (TB) taken from Pigeon et al. (1996). The yellow line shoes a weighted combination of the monoarticular flexor muscles that are represented by the MEF in the model. They are weighted according to their proportion of the joint torques, see Aumüller et al. (2017); Sobotta (2010). The figure was taken from Suissa (2017) with kind permission of the author.

3.2.5 The full-body human model *allmin*

In Chapter 8 (Manuscript 5), a full-body human model is used (Figure 3.5). It is a multibody model with 15 rigid bodies that are connected via 14 joints. 36 antagonistically arranged muscle-tendon units move the skeleton. The model is implemented using a multibody simulation code in C/C++.

A detailed description of this model can be found below. Note that large parts of the following model description were submitted as electronic supplementary material accompanying Stollenmaier et al. (2020a). It was written in collaboration with Johannes Walter, Marc Jacob, Patrick Lerge, and Syn Schmitt.

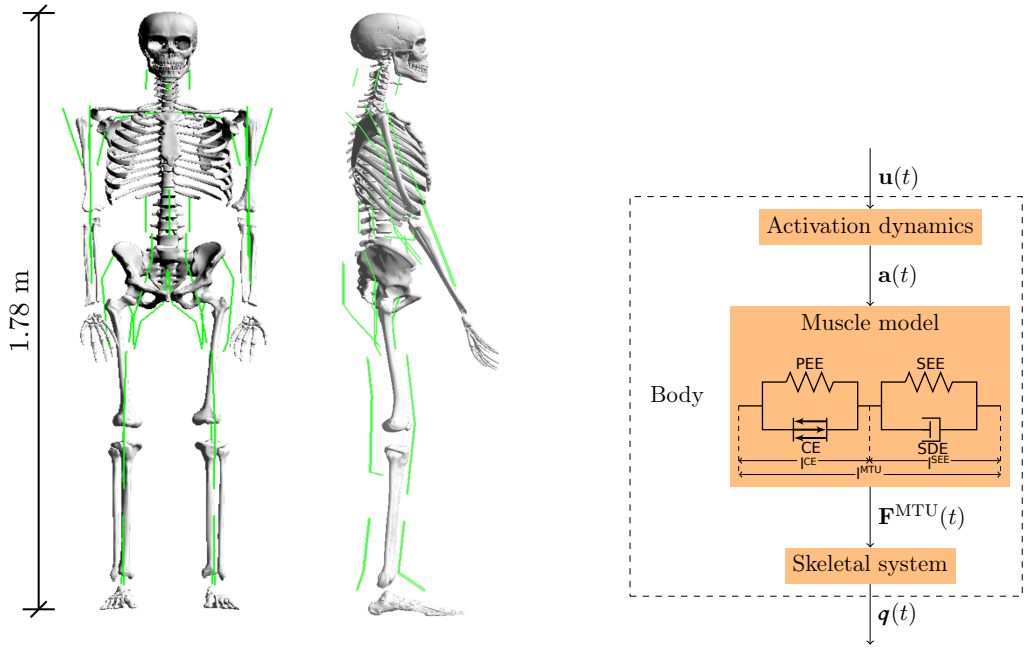

(a) (b)

Figure 3.5: **Visualization of the full-body model *allmin*.** (a) Frontal and side view of the visualization of the musculoskeletal model of the human body. The green lines show the muscle geometry. (c) Structure of the model: the motor command $\mathbf{u}(t) \in \mathbb{R}^{n^{\mathrm{MTU}}}$ is fed into the model of activation dynamics (Hatze, 1977; Rockenfeller and Günther, 2018) of muscles which relates the neuronal stimulation to muscular activity $\mathbf{a}(t) \in \mathbb{R}^{n^{\mathrm{MTU}}}$ that drives the muscle model (Haeufle et al., 2014b). The muscles produce forces $\mathbf{F}^{\mathrm{MTU}}(t) \in \mathbb{R}^{n^{\mathrm{MTU}}}$ that act on the rigid bodies of the skeletal system. The resultant joint torques $\boldsymbol{\mathcal{F}}^{\mathrm{MTU}}$ depend on the respective moment arms $\frac{\partial \mathbf{l}^{\mathrm{MTU}}}{\partial \boldsymbol{q}}$. In combination with external forces, this results in a movement of the DoFs $\boldsymbol{q}(t) \in \mathbb{R}^{n^{\mathrm{DoF}}}$ of the body.

The musculoskeletal model *allmin* consists of $n^{\mathrm{RGB}} = 15$ rigid bodies (see Table A2.2). The rigid bodies are connected via 14 joints (see Table A2.1) including $n^{\mathrm{DoF}} = 20$ degrees of freedom. Each degree of freedom (DoF) (except for the wrist) is controlled by an agonistic-antagonistic

setup (AAS) beeing congruent with the elementary biological drive (EBD) as described by Schmitt et al. (2019a). The musculoskeletal model is actuated by $n^{\mathrm{MTU}} = 36$ muscle-tendon units (MTUs) (see Table A2.4 and Figure 3.5a for first impression).

The model is implemented in C/C++ code within our in-house multi-body simulation code *demoa*.

3.2.5.1 The Multibody System

The skeletal system is modeled as a chain of rigid bodies, connected by rotational joints and described by differential equations. The resulting DoFs $\boldsymbol{q}(t) = [q_1(t), \ldots, q_{n^{\mathrm{DoF}}}(t)]^T \in \mathbb{R}^{n^{\mathrm{DoF}}}$ of these rotational joints describe the movement of the rigid bodies over time and are referred to as generalized coordinates. For the equations of motion, a Lagrangian formulation with the generalized coordinates $\boldsymbol{q}(t)$ as state variables is realized (see Section 3.2), which can be set up algorithmically, e.g. as described by Legnani et al. (1996). The evaluation of this algorithm leads to the differential equation of motion of the rigid body system in the form

$$\mathbf{M}(\boldsymbol{q})\ddot{\boldsymbol{q}} + \mathbf{C}(\boldsymbol{q}, \dot{\boldsymbol{q}}) = \boldsymbol{\mathcal{F}}, \tag{3.7}$$

where $\mathbf{M} \in \mathbb{R}^{n^{\mathrm{DoF}} \times n^{\mathrm{DoF}}}$ is the mass matrix, $\mathbf{C} \in \mathbb{R}^{n^{\mathrm{DoF}}}$ is a vector of gravitational, centrifugal and Coriolis forces and $\boldsymbol{\mathcal{F}} \in \mathbb{R}^{n^{\mathrm{DoF}}}$ is a vector of forces (internal and external) acting on the mechanical part of the system. Hereby $\mathcal{F}$ includes forces, e.g. due to contact of the body to the environment (external), as well as forces of the biological structures, such as muscles, joint limitations (internal).

3.2.5.2 Joint limitations

The joint limitations are modeled as linear one-sided spring-damper elements, acting directly on the respective DoF:

$$\mathcal{F}_i^{\mathrm{lmt}} = \begin{cases} k_l(q_i - q_{l,i}) + d_l\dot{q}_i, & q_i < q_{l,i} \\ 0, & q_{l,i} \leq q_i \leq q_{u,i} \\ k_u(q_i - q_{u,i}) + d_u\dot{q}_i, & q_i > q_{u,i} \end{cases} \tag{3.8}$$

with the lower and upper threshold angles $q_{l/u}$, corresponding to the respective range of motion (RoM) (Table A2.1), and linear spring and damping parameters $k_{l/u} = 100\,[\frac{\mathrm{Nm}}{\mathrm{rad}}]$ and $d_{l/u} = 0.001\,[\frac{\mathrm{Nm{\cdot}s}}{\mathrm{rad}}]$. For the joints of the lumbar and cervical spine, as well as the wrist, the same force law is used to model passive properties with different parameters. The upper and lower threshold angles are set to $q_{l/u} = 0$ and the spring and damping parameters are set to $k_{cs} = 10\,[\frac{\mathrm{Nm}}{\mathrm{rad}}]$, $d_{cs} = 0.2\,[\frac{\mathrm{Nm{\cdot}s}}{\mathrm{rad}}]$, $k_{ls} = 20\,[\frac{\mathrm{Nm}}{\mathrm{rad}}]$, $d_{ls} = 0.2\,[\frac{\mathrm{Nm{\cdot}s}}{\mathrm{rad}}]$, $k_{wr} = 15\,[\frac{\mathrm{Nm}}{\mathrm{rad}}]$, $d_{wr} = 1\,[\frac{\mathrm{Nm{\cdot}s}}{\mathrm{rad}}]$.

3.2.5.3 Muscles

The muscles are modeled as lumped muscles, i.e. they represent a multitude of anatomical muscles and motor units. A list of all included muscle elements can be found in Table A2.4. The MTU structure is modeled using an extended Hill-type muscle model as described in Haeufle et al. (2014b) with muscle activation dynamics as introduced by Hatze (1977) and

simplified by Rockenfeller and Günther (2018). Herein, the muscles are activated using a 1st order differential equation of normalized calcium ion concentration (Rockenfeller et al., 2014)

$$\dot{\gamma}(t) = M_{\mathrm{H}}(u(t) - \gamma(t)) \tag{3.9}$$

and a nonlinear mapping onto the muscles activation

$$a(t) = \frac{a_0 + \varpi}{1 + \varpi}, \tag{3.10}$$

with $\varpi(\gamma(t), l^{\mathrm{CE}}(t)) = (\gamma(t) \cdot \rho(l^{\mathrm{CE}}))^{\nu}$ and $\rho(l^{\mathrm{CE}}) = \varpi^{\mathrm{opt}} \cdot \frac{l^{\mathrm{CE}}}{l^{\mathrm{opt}}} = \gamma_{\mathrm{c}} \cdot \rho_0 \cdot \frac{l^{\mathrm{CE}}}{l^{\mathrm{opt}}}$. The parameter values are chosen muscle non specifically and are given in Table A2.5.

The muscle model is a macroscopic model consisting of four elements: the CE, the PEE, the SEE and SDE, as illustrated in Figure 3.5b. Herein, the muscle fibers and their contraction dynamics are described by a contractile element (CE) representing the cross-bridge-cycle of the myosin heads and a parallel elastic element (PEE) representing the passive connective tissue in the muscle belly. The viscoelastic properties of tendons are approximated using a series elastic element (SEE) and a serial damping element (SDE).

The inputs to the muscle model are the length of the MTU l^{MTU}, the contraction velocity of the MTU $\dot{l}^{\mathrm{MTU}}$ and the muscular activity a. The output of the muscle model is a one-dimensional muscle force F^{MTU}. This force drives the movement of the skeletal system.

For the routing of the muscle path around the joints, deflection ellipses are implemented as described by Hammer et al. (2019). The muscle path can move within these ellipses and is deflected as soon as it touches the boundary. For the investigations presented here, we set the length of both half-axes of all ellipses to zero, resulting in fixed via points. The position of these points can be found in Table A2.3. The resulting moment arms translate the muscle force $\mathbf{F}^{\mathrm{MTU}}$ to generalized forces $\boldsymbol{\mathcal{F}}^{\mathrm{MTU}}$ acting on the DoFs of the system

$$\boldsymbol{\mathcal{F}}^{\mathrm{MTU}} = \frac{\partial \mathbf{l}^{\mathrm{MTU}}}{\partial \boldsymbol{q}} \cdot \mathbf{F}^{\mathrm{MTU}}. \tag{3.11}$$

All in all, the governing model dependencies for all muscles $i = 1, ..., n$ are:

$$\begin{aligned}
\dot{l}_i^{\mathrm{CE}} &= f^{\mathrm{CE}}(l_i^{\mathrm{CE}}, l_i^{\mathrm{MTU}}, \dot{l}_i^{\mathrm{MTU}}, a_i) && (3.12)\\
\dot{a}_i &= f^{a}(a_i, u_i, l_i^{\mathrm{CE}}) && (3.13)\\
F_i^{\mathrm{MTU}} &= F_i^{\mathrm{MTU}}(l_i^{\mathrm{MTU}}, \dot{l}_i^{\mathrm{MTU}}, l_i^{\mathrm{CE}}, a_i) && (3.14)\\
\ddot{\boldsymbol{q}} &= f^{\boldsymbol{q}}(\dot{\boldsymbol{q}}, \boldsymbol{q}, \mathbf{F}^{\mathrm{MTU}}, \boldsymbol{\mathcal{F}}^{\mathrm{lmt}}, \boldsymbol{\mathcal{F}}^{\mathrm{ext}}), && (3.15)
\end{aligned}$$

where $\boldsymbol{q} = \{q_i\}_{i=1}^{n^{\mathrm{DoF}}}$ denotes a generalized state vector that contains all joint angles and $\mathbf{F}^{\mathrm{MTU}} = \{F_i^{\mathrm{MTU}}\}_{i=1}^{n}$, $\boldsymbol{\mathcal{F}}^{\mathrm{lmt,i}} = \{\mathcal{F}_i^{\mathrm{lmt}}\}_{i=1}^{n}$ and $\boldsymbol{\mathcal{F}}^{\mathrm{ext}} = \{\mathcal{F}_i^{\mathrm{ext}}\}_{i=1}^{n}$ contain the muscle forces, the joint limitation forces and the external forces, respectively.

3.3 Models of human motor control

How do the muscles need to be stimulated in order to generate a desired movement?

To investigate biological motor control theories using the aforementioned computational musculoskeletal models, control models that determine the muscle stimulations over time need to be formulated. In the research field of human motor control, there are many theories on how movement is planned and controlled (for reviews on this topic see, e.g., Krakauer and Shadmehr, 2007; Latash et al., 2010; Nishikawa et al., 2007; Östh et al., 2015; Scott and Norman, 2003; Wolpert, 1997; Wolpert et al., 2011), but there are still various open questions (Karniel, 2011; Nordin et al., 2017). The overall question that motivated this particular work is how human movement is generated and what happens if the neuronal control is perturbed. A concrete aspect of this quite general question that we focused on is the contribution of muscle dynamics to biological motor control. In particular, we investigated how the control can be simplified due to the intrinsic characteristics of the musculoskeletal system. Therefore, we looked at control concepts that explicitly make use of these characteristics.

In motor control theory, the term *internal model* describes the neural representation of the relationship between action and consequences that are updated with experience (Latash, 2012), possibly located in the cerebellum (Kawato, 1999). More precisely, they describe an input-output relationship between the control signals and the resulting movement (forward internal models) or the inverse (inverse internal models) that can be used to control movements (Wolpert et al., 1998). Due to the large feedback delays in biological systems in contrast to robotic systems, fast and smooth movements cannot be achieved when the muscular stimulation is controlled only based on feedback (Kawato, 1999; Ostry and Feldman, 2003; Wolpert et al., 1998). Therefore, some kind of feed-forward control is likely to be involved. To this end, inverse internal models could determine the muscular stimulation that is necessary to obtain a desired movement. In addition to that, forward internal models could be used to predict the movement based on an efference copy to estimate the error between actual and desired movement without a time delay (Wolpert et al., 1998) with the possible use to finetune the inverse model (see Section 10.2). However, it is unclear how detailed these models need to be in order to control human movement. The inverse dynamics model hypothesis proposes that the nervous system learns an inverse dynamics model of the controlled object. On the other hand, the equilibrium point control hypothesis argues that complex computations can be avoided by exploiting the spring-like properties of the musculoskeletal system and the proprioceptive feedback loops (Kawato, 1999; Wolpert et al., 1998). The latter hypothesis is used and evaluated in this work.

3.3.1 Equilibrium point control

The equilibrium point hypothesis (Feldman, 1986) is based on the observation that the antagonistic setup of the muscle-tendon units with tuneable viscoelastic characteristics in the joint allows for the emergence of *equilibrium positions* or *equilibrium postures* (EPs) (Feldman and Levin, 2009; Kistemaker et al., 2007b). These EPs (set points) are stable positions where the sum of all torques acting on a joint is zero (Figure 3.6) and short external perturbations can be compensated due to the spring-like properties of muscles (McIntyre and Bizzi, 1993). Given

a constant set of open-loop muscle stimulations, an EP is reached and stabilized due to the passive characteristics of the muscle-tendon unit, without the need for any neuronal feedback control (Figure 7.2). Herein, the resulting EP depends on the external forces that act on the body.

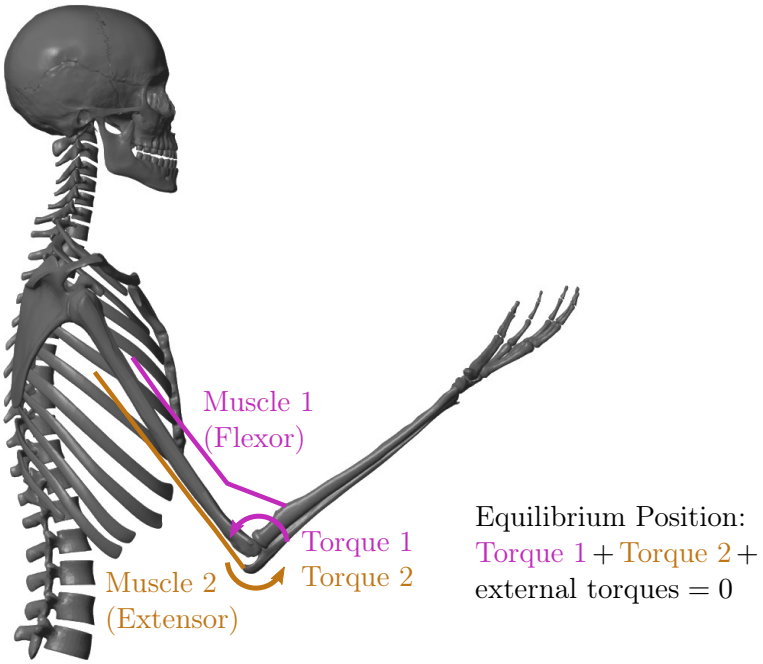

Figure 3.6: **Emergence of an equilibrium position (EP) for a joint that is actuated by two antagonist muscles (elementary biological drive).** The forces that the muscles produce depend on their activity a and the current lengths l^{CE} of their muscle fibers. Depending on the muscles' lever arms, they produce a torque acting on the joint. An EP is reached when the sum of these torques and external torques is zero.

Using a continuous sequence of these EPs to generate a movement is the basis of equilibrium trajectory control (Feldman and Levin, 2009; Flash, 1987; Gribble and Ostry, 2000; Gribble et al., 1998). Furthermore, due to the dynamics of the musculoskeletal system, smooth trajectories can be generated by a combination of only a few discrete EPs in intermittent control concepts (Bayer et al., 2017; Brändle et al., 2020; Günther and Ruder, 2003; Kistemaker et al., 2006; Koike et al., 2011; Wochner et al., 2020). It has been observed that shifting between EPs intermittently leads to faster movements (Kistemaker et al., 2006). Even though, in this formulation, the feed-forward signal is a piecewise constant function over time, a smooth trajectory emerges from the muscles' activation and contraction dynamics and the inertia of the limbs. In this case, the inverse internal model needs to relate a desired movement with given boundary conditions to a suitable combination of equilibrium positions over time. So, there is no need for solving the complex inverse dynamics problem in order to control movement. The observation that smooth movements can be generated solely based on a feedforward signal has

an impact on the understanding of the role and necessity of feedback. Nevertheless, we include a model of proprioceptive feedback in our model as it promises to allow for more valid reactions to external perturbations.

In our models, the model of biological motor control combines a feed-forward command $\mathbf{u}^{\text{open}}(t)$ with a feedback signal $\mathbf{u}^{\text{closed}}(t)$ that incorporates proprioceptive feedback (Figure 3.7). Therefore, this model can be called a hybrid equilibrium point controller as it combines the open-loop command (α model) with a model of the stretch reflex that is based on muscle spindle feedback (λ model). The total motor command $\mathbf{u}(t)$ is a sum of those components and represents α-motor neuron firing rate. For each muscle i, the muscle stimulation is then calculated as

$$u_i(t) = \left\{ u_i^{\text{open}}(t) + u_i^{\text{closed}}(t) \right\}_0^1 , \tag{3.16}$$

where the operation $\{u_i\}_0^1$ sets values $u_i < 0$ to 0 and $u_i > 1$ to 1. This formulation is based on the assumption that every muscle is stimulated by one α-motor neuron that linearly adds the central open-loop input and the afferent feedback signal. The model of the stretch reflex assumes that muscle spindles detect changes in the length and contraction velocity of muscle fibers and induce α-motor neuron activity if a certain threshold is passed.

For the forward-dynamic simulation of human movement that was described above, the muscle stimulations need to be determined beforehand in order to generate a movement. However, finding the muscle stimulations for a given movement task is non-trivial due to the redundancy of the musculoskeletal system (degree of freedom problem or motor equivalence problem, see Bernstein (1967), Shadmehr (1991)). For example, for goal-directed movements between two points, infinitely many trajectories are possible and even for one certain trajectory, many combinations of muscle stimulations lead to the same motion. Therefore, assumptions have to be made to resolve the redundancy and determine a unique set of muscle stimulation patterns. Many models resort to (bio-inspired) optimality principles and define a cost function that allows for the optimization of the muscle stimulations (Alexander, 1997; Flash and Hogan, 1985; Uno et al., 1989; Wochner et al., 2020). Using our neuro-musculoskeletal model, the open-loop muscle stimulations $\mathbf{u}^{\text{open}}(t)$ can be optimized assuming that the movement consists of a limited number of EPs and setting a desired level of muscle co-contraction (for more details see Chapter 4 and Chapter 7).

The closed-loop component $\mathbf{u}^{\text{closed}}(t)$ incorporates proprioceptive feedback since it represents a simplified version of muscle spindle feedback by comparing the actual lengths and contraction velocities $(\mathbf{l}^{\text{CE}}(t), \dot{\mathbf{l}}^{\text{CE}}(t))$ of the muscle fibers (contractile elements (CEs)) to desired values $(\boldsymbol{\lambda}(t), \dot{\boldsymbol{\lambda}}(t))$. This formulation of the stretch reflex is based on the assumption that the muscle spindles provide accurate time-delayed information about the muscle fiber lengths and contraction velocities (Kistemaker et al., 2006). The closed-loop signal $\mathbf{u}^{\text{closed}}(t)$ for each muscle i is calculated as

$$u_i^{\text{closed}}(t) = \frac{k_p}{l_i^{\text{CE,opt}}} \left(l_i^{\text{CE}}(t-\delta) - \lambda_i(t) \right) + \frac{k_d}{l_i^{\text{CE,opt}}} \left(\dot{l}_i^{\text{CE}}(t-\delta) - \dot{\lambda}_i(t) \right) , \tag{3.17}$$

where k_p and k_d are the feedback gains, δ denotes a time delay and $l_i^{\text{CE,opt}}$ stands for the optimal length of the contractile element (Bayer et al. (2017); Kistemaker et al. (2007b)). Note that not all our models include velocity feedback. Due to the time it takes to acquire and process sensor

information, time delays in the feedback loop are inevitable (Nishikawa et al., 2007). Depending on the chosen time lag, the model represents a short- or long-latency feedback mechanism.

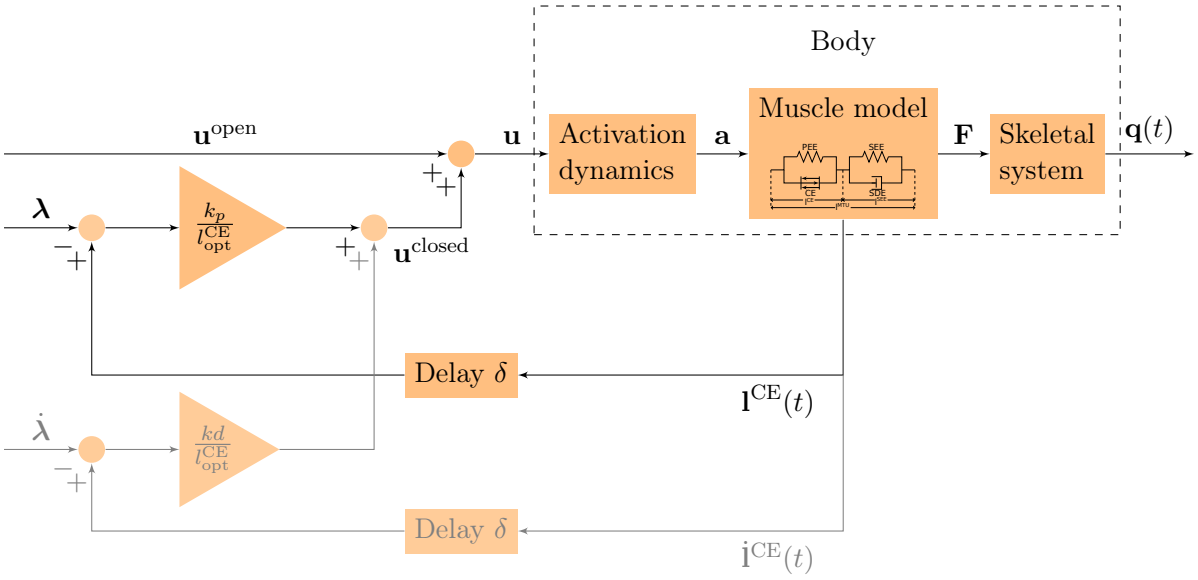

Figure 3.7: **Schematic diagram of our neuro-musculoskeletal models.** The total motor command $\mathbf{u}$ is a sum of the open-loop signal $\mathbf{u}^{\text{open}}$ and the time-delayed feedback signal $\mathbf{u}^{\text{closed}}$. It is fed into the model of the activation dynamics of muscles which relates the neuronal stimulation to muscular activity $\mathbf{a}$ that drives the muscle model. The muscles produce forces $\mathbf{F}$ that act on the skeletal system resulting in a simulated movement $\mathbf{q}(t)$ of the body. In the time-delayed feedback loop, the sensory system which represents a simplified version of the muscle spindles measures the current lengths and contraction velocities of the muscle fibers $(\mathbf{l}^{\text{CE}}(t), \dot{\mathbf{l}}^{\text{CE}}(t))$. They are compared to the desired values $(\boldsymbol{\lambda}, \dot{\boldsymbol{\lambda}})$ and the resulting feedback error is multiplied by the feedback gains k_p and k_d, normalized by the muscle's optimal fiber length $l^{\text{CE,opt}}$ (see Equation (3.17)). Note that not all our models incorporate velocity feedback (gray lines).
Explanation of the control scheme symbols:
■ : block that transforms the input signal to an output signal,
● : addition or subtraction of the input signals, depending on the signs at its input,
▶ : multiplication with the factor specified in the triangle.

3.4 Bio-inspired robotic models

How can biorobotics be a good addition to computer simulations of human movements?

Biologically inspired robots use principles from neuromechanics and transfer them to a physical model. In doing so, they can out-perform other designs for certain tasks (Nishikawa et al., 2007). For example, McMahan et al. (2006) developed a robotic arm that is inspired by the design of octopus tentacles and that impresses with a high payload and range of motion while having a soft compliant structure. Other famous examples are humanoid robots that mimic the human body (Albu-Schäffer et al., 2008; Buschmann et al., 2007; Hirose and Ogawa, 2007) or parts of it (Kalveram et al., 2008; Niiyama et al., 2012; Radkhah et al., 2011) and other animal-inspired models (Lin et al., 2011; Mergner et al., 2006; Renjewski and Seyfarth, 2012; Rutishauser et al., 2008). The field of neuro-robotics describes the consolidation of neuroscience and robotics to design robots that are especially well equipped for the close interaction with humans, for example in rehabilitation or personal assistance (Vitiello et al., 2015). Besides the advantages in the design of robots for various applications, bio-inspired robots are also a valuable tool in the development and testing of biological hypotheses. For example, parts of the robot can be disabled or removed without ethical limitations and even structural limits can be tested. Also, all sensory signals and physical states can be recorded and analyzed (Hoffmann and Pfeifer, 2011). In addition to that, the practicability of motor control hypotheses can be tested under real-world conditions. In contrast to mathematical models, physical models necessarily obey physical laws like friction or impact dynamics (Nishikawa et al., 2007). In particular, a combination of a biologically inspired robot with a resembling mathematical model and human experiments can reveal valuable insights into the control of human movements. Kalveram and Seyfarth (2009) proposed such a *test trilogy* of simulation test, hardware test, and behavioral comparison test to investigate movement generation theories. To this end, however, both the biorobotic and the mathematical model need to incorporate the necessary level of physiological detail as, for example, some control concepts rely on the muscular characteristics (see Section 3.3). In biorobotic models, these muscles can be mimicked by pneumatic actuators (Boblan et al., 2004; Klute et al., 2002; Wolfen et al., 2018) in combination with cables as tendons (Haegele et al., 2015; Shin et al., 2011).

We compared our simulation of arm movements with the biologically inspired robot *Ataro*. Both models reproduced human experimental data using the same control concept (see Chapter 7). A detailed description of this robotic model can be found in Appendix A5.

3.5 Quantifying morphological computation

How can we quantify how much the morphology of the system contributes to the observed behavior?

As mentioned before, the intrinsic properties of the muscle-tendon structures and their zero-time delay response stabilize the system, in particular in response to external perturbations (Brown et al., 1995; Gerritsen et al., 1998; John et al., 2013; Kukillaya et al., 2009; Nishikawa

et al., 2007; Proctor and Holmes, 2010; Wagner and Blickhan, 1999). This self-stabilizing behavior simplifies the control of movement and one can say that the morphology of the system and its interaction with its environment contribute to the observed behavior. This contribution has been termed as *morphological computation* (Ghazi-Zahedi et al., 2016; Paul, 2006; Pfeifer and Iida, 2005) or more recently as the more general term *morphological intelligence* (Ghazi-Zahedi, 2019a). It describes the computation that the body and its environment perform that otherwise would have to be conducted by the controller, or in a more biological sense: by the brain (Pfeifer and Bongard, 2006). It is possible to characterize this contribution by applying an information-theoretic approach: the concept of quantifying morphological computation (Ghazi-Zahedi, 2019a; Ghazi-Zahedi et al., 2016; Zahedi and Ay, 2013). Alternatively, the *control effort*, i.e. the minimum amount of information that is processed in the controller to perform a certain movement, can be measured (Haeufle et al., 2014b, 2020b).

In our study, we used $\mathrm{MC_W}$ (Zahedi and Ay, 2013) to quantify morphological computation on different levels on the neuronal control hierarchy (Chapter 6). A short summary of this method is given here, more details on the background, the implementation, and other measures can be found in Chapter 6 and Appendix A4.

For the calculation of $\mathrm{MC_W}$, the system is described by a causal diagram of the sensorimotor loop (Figure 3.8). Capital letters denote random variables, lower-case letters stand for a specific value that a random variable can take and Greek letters refer to generative kernels, i.e., kernels that describe a causal relationship between random variables. The world dynamics kernel $\alpha(w'|w,a)$ describes how the next world states W' depends on the current world state W and the current action A (Figure 3.8a). If we assume that the current world state W does not influence the next world state W', the world dynamics kernel reduces to $\tilde{\alpha}(w'|a)$ (Figure 3.8b). Using the Kullback-Leibler divergence (Cover and Thomas, 2006), it can be measured how much the observed behavior differs between those two assumptions:

$$\mathrm{MC_W} := \sum_{w',w,a} p(w',w,a) \log_2 \frac{\alpha(w'|w,a)}{\tilde{\alpha}(w'|a)} \tag{3.18}$$

$$= I(W';W|A)\,, \tag{3.19}$$

where $p(w',w,a)$ denotes the joint probability distribution of occurrences of (w',w,a).

So, $\mathrm{MC_W}$ is defined as the Kullback-Leibler divergence between the distribution where the world depends on the previous state and the actuator signal and the distribution where it only depends on the actuator signal. Herein, the Kullback-Leibler divergence quantifies how much the entropy (average information content of an outcome) differs between the two distributions (MacKay, 2003). Therefore, $\mathrm{MC_W}$ quantifies how much the information content differs between including the previous state or not, i.e. how much information content the previous state provides about the next state. Hence, $\mathrm{MC_W}$ is high when the current state strongly influences the next state, meaning that the system exploits its physical properties. Figure 3.9 shows an illustrative example of the calculation of $\mathrm{MC_W}$.

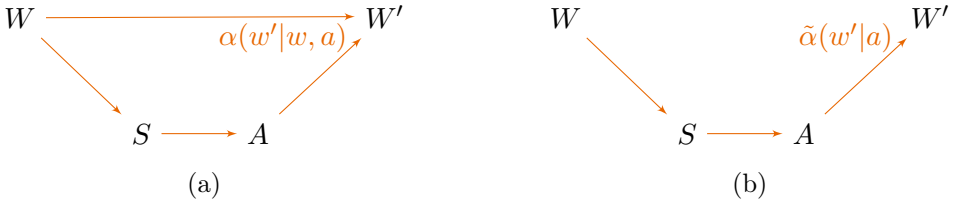

Figure 3.8: **Visualization of the causal diagrams of the sensorimotor loop that underlie the calculation of** $\mathrm{MC_W}$. With: W: current world state, including the system's morphology and the part of the environment that it affects, W': next world state, S: output of the sensors that is available to the controller, A: input to the actuators. (a) Causal diagram for a reactive system. (b) Causal diagram assuming that the previous world state W does not influence the next world state W'.

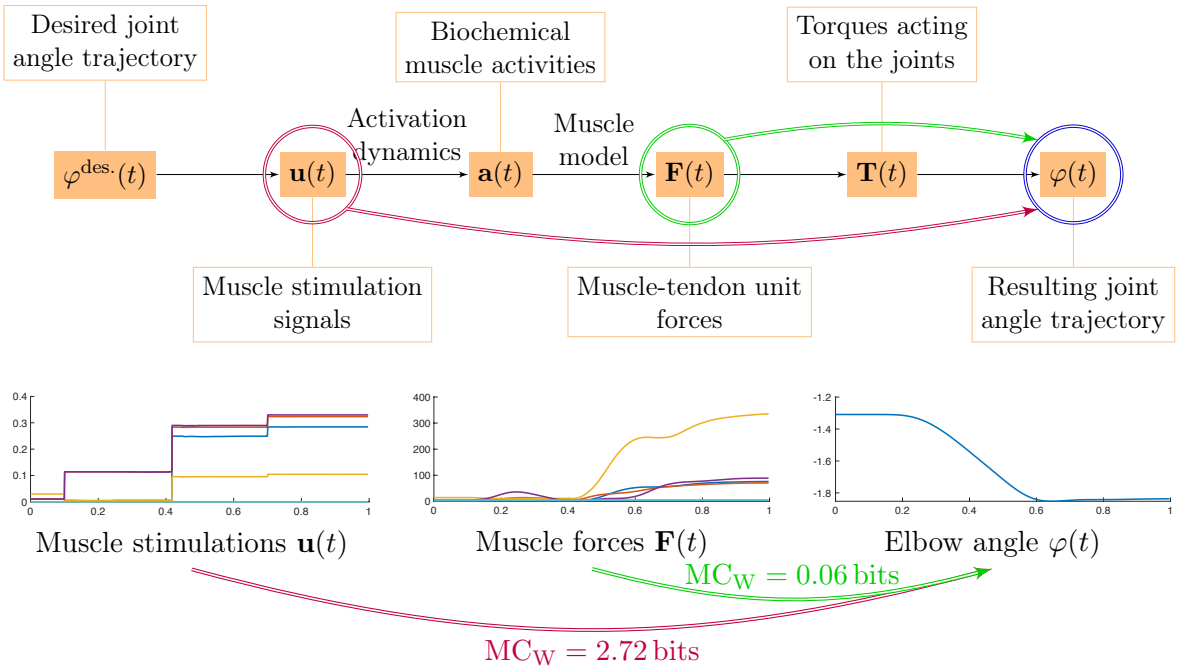

Figure 3.9: **Illustrative example for the calculation of** $\mathrm{MC_W}$**.** The top figure shows the chain of signals that leads to a movement. The lower figures show the muscle stimulations and forces of four arm muscles that move the arm around the elbow joint with the resulting elbow angle trajectory. Calculating morphological computation by using the muscle stimulations $\mathbf{u}$ as actuator and the elbow angle φ as world state leads to a much higher value for $\mathrm{MC_W}$ (2.72 bits) than using the muscle forces $\mathbf{F}$ as actuator (0.06 bits). This means that most of the morphological computation in this system is performed somewhere between the muscle stimulations and the forces, namely by the activation dynamics and the muscle model.

4 | Simulating perturbed arm movements

While the mechanical and muscle parameters of the arm model *Arm26* (Section 3.2.4) are based on literature or chosen to match experimental moment arm data, it was still an open question whether the combination of the musculoskeletal model with the chosen control approach (Section 3.3) is capable of reproducing human movements, in particular in the presence of external perturbations. Therefore, we simulated static perturbations of the inertia and damping properties of the arm, as well as dynamic torque perturbations for one-degree-of freedom movements around the elbow joint. These perturbations are relevant in everyday life, as they represent interactions with other people or objects as for example with technical assistive devices. The controller consists of a feed-forward motor command and feedback based on muscle fiber length and contraction velocity representing short-latency (25 ms) or long-latency (50 ms) stretch reflexes as the first neuronal responses elicited by an external perturbation. To determine the open-loop control signal, we parametrized the control signal resulting in a piecewise constant stimulation over time for each muscle. Interestingly, such an intermittent open-loop signal results in a smooth movement that is close to experimental observations. So, our model can generate the unperturbed point-to-point movement solely by the feed-forward command. The feedback only contributed to the stimulation in perturbed movements. We found that the relative contribution of this feedback is small compared to the feed-forward control and that the characteristics of the musculoskeletal system create an immediate and beneficial reaction to the investigated perturbations. The novelty of these findings is (1) the reproduction of static as well as dynamic perturbation experiments in one neuro-musculoskeletal model with only one set of basic parameters. This allows to investigate the model's neuro-muscular response to the perturbations that – at least to some degree – represent stereotypical interactions with the environment; (2) the demonstration that in feed-forward driven movements the muscle characteristics generate a mechanical response with zero-time delay which helps to compensate for the perturbations; (3) that this model provides enough biomechanical detail to allow for the prediction of internal forces, including joint loads and muscle-bone contact forces which are relevant in ergonomics and for the development of assistive devices but cannot be observed in experiments.

Note that large parts of the content of this chapter were published in *Frontiers in Bioengineering and Biotechnology*. For details on this publication, including a list of authors, see Manuscript 1 in Chapter 2.

4.1 Introduction

Humans generate goal-directed movement by an interplay between the nervous system, the biomechanical structures, and the environment, where high-level motor control is fine-tuned to the dynamics of the low-level muscular system and exploits its characteristics (Scott, 2004). Understanding and predicting this dynamic interplay by means of a computational model is relevant for two reasons: firstly, it allows gaining insight into the hierarchical structure of motor control and the sensorimotor integration of muscle-tendon dynamics and reflexes to control (Berniker et al., 2009; Campos and Calado, 2009; Kistemaker et al., 2013; Latash, 2010). Secondly, it provides the opportunity to study internal forces in the musculoskeletal system which are relevant in ergonomics and for the development of assistive devices and otherwise experimentally not accessible (Holzbaur et al., 2005; Pennestrì et al., 2007).

To this end, we here propose a model of human goal-directed arm movements which fulfills the following criteria: **(a)** it represents the biomechanical structures to a level of detail which allows the prediction of internal joint loads and muscle-bone contact forces; **(b)** it considers muscle-tendon based short- or long-latency reflexes as the first neuronal responses elicited by an external perturbation; **(c)** it reproduces experimentally observed responses to static as well as dynamic external perturbation forces which allow to investigate the model's neuromuscular response and – at least to some degree – represent stereotypical interactions with the environment.

Individually, these criteria have been fulfilled in models before. For criterion (a), models typically consider muscle fiber characteristics (Hill-type muscle models, e.g., Haeufle et al. (2014b); Millard et al. (2013); Siebert and Rode (2014)), tendon non-linear elasticity, neuromuscular activation dynamics (e.g., Hatze, 1977; Rockenfeller et al., 2015), antagonistic setup (e.g., Schmitt et al., 2019a), and anatomical muscle routing (e.g., Hammer et al., 2019; Holzbaur et al., 2005). Such models are used for ergonomics or for the development of assistive devices, but, to our knowledge, do not fulfill at least one of the other two criteria (Chadwick et al., 2009; Glenday et al., 2019; Holzbaur et al., 2005; Loeb, 2012).

Musculoskeletal models which fulfill criterion (b) have also been developed (e.g., Bayer et al. (2017); Gribble and Ostry (2000); Kistemaker et al. (2006); Lan and Zhu (2007), review: Todorov (2004)). Two studies further employed perturbations to demonstrate the benefit of combining muscle spindle and Golgi tendon organ signals (Kistemaker et al., 2013) and the role of muscular characteristics in stabilization against different perturbations (Pinter et al., 2012). However, none of these models fulfills criterion (a) as they do not account for anatomical muscle routing. Furthermore, although the latter two studies investigate the reaction to perturbations, they do not fulfill criterion (c): they employ the perturbations to investigate their research questions, but they do not compare their perturbation response to experimental data (Kistemaker et al., 2013; Pinter et al., 2012).

Finally, many models successfully reproduce data from perturbation experiments (criterion (c), reviews see Campos and Calado (2009); Wolpert and Ghahramani (2000)). Examples are the predicted response to static perturbations mimicking changes in inertia or damping (Bhanpuri et al. (2014)), or to dynamic torque perturbations (Kalveram et al. (2005)). Both models incorporate feedback but have no representation of the muscles. Furthermore, they consider feedback on the joint level and not on the muscular level required to investigate sensorimotor integration. In addition to that, none of these models represent the muscular

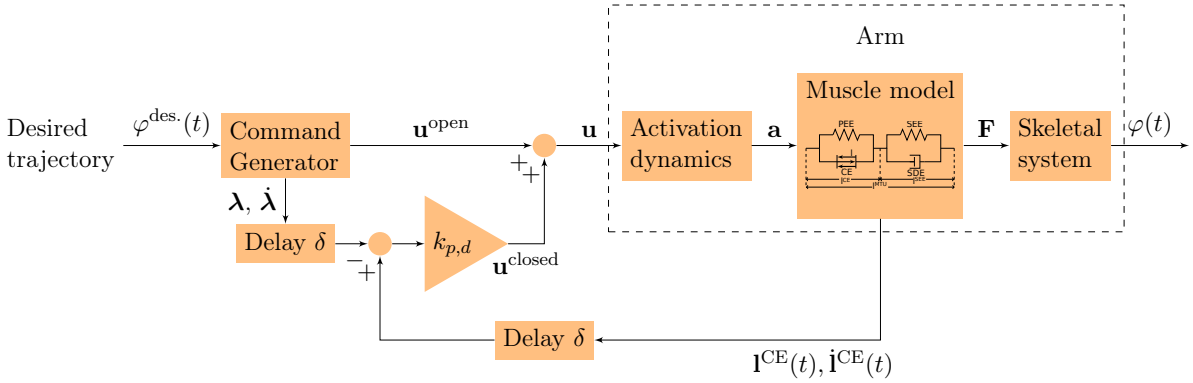

Figure 4.1: **Schematic diagram of the neuro-musculoskeletal model.** The desired trajectory $\varphi^{\text{des.}}(t)$ is a minimum jerk trajectory between a desired starting and an ending point. The command generator maps this trajectory to an open-loop motor command $\mathbf{u}^{\text{open}}$ and to desired muscle fiber lengths and contraction velocities ($\boldsymbol{\lambda}$, $\dot{\boldsymbol{\lambda}}$) that correspond to the desired trajectory. The total motor command $\mathbf{u}$ is fed into the model of the activation dynamics of muscles which relates the neuronal stimulation $\mathbf{u}$ to muscular activity $\mathbf{a}$ that drives the muscle model. The muscles produce forces $\mathbf{F}$ that act on the skeletal system resulting in a simulated movement $\varphi(t)$ of the arm. In the time-delayed feedback loop, the sensory system which represents a simplified version of the muscle spindles measures the current lengths and contraction velocities of the muscle fibers ($\mathbf{l}^{\text{CE}}(t), \dot{\mathbf{l}}^{\text{CE}}(t)$). They are compared to the desired values ($\boldsymbol{\lambda}$, $\dot{\boldsymbol{\lambda}}$) and the resulting feedback error is multiplied by the feedback gains k_p and k_d (see Equation (4.4)).

characteristics to fulfill criterion (a).

The purpose of this study was to develop a neuro-musculoskeletal model that fulfills all three criteria. The approach results in a neuro-musculoskeletal model that shows valid responses to both static and dynamic perturbations as reported in the literature (Bhanpuri et al., 2014; Kalveram and Seyfarth, 2009). These responses match those of previous motor control models but allow a novel interpretation of the relative contribution of feedback and biomechanical characteristics as well as the calculation of internal forces. This contribution is a step in the attempt to foster the dual use of musculoskeletal models as tools to study motor control models and as tools for the development of a virtual design and testbed for ergonomics or assistive devices.

4.2 Methods

In order to simulate goal-directed arm movements, we combine a musculoskeletal model of the arm including two degrees of freedom and six muscles (based on Driess et al. (2018); Kistemaker et al. (2007a); Suissa (2017)) with a neuronal control model (based on the concept of Bhanpuri et al. (2014)). Both parts are described in more detail in the following. The structure of the neuro-musculoskeletal model is illustrated in Figure 4.1.

To investigate the model's interaction with the environment and compare it to experimental results, static perturbations of the inertia and viscosity properties of the arm (as reported in Bhanpuri et al. (2014)) as well as dynamic torque perturbations (as reported in Kalveram et al. (2005)) are applied. An overview over the applied perturbations is given in Figure 4.2.

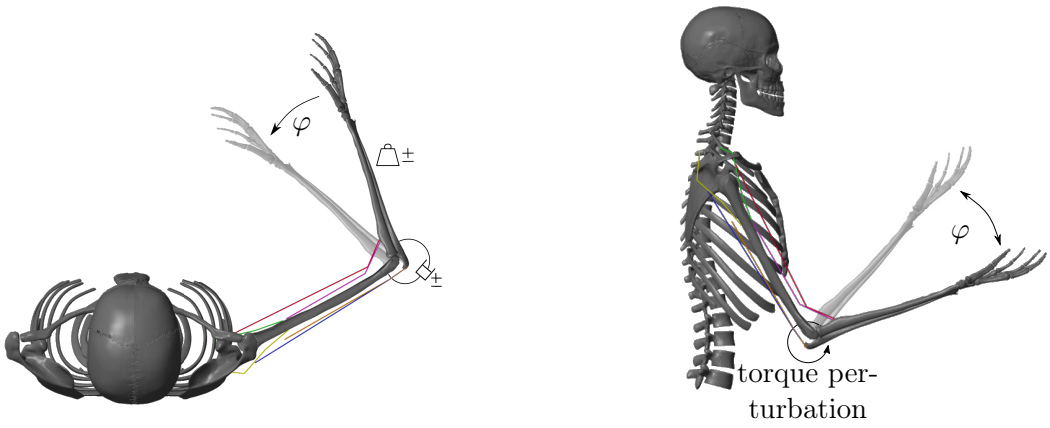

① **Static perturbations:**

a	+	Increased damping
b	−	Decreased damping
c	+	Increased inertia
d	−	Decreased inertia

② **Dynamic torque perturbations:**

a	↑	Positive impulse, flexion
b	↑	Negative impulse, flexion
c	↓	Positive impulse, extension
d	↓	Negative impulse, extension

Figure 4.2: **Overview over the applied static and dynamic perturbations.**
① The static perturbations of the inertia and viscosity properties of the arm during a flexion movement in the horizontal plane (without gravity) are: **a** Increased damping ($+0.30\,\mathrm{N\,m\,s/rad}$) **b** Decreased damping ($-0.31\,\mathrm{N\,m\,s/rad}$) **c** Increased inertia ($+0.039\,\mathrm{kgms^2}$) **d** Decreased inertia ($-0.032\,\mathrm{kgms^2}$), in accordance with Bhanpuri et al. (2014).
② During the dynamic torque perturbations a constant torque that mimics gravity ($-1.5\,\mathrm{N\,m}$) is applied. Hence, we visualized this movement as a movement in the vertical plane. The perturbation is a temporal torque impulse in or against the direction of movement: **a** Positive torque impulse ($+5\,\mathrm{N\,m}$) during a flexion movement **b** Negative torque impulse ($-5\,\mathrm{N\,m}$) during a flexion movement **c** Positive torque impulse ($+5\,\mathrm{N\,m}$) during an extension movement **d** Negative torque impulse ($-5\,\mathrm{N\,m}$) during an extension movement, in accordance with Kalveram et al. (2005).

4.2.1 Musculoskeletal model of the arm

The musculoskeletal model *Arm26* (2 degrees of freedom, six muscles, see Bayer et al. (2017); Driess et al. (2018)) of the human arm is described in detail in Section 3.2.4. The arm model consists of two rigid bodies (lower and upper arm) that are connected via two one-degree-of-freedom revolute joints that represent the shoulder (glenohumeral) and elbow joint (see Figure 4.1, within dashed box for schematics and Figure 4.2 for a visualization). Active forces

are generated by six muscle-tendon units (MTUs, see Figure 4.2), four monoarticular (shoulder anteversion, shoulder retroversion, elbow flexor, elbow extensor) and two biarticular muscles (biarticular flexor, biarticular extensor). The muscles are stimulated by a neuronal control stimulation signal $\mathbf{u}$. The model of the activation dynamics predicts the activity $\mathbf{a}$ of the muscle depending on the current muscle stimulation, considering the fiber length dependency (Hatze, 1977) (see Figure 4.1). Depending on the muscular activity, the force of each MTU, is modeled using a Hill-type model accounting for force-length-velocity characteristics, tendon and parallel tissue elasticity, and damping in the tendon (Haeufle et al. (2014b)). Muscle path geometry, i.e., origin, insertion and path deflection, is implemented to match experimental lever arm data. For the joint angle-dependent deflection geometry, we used the via-ellipse approach confining the path of the muscle to geometric ellipses attached to the rigid bones (Hammer et al., 2019). This algorithm allows to calculate muscle-bone contact forces and applies forces to the bones such that internal joint loadings can be predicted.

The parameters used in the models are not subject-specific but represent a generic man and are collected from different sources (among others: Bhanpuri et al. (2014); Kistemaker et al. (2006); Mörl et al. (2012); van Soest et al. (1993a)) that are listed in detail in Section 3.2.4. Due to the muscle-tendon model in combination with anatomical muscle routing, our model provides the necessary level of biomechanical detail to determine internal muscular and joint loads as well as muscle-bone contact forces. Hence, criterion (a) that we established in the introduction is fulfilled.

The experimental perturbations that we reproduce in this simulation study were confined to the elbow joint. Thus, we here fix the shoulder joint to 30° such that only one-degree-of-freedom movements are possible. Hence, the monoarticular shoulder muscles have no effect on the movement and are excluded from our investigations. To make the results comparable to experiments, the inertia properties of the forearm were changed according to an arm that is attached to an exoskeleton robot that was used by Bhanpuri et al. (2014).

4.2.2 Control model

The neuronal control model is illustrated in Figure 4.1. It is based on the control model that was proposed by Bhanpuri et al. (2014) to reproduce static perturbations in a torque-driven model of the arm. The input to the controller is a desired trajectory $\varphi^{\text{des.}}(t)$ that is considered to be a result of the movement planning. The controller consists of an open-loop command $\mathbf{u}^{\text{open}}$ and a closed-loop signal $\mathbf{u}^{\text{closed}}$ that incorporates proprioceptive feedback. The total stimulation u_i is the sum of those components and represents α-motor neuron activity. For each muscle i, it is calculated as

$$u_i(t) \coloneqq \left\{ u_i^{\text{open}}(t) + u_i^{\text{closed}}(t) \right\}_0^1 , \tag{4.1}$$

where the operation $\{x\}_0^1$ sets values $x < 0$ to 0 and $x > 1$ to 1.

The total motor command $\{u_i(t)\}_{i=1}^6$ is fed into the musculoskeletal model resulting in a simulated movement $\varphi(t)$ of the arm. This control approach can be classified as a modified hybrid equilibrium point (EP) controller where the open-loop signal is intermittent while the feedback signal is continuous (see Kistemaker et al. (2006)).

4.2.2.1 Movement planning

We assume that a higher-level structure conducts planning of the movement and provides a desired kinematic movement trajectory $\varphi^{\text{des.}}(t)$ as an input to the lower-level control structures that are modeled here. Therefore, the input to our controller is the desired trajectory which we determined by generating a minimum-jerk trajectory between desired starting and ending angles. To this end, a fifth-order polynomial approach for the desired angle trajectory $\varphi^{\text{des.}}(t)$ is chosen in accordance with Flash and Hogan (1985) who have shown that their mathematical model shows the typical bell-shaped velocity profile and predicts experimental observations of voluntary unconstrained point-to-point movements in a horizontal plane.

4.2.2.2 Open-loop control generates reference trajectory

The command generator maps the desired trajectory $\varphi^{\text{des.}}(t)$ to an open-loop motor command $\mathbf{u}^{\text{open}}$ and to desired contractile element lengths and velocities ($\boldsymbol{\lambda}$, $\dot{\boldsymbol{\lambda}}$) that correspond to the desired trajectory. Using a musculoskeletal model, the generation of these motor commands is nontrivial since the system is redundant (degree of freedom problem, see Bernstein (1967), Shadmehr (1991)) and nonlinear. In addition to that, the fact that the activation dynamics and the muscle model are described by first-order differential equations including time delays and the resulting time-dependency prohibits the straight-forward calculation of the inverse problem.

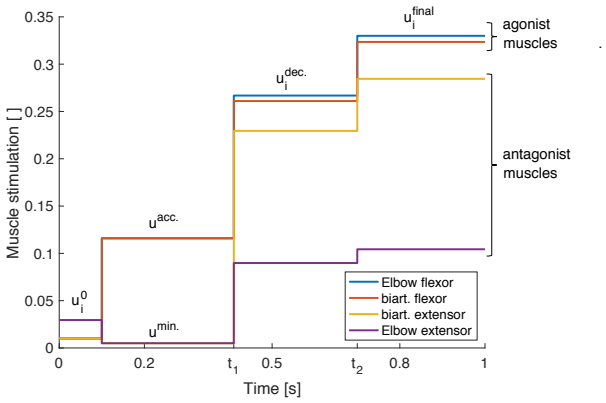

Figure 4.3: **Triphasic stimulation pattern for a flexion movement.** Starting from the initial position at $t = 0.1\,\text{s}$, during the acceleration phase, mainly the agonist muscles are active. In the second phase between $t = t_1$ and $t = t_2$, both muscle groups are active, braking the movement. In the last phase for $t > t_2$, again both muscle groups are active in order to reach the final position and hold it with a desired level of co-contraction.

To simplify this process, instead of deriving a continuous set of stimulations over time, we introduce a triphasic stimulation pattern with a limited number of parameters (see Equation (4.2), illustrated in Figure 4.3). It is inspired by the three phases that have been observed in muscle surface electromyogram (EMG) patterns during fast point-to-point movements (see e.g., Wachholder and Altenburger (1926), Wierzbicka et al. (1986) and Kistemaker et al. (2006)): an acceleration phase where mostly the agonist muscles are active which is followed by a braking

phase and a final phase which keeps the arm in the desired final position. Hence, the muscles are divided into two groups: the agonists and the antagonists for a movement. We define the muscle stimulations over time for those muscle groups as

$$u_i^{\text{open}}(t) \coloneqq \begin{cases} u_i^0 & \text{for } t < 0.1\,\text{s} \\ u_i^{\text{acc.}} = \begin{cases} u^{\text{acc.}} & \text{for agonist muscles} \\ u^{\text{min.}} & \text{for antagonist muscles} \end{cases} & \text{for } 0.1\,\text{s} \leq t < t_1 \\ u_i^{\text{dec.}} & \text{for } t_1 \leq t < t_2 \\ u_i^{\text{final}} & \text{for } t_2 \leq t\,. \end{cases} \tag{4.2}$$

Following this approach, the control parameters that are required to follow the desired trajectory need to be determined.

The initial and the final position are determined to be stable equilibrium positions, i.e.

$$\dot{\varphi} = 0 \quad \text{and} \quad \ddot{\varphi} = 0\,, \tag{4.3}$$

which leads to the condition that the net joint moment vanishes in these positions. This allows for the determination of the necessary muscle stimulations u_i^0 and u_i^{final} to hold the initial and the final position by minimizing $\sum_{i=1}^{4}(u_i - u^{\text{des.}})$ subject to the constraint that the sum of all torques acting on a joint is zero, i.e. the system is in a stable equilibrium position. Herein, the desired level of stimulation $u^{\text{des.}}$ allows influencing the level of co-contraction. The condition that the system is supposed to be in equilibrium at $t = 0$ defines the initial conditions. The final phase starts at $t_2 = 0.7\,\text{s}$ which is approximately the time when the final position is reached.

The dynamic movement between those equilibrium positions ($0.1\,\text{s} < t < t_2$) is parametrized such that it is close to the desired trajectory $\varphi^{\text{des.}}(t)$:

In the acceleration phase, the muscle stimulation $u^{\text{acc.}}$ and the switching time t_1 are optimized using a Bayesian optimization approach (see for example Brochu et al. (2010)) where the squared point-wise difference between the current trajectory and the desired trajectory is minimized. The minimal level of stimulation $u^{\text{min.}}$ is set to a fixed value (0.005) in order to reduce the search space for possible stimulations.

The muscle stimulation pattern $u_i^{\text{dec.}}$ in the braking phase is determined analogously to the stimulations u_i^{final} but with a lower level of co-contraction to reach the final position following the desired pathway.

In the following, these optimized muscle stimulation patterns are used as open-loop signals $u_i^{\text{open}}(t)$. If no external perturbation occurs, this stimulation pattern generates a trajectory that is close to the desired minimum jerk trajectory $\varphi^{\text{des.}}(t)$. This trajectory will be used as reference hereafter.

4.2.2.3 Closed-loop response to perturbations

If a perturbation occurs, the movement trajectory changes. As a consequence, the actual fiber lengths and contraction velocities differ from the values from the reference trajectory. In this case, the feedback loop modifies the control signal, see Equation (4.1). This proprioceptive feedback is incorporated in the closed-loop signal $u_i^{\text{closed}}(t)$ by comparing the actual lengths and contraction velocities $(\mathbf{l}^{\text{CE}}(t), \dot{\mathbf{l}}^{\text{CE}}(t))$ of the muscle fibers (contractile elements (CEs)) of

the muscles to desired values ($\boldsymbol{\lambda}(t)$, $\dot{\boldsymbol{\lambda}}(t)$). The desired CE lengths and velocities ($\boldsymbol{\lambda}$, $\dot{\boldsymbol{\lambda}}$) are set to the values ($\mathbf{l}^{\mathrm{CE}}(t), \dot{\mathbf{l}}^{\mathrm{CE}}(t)$) recorded during an unperturbed movement. So, as long as there is no external perturbation, the feedback error is zero and hence the closed-loop signal vanishes.

Since the information about the current state of the muscle only becomes available with a neuronal delay, a time lag δ is introduced. To investigate different hierarchy levels of feedback mechanisms, we tested both, a short-latency and a long-latency stretch reflex. For the short-latency response, the time delay is set to 25 ms in accordance with similar arm models (Bayer et al., 2017; Gribble et al., 1998; Kistemaker et al., 2006) which is in a physiologically plausible range (R1 response Kurtzer et al. (2014); Scott (2016),Pruszynski et al. (2011); Weiler et al. (2016)). This short-latency feedback represents a simplified model of the spinal, mono-synaptic muscle spindle reflex (Pruszynski and Scott, 2012; Weiler et al., 2019), assuming that the muscle spindles provide accurate time-delayed information about the muscle fiber lengths and contraction velocities (Kistemaker et al., 2006). Since experimental findings indicate that the long-latency stretch reflex plays an important role in the reaction to mechanical perturbations in goal-directed reaching movements (e.g., Kurtzer et al., 2014; Weiler et al., 2016), we also implemented a long-latency feedback loop by setting the time delay to 50 ms (R2 response Scott (2016),Pruszynski et al. (2011)). Since both, short- and long-latency feedback are implemented with the same mathematical model (see below) and lead to similar results, we focus in the following on the long-latency response, while the short-latency responses to the perturbations can be found in Appendix A3. By considering these muscle-tendon based reflexes, our model fulfills criterion (b) that we suggested in the introduction.

The closed-loop signal $u_i^{\mathrm{closed}}(t)$ for each muscle i is calculated as

$$u_i^{\mathrm{closed}}(t) := \frac{k_p}{l^{\mathrm{CE,opt}}}(l_i^{\mathrm{CE}}(t-\delta) - \lambda_i(t-\delta)) + \frac{k_d}{l^{\mathrm{CE,opt}}}(\dot{l}_i^{\mathrm{CE}}(t-\delta) - \dot{\lambda}_i(t-\delta))\,, \tag{4.4}$$

where k_p and k_d are the feedback gains and $l^{\mathrm{CE,opt}}$ stands for the optimal length of the contractile element. The feedback gains k_p and k_d as well as the desired level of co-contraction in the braking phase $u^{\mathrm{des.,dec.}}$ play an important role in the way how the system reacts to perturbations. Therefore, they are optimized in order to reproduce the answer to all four static perturbations seen in experiments.

In the objective function for this optimization, we incorporated the quantities early velocity and dysmetria (as used by Bhanpuri et al. (2014), illustrated in Figure 4.4) that we also use as evaluation criteria for the static perturbations below. *Early velocity* is defined as the joint angle velocity 155 ms after the first time the velocity exceeds 10 °/s. *Dysmetria* is defined as the difference between the final position (at t=1 s) and the position at the time of first correction. Herein, the time of first correction is the time when the absolute value of the angular velocity is smaller than 2 °/s or the absolute value of the angular acceleration falls below 2 °/s^2. The objective function is minimized using the pattern search algorithm in Matlab® and is defined as

$$\sum_{\substack{\text{static}\\ \text{perturbation types}}} \left[\left(\frac{\begin{array}{c}\text{early velocity difference simulation}\\ \text{- mean early velocity difference experiment}\end{array}}{\text{maximal standard deviation early velocity difference experiment}} \right)^2 + \left(\frac{\begin{array}{c}\text{dysmetria difference simulation}\\ \text{- mean dysmetria difference experiment}\end{array}}{\text{maximal standard deviation dysmetria difference experiment}} \right)^2 \right]$$

$$= \sum_{\substack{\text{static}\\ \text{perturbation types}}} \left[\left(\frac{\Delta v^0_{\text{sim}} - \mu(\Delta v^0_{\text{exp}})}{\max \sigma(\Delta v^0_{\text{exp}})} \right)^2 + \left(\frac{\Delta d_{\text{sim}} - \mu(\Delta d_{\text{exp}})}{\max \sigma(\Delta d_{\text{exp}})} \right)^2 \right], \tag{4.5}$$

with v^0: early velocity, d: dysmetria, μ: mean, σ: standard deviation, Δ: difference that is calculated as the early velocity/dysmetria of the perturbed movement minus the early velocity/dysmetria of the reference movement.

The whole set of resulting control parameters can be found in Table A3.1. To quantify the influence of these control parameters on the resulting movements, we performed a sensitivity analysis (see Section 4.3.5).

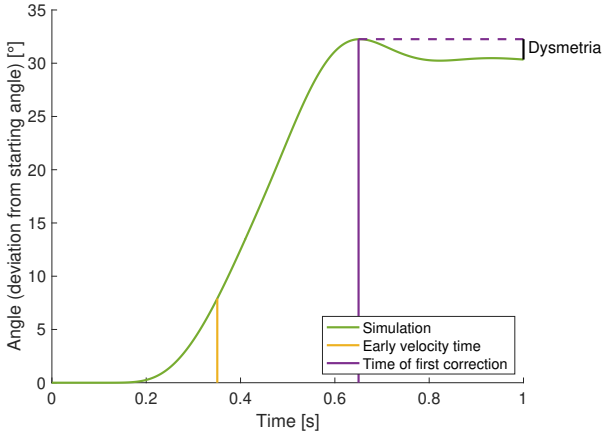

Figure 4.4: **Illustration of the determination of early velocity and dysmetria.** *Early velocity* is defined as the joint angle velocity 155 ms after the first time the velocity exceeds 10 °/s. *Dysmetria* is defined as the difference between the final position (at t=1 s) and the position at the time of first correction.

4.2.3 Simulation experiments

To test whether this model also fulfills criterion (c) from the introduction, we simulated its response to static and dynamic perturbations.

4.2.3.1 Static perturbation of inertia and viscosity

Bhanpuri et al. (2014) performed experiments where healthy subjects carried out goal-directed single-joint arm movements while the arm was attached to an exoskeleton robot. Each subject performed two blocks with 40 trials each of which 36 trials were null trials (without perturbation). In the perturbation trials, the robot exerted a force to mimic changes in the dynamic properties of the arm, in particular inertia and viscosity. The movements were performed in a horizontal plane (Figure 4.2 ①).

In our computer simulation, we adapted the moment of inertia of the modeled forearm to account for the influence of the robot arm to be able to compare our simulation results to their experiments. In accordance with Bhanpuri et al. (2014), the static perturbations were an increase in moment of inertia ($+0.039\,\mathrm{kgms}^2$), a decrease in inertia ($-0.032\,\mathrm{kgms}^2$), an increase in damping ($+0.30\,\mathrm{N\,m\,s/rad}$) or a decrease in damping ($-0.31\,\mathrm{N\,m\,s/rad}$) (Figure 4.2 ①).

Evaluation criterion In order to compare the simulation results to the experimental data, we introduced an evaluation criterion as used by Bhanpuri et al. (2014). They investigate the relation between early velocity and dysmetria, as defined above in Section 4.2.2.3 and illustrated in Figure 4.4.

4.2.3.2 Dynamic torque perturbation

In analogy with the experiments described in Kalveram and Seyfarth (2009); Kalveram et al. (2005), a dynamic torque perturbation was applied to the simulated pointing movement (Figure 4.2 ②). A constant torque that mimics gravity ($-1.5\,\mathrm{N\,m}$) is applied. The perturbation is an additional temporal torque change in or against the direction of movement ($\pm 5\,\mathrm{N\,m}$). The perturbation starts after 25% of the movement (corresponds to 7.5° of 30° in total) and lasts 37.5 ms. Hence, relative to the total movement, we apply the same perturbation as Kalveram et al. (2005). The starting and final position and all other biomechanical and control parameters are identical to the static perturbation simulations ①.

Evaluation criterion For the dynamic torque perturbation, we chose the quotient of the angular velocity at the elbow joint at the beginning and at the end the perturbation as an evaluation criterion:

$$\text{velocity quotient} := \frac{\text{angular velocity at the beginning of the perturbation}}{\text{angular velocity at } \Delta t \text{ after the beginning of the perturbation}}. \quad (4.6)$$

Setting Δt to the duration of the perturbation (37.5 ms), the velocity quotient relates the angular velocity at the beginning of the perturbation to the one at the end of the perturbation. This allows investigating the muscle-dominated response to the perturbations. In addition to that, we also evaluate the velocity quotient of the angular velocity at Δt =100 ms after the beginning of the perturbation, which quantifies also the first neuronal response.

4.2.3.3 Implementation

The arm model and the optimization and analysis scripts are implemented using Matlab®/ Simulink® version 2018a with the Simscape Multibody™environment. For all simulations, the

variable-step Matlab ODE solver *ode15s* with relative solver tolerance 1×10^{-5} has been used. The absolute tolerance and the minimum/maximum/initial step size are set to be determined automatically.

For comparison, the experimental results were digitized from Bhanpuri et al. (2014) and Kalveram and Seyfarth (2009). For a smooth appearance and for the calculation of the angular velocity, we fitted a smoothing spline to the digitized discrete data (using the curve fitting toolbox in Matlab®).

4.2.4 Open-loop and torque-driven model as comparison

To investigate the influence of the implemented feedback mechanism, we applied the same perturbations to an open-loop controlled version of our model, i.e. without the implemented feedback loop ($k_p = 0$ and $k_d = 0$).

In addition to that, we implemented an idealized torque-driven model to compare the reaction to external forces to those of the musculoskeletal model. This comparison allows investigating the contribution of the viscoelastic reaction forces which are generated by the muscle-tendon contraction dynamics (*preflex* forces). The torque-driven model uses the same mechanical parameters (segment lengths, masses, inertia) as the musculoskeletal model. To determine the torque that is necessary to reproduce the musculoskeletal model's movement, we recorded the net joint torque that is applied by the muscles during both the unperturbed movement. In accordance with the model of Bhanpuri et al. (2014), the feedback is based on the joint positions with a delay of 100 ms representing a long-latency reflex.

4.3 Results

We here show the results for the long-latency feedback loop (50 ms delay). The short-latency responses (25 ms delay) to the perturbations is quite similar and can be found in Appendix A3.

4.3.1 Intermittent open-loop signals reproduce unperturbed movement

The simulation of the unperturbed movement is in good agreement with the desired minimum jerk trajectory and with the experimental data (see Figure 4.5 and Figure 4.7, orange curves). As mentioned above, without perturbations the feedback signal vanishes. So, the movement is solely controlled by the open-loop command which is a piecewise constant function over time. This unperturbed movement is the reference for the perturbed cases.

4.3.2 Static perturbation of inertia and viscosity

In presence of the static perturbations, the simulation and experimental results show the same qualitative behavior in the relation between early velocity difference and dysmetria difference (Figure 4.5a). An increase in inertia leads to a lower early velocity which results in higher dysmetria. A decrease in inertia causes an increase in early velocity which leads to lower dysmetria. For the damping perturbations, it is the other way round. The comparison of the movement trajectory in the simulation (Figure 4.5b) and the experiments of Bhanpuri et al. (2014) (Figure 4.5c) shows a qualitatively and quantitatively similar behavior at the beginning

of the movement. Towards the end of the movement, the subject in the experiment tends to take longer to reach the final position, especially for the damping perturbations. Note that we only compared our results with experimental trajectories of one typical control subject and with early velocity/dysmetria difference of a small control group, respectively, while we used generic, not subject-specific parameters for the mechanical description of the limb.

The open-loop controlled system shows a similar response to the static perturbations as the closed-loop version and also as the subjects in the experiment (Figure 4.6a and Figure 4.6b). However, in three of four cases, the closed-loop controller leads to better results than the open-loop approach and also the sum of all cases is smaller (Figure 4.6a vs. Figure 4.6b and Table 4.1). The only case that does not profit from the feedback and leads to similar results is the decreasing of inertia.

The trajectories generated by the torque-driven model do not reach the desired target position without feedback (Figure 4.6c). With feedback, the trajectories get closer to what has been observed in the experiments, but there are oscillations around the target position (Figure 4.6d).

An increase in arm inertia causes an overshoot of the movement using the musculoskeletal model with and without feedback while the forward-controlled torque model predicts an undershoot (Figure 4.6). The former counter-intuitive behavior was also observed in the experiments (Figure 4.5c).

	Closed-loop	Open-loop
Increased damping	0.19	4.43
Decreased damping	0.03	1.77
Increased inertia	0.43	0.69
Decreased inertia	3.19	2.87
Sum of all cases	3.84	9.76

Table 4.1: **Quantification of the difference between simulation and experiment for case ① by evaluating the cost function (Equation (4.5)) that was used in the optimization of the closed-loop control parameters and splitting it into the contributions of the different perturbations.** Hence, for the single cases, a value smaller than one means that the result lies within the experimental standard deviation area (taking the maximum standard deviation in each direction).

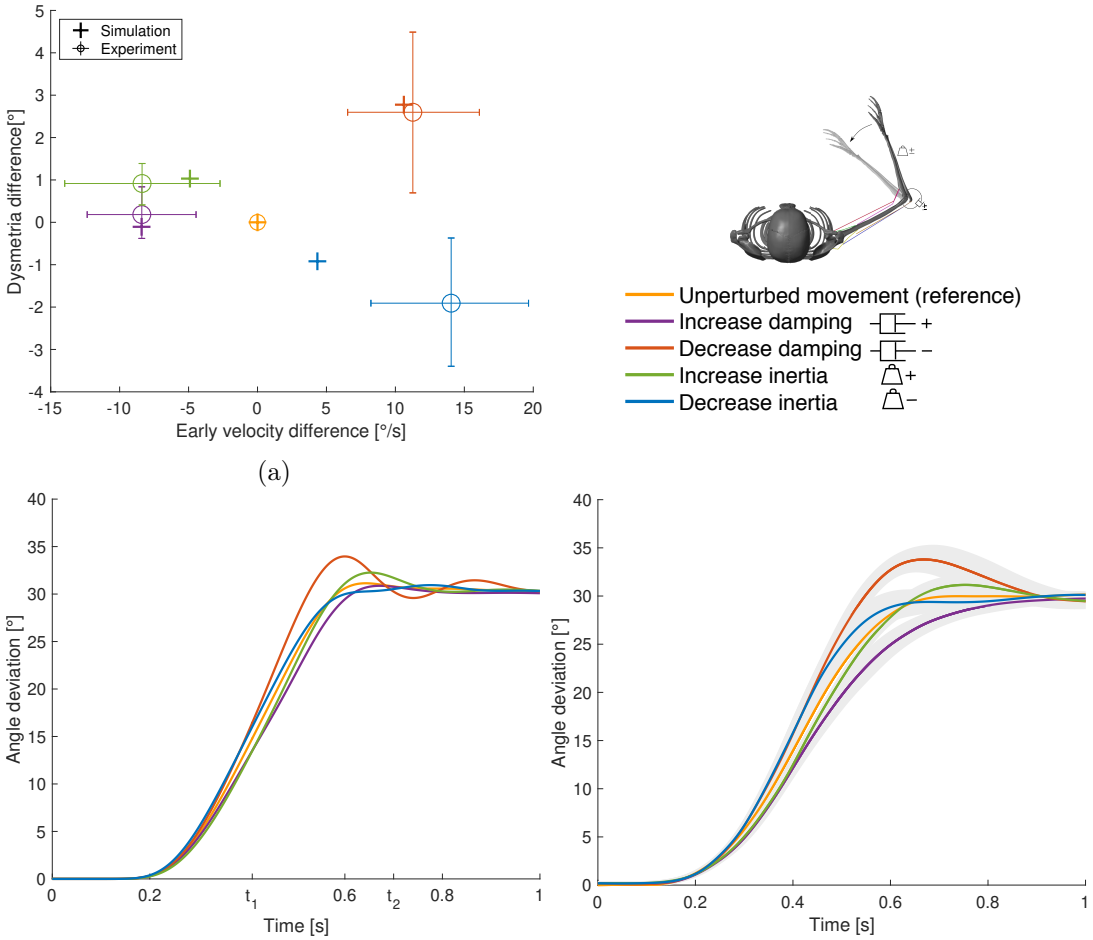

(a)

(b) Simulation

(c) Experiment (Bhanpuri et al. (2014))

Figure 4.5: **Results for case** ①. (a) Evaluation criterion for the static perturbations: Early velocity difference in relation to the dysmetria difference (both calculated as the early velocity/dysmetria of the perturbed movement minus the early velocity/dysmetria of the reference movement) shown for both, simulation and experiment. The experimental results are digitized from Bhanpuri et al. (2014), the control group averages (n=11) are shown and the error bars indicate standard deviation. (b) our simulation results and (c) experimental results digitized from Bhanpuri et al. (2014) for one typical control subject in null condition (reference) and with perturbations (shaded areas indicate standard deviation).

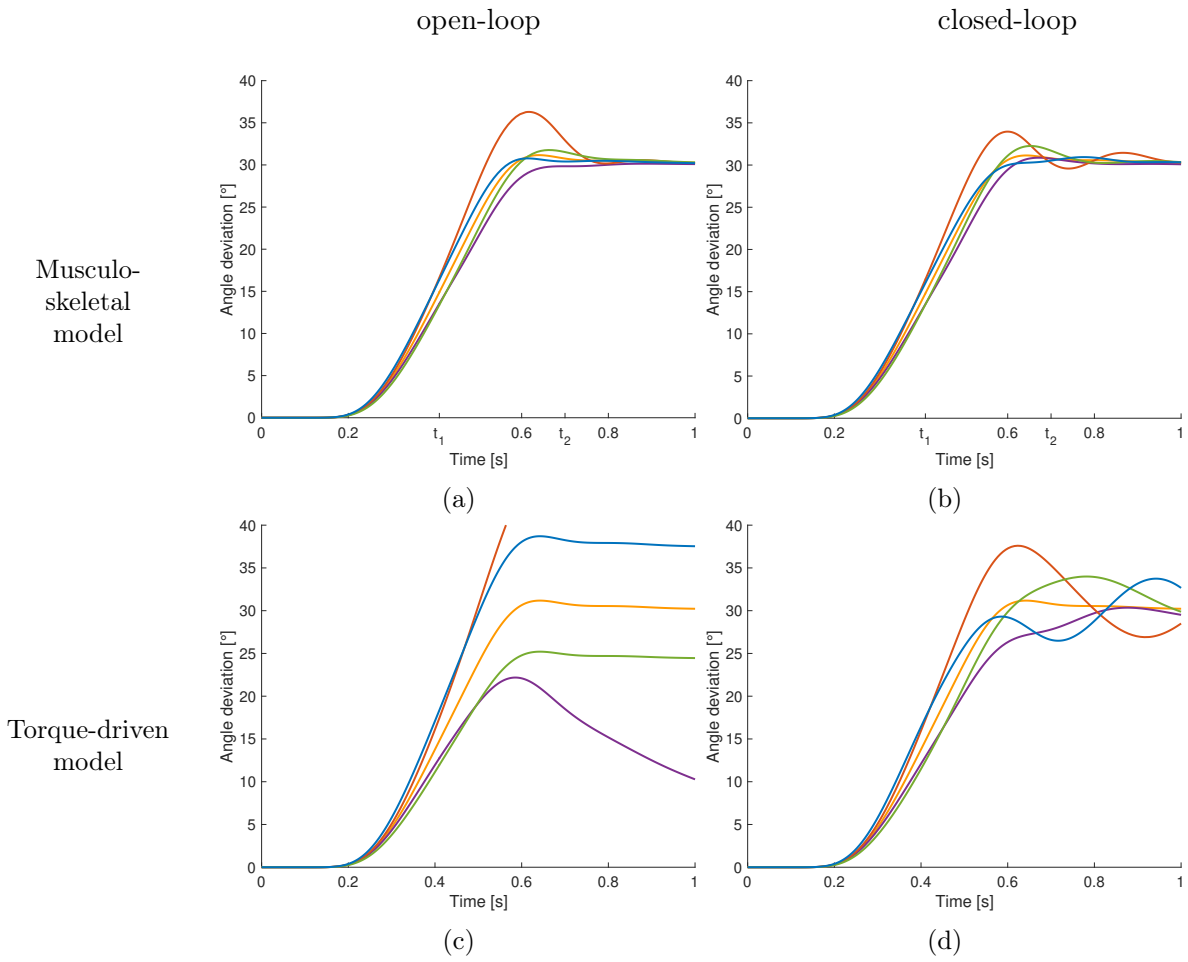

Figure 4.6: **Comparison to open-loop and torque-driven model for case ①.** (a) Resulting trajectories when controlling the musculoskeletal model open-loop, (b) trajectories when controlling the musculoskeletal model closed-loop, (c) trajectories when controlling a purely torque-driven model open-loop and (d) trajectories when controlling a purely torque-driven model closed-loop.

4.3.3 Dynamic torque perturbation

The response to the dynamic perturbations in the simulation is qualitatively similar to what has been observed in the experiments (Figure 4.7b and Figure 4.7c). Most relevant here is the reaction directly after the perturbation which reflects in a change in angular velocity. Therefore, we calculated the relation between the angular velocity in the elbow joint at the beginning and the end of the perturbation (Figure 4.7a, $\Delta t = 37.5\,\text{ms}$). For a perturbation in the direction of the movement, the velocity is approximately doubled while it is halved for perturbations against the direction of movement. The velocity quotient between the velocity in the beginning and the one 100 ms after the beginning of the perturbation (Figure 4.7a, $\Delta t = 100\,\text{ms}$) deviates more from the experiment than the one after 37.5 ms.

Note that no parameters were tuned to match the perturbed trajectories. For all static and dynamic perturbation types, the same feedback gains, delays and desired levels of co-contraction are used. For case ②, some parameters need to be re-optimized in comparison to ① to compensate for the constant torque that mimics gravity and to allow for an extension movement. The whole set of control parameters can be found in Table A3.1.

The open-loop controlled system shows a similar response to the dynamic perturbations as the closed-loop version and also as the subjects in the experiment (Figure 4.8a).

The trajectories generated by the torque-driven model do not reach the desired target position without feedback (Figure 4.8c). With feedback, the trajectories get closer to what has been observed in the experiments, but there are oscillations around the target position (Figure 4.8d).

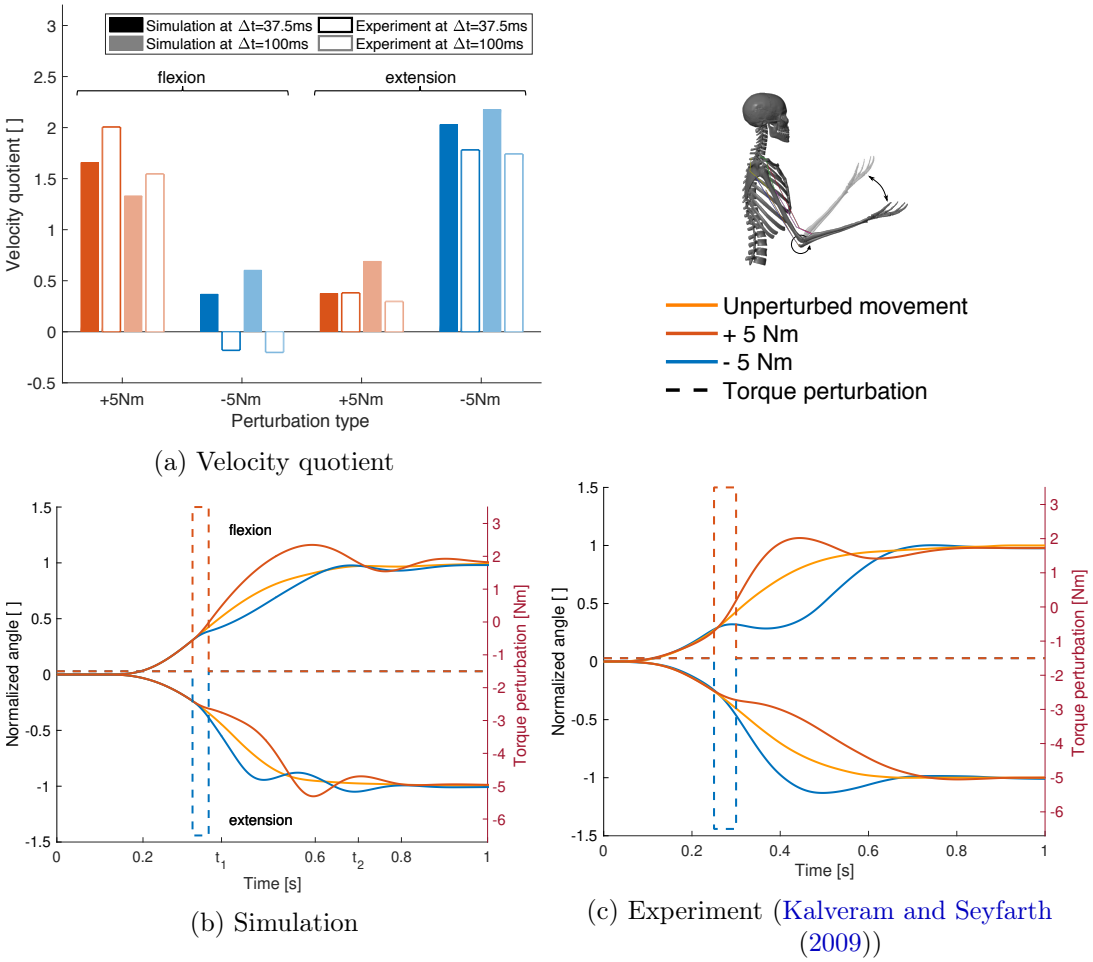

(a) Velocity quotient

(b) Simulation

(c) Experiment (Kalveram and Seyfarth (2009))

Figure 4.7: **Results for case** ②. (a) Evaluation criterion for the dynamic perturbations: The quotient of the angular velocity at the beginning of the perturbation and after Δt (37.5 ms and 100 ms, see Equation (4.6)) shown for both, the simulation results (filled bars) and the experimental results (empty bars) for all four perturbation types (experimental results are digitized from Kalveram and Seyfarth (2009)). (b) Joint angle trajectories for the four different perturbation types in our simulation and (c) in the experiment (digitized from Kalveram and Seyfarth (2009)). Note that the experimental results show the trajectory for one typical control subject. The upper curves show flexion movements, the lower curves show extension movements. The dashed lines visualize the applied torque perturbations.

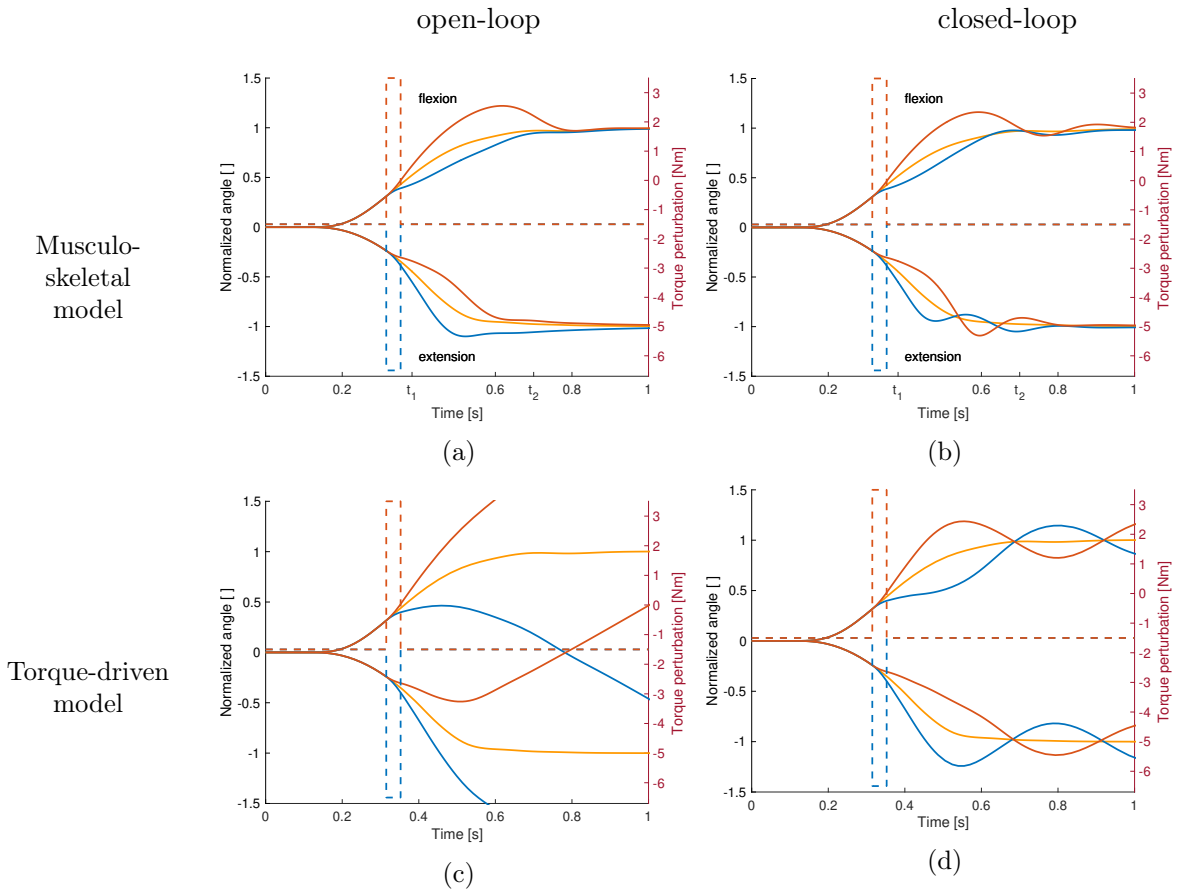

Figure 4.8: **Comparison to open-loop and torque-driven model for case ②.** (a) Resulting trajectories when controlling the musculoskeletal model open-loop, (b) trajectories when controlling the musculoskeletal model closed-loop, (c) trajectories when controlling a purely torque-driven model open-loop and (d) trajectories when controlling a purely torque-driven model closed-loop with the same controller as described above.

4.3.4 Internal force responses

Our model approach allows for analyses of internal muscular and joint force responses as well as the proprioceptive feedback signals that cannot be observed in experiments. To show the possibilities this method offers, we evaluated the joint angle, muscle stimulation and resulting activity, internal muscle and joint forces and active joint torque exemplary for one static and one dynamic perturbation case and for one muscle (Figure 4.9). The changes in the total muscle stimulation are due to the implemented feedback mechanism: For example in Figure 4.9b, the perturbation acts against the direction of movement, so the muscle stimulation is increased to compensate for it. Also the muscle force is increased as a consequence of the perturbation. In consequence, the contact force and the constraint force in the elbow joint are increased as well.

4.3.5 Sensitivity analysis

We perform a local, first order differential sensitivity analysis by varying the control parameters listed in Table A3.1 one-at-a-time (e.g., Dickinson and Gelinas, 1976; Morio, 2011; Rockenfeller, 2016). We calculate absolute and relative sensitivities as defined below and choose scalar state variables for the different cases. The relative change of a parameter x is set to $\Delta = 1 \times 10^{-3} \cdot x$, i.e. we perform a local sensitivity analysis without taking into account the physiological range of the parameters (Rockenfeller et al., 2015; ten Broeke, 2017).

4.3.5.1 Absolute sensitivity of the trajectory per time step

We define the absolute sensitivity coefficient as

$$S_{\text{abs.}} := \frac{f(x+\Delta) - f(x)}{\Delta}, \tag{4.7}$$

which approximates the derivative of $f(x)$ in the direction of the parameter x for Δ small enough.

As scalar state variable we choose the difference between the simulated and the experimental trajectory. For every time step, we sum this trajectory difference over all four perturbation cases and add the unperturbed case for each the static and the dynamic perturbations. In doing so, the time evolution of the sensitivity of the trajectory to the control parameters can be investigated.

4.3.5.2 Relative sensitivity of one characteristic measure

We define the relative sensitivity coefficient as

$$S_{\text{rel.}} := \frac{\frac{f(x+\Delta)-f(x)}{f(x)}}{\frac{\Delta}{x}} = S_{\text{abs.}} \cdot \frac{x}{f(x)}, \tag{4.8}$$

i.e. it is a normalized approximation for the derivative of the state variable $f(x)$ in the direction of the parameter x for Δ small enough (e.g., Lehman and Stark, 1982). This relative sensitivity is sometimes referred to as *elasticity* (ten Broeke, 2017). The advantage of the normalization is that the resulting sensitivity indicator is easier to interpret and more comparable between

different cases or even across models (Rockenfeller et al., 2015; Scovil and Ronsky, 2006). Using this definition, the relative sensitivity indicates the percentage change in the state variable per percentage change in the parameter value. For example, a relative sensitivity $S_{\text{rel.}} = 2$ indicates that a $m\%$ change of the input parameter x results in a $2m\%$ change of the output $f(x)$.

As scalar state variable that describes the behavior in reaction to the perturbations, we choose a measure that describes the characteristics of the reaction to the perturbations. For the static perturbations, we choose the cost function (4.5). For the dynamic perturbations, we calculate the difference between the velocity quotient (4.6) in the simulation and the one in the experiment and sum it over all four types of perturbations.

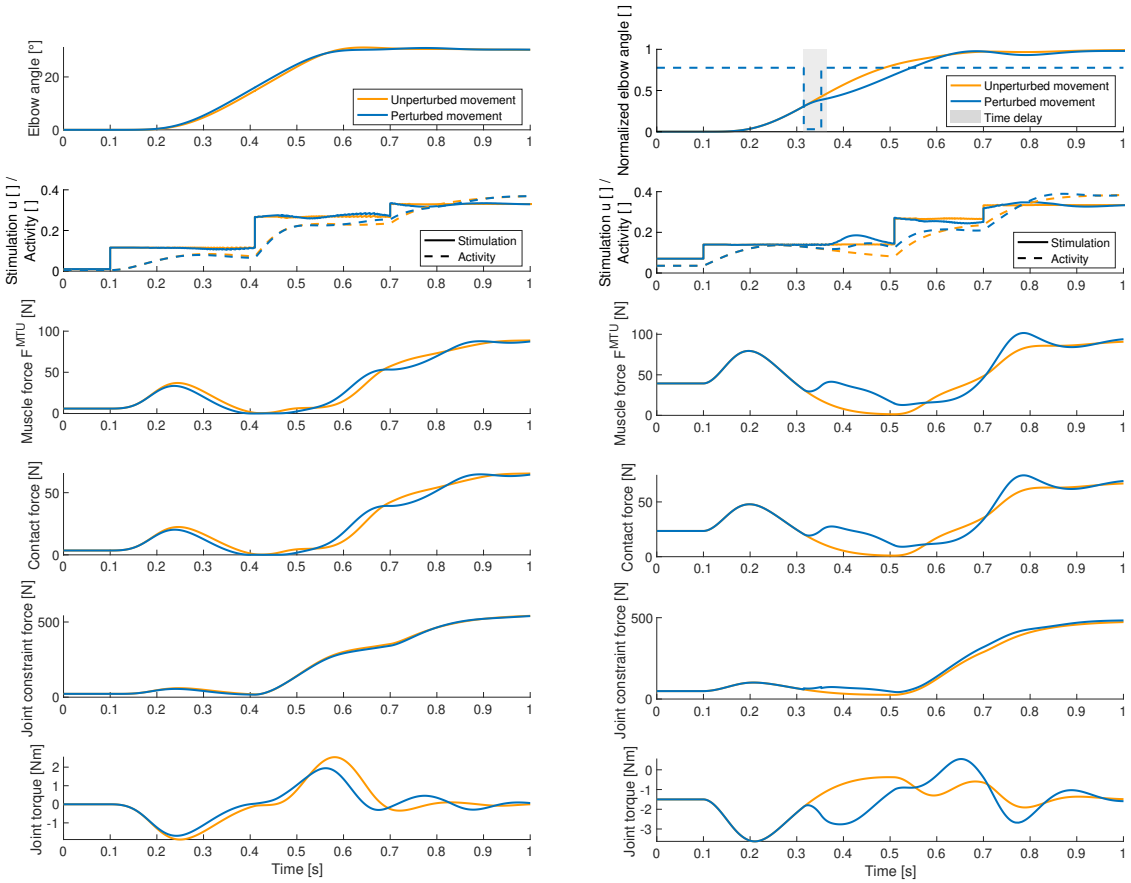

(a) Increased inertia

(b) Flexion movement with a negative torque impulse perturbation

Figure 4.9: **Selection of quantities that can be investigated using our model.** Elbow joint angle, muscle stimulation and activity, muscle force, muscle-bone contact force, joint constraint force and active joint torque for the unperturbed trajectory (orange) and for a perturbed movement (blue). These results are exemplary shown for the elbow flexor muscle and (a) for an increase in inertia and (b) for a flexion movement with a negative torque impulse perturbation. Here, the gray area visualizes the length of the time delay in the controller (50 ms), i.e. the time after the perturbation before the feedback mechanism is activated. Note that the total muscle stimulation in the unperturbed case is equal to the open-loop contribution in the perturbed case. For all forces, the resultant force is shown. The contact force is the force at the first deflection ellipse (positions of the ellipses see electronic supplementary material). The active joint torque represents the torque acting on the joint that is a consequence of the muscle forces.

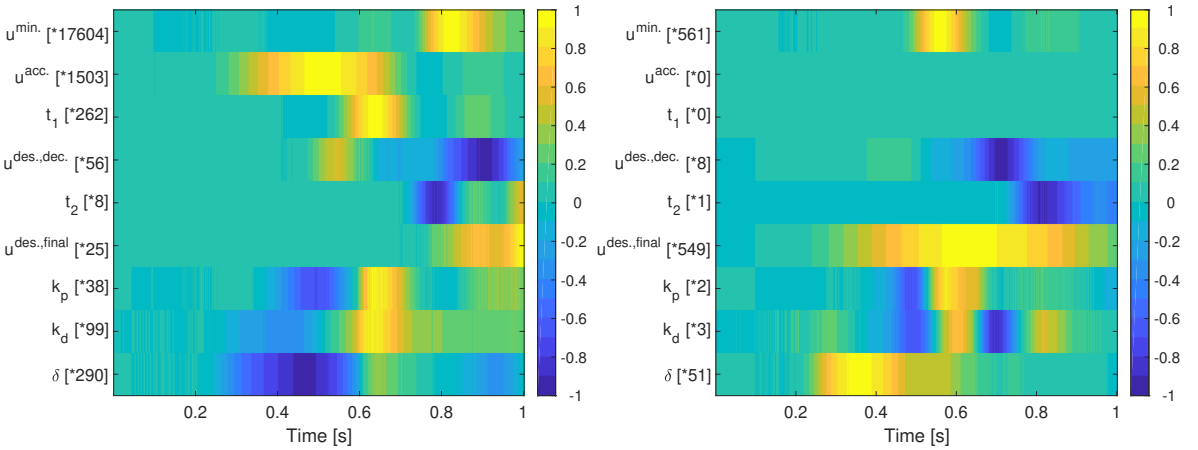

(a) Static perturbations (b) Dynamic perturbations

Figure 4.10: **Normalized absolute sensitivity** $S_{\text{abs.}}$ over time for (a) the static and (b) the dynamic perturbations. Each line represents one of the varied parameters. For visualization purposes, all sensitivities are normalized by dividing them by the maximum absolute value per parameter. This maximum absolute value is shown in the square brackets after the name of each parameter to denote the differences in magnitudes.

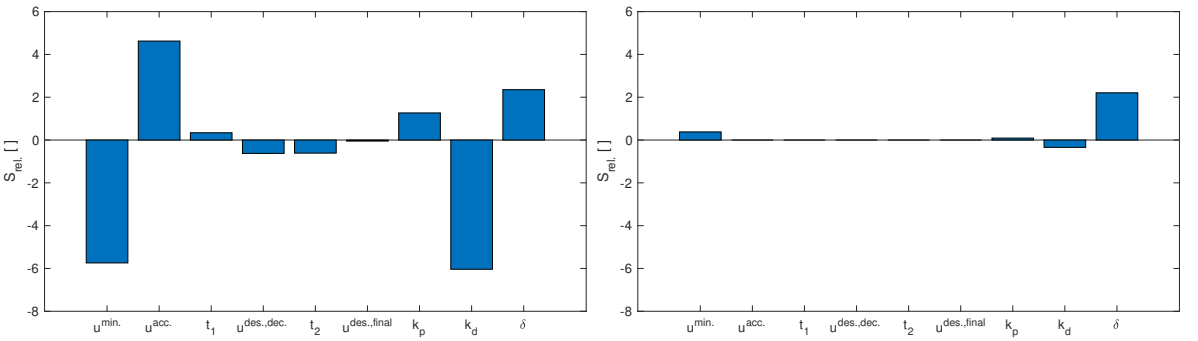

(a) Static perturbations (b) Dynamic perturbations

Figure 4.11: **Relative sensitivity** $S_{\text{rel.}}$ for each of the varied parameters for (a) the static perturbations using the cost function (4.5) as characteristic measure and (b) the dynamic perturbations using the summed difference between the velocity quotient (4.6) in the simulation and in the experiment.

4.4 Discussion

Our goal was to propose a model of human goal-directed arm movements which fulfills all three criteria that we formulated in the introduction: Our neuro-musculoskeletal model shows valid responses to both static and dynamic perturbations and therefore fulfills criterion (c). This alone is novel, as typically only one category of perturbations is studied and reproduced by previous models. The predicted response to both types of perturbations is an emerging behavior of the sensorimotor integration in the model which was achieved by fulfilling the other two criteria, both specifying the level of detail of the modeling. The high level of biomechanical detail allows predicting muscle-tendon based proprioceptive feedback signals, internal muscle forces, muscle-bone contact forces, and joint loads (Figure 4.9), all of which require the representation of muscle-tendon complexes and geometrical muscle routing in the model (criterion (a)). In consequence, kinematic- or torque-based control concepts of human motor control are not applicable, as a control input is required on the muscular level for our model (one for each muscle). The proposed controller is a combination of an open-loop controller and a low-level muscle spindle signal based controller (criterion (b)). The open-loop controller generates a (close-to) minimum jerk trajectory for the unperturbed movement. Only in the presence of a perturbation, the closed-loop control contributes to the muscle stimulations. Thus, this model allows for gaining insights into the sensorimotor integration in response to external forces.

The experimental data on the applied static (Bhanpuri et al., 2014) and dynamic perturbations (Kalveram and Seyfarth, 2009) that we used to validate our model response has been previously reported in the literature. The static perturbations represent changes in inertia and viscosity continuously affecting the dynamics of the lower arm (Bhanpuri et al., 2014). Such force fields have been a valuable tool to investigate motor control models (e.g., Pinter et al., 2012) and, particularly, motor adaptation (e.g., Gribble and Ostry (2000); Kistemaker et al. (2010), review: Franklin and Wolpert (2011)). Please note that in this contribution we focused on the non-adaptive neuro-muscular response in the sense of a sudden response to an unexpected perturbation in between a large set of null-trials, thus, neglecting motor learning (e.g., Burdet et al., 2006; Shadmehr et al., 2010; Yang et al., 2007). This is also the case for the dynamic perturbations, which represent a sudden and time-limited external torque. These perturbations represent a broad spectrum of systematic perturbations as they may occur in ergonomically relevant scenarios or in the interaction with assistive devices.

Individually, the response to these perturbations have been reproduced by motor control models before (static: (Bhanpuri et al., 2014) and dynamic: (Kalveram and Seyfarth, 2009)). Both models reproduced the experimental kinematics by means of a torque in the elbow joint. Both have an inverse model which, due to the simple equations of the model, can analytically compute the required open-loop torque to achieve a desired joint trajectory. The model proposed by Bhanpuri et al. (2014) compensated for the static perturbations with a long-latency (100 ms) negative feedback control on the error between desired (minimum-jerk) and actual elbow joint angle trajectory. The model proposed by Kalveram and Seyfarth (2009) is quite similar. However, it proposes zero-time-delay negative feedback representing the tunable mechanical elasticity of the muscles. Both models did not consider muscle contraction dynamics and, therefore, do not allow to investigate the sensorimotor interplay in consequence of such perturbations. The model presented here transfers these control concepts to the more physiologically detailed musculoskeletal model. As a consequence, it validly reproduces the response

to both static and dynamic perturbations and, in addition, allows for further insights into the neuromuscular interplay of arm movements and internal dynamics in response to such perturbations (Figure 4.9), as we will discuss in the following.

4.4.1 Unperturbed movements: intermittent open-loop control

In our model, the unperturbed reference movement is solely generated by an open-loop command. Although other musculoskeletal models show that feedback signals may play a role in the generation of unperturbed arm movements (e.g., Bizzi et al., 1992; Desmurget and Grafton, 2000; Kambara et al., 2009; Kistemaker et al., 2006), we chose this approach to closely resemble the motor control models previously used to investigate these perturbations (Bhanpuri et al., 2014; Kalveram et al., 2005). To be able to determine an open-loop control signal in our neuro-muscular model, we parametrized the control signal resulting in a piecewise constant stimulation over time for each muscle (Figure 4.3). Hereby we exploit the advantage of neuromusculoskeletal models that allow stable open-loop starting and target positions due to the passive viscoelastic characteristics of the muscles and the length dependence of the activation dynamics (Kistemaker et al., 2005, 2007a). Such so-called *equilibrium points* (Feldman, 1986) can be found without and with gravity. Previously, complete equilibrium trajectories have been proposed as control concept for smooth movements, where each point on the kinematic trajectory is an equilibrium point (Bizzi et al., 1992; Flash and Hogan, 1985). Kistemaker et al. (2006) composed their open-loop signal from several intermittent equilibrium points resulting in a piecewise constant stimulation over time for every muscle. Also, our controller generates an intermittent purely open-loop stimulation to generate the desired movement.

This intermittent control has two characteristics worth mentioning. Firstly, it is interesting to see that it actually results in a smooth movement – without gravity: Figure 4.6a and with gravity: Figure 4.8a. This is a result of the activation dynamics, the viscoelastic properties of the muscle-tendon units, and the inertia of the lower arm. Secondly, it can achieve the required velocity purely controlled by an open-loop signal. This is in contrast to previous intermittent equilibrium point control, where proprioceptive feedback was included to achieve fast movements (Kistemaker et al., 2006). While their intermittent control points all were equilibrium points taken directly from their desired trajectory, the intermittent control parameters in our optimization are free, allowing us to match the velocity of the experiments purely by open-loop control.

4.4.2 Perturbed movements: hierarchical levels of feedback

An external force applied to the arm during the movement generates a deviation from the planned/anticipated movement. With our model, we can study the response of the neuromusculoskeletal system on several hierarchical levels:

Musculoskeletal response: The evaluation of the stimulation signals (Figure 4.9) shows that the relative contribution of the feedback signal is small (always $<$16% for 25 ms delay, $<$34% for 50 ms delay, even less for the static perturbations), i.e. the stimulation comes predominantly from the open-loop controller. We therefore repeated the perturbation simulations with open-loop control. Interestingly, even when solely driven by an open-loop command, the system already shows a similar response to the perturbations as the healthy subjects in the experiments

(Figure 4.6a and Figure 4.8a). The reason for this is that the antagonistically arranged muscle models account for the non-linear force-length-velocity relationship of muscle fibers and the passive non-linear elasticities of tendons. This relationship basically acts as a zero-time-delay peripheral feedback (previously termed *preflex*, (Brown et al., 1995)). In consequence, the force produced by the muscles changes not only with changes in stimulation but also with changes in the length and contraction velocity of the muscle fibers – which change during the movement. Hence, our open-loop controlled system includes an internal feedback mechanism on the muscular level. The role of this effect becomes strikingly clear in comparison to a torque-based model that was able to reproduce the unperturbed movement but failed to adequately respond to the perturbations in the open-loop scenario. So, the difference between the open-loop controlled musculoskeletal model (Figure 4.6a and Figure 4.8a) and the torque-driven model (Figure 4.6c and Figure 4.8c) is the consequence of the immediate physical response due to the impedance of the muscular system. The relevance of this immediate response is also emphasized by the velocity quotient evaluated at 37.5 ms after the perturbation (Figure 4.7a) as it is independent of the feedback signal and thus reflects the musculoskeletal response. The resemblance of this velocity quotient to the experiment indicates that the system's state is adequately represented as it characterizes the initial response to perturbations. This means that the first zero-time-delay response is provided by the muscle-tendon units and it shows already correct qualitative responses to the perturbations. This indicates that the relative importance of feedback over feed-forward may be diminishing in the presence of muscular characteristics (Pinter et al., 2012), which is particularly interesting with respect to assistive devices for rehabilitation. Furthermore, the capability of the musculoskeletal system to stabilize against external perturbations (Brown et al., 1996; Wagner et al., 2007) may allow reducing the informational control effort (Haeufle et al., 2014a, 2020b) by exploiting the capability of morphological computation of the biomechanical system (Ghazi-Zahedi et al., 2016).

First neuronal response: The next level of response to the perturbation is the short- or long-latency feedback mechanism that we implemented in our model. Both the short- and the long-latency feedback lead to the same qualitative behavior (see Appendix A3 for short-latency results). Depending on the type of perturbation, the feedback in our model helps to bring the simulated trajectory closer to the experiment (Table 4.1). For the damping perturbations, the closed-loop controlled system is less sensitive to the perturbations than the version without feedback, because the feedback works against the perturbations during the whole movement. Therefore, with feedback, the movement is closer to the unperturbed trajectory which is closer to the experiment than the open-loop version of the model. When perturbing the inertia properties, feedback enhances the effect of the perturbation which leads to a trajectory that is further away from the experiment. This becomes visible in the quantification criterion *dysmetria*, which evaluates the deviation in the target position due to the static perturbations. On the other hand, the quantification criterion *early velocity* for the static perturbations is only little affected by the feedback because it is measured in the early phase of the movement where feedback does not play a big role due to its delay. Also for the dynamic perturbation, feedback improves the response. However, this is only little reflected in the chosen quantification criterion (velocity quotient, Figure 4.7a) since it takes into account the velocity before the perturbation and 37.5 ms or 100 ms after the perturbation, respectively, while the feedback delay is 50 ms. Hence, the model prediction benefits from the sensorimotor integration on the lower-level reflex level in response to these perturbations.

More complex long-latency feedback and higher-level adaptation: In addition to the musculoskeletal response and the simple short- and long-latency feedback, more complex long-latency feedback and higher-level control would be able to further handle the late consequences of perturbations. While data on dynamic perturbations in human arm movements indicate only a small response in the time-window of short-latency reflexes – as in our model –, it shows well-tuned and adequate responses of long-latency reflexes (45–100 ms, Kurtzer et al. (2008)). Such long-latency feedback (100 ms) has been used by Bhanpuri et al. (2014) to compensate for the static perturbations in their torque-driven model, an effect we can reproduce in our torque model as well (Figure 4.6d and Figure 4.8d) where responses get closer to the experiment than without feedback but tend to oscillate around the final positions. Currently, our neuro-musculoskeletal model does only consider the muscle-fiber-length- and velocity-dependent aspects of long-latency reflexes. More complex or higher-level feedback strategies seem not necessary to reproduce the immediate perturbation response.

Relevance for motor control: We interpret these findings such that muscles generate an immediate zero-time-delay impedance response. Short-latency feedback and our simplified representation of long-latency feedback have little influence, and not necessarily beneficial for all types of unexpected interaction forces. More complex long-latency feedback could then consider an internal model of limb dynamics (Kurtzer et al., 2014, 2008) for an adequate complex response. However, this is not implemented in our model (Equation (4.4)). Therefore, the detailed modeling of the low-level neuro-muscular control mechanism is suggested to be important to understand (i) higher-level control mechanisms, (ii) their disturbances in patients with movement disorders and (iii) to develop effective assistive devices to compensate for those disturbances.

4.4.3 Model assumptions and limitations

To derive control parameters, we made a few assumptions. The most prominent assumption was the triphasic pattern (Equation (4.2)) which was our approach to tackle the inverse model problem: finding required control signals for the desired trajectory. Our approach was inspired by the observation of triphasic patterns in muscle surface electromyograms (EMG) (see e.g., Wachholder and Altenburger (1926), Wierzbicka et al. (1986) and Kistemaker et al. (2006)) and has been discussed in detail above (Section 4.4.1). Other approaches tackled this inverse problem by reducing the biomechanical complexity: Examples are ideal torque generators in the joints (e.g., Bhanpuri et al., 2014), linear or non-linear spring ,and spring-damper models (e.g., Kalveram and Seyfarth, 2009; Kalveram et al., 2005), or simplified muscle models which contain no tendons, no activation dynamics and an entire model without any neuronal delays (Teka et al., 2017). Furthermore, inverse relations between a desired movement and control may also be resolved for musculoskeletal models by more elaborate optimizations (Driess et al., 2018; Kistemaker et al., 2014; Todorov, 2004), although it is not easy to determine a physiologically relevant cost function (Berret et al., 2011; Loeb, 2012; Todorov, 2004). A third option entirely circumvents the inverse problem by iterative motor learning (e.g., Gribble and Ostry, 2000; Kambara et al., 2009).

Some of the control parameters were chosen by hand while others were optimized to match the unperturbed or perturbed trajectories (see Table A3.1). To investigate the influence of the control parameters on the resulting movement, we performed a sensitivity analysis (see

Section 4.3.5). We quantified the sensitivity to small changes of the control parameters in two ways: a) by measuring the effect on the trajectory (time-based measure) or b) by measuring the effect on a scalar characteristic measure that describes the behavior (cost function used in the optimization Equation (4.5); velocity quotient Equation (4.6)). Note that these sensitivity indicators need to be treated carefully as for example the relative sensitivity to a change of the time delay δ around the reference value of 50 ms is relatively high (Figure 4.11) while a change of the time delay from 50 ms to 25 ms or 100 ms without re-optimizing the other control parameters has only little influence on the qualitative behavior in reaction to the perturbations (results not shown here). This is due to the fact that the chosen state variables are sums over several cases and non-linear functions of the input parameters. The influence is even smaller when re-optimizing the other control parameters after changing the time delay from 50 ms to 25 ms (see Appendix A3) or 100 ms (not shown here). In doing so, the changes in the delay can be compensated for by adapting the other control parameters. We assume that the nervous system similarly adapts the motor control when for example the feedback delay changes. Overall, the sensitivity analysis shows that some control parameters do have a relevant influence on the results. However, the overall behavior is only little affected when the other control parameters are re-optimized to compensate for the change.

The second assumption for the control is further related to the biomechanical representation: the type of feedback. Torque models and other simplified models often use the joint angle as the control level to account for deviations between desired and actual trajectory (e.g., Bhanpuri et al., 2014; Kalveram et al., 2005). In our model, however, we use muscle spindle signal based feedback and assume that it provides direct feedback of the muscle fiber length and contraction velocity. We neglect other types of proprioceptive feedback, for example from Golgi tendon organs, which may provide a link to joint-based control (Kistemaker et al., 2013). Furthermore, more detailed representations of the proprioceptors (Loeb and Mileusnic, 2016) allow for a detailed analysis of, e.g., the role of alpha-gamma co-activation (Lan and Zhu, 2007; Lan and He, 2012).

Finally, one crucial assumption is the neuronal delay, as it strongly influences the interpretation of the location of the feedback in the neuronal hierarchy. By assuming zero time delay, Kalveram et al. (2005) located the negative feedback control at the biomechanical level – a common approach which is not always clearly separated from afferent signals (e.g., Teka et al., 2017). Experimental findings show that the short-latency reflex can produce more sophisticated responses to perturbations than previously thought (Weiler et al., 2019). This short-latency feedback occurs after a time delay of approximately 20–50 ms after a perturbation (Kurtzer et al., 2014; Pruszynski and Scott, 2012; Shemmell et al., 2010). Other delays in the order of 50–100 ms represent long-latency reflexes (Kurtzer, 2015; Pruszynski and Scott, 2012; Shemmell et al., 2010; Weiler et al., 2016), as used for example by Bhanpuri et al. (2014); Gribble and Ostry (2000). Several studies have shown that the long-latency stretch response plays an important role in the reaction to mechanical perturbations in goal-directed reaching movements (e.g., Kurtzer et al., 2014; Weiler et al., 2016). In our model, using 25 ms delay, the implemented feedback mechanism represents a simplified model of the spinal, mono-synaptic muscle spindle reflex (Pruszynski and Scott, 2012; Weiler et al., 2019), assuming that the muscle spindles provide accurate time-delayed information about the muscle fiber lengths and contraction velocities (Kistemaker et al., 2006). However, this model of the afferent feedback does not accurately reflect the natural muscle spindle feedback which is only sensitive to the muscle's

local stretch (Kurtzer et al. (2014), see Scott (2016) for an overview) while our formulation reacts to stretch and shortening. Therefore, choosing a time delay of 50 ms and thus modeling a long-latency reflex seems more appropriate. However, this model considers only the muscle-fiber-length- and contraction-velocity-dependent part of the long-latency feedback and neglects other aspects. This becomes visible in the velocity quotient after 100 ms (Figure 4.7a) which characterizes the behavior at the end of the first neuronal response. It is further away from the experiments than the velocity quotient after 37.5 ms, suggesting that our long-latency feedback model does not include all relevant feedback mechanisms. Experimental findings indicate that long-latency feedback represents the net impact of spinal and cortical circuits and thus includes several independent processes (e.g., Kurtzer et al., 2014; Pruszynski et al., 2011) that for example account for limb biomechanics (Kurtzer, 2015) or evoke responses in muscles that were not stretched (Weiler et al., 2018). The reaction after more than 100 ms after the perturbation is influenced by more complex and higher-level feedback mechanisms and voluntary activities (Kurtzer, 2015; Pruszynski and Scott, 2012; Weiler et al., 2016) that are not represented in our model. Although the resulting reactions of our model to the perturbations seem quite sensitive to the chosen delay time (see Section 4.3.5), the results were quite similar for choosing 25 ms, 50 ms or even 100 ms delay (the latter results are not shown in this contribution). Our model reproduces the response to the perturbation by using short-latency feedback (25 ms) which represents spinal control layers or long-latency feedback (50 ms) which has spinal and supraspinal influences. Once more this emphasizes the decentralized control. However, as the feedback contribution was rather small and did not improve the response in all cases, it is likely that more sophisticated models, which may, for example, include multiple layers of feedback including more complex long-latency feedback (Kurtzer et al., 2008) would improve the model prediction.

As with the control and feedback assumptions, also the level of detail of the musculoskeletal model has its limitations. Although our muscle model represents contraction dynamics quite well (Haeufle et al., 2014b), it does not consider recent findings on the behavior of muscles under eccentric loading conditions (Tomalka et al., 2017), on the possible role of short-range stiffness (De Groote et al., 2017; Nichols and Houk, 1976), or the effect of transversal loading (Siebert et al., 2014). As we see significant force changes in the dynamic perturbations originating from the muscle's passive characteristics (Figure 4.9), these new findings may also influence the response. Ultimately, for the study of internal contact forces, finite-element models may allow a more detailed analysis (Röhrle et al., 2016) but significantly increase the complexity of finding an adequate controller (Martynenko et al., 2017).

4.4.4 Conclusion

For our study, the focus was on the valid prediction of the response to static and dynamic external perturbations while providing the possibility to investigate the neuromuscular interplay at a level that allows predicting muscle-bone contact forces and joint loadings. As our model with its assumptions and limitations still fulfills the initially stated criteria, we consider it a starting point to further develop models with the integrated use: studying motor control and ergonomics with the same model for research questions where they overlap, e.g., for the development and ergonomic risk assessment of assistive devices.

5 | Simulating the response to assistive forces of wearables

In the previous chapter, we found that our arm model can reproduce human movements with and without external mechanical perturbations. Such mechanical perturbations can for example be introduced by a wearable assistive device. Therefore models of the human arm may help to estimate design parameters like peak torque and power of such assistive devices by predicting required forces to compensate for motor control impairments. This chapter focuses on the idea of compensating hypermetria (overshoot), a motor control deficit that may occur in neurodegenerative diseases, by a simple assistive device. As musculoskeletal dynamics play an important role in the interaction between an assistive device and the neuro-musculoskeletal system, we hypothesized that their consideration in the model might influence the predicted design parameters. To test this, we simulated two-degree-of-freedom point-to-point arm movements with our neuro-musculoskeletal model (Section 3.2.4). By introducing inconsistent neuronal control parameters, we induced hypermetria. We implemented mechanical and low-level assistive torque strategies in simulation which lead to a reduction of hypermetria. We quantified the difference between required peak torque and mean power as predicted by our neuro-musculoskeletal model in comparison with a torque-driven arm model. We found that, depending on the type of assistance, the predicted torques and powers can differ by more than a factor of 10 between musculoskeletal and torque-driven arm models. We conclude that the magnitude of torque and power required to reduce hypermetria by simple wearable assistive devices may be significantly underestimated if muscle-tendon characteristics are not considered.

Note that large parts of the content of this chapter were accepted for publication at the conference *BioRob2020*. For details on this publication, including a list of authors, see Manuscript 2 in Chapter 2.

5.1 Introduction

Neurodegenerative diseases may cause progressive motor control impairments. The number of individuals affected by such impairments increases worldwide due to aging populations (Logroscino et al., 2018). Currently, there are only symptomatic treatments and medicines to slow down the disease development (Durães et al., 2018). Hence, a growing number of people is expected to benefit from progressive motor assistance in the next decades.

Wearable assistive devices promise to improve the quality of life of people with impaired motor control (Frisoli, 2018; Fromme et al., 2019; Soekadar et al., 2015; Varghese et al., 2018). In the early stage of motor disability of neurodegenerative origin, wearable assistive devices may need to provide relatively small assistive forces to improve movement coordination, e.g.,

to correct unwanted hypermetria (overshoot) in goal-directed arm movements (Bhanpuri et al., 2014; Topka et al., 1998a). By matching force and torque specifications of assistive devices to the impairment level (subject-specific), it would be possible to minimize weight, volume, and cost, potentially increasing user acceptance (Fromme et al., 2019; Varghese et al., 2018). To this end, it would be useful to have adequate computer simulations allowing to predict force and torque requirements, as well as to test control concepts, already in the design phase.

In the literature, motor control models exist which consider and predict impaired movement generation (e.g., Bhanpuri et al. (2014); Mugge et al. (2012)), as well as models describing the response of the (neuro-)musculoskeletal system to external forces (Petrič et al., 2019; Stollenmaier et al., 2020b). Here, the muscle-tendon contraction dynamics are particularly important (Pinter et al., 2012) as they generate the first viscoelastic reaction forces to external perturbations, termed *preflexes* (Brown et al., 1995). Therefore, the integration of impaired motor control models, musculoskeletal dynamics, and assistive forces into one simulation framework is required for the model-based design of wearable assistive devices.

The purpose of this study is to use such an integrated simulation framework to test to which degree the musculoskeletal preflexive forces would influence the design of wearable assistive devices. We focus our analysis on a simplified assistance scenario, i.e., the reduction of hypermetria (overshoot) in goal-directed arm movements through mechanical or low-level controlled assistive torques. We hypothesized that neglecting the muscle-tendon preflex forces (passive viscoelasticities) results in different predictions for the torque and power requirements of the device. We expect this investigation to benefit the design process of wearable assistive devices for early-stage neurodegenerative diseases, i.e., for those applications requiring minimal assistance (light, user-customized) and for which complex EMG-based control schemes might be unfeasible due to impaired neuronal control signals.

5.2 Methods

We simulated goal-directed vertical human arm movements in the sagittal plane. We chose a task in analogy to experiments where subjects point with the index finger to markers appearing on a vertical screen. Going from the start to the target position requires to retract slightly, and afterward extend the finger (typically by elbow flexion) to avoid collision with the screen.

5.2.1 Musculoskeletal model

The musculoskeletal model that we used has been published in a previous work (Stollenmaier et al., 2020b), where it has been shown that it validly reacts to static and dynamic external forces for single-joint arm movements. The response of the model matched that of experimental results under similar perturbations (Bhanpuri et al., 2014; Kalveram et al., 2005).

Here, we used the same model to investigate a movement with two degrees of freedom. The novelty is that we modeled a neuronal impairment leading to hypermetria (overshoot) and additional external assistive torques to reduce the hypermetria.

The model consists of two rigid bodies (lower arm and upper arm) that are connected via two revolute joints (shoulder and elbow, see Figure 5.1). This skeletal structure is actuated by six antagonistically arranged muscle-tendon units (MTUs) (four monoarticular and two biarticular muscles) that are routed anatomically (Hammer et al., 2019) and apply active forces to the

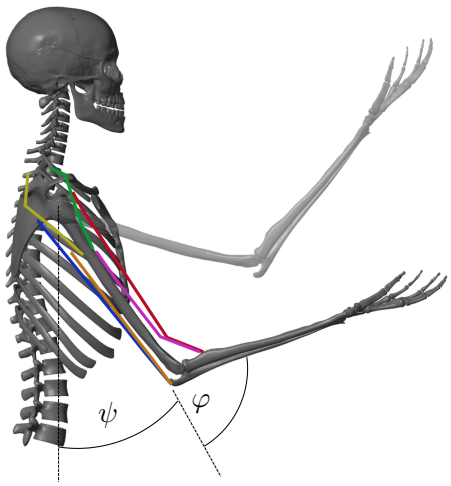

Figure 5.1: **Musculoskeletal model that is used for the computer simulations of the arm movements.** The colored lines represent the six muscles that are modeled using an extended Hill-type muscle model. We investigate the two-degree-of-freedom point-to-point arm movement that is visualized here.

bodies. The MTUs are modeled using a Hill-type model that accounts for muscle fiber and tendon characteristics (Haeufle et al., 2014b), in combination with a model of muscle activation dynamics that considers the fiber length dependency (Hatze, 1977; Rockenfeller et al., 2015) (see Stollenmaier et al. (2020b) for detailed model description and model parameters).

5.2.2 Motor control model

A key characteristic of the antagonistic musculoskeletal setup is the emergence of open-loop stable equilibrium positions (Kistemaker et al., 2006). More precisely, for each combination of open-loop stimulations $\mathbf{u}^{\text{open}}(t)$, the antagonistic muscle forces equilibriate in a specific posture $\mathbf{q}^{\text{EP}_j}(\mathbf{u}^{\text{open}}(t))$ (EP for equilibrium posture). Moreover, each EP can be held with different combinations of stimulations (redundancy), resulting in different levels of co-contraction and thus different joint stiffnesses (due to the non-linear elasticity of the tendons (Bayer et al., 2017)). An external force applied to the model in equilibrium results in immediate (zero-time-delay) viscoelastic restoring forces, the so-called preflex forces (Brown et al., 1995).

In addition to the open-loop control, the model considers a time-delayed ($\delta = 10\,\text{ms}$) monosynaptic muscle spindle reflex as a closed-loop component $\mathbf{u}^{\text{closed}}(t)$ minimizing the difference between desired (λ) and actual (l^{CE}) muscle fiber length (see Figure 5.2). This feedback further increases the stability of an EP, but as a time-delayed neuronal response.

Combined, the motor command for each muscle i is

$$\begin{aligned} u_i(t) &= \left\{ u_i^{\text{open}}(t) + u_i^{\text{closed}}(t) \right\}_0^1 \\ &= \left\{ u_i^{\text{open}}(t) + k_p \Big(l_i^{\text{CE}}(t-\delta) - \lambda_i(t) \Big) \right\}_0^1, \end{aligned} \tag{5.1}$$

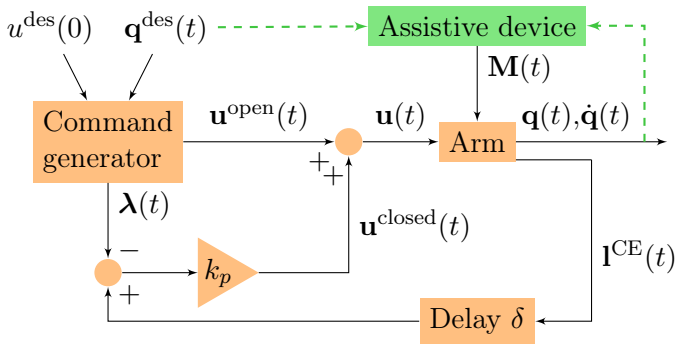

Figure 5.2: **Schematic diagram of the bio-inspired motor control model including an external assistive torque.** The motor command $\mathbf{u}(t)$ is a sum of an open-loop and a closed-loop signal. The time-delayed feedback loop incorporates proprioceptive feedback (mono-synaptic reflexes) by comparing the actual muscle fiber lengths $\mathbf{l}^{\text{CE}}(t)$ to desired values $\boldsymbol{\lambda}(t)$. Here, the observable state $\mathbf{q}(t) = [\varphi(t), \psi(t)]$ contains the elbow and shoulder angle, respectively. An external torque $\mathbf{M}(t)$ is applied to the joints, representing an ideal assistive device.

where $k_p > 0$ is a feedback gain. The operation $\{x\}_0^1$ sets values $x < 0$ to 0 and $x > 1$ to 1.

To determine the control parameters, the command generator maps the desired trajectory $\mathbf{q}^{\text{des}}(t)$ and the initial muscle co-contraction level $u^{\text{des}}(0)$ to the open-loop signals $\mathbf{u}^{\text{open}}(t)$ and to desired muscle fiber lengths $\boldsymbol{\lambda}(t)$. For the vertical pointing movement investigated here, we assume an intermittent switching (Bayer et al., 2017; Kistemaker et al., 2006) between three EPs: the initial posture $\mathbf{q}^{\text{EP}_0}$, an intermediate position retracting the index finger to avoid collision with the screen $\mathbf{q}^{\text{EP}_1}$, and the target posture $\mathbf{q}^{\text{EP}_2}$. This assumption results in piece-wise constant open-loop signals $u_i^{\text{open}}(t)$. Their values are determined individually by minimizing the sum of the difference between muscle stimulations and the desired level of co-contraction at each equilibrium position $\mathbf{q}^{\text{EP}_j}$ (Bayer et al., 2017):

$$\sum_{i=1}^{6} (u_i^{\text{open,EP}_j} - u^{\text{des,EP}_j}) \rightarrow \min, \tag{5.2}$$

subject to the constraint that the sum of all torques acting on the joints is zero (equilibrium, optimized with *fmincon*, Matlab®). The corresponding desired muscle fiber lengths $\boldsymbol{\lambda}^{\text{EP}_j}$ are set to the muscle fiber lengths $\mathbf{l}^{\text{CE}}$ in the equilibrium positions.

Due to the impedance characteristics of the musculoskeletal system and the closed-loop reflex contribution, this intermittent control results in smooth movements (Bayer et al., 2017). To represent an actual human-like movement, the remaining control parameters (the shoulder and elbow angle for the second EP ($\mathbf{q}^{\text{EP}_1}$), the desired level of co-contraction for the second and the third EP ($u^{\text{des,EP}_{1/2}}$), the starting times for the second and the third EP and the feedback gain (k_p)) are optimized. The optimization is done using a pattern search algorithm minimizing the quadratic difference between the simulated and an exemplary unimpaired trajectory, which we assume to be the desired trajectory $\mathbf{q}^{\text{des}}(t)$. All optimizations and simulations are performed in Matlab® 2018a/b.

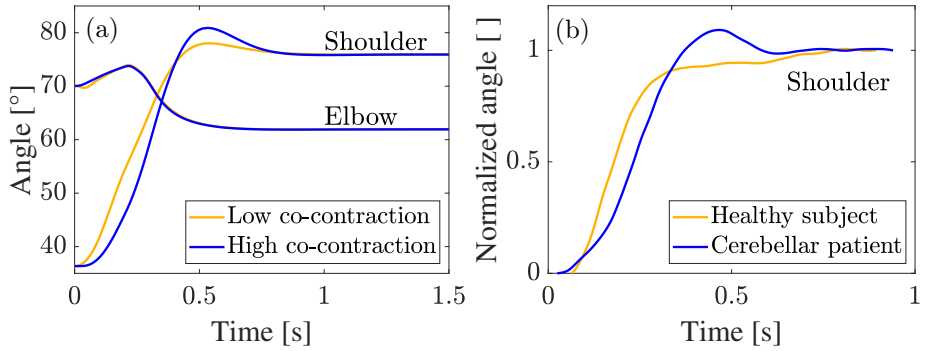

Figure 5.3: **Dysmetric movements in computer simulation and human experiment.** (a) Simulated healthy trajectory for a point-to-point movement and trajectory resulting from a neuronal perturbation. (b) Shoulder angle trajectory for a vertical pointing movement (task slightly different from our objective) for a healthy subject and a cerebellar patient. These data are digitized, normalized and replotted from Topka et al. (1998a).

5.2.3 Neuronal impairment of motor control

In order to simulate impaired motor control, we generated hypermetric (overshooting) behavior with a perturbation on the neuronal level. We exemplary chose a perturbation of the initial muscle co-contraction level which defines the system's initial state (first EP, before the movement starts). For the "healthy" reference movement, the initial co-contraction level is set to $u^{\text{des}}(0) = 0.1$, which means that the desired starting posture $\mathbf{q}^{\text{EP}_0}$ is held with a low level of co-contraction. The control parameters that govern the subsequent movement (second and third EP and feedback gain) are optimized considering this initial state (see above). The "impaired" movement is then generated by increasing the co-contraction in the initial posture ($u^{\text{des}}(0) = 0.5$) without re-optimizing the other control parameters. This mismatch between the motor command and the initial conditions leads to a movement that differs from the desired one. The higher initial co-contraction level results in a slower acceleration of the arm motion due to two factors: (1) the antagonistic muscles are initially more active and therefore generate higher eccentric viscous muscle forces dampening the movement; (2) the higher activity of the antagonistic muscles results in a slower muscle deactivation due to the non-linearity of the activation dynamics (see Fig. 7a in Bayer et al. (2017)) that further intensifies the first effect. The initially slower arm movement causes a larger error in the feedback loop, further intensified by its neuronal delay and eventually resulting in hypermetria (overshooting), predominantly in the shoulder (Figure 5.3a). We chose the initial co-contraction levels described above (0.1 and 0.5), because the amplitude of the overshoot generated by this model of the neuronal impairment roughly matches those reported in the literature for patients suffering from cerebellar ataxia (Topka et al., 1998a) (Figure 5.3b). This model of impairment leads to a behavior qualitatively and quantitatively similar to what has been observed in cerebellar patients, but its validity with respect to the underlying neurological disorder has not been investigated and is not subject of this study.

5.2.4 Model of assistive device for correcting impairment

To test how an assistive device could potentially compensate for such an overshoot, i.e. reduce the amplitude of the overshoot, we implemented different strategies for applying an assistive torque $\mathbf{M}(t) = \left[M^{\varphi}(t), M^{\psi}(t)\right]$ to the arm (Figure 5.2).

5.2.4.1 Constant torque

A simple strategy which requires no online feedback and no knowledge of the desired trajectory is a constant torque M_{const}, applied to the shoulder joint from the beginning of the movement until shortly after the maximum of the overshoot in the impaired movement is reached:

$$\begin{aligned} M^{\psi}(t) &= M_{\text{const}}(t) \\ &= \begin{cases} M_{\text{const}} & \text{for } 0.05 \text{ s} \leq t \leq 0.62 \text{ s} \\ 0 & \text{else.} \end{cases} \end{aligned} \tag{5.3}$$

5.2.4.2 Viscous damping

A strategy which could be implemented purely by passive mechanics is a viscous damping torque M_d applied to the shoulder joint:

$$M^{\psi}(t) = M_d(t) = d \cdot \dot{\psi}(t)\,, \tag{5.4}$$

with angular velocity of the shoulder $\dot{\psi}(t)$ and damping constant d.

5.2.4.3 Difference in torque

Based on inverse dynamics analysis of the kinematics, an assistive torque could be determined by calculating the difference in torque $\mathbf{M}_{\text{diff}}$ between the impaired and healthy movement for both joints and applying it to the respective joint. In our model, the torque in the healthy $\mathbf{M}_{\text{healthy}}(t)$ and impaired $\mathbf{M}_{\text{impaired}}(t)$ movement is determined by measuring the net joint torque generated by the muscles.

$$\mathbf{M}(t) = \mathbf{M}_{\text{diff}}(t) = \mathbf{M}_{\text{healthy}}(t) - \mathbf{M}_{\text{impaired}}(t)\,. \tag{5.5}$$

5.2.4.4 PD controller

Finally, we tested a PD controller $\mathbf{M}_{PD}$ acting on both joints (elbow and shoulder). It uses the current state $\mathbf{q}(t)$ as the input signal and the simulated healthy movement as the reference trajectory $\mathbf{q}_{\text{ref}}(t)$.

$$\begin{aligned} \mathbf{M}(t) &= \mathbf{M}_{PD}(t) \\ &= \kappa_p(\mathbf{q}_{\text{ref}}(t) - \mathbf{q}(t)) + \kappa_d(\dot{\mathbf{q}}_{\text{ref}}(t) - \dot{\mathbf{q}}(t))\,. \end{aligned} \tag{5.6}$$

5.2.5 Idealized torque-driven model for comparison

We implemented an idealized torque-driven model to compare the reaction to assistive torques to those of the musculoskeletal model. This comparison allows for the investigation of the contribution of the preflex forces. The torque-driven model uses the same mechanical parameters (segment lengths, masses, inertia) as the musculoskeletal model. To determine the torque that is necessary to reproduce the musculoskeletal model's movement, we recorded the net joint torque that is applied by the muscles during both the healthy and the impaired movement. No feedback mechanism is implemented, i.e. the torque-driven model is controlled purely open-loop.

5.3 Results and discussion

5.3.1 Constant torque and viscous damping

In the musculoskeletal model, a constant assistive torque M_{const} of adequate magnitude leads to reduced movement velocity and a reduction of the amplitude of the overshoot in the shoulder joint (Figure 5.4a). The same holds for the assistive damping torque M_d representing viscous damping (Figure 5.4c).

In the torque-driven model, these simple assistive torques also reduce the magnitude of the overshoot (Figure 5.4e). However, the required torque level is less than 1/10 compared to the ones in the muscle-driven model. This difference in the magnitude of the predicted assistive torque becomes even clearer when applying the same levels of constant torque to both models (Figure 5.4 (a) vs. (d) and (b) vs. (e)).

Please note: in the torque-driven model, the assistive torques lead to changes in the trajectory and a diverging endpoint. This is expected, as the model is driven by an open-loop torque command and these assistive torques do not enforce (control) the desired movement or endposition. In the musculoskeletal model, there is no systematic change in the trajectory and the final position is reached due to the neuromuscular dynamics, i.e., the low-level reflex and the passive viscoelastic properties resulting in a stable equilibrium at the target.

Hence, the results using a musculoskeletal model indicate that an assistive device imposing a simple constant torque or damping to the shoulder joint may be sufficient to decrease the amplitude of an overshoot without affecting the endpoint accuracy. This is in agreement with experimental observations that mechanical damping may reduce overshoot (Bhanpuri et al., 2014) and tremor (Aisen et al., 1993). However, this requires higher torque and damping than expected from a torque-driven model.

5.3.2 Difference in torque

As expected, applying the torque difference between the impaired and the healthy movement ($\mathbf{M}_{\text{diff}}$) to the torque-driven model results in a perfect correction resulting in the originally desired, healthy trajectory ($\mathbf{q}_{\text{ref.}}$). (Figure 5.5b). In the musculoskeletal model, however, $\mathbf{M}_{\text{diff}}$ does not reduce the amplitude of the overshoot (Figure 5.5a). On the contrary, it even increases the overshooting behavior.

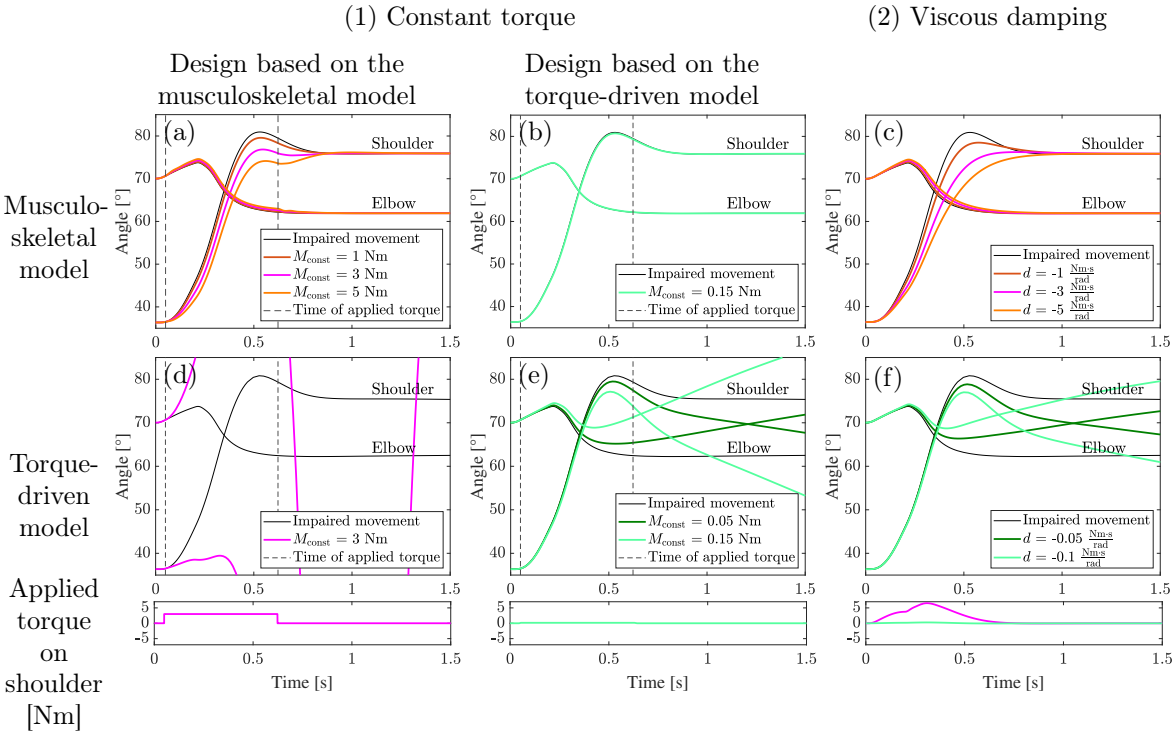

Figure 5.4: **Results for constant torque and viscous damping.** Applying (1) a constant torque M_{const} and (2) viscous damping M_d to the impaired movement to counteract the overshoot as described in Equation (5.3) and Equation (5.4). The last row shows the torque that is applied to the shoulder joint. The magnitude of these assistive torques depends on whether the design is based on the predictions made by a musculoskeletal model or a torque-driven model. A torque level of $M_{\text{const}} = 3\,\text{Nm}$ reduces the overshoot to a healthy level in the musculoskeletal model but causes dramatic deviations from the trajectory in the torque model. However, a torque level of $M_{\text{const}} = 0.15\,\text{Nm}$ sufficiently reduces the overshoot in the torque model, but has no visible effect in the musculoskeletal model. Also for M_d, the required damping value in the musculoskeletal model is much larger ($d = -0.1\,\text{Nms} \cdot \text{rad}^{-1}$ vs. $d = -3\,\text{Nms} \cdot \text{rad}^{-1}$).

While the torque difference, e.g. determined by inverse dynamics (Riener and Straube, 1997), may be helpful for diagnostics, our results suggest that it may cause an increase rather than a reduction of the impairment if it is directly used as a control signal for an assistive device.

5.3.3 PD controller

The feedback gains of the PD controller are tuned such that the resulting torque reduces the amplitude of the overshoot without slowing down the movement. For both models the same proportional gain $\kappa_p = 1\,\text{Nm} \cdot \text{rad}^{-1}$ and derivative gain $\kappa_d = 15\,\text{Nms} \cdot \text{rad}^{-1}$ are used. This results in faster acceleration at the beginning of the movement, thus replicating the healthy

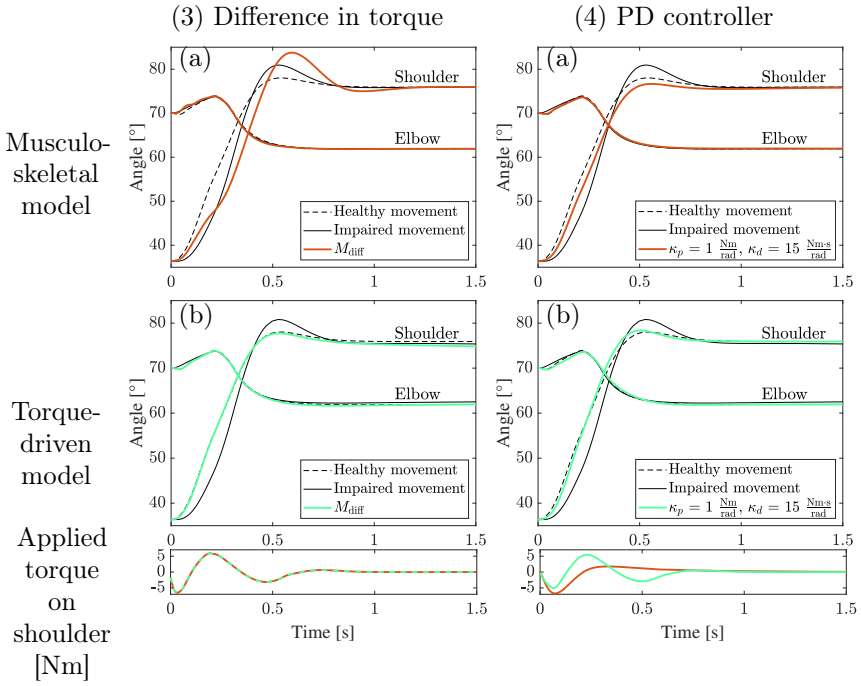

Figure 5.5: **Results for difference in torque and PD controller.** Applying (3) the difference in torque $\mathbf{M}_{\text{diff}}$ between the healthy and the impaired movement (Equation (5.5)) and (4) a torque $\mathbf{M}_{PD}$ that is generated by a PD controller (Equation (5.6)) to the impaired movement in both (a) the musculoskeletal model and (b) the torque-driven model. Please note that the small divergence in the end position in the torque-driven model (3b) is caused by numeric errors which accumulate in this chaotic system.

movement almost exactly in both models (Figure 5.5). This occurs because the PD controller corrects the error in angle and velocities without a time delay. Therefore, the lack of acceleration at the beginning of the movement that leads to the overshoot in the impaired movement is corrected instantly, before the time-delayed reflex could react to it and induce an overshoot. However, the realization of such an assistive device would require exact knowledge of the desired reference trajectories, which poses the challenge of user motion intention recognition (Huang et al., 2015).

5.3.4 Comparison of peak torque and power consumption

The type of arm model used to predict the reaction to the assistive torques influences the magnitude of torque necessary to compensate for the overshoot. To quantify this difference in the comparison between a muscle-tendon- and a torque-driven model, we calculated the respective peak torque and mean power of the investigated assistive torques (Figure 5.6). These two quantities are often design parameters of an assistive device.

Applying a constant torque M_{const} or viscous damping M_d to compensate for the overshoot

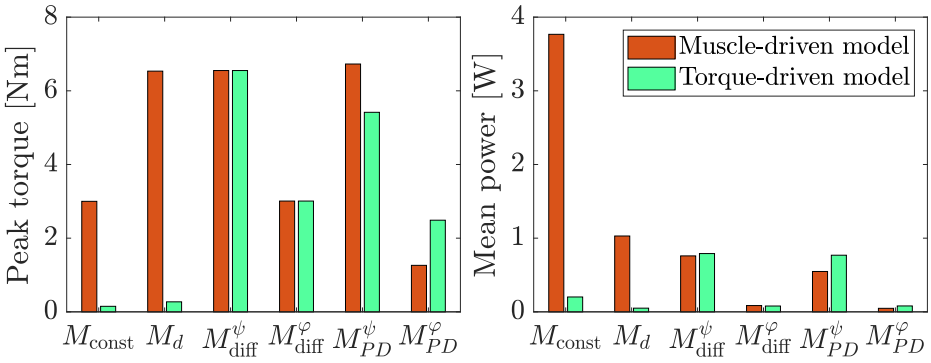

Figure 5.6: **Comparison of the peak torque and mean power consumption of the assistive torque for each type of assistive device applied on the muscle-driven and the torque-driven model.** For this comparison, we selected the parameters that lead - if possible - to a sufficient reduction of the overshoot in each of the respective cases ($M_{\text{const}} = 3\,\text{Nm}$ or $0.15\,\text{Nm}$, $d = -3\,\text{Nms}\cdot\text{rad}^{-1}$ or $-0.1\,\text{Nms}\cdot\text{rad}^{-1}$ for the muscle- and the torque-driven model, respectively). The mean power consumption is calculated as $\bar{P} = \frac{\int_{t_1}^{t_2} M\cdot\dot{q}\,\mathrm{d}t}{t_2-t_1}$.

requires much higher peak torque and mean power in the musculoskeletal model than in the torque-driven model. For more information-driven assistive approaches, like applying the difference in torque $\mathbf{M}_{\text{diff}}$ or using a PD controller $\mathbf{M}_{PD}$, the predicted peak torque and mean power are in the same magnitude for both the musculoskeletal model and the torque-driven model (Figure 5.6).

5.3.5 Model limitations

We neither considered a detailed model of the neuronal impairment, nor any long-latency contribution to the feedback, nor motor learning in the model, all of which may alter the response to external forces. Including these features in our model, followed by empirical validation, would be required in the future.

The torque-driven arm model (without assistive torque) does not consider any type of feedback. We chose this explicitly, as any type of feedback would approximate the neuro-musculoskeletal properties to some degree. The various possible degrees of model representation, from simple impedance to more detailed antagonistic viscoelastic setups (Pinter et al., 2012), would lay between the two approaches considered here.

Finally, the assistive device is modeled in simplified terms. It is assumed to apply an idealized external torque to the joints while not examining the force transmission to the human and not considering the weight, inertia, or internal friction of such an assistive device. Also, we do not address the issue of user intention recognition (Huang et al., 2015), which is always difficult, but required to provide a desired trajectory for classical control approaches like $\mathbf{M}_{PD}$.

5.4 Conclusion

The magnitude of peak torque and mean power required to reduce an overshoot-like motor control impairment by a mechanically simple assistive device may be underestimated if muscle-tendon characteristics are not considered. Overshoot, as observed in cerebellar patients (Bhanpuri et al., 2014; Riener and Straube, 1997; Topka et al., 1998a), is only one motor control impairment which may progress due to neurodegeneration. Also tremor in Multiple Sclerosis patients may be reduced by mechanical damping (Aisen et al., 1993). For all progressive motor control impairments due to neurodegeneration, such simple devices would be preferable over bulky powerful exoskeletons, especially in the early phase where potentially small assistance is sufficient. Furthermore, neuronal impairments cause incorrect motor control signals to the muscles rendering muscle electromyography as the driving signal for powered exoskeletons unfeasible. Simple mechanistic devices seem promising, but their design requires a model of the neuronal impairment and, as our results suggest, the consideration of musculoskeletal dynamics and the preflex forces they generate.

6 | Quantifying morphological computation on different neuronal control hierarchy levels

The simulated perturbed movements in Chapter 4 indicated that the musculoskeletal system significantly contributes to the resulting movement as the feedback contribution with optimized feedback gains was rather small (Figures 4.6 and 4.8). To quantify how much the muscle-tendon structures contribute, in this chapter, we applied the concept of quantifying morphological computation (Section 3.5). In particular, we were interested in how morphological computation differs between the levels on the neuronal control hierarchy: Voluntary movements, like point-to-point or oscillatory human arm movements, are generated by the interaction of several structures. High-level neuronal circuits in the brain are responsible for planning and initiating a movement. Spinal circuits incorporate proprioceptive feedback to compensate for deviations from the desired movement. Muscle biochemistry and contraction dynamics generate movement driving forces and provide an immediate physical response to external forces, like a low-level decentralized controller. A simple central neuronal command like "initiate a movement" then recruits all these biological structures and processes leading to complex behavior, e.g., generating a stable oscillatory movement in resonance with an external spring-mass system. It has been discussed that the spinal feedback circuits, the biochemical processes, and the biomechanical muscle dynamics contribute to the movement generation, and, thus, take over some parts of the movement generation and stabilization which would otherwise have to be performed by the high-level controller. However, it is unknown whether morphological computation actually differs between these different hierarchical levels of the control system. To investigate this, we simulated point-to-point and oscillatory human arm movements with our neuro-musculoskeletal model (Section 3.2.4). We then quantified morphological computation on the different hierarchy levels. The results show that morphological computation is highest for the most central (highest) level of the modeled control hierarchy, where the movement initiation and timing are encoded. Furthermore, they show that the lowest neuronal control layer, the muscle stimulation input, exploits the morphological computation of the biochemical and biophysical muscle characteristics to generate smooth dynamic movements. This study provides evidence that the system's design in the mechanical as well as in the neurological structure can take over important contributions to control, which would otherwise need to be performed by the higher control levels.

Note that large parts of the content of this chapter were submitted to *Frontiers in Robotics and AI* and accepted for publication. For details on this manuscript, including a list of authors, see Manuscript 3 in Chapter 2.

6.1 Introduction

In biological systems, voluntary movements are generated through a sequence of different processing units. From the motor cortex to the spinal cord to the stimulation signal running down the motor neuron to the muscle membrane. These processing units can be interpreted as a neurological, hierarchical control system (Karniel, 2011; Loeb et al., 1999). While it seems obvious that the neuronal structures are responsible for the initiation and execution of goal-directed movements, it has been discussed that also the morphology of a system contributes to the control (Blickhan et al., 2007; Ghazi-Zahedi et al., 2016; Iida et al., 2004; Paul, 2006; Pfeifer and Iida, 2005). In particular in human arm movements, several control theories explicitly rely on the viscoelastic muscle characteristics to generate dynamic movements (e.g., impedance control (Hogan, 1984), equilibrium point control (Bayer et al., 2017; Kistemaker et al., 2006, 2007a,a)). Here, the muscles serve as a low-level zero-delay reflexes (termed *preflexes* (Brown et al., 1995)) capable of stabilizing the system against external perturbations (Gerritsen et al., 1998; Haeufle et al., 2010b; John et al., 2013; Loeb et al., 1999; Proctor and Holmes, 2010; van Soest et al., 1993a). Such contributions of the morphology have been termed "intelligence by mechanics" (Blickhan et al., 2007), "exploitive actuation" (Haeufle et al., 2012b; Kalveram et al., 2012; Rieffel et al., 2010), or "morphological computation" (Ghazi-Zahedi et al., 2016; Paul, 2006; Pfeifer and Iida, 2005). Morphological computation, in this sense, captures the concept that control is partially performed by the controlled system interacting with the environment. More precisely, that part of the information processing necessary to generate a desired movement is performed by the morphological characteristics of the system, i.e., by its hard- or wet-ware.

Characterizing this contribution of the system's morphology to its behavior is possible by quantifying morphological computation (MC) (Ghazi-Zahedi, 2019a; Ghazi-Zahedi et al., 2016; Zahedi and Ay, 2013). This requires a causal model of a reactive system's sensorimotor loop. The model must allow a clear separation of the system into a controller, actuator signals, sensor signals, and the physical system termed *world*, which includes the environment (in engineering this is typically called the *plant*). In a nutshell, the quantitative measure of morphological computation ($\mathrm{MC_W}$) then quantifies the contribution of the world state W and the actuator signal A to the further time evolution of the world state, i.e., the next world state W'. $\mathrm{MC_W}$ is high, if the current world state W has a strong influence on the next world state W', i.e., the system exploits its physical properties. Thus, it is possible to quantify morphological computation in causal models where A and W can be observed, e.g., in neuro-muscular models (Ghazi-Zahedi et al., 2016).

The open question is, however, where in the biological control system A and W should be separated. Is A the output of the neurons that innervate the muscles (α motor neurons) and therefore initiate muscle contraction? Or is A much higher in the control hierarchy: the output of the central nervous system, i.e., the signals that initiate a movement? One could argue for the latter separation, as the decentralized low-level control circuits, like mono-synaptic reflexes, are hard-wired into the spinal cord and are therefore rather part of the system than part of the controller. Or has A even to be located much lower in the control hierarchy: the output force of the muscles? The argument for this level of separation would be that muscles with their non-linear viscoelastic properties serve as low-level zero-delay reflexes (*preflexes*) contributing to control. Furthermore, they adapt during our life-time to the requirements of our daily activities. From our point of view it is unclear where to separate between W and A and how

this decision influences the calculation of MC. Furthermore, it is unclear, to which extend higher-level control can exploit morphological computation of the lower-level structures – in actual units of bit.

This is not only relevant for the understanding of biological systems, but also for bio-inspired and bio-mimetic robotics. Much effort has been taken to develop new robotic design concepts exploiting material properties (Kim et al., 2013; Polygerinos et al., 2017; Rus and Tolley, 2015) such as viscoelastic muscle-like actuators in arm movements (Boblan et al., 2004; Driess et al., 2018), elasticity in legged locomotion (Hubicki et al., 2016; Hutter et al., 2013; Iida et al., 2009; Niiyama et al., 2012; Ruppert and Badri-Spröwitz, 2019; Sprowitz et al., 2013) or morphology which empowers hopping (Nurzaman et al., 2015), goal-directed swimming (Manfredi et al., 2013), crawling (Shepherd et al., 2011), or even grasping (Deimel and Brock, 2016). However, also in these approaches, the hierarchy of morphological computation has not yet been quantified.

The purpose of this study was therefore to investigate morphological computation in a hierarchical control system. The novelty of our approach was to quantify morphological computation on different control levels to better understand the hierarchy. This is relevant for two reasons: (1) it further evaluates and validates the quantification concept of MC and (2) shows how the biological control system may benefit from its hierarchical control structure and its non-linear actuators, i.e., the muscles. For this, we resort to computer simulations of human arm movements with a model that considers joint dynamics, muscles, reflexes, central pattern generators, and higher-level control.

6.2 Methods

To investigate morphological computation in a hierarchical control system, we simulate human arm movement with a neuro-musculoskeletal model (Stollenmaier et al., 2020b) (see also electronic supplementary material). In this model, it is possible to access all state signals, i.e., the state of the control logic, the input to the low-level controller, the control signal, the muscles' active state (biochemistry), the muscles' force, the generated joint torques, and the resulting joint angles (Section 6.2.1). Thus, we can access all levels of the neuro-muscular control hierarchy to quantify morphological computation (Section 6.2.3).

6.2.1 Neuro-muscular model

The neuro-muscular model of human arm movements has been developed to study neuronal motor control concepts in the interaction with the musculoskeletal model. For this purpose, we combined a computational motor control model of goal-directed arm movements with a musculoskeletal model. We will shortly summarize the approach here and refer to Section 3.2.4 and Appendix A4.3 for the details of the model.

The model consists of several hierarchical layers (Figure 6.1), which we will describe shortly in the following, starting from the lowest hierarchical level (right-hand side). The chosen model parameters represent a generic man and are collected from different sources (Bhanpuri et al. (2014); Kistemaker et al. (2006); Mörl et al. (2012); van Soest et al. (1993a) and others, listed in detail in Appendix A1).

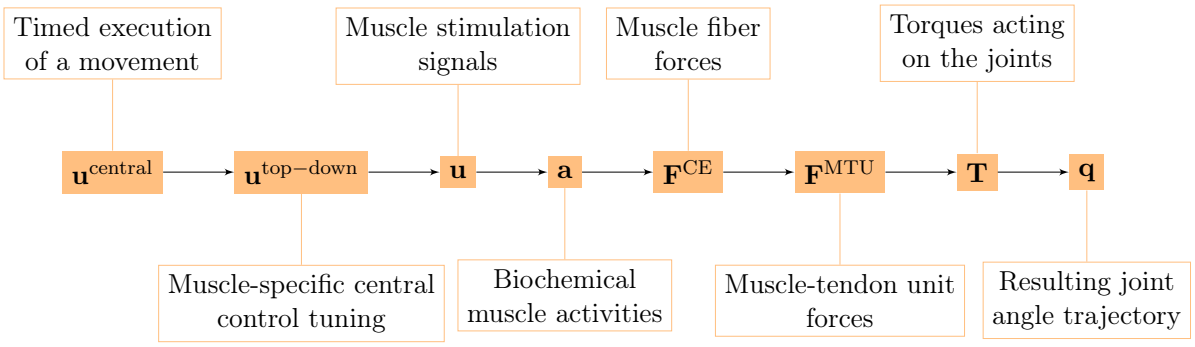

Figure 6.1: **Overview over the hierarchy levels in our neuro-muscular model of the arm.** The function of each level is described in detail in the main text.

Angles

The musculoskeletal model predicts two-degree-of-freedom arm movements in the sagittal plane (see Figure 6.3). Its dynamics are determined by two rigid bodies (lower and upper arm) that are connected via two one-degree-of-freedom revolute joints that represent the shoulder and elbow joint. This can be described by double-pendulum equations of motion, i.e., second-order ordinary differential equations. The outputs of this layer are the predicted joint angles which correspond to the experimentally observable state ($\mathbf{q} \in \mathbb{R}^2$).

Torques

The rigid bodies are driven by joint torques, which are calculated based on anatomical muscle paths (Hammer et al., 2019) and translating forces at the muscle origin, insertion, and via-points into joint torques. The outputs of this layer are the predicted joint torques ($\mathbf{T} \in \mathbb{R}^2$).

Muscle-tendon unit forces

Active forces are generated by six muscle-tendon units (MTUs), four monoarticular and two biarticular muscles. The force of each MTU is modeled using a Hill-type model accounting for muscle fiber and tendon characteristics (Haeufle et al. (2014b)). The dynamic of each MTU is modeled by a first-order ordinary differential equation. The outputs of this layer are the predicted muscle-tendon unit forces ($\mathbf{F}^{\text{MTU}} \in \mathbb{R}^6$).

Muscle fiber forces

The model of the muscle fibers, termed contractile elements (CEs), considers the dependence of the active fiber force on fiber length and contraction velocity known from biological muscle fibers. The outputs of this layer are the predicted muscle fiber forces ($\mathbf{F}^{\text{CE}} \in \mathbb{R}^6$).

Biochemical muscle activity

The biochemical processes that lead from a neuronal muscle stimulation to a force generation can be modeled by a first-order ordinary differential equation. The implemented model of the activation dynamics further considers the fiber length dependency of this process (Hatze, 1977; Rockenfeller et al., 2015). The outputs of this layer are the predicted muscle fiber activity states ($\mathbf{a} \in \mathbb{R}^6$).

Muscle stimulation signals

The bio-inspired hybrid equilibrium point controller exploits muscle characteristics by combining a feed-forward command ($\mathbf{u}^{\text{open}}(t)$) with spinal feedback on muscle fiber lengths ($\mathbf{u}^{\text{closed}}(t)$). This feedback represents a simplified version of the mono-synaptic muscle spindle reflex, as-

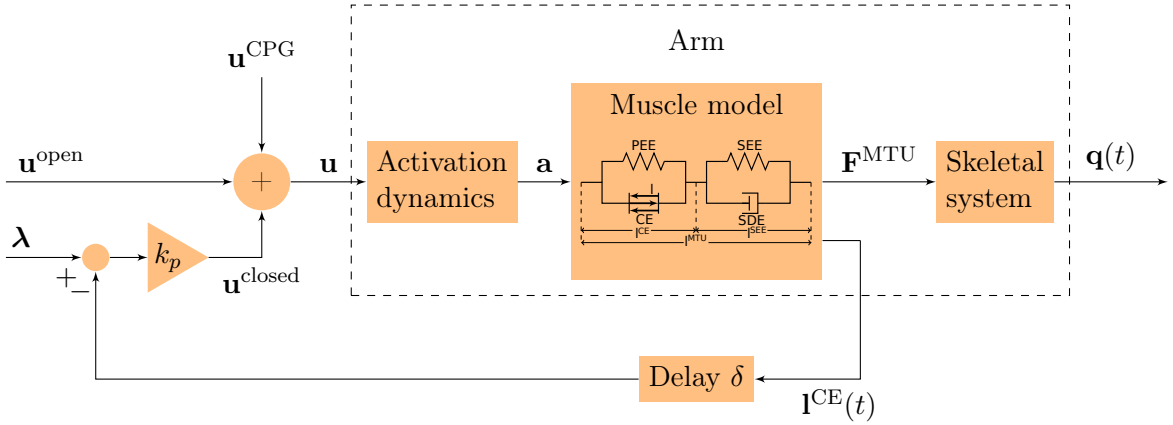

Figure 6.2: **Schematic diagram of the motor control model.** The motor command $\mathbf{u}$ is a sum of an open-loop and a closed-loop signal. The time-delayed feedback loop incorporates proprioceptive feedback (mono-synaptic reflexes) by comparing the actual muscle fiber lengths $\mathbf{l}^{\text{CE}}(t)$ to desired values $\boldsymbol{\lambda}$. $\mathbf{q}(t) = (\varphi(t), \psi(t))$ contains the elbow and shoulder angle, respectively.

suming that the muscle spindles provide accurate time-delayed information about the muscle fiber lengths $\mathbf{l}^{\text{CE}}(t)$ (Kistemaker et al., 2006). The total motor command u_i for each muscle i is a sum of those components and is calculated as

$$\begin{aligned} u_i(t) &= \left\{ u_i^{\text{open}}(t) + u_i^{\text{closed}}(t) + u_i^{\text{CPG}}(t) \right\}_0^1 \\ &= \left\{ u_i^{\text{open}}(t) + \frac{k_p}{l^{\text{CE,opt}}} \left(\lambda_i(t) - l_i^{\text{CE}}(t-\delta) \right) + u_i^{\text{CPG}}(t) \right\}_0^1 , \end{aligned} \tag{6.1}$$

where k_p is a feedback gain and the time delay δ is set to 10 ms representing a short-latency reflex delay which is in a physiologically plausible range (Houk and Rymer, 1981; More et al., 2010). $l^{\text{CE,opt}}$ stands for the optimal length of the contractile element (CE). The operation $\{x\}_0^1$ sets values $x < 0$ to 0 and $x > 1$ to 1. The signal u_i^{CPG} represents a central pattern generator (CPG). The outputs of this layer are the predicted muscle stimulation signals (α-motor neuron activities $\mathbf{u} \in \mathbb{R}^6$).

Muscle-specific central control tuning

The low-level controller gets two top-down input signals: The open-loop muscle stimulation $u_i^{\text{open}}(t)$ and the desired muscle fiber lengths $\lambda_i(t)$. Here, they represent an intermittent control approach, because they are piecewise constant functions over time. Herein, each constant value represents an *equilibrium posture* (EP), i.e. the system is in a stable equilibrium in these positions. The calculation of these central control signals for a given movement is described in detail in Appendix A4.3. The outputs of this layer are the top-down central commands to each low-level reflex circuit ($\mathbf{u}^{\text{top-down}} \in \mathbb{R}^{12}$).

Timed execution of a movement

The output of our highest level of motor control is a single piecewise constant signal used to

time the selection of equilibrium points meaning that all sub-circuits are switched at the same time ($\mathbf{u}^{\text{central}} \in \mathbb{R}^1$).

6.2.2 Simulation experiments

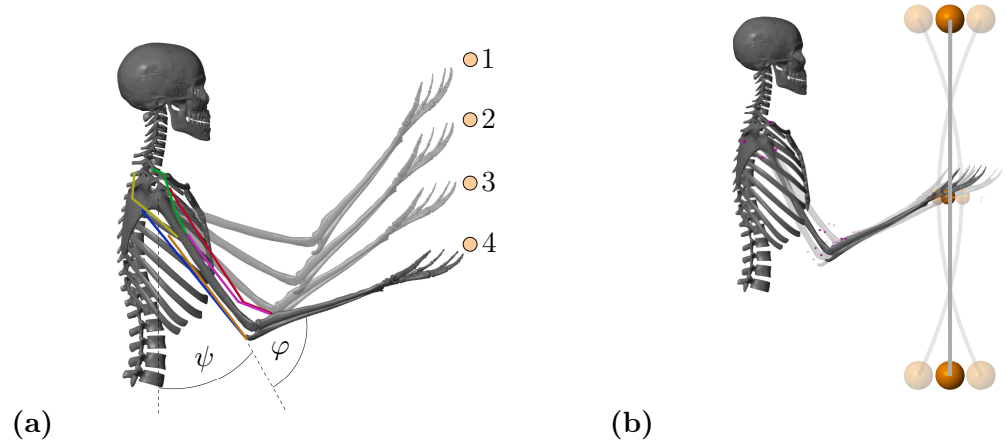

Figure 6.3: **Visualization of the musculoskeletal model that was used for the computer simulations of the arm movements.** The colored lines represent the modeled muscles. **(a)** Goal-directed point-to-point movement between the points 1 to 4 and **(b)** dynamic oscillation movements with a vibrating rod.

Movement 1: Point-to-point movements

The first movement investigated here is a point-to-point movement along a vertical line. Different movements between four target positions were evaluated (see Figure 6.3 (a) and Appendix A4.2). The central pattern generator is inactive for those movements ($\mathbf{u}^{\text{CPG}}(t) = 0$). An animation of the movement is provided as electronic supplementary material accompanying Haeufle et al. (2020a).

To consider the natural variation of this movement, we repeated the simulation of the movement $1 \rightarrow 4$ seven times. Each simulation only differed in the equilibrium postures (EPs) for the starting joint angles, the peak elbow joint angle, and the target joint angles. We determined these angles from motion capture data of a single subject performing the movement seven times. This natural variation of the angles resulted in different signals on the muscle-specific central control level, i.e., different $\mathbf{u}^{\text{top-down}}$ signals. All other parameters of the controller were kept constant.

Movement 2: Dynamic oscillatory movements
For the second movement, a vibrating rod was added to the hand in the model (see Figure 6.3 (b) and Heinrich (2019)). The technical specifications of the rod can be found in Appendix A4. To excite the rod, as done in training and rehabilitation exercises, a sinusoidal signal $\mathbf{u}^{\mathrm{CPG}}$ mimicking the output of a central pattern generator (CPG) is added to the motor command $\mathbf{u}$:

$$\mathbf{u}^{\mathrm{CPG}}(t) = \hat{u} \cdot \sin(2\pi \cdot f^{\mathrm{CPG}} \cdot t + \phi_0)\,, \tag{6.2}$$

with $\hat{u} = 0.1$: amplitude, f^{CPG}: frequency, ϕ_0: phase. The muscles are synchronized by setting $\phi_0 = 0$ for flexing muscles and $\phi_0 = \pi$ for extending muscles.

The oscillation is exited for $0 \leq t \leq 4$s. After this, $\mathbf{u}^{\mathrm{CPG}} = 0$ and the oscillation is then only a result of the dynamics of the system and not of the controller anymore. An animation of the movement is provided as electronic supplementary material accompanying Haeufle et al. (2020a).

To consider the natural variation of this movement, we analyzed the frequency pattern of a single subject performing a swing-rod exercise. The fast-fourier-transform spectrum indicates a frequency variance of 0.2Hz. We therefore repeated the simulation 14 times with a set of random CPG frequencies $f^{\mathrm{CPG}} = 3.8 \pm 0.2$Hz.

Details on the human experiments to estimate natural variability: Two healthy subjects participated in the study. The experimental procedure was approved by the local ethics committee (886/2018BO2). All participants gave their informed consent prior to participation. The movements were recorded with a 12-camera motion capturing system (Vicon Motion Systems Ltd, UK) using a marker set with 29 retro-reflecting markers. Using the recorded marker positions over time, shoulder and elbow angles were reconstructed (Rettig et al., 2009). The reconstructed joint angle trajectories were smoothed with a Savitzky-Golay polynomial filter (of order 4 and with a window size of 41 sampling points).

6.2.3 Quantifying morphological computation

The following paragraphs will only give a brief introduction to the quantification of MC. For a full discussion on this issue, please read (Ghazi-Zahedi, 2019a) or Appendix A4.1. Quantifying MC requires a causal model of the sensorimotor loop which divides a cognitive system into a brain, actuators, environment, and sensors. In the context of this work, we are focusing on reactive systems which means that the actuators are directly connected with the sensors. A cognitive system is then fully described by the following set of Markov processes:

$$\beta\colon \mathcal{W} \longrightarrow \Delta_{\mathcal{S}} \qquad [\beta(s|w)] \tag{6.3}$$
$$\pi\colon \mathcal{S} \longrightarrow \Delta_{\mathcal{A}} \qquad [\pi(a|s)] \tag{6.4}$$
$$\alpha\colon \mathcal{W} \times \mathcal{A} \longrightarrow \Delta_{\mathcal{W}} \qquad [\alpha(w'|w,a)], \tag{6.5}$$

where $w \in \mathcal{W}$ is the value of the world state W, $s \in \mathcal{S}$ is the value of the sensor state S, and $a \in \mathcal{A}$ is value of the actuator state A. We call $\beta(s|w)$ the sensor map, as it describes how the agents perceive the environment, $\pi(a|s)$ the policy, as it describes how the agent chooses an action as a reaction to a sensor, and finally we call $\alpha(w'|w,a)$ the world dynamics kernel, as it describes how the next world state W' depends on the current world state W and the

current action A. It is important to note here that the world state W captures everything physical. This means that the world state W captures the state of the system's body and its environment.

To quantify MC, we take a closer look at the world dynamics kernel $\alpha(w'|w,a)$. Assume that the next world state W' does not depend on the current world state W but only on the current action A. This means that the world dynamics kernel reduces to $\tilde{\alpha}(w'|a)$. In this case, it is fair to say that the system shows no MC at all, since the behavior is fully controlled by the action A. Any measured divergence from this assumption means that the current world state W had an influence on the next world state W', and hence, the system is exploiting the physical properties of its body and its interactions with the environment. This can be measured by the Kullback-Leibler Divergence (Cover and Thomas, 2006) in the following way:

$$\mathrm{MC_W} := \sum_{w',w,a} p(w',w,a) \log_2 \frac{\alpha(w'|w,a)}{\tilde{\alpha}(w'|a)}. \tag{6.6}$$

The output of our models contains discrete numerical data, i.e., S, A, and W are discrete variables. Therefore, we will summarize the approach for discrete variables here. For a discussion on how to estimate $\mathrm{MC_W}$ on continuous state spaces, please see (Ghazi-Zahedi, 2019a).

The joint distribution $p(w',w,a)$ can be estimated by a frequency method, i.e., by counting the number of occurrences of each triplet (w',w,a) normalized by the number of samples in the data. This leads to the following estimation for $p(w',w,a)$:

$$p(w',w,a) = \frac{c_{w',w,a}}{N}, \tag{6.7}$$

where $c_{w',w,a}$ is the number of occurrences of (w',w,a) and N is the total number of samples.

$\mathrm{MC_W}$ can now be calculated in the following way:

Algorithm 1 Algorithm for $\mathrm{MC_W}$.

1: $p(w',w,a) \leftarrow (0)_{|W|\times|W|\times|A|}$ {Matrix with $|W|\times|W|\times|A|$ entries set to zero}
2: **for** $t = 1,2,\ldots,T-1$ and $w_{t+1}, w_t \in w^*, a_t \in a^*$ **do**
3: $\quad p(w_{t+1},w_t,a_t) \leftarrow p(w_{t+1},w_t,a_t) + 1$
4: **end for**
5: $p(w',w,a) \leftarrow p(w',w,a)/(T-1)$
6: Estimate $p(w',a)$ from w^*, a^* or by summing over w
7: $p(w'|w,a) = {}^{p(w',w,a)}/_{\sum_{w'} p(w',w,a)}$
8: $p(w'|a) = {}^{p(w',a)}/_{\sum_{w'} p(w',a)}$
9: $\mathrm{MC_W} = \sum_{w',w,a} p(w',w,a) \log_2 \frac{p(w'|w,a)}{p(w'|a)}$

The value calculated in line 9, $\mathrm{MC_W}$, represents the morphological computation primarily used in this work. Sometimes it is further interesting to take a look at the state-dependent morphological computation, i.e., the time evolution of the quantity. This requires minimal changes to the original algorithms. Instead of calculating the probability-weighted sum over all states (line 9 in Algorithm 1), which leads to a single number as a result, the measures are evaluated n-tuple in the data set. This means that for $\mathrm{MC_W}$, the logarithm is evaluated for every triple w_{t+1}, w_t, a_t (see Alg. 2).

Algorithm 2 Algorithm for state-dependent $\mathrm{MC}_{\mathrm{W}}(t)$.

1: Perform steps 1–8 from Alg. 1
2: **for** $t = 1, 2, \ldots, T-1$ and $w', w \in w^*, a \in a^*$ **do**
3: $\quad \mathrm{MC}_{\mathrm{W}}(t) = \log_2 \frac{p(w'|w,a)}{p(w'|a)}$
4: **end for**

In conclusion, in order to quantify MC, we need time signals of the World and Actuator states, W and A, respectively. This means that it is necessary to separate the state variables of the system into W and A.

The neuro-muscular model investigated here has several hierarchical levels (Fig. 6.1). For this study, we systematically separated the state variables between all of these different hierarchy levels and calculated MC for each possible hierarchy level.

There are two possible approaches to select W and A and then calculate MC (Figure 6.4): The first approach (Figure 6.4 (a)) relates to the evaluation of experimental data, where usually not all state variables can be recorded (especially in biological systems). Here, W is always the mechanical system state $\mathbf{q}(t)$, i.e., the joint positions (and for the oscillation movement also the position of the rod mass relative to the hand). A on the other hand contains only signals of one hierarchy level. We term this approach "selected hierarchy levels" and term the respective morphological computation $\mathrm{MC}_{\mathrm{W}}^{\mathrm{sel}}$.

The second approach (Figure 6.4 (b)) always includes all signals. It represents a clear cut at a specific level. All signals below this cut-level are combined into W and all above into A. We termed this approach "accumulated hierarchy levels" and termed the respective morphological computation $\mathrm{MC}_{\mathrm{W}}^{\mathrm{acc}}$.

6.2.4 Statistical analysis

Each simulation run provides data to calculate morphological computation on all different hierarchy levels. Each hierarchy level is then quantified by a single scalar quantity MC_{W} representing the respective morphological computation (see line 9 in Algorithm Algorithm 1). By varying the control parameters as described above, the resulting MC_{W} values represent a natural variation for the same movement. The hypothesis (H_0) was that there is no significant difference in MC between hierarchy levels across all repetitions of the movement. Each hierarchy thus represents a different group and we used ANOVA to test whether these groups differ. The normal distribution was tested with a Shapiro-Wilk test (with $\alpha = 0.1$ to keep the beta error in check). The test confirmed normal distribution in the majority of the groups (17 out of 28). This should not influence the result, since ANOVA is robust to deviations form normal distribution, especially here where each group has the same number of samples. As the different hierarchy levels are taken from the same simulation, they are not independent. To test their statistical difference, we therefore analyzed the data with a repeated measures ANOVA. We further used a pairwise post hoc test with Bonferroni correction to analyze which levels actually differ.

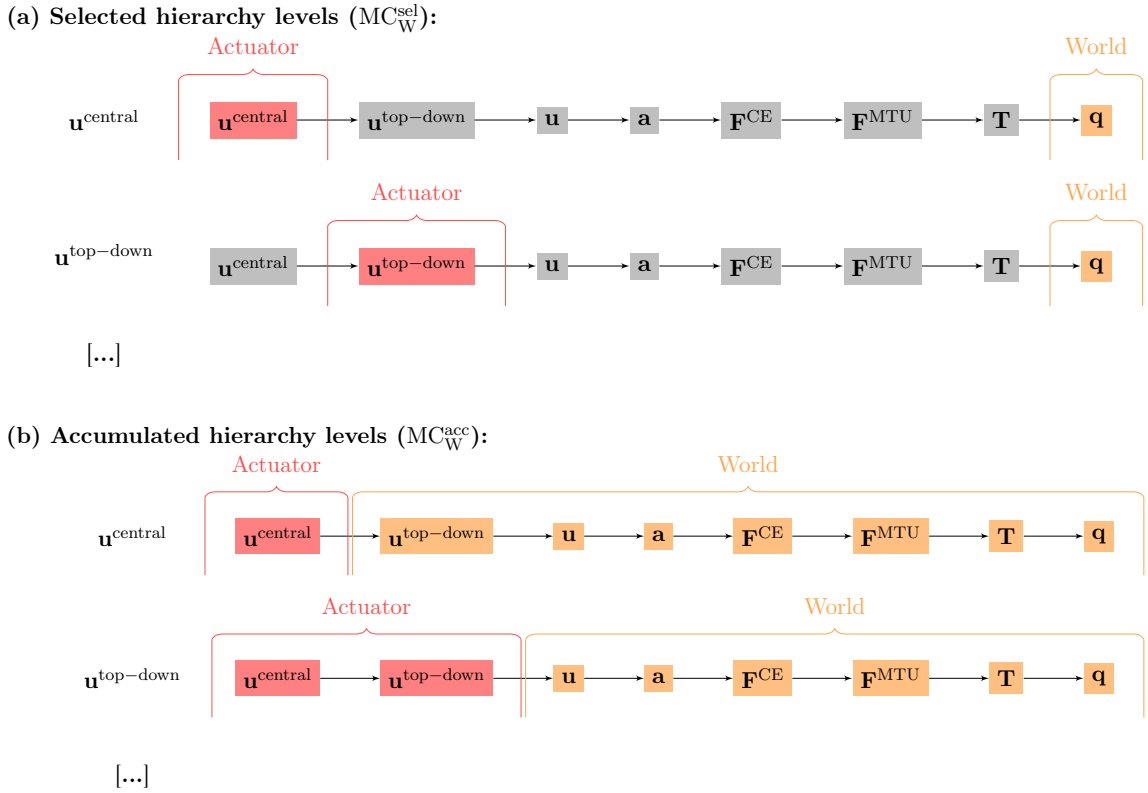

Figure 6.4: **Visualization of the difference of the calculation of MC_W using (a) selected and (b) accumulated hierarchy levels as actuator signal A and world state W.** Note that for the oscillation movements, the observable state $\mathbf{q}$ includes both the joint angles and the rod position.

6.3 Results

Morphological computation is highest for the most central level of the control hierarchy investigated here ($\mathbf{u}^{central}$). This holds for all four types of point-to-point movements we evaluated (Figure 6.5) as well as for the dynamic oscillation movement (Figure 6.7). Going further down in the control hierarchy, MC always decreases for the accumulated scenario (MC_W^{acc}), and almost always for the selected (MC_W^{sel}) with one exception: the torque. Choosing the torque $\mathbf{T}$ as actuator signal, the value for MC is higher than using one of the next higher-level signals of actuation. Please note that the figures are shown in logarithmic scale to allow a better comparison of the large differences between MC for the different hierarchy levels.

In general, using accumulated hierarchy levels results in smaller morphological computation than using selected hierarchy levels ($MC_W^{acc} < MC_W^{sel}$). Furthermore, pointing movements have a lower morphological computation than the dynamic oscillation movements.

The reproduction of the experimentally observed variation of the movement $1 \rightarrow 4$ in simulation also leads to a variation of MC_W. This variation is relatively small compared to the

overall difference between hierarchy levels. Therefore, an ANOVA test reveals statistical significant differences between the hierarchy levels. However, not all levels are significantly different. Especially u^{central} and $u^{\text{top-down}}$, as well as F^{CE} and F^{MTU} do not differ significantly in MC.

6.3.1 Noise in point-to-point movements

In the pointing movements, all state variables are smooth, which is a result of the noise-free formulation of the continuous control signals. Therefore, the highest control levels produce very simple control signals, i.e., piecewise constant signals in time (see above and Appendix A4.3 for more details).

To test whether this smooth definition has an influence on the result, we added random (uniformly distributed) noise to the muscle stimulation signals $\mathbf{u}$ (noise levels: medium: $40/300 \cdot (u_{\max} - u_{\min})$, high: $80/300 \cdot (u_{\max} - u_{\min})$). This changes the previously consistent trend: the higher the added noise, the lower the MC at the level of the muscle stimulation $\mathbf{u}$ (Figure 6.6). At the same time, MC between at the muscle activity level $\mathbf{a}$ increases. This leads to the fact, that - after adding noise to the stimulation signal - MC with $\mathbf{u}$ as actuator signal is lower than the calculation with $\mathbf{a}$ as actuator signal. However, this change in trend is only true if morphological computation is evaluated on selected signals ($\text{MC}_{\text{W}}^{\text{sel}}$). For $\text{MC}_{\text{W}}^{\text{acc}}$, the trend is never reversed. Noise only slightly shifts the values (not shown).

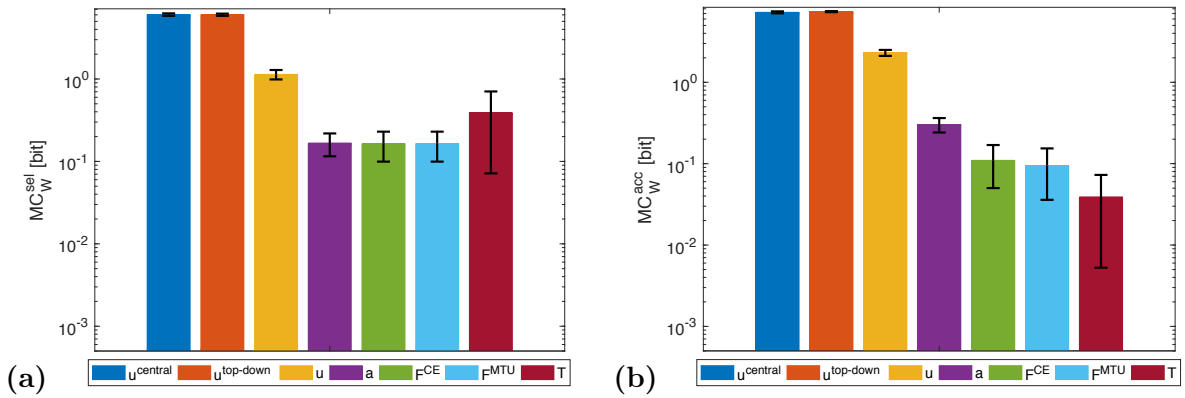

Figure 6.5: **Point-to-point movement:** Morphological computation MC_W on different hierarchy levels for an exemplary point-to-point movement ($1 \rightarrow 4$, see Figure 6.3 (a)). Morphological computation was evaluated using **(a)** selected (MC_W^{sel}) and **(b)** accumulated hierarchy levels (MC_W^{acc}). Note that a logarithmic scale is used for the y-axis. Shown are the mean $\pm$ 1.96 times standard deviation ($\approx$ 95% confidence interval) of seven simulation runs with different starting, intermittent, and target equilibrium postures taken from the natural variation observed in a human experiment. As tested by an ANOVA, there are significant differences in MC_W between the different hierarchy levels. The pairwise post-hoc test revealed that for MC_W^{sel} there are two groups with similar mean: the highest two levels $u^{central}$, $u^{top-down}$, and the three levels a, F^{CE}, and F^{MTU}. The levels u and T differ from all others. For MC_W^{acc}, the three lowest levels F^{CE}, F^{MTU}, and T are one group. All other levels differ from all others. All significance levels were set to $p < 0.05$. The limit of the y-axis is set to the maximum MC value that would result from having a constant signal as input. Plots of the results of the other movements can be found in Appendix A4.4, but show the same trends.

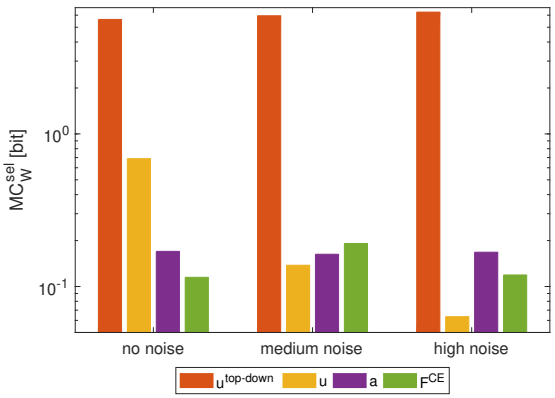

Figure 6.6: **Influence of noise on morphological computation.** Morphological computation for selected hierarchy levels (MC_W^{sel}) for a point-to-point movement ($1 \rightarrow 4$). The noise was added to the muscle stimulation **u** (noise levels: medium: $40/300 \cdot (u_{max} - u_{min})$, high: $80/300 \cdot (u_{max} - u_{min})$). As a result, MC_W^{sel} at the muscle stimulation level decreases and increases in adjacent hierarchy levels. Note that a logarithmic scale is used for the y-axis.

6.3.2 Dynamic oscillatory movements

The general trend of decreasing morphological computation for lower hierarchy levels was the same in the dynamic oscillation movements (Figure 6.7).

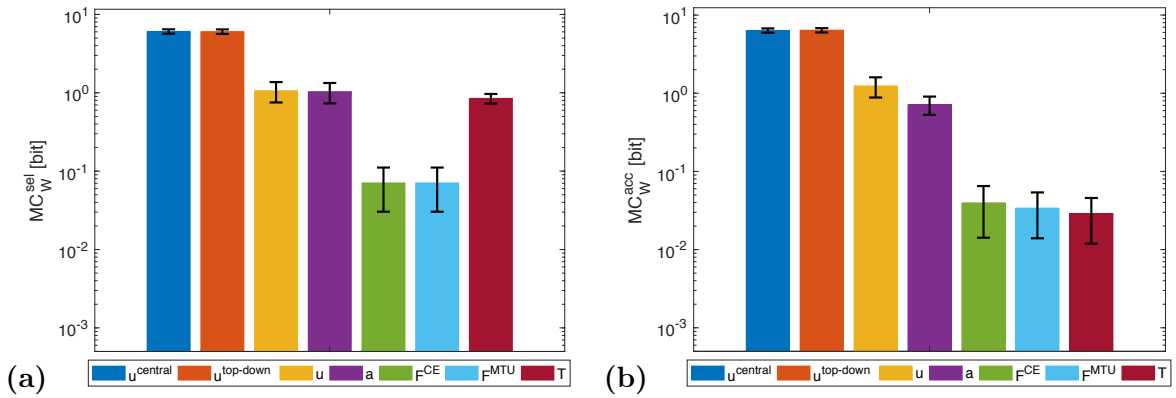

Figure 6.7: **Dynamic oscillation movement:** Morphological computation MC_W for **(a)** selected (MC_W^{sel}) and **(b)** accumulated hierarchy levels (MC_W^{acc}). Shown are the mean $\pm$ 1.96 times standard deviation ($\approx$ 95% confidence interval) of 14 simulation runs with a set of random CPG frequencies in the spectrum observed in a human experiment. As tested by an ANOVA, there are significant differences in MC_W between the different hierarchy levels. The pairwise post-hoc test revealed that for MC_W^{sel}, the highest levels $u^{central}$ and $u^{top-down}$ have similar means, so do the muscle stimulation u, activity a, as well as the forces F^{CE} and F^{MTU}. Only the torque level T differs from all other groups. For MC_W^{acc}, the highest levels $u^{central}$ and $u^{top-down}$ have similar means, so do the lowest levels F^{CE}, F^{MTU}, and T. All significance levels were set to $p < 0.05$. The limit of the y-axis is set to the maximum MC value that would result from having a constant signal as input. Note that a logarithmic scale is used for the y-axis.

However, the dynamic oscillation data has different phases. In the initial phase ($t \leq 4$s), the rod is excited by sinusoidal muscle stimulation signals with a frequency tuned to the rod's resonance (Figure 6.9). In this phase, everything oscillates in sync and the morphological computation is on average smaller. Once the CPG is turned off ($t > 4$s), the control signals become relatively steady – only influenced by the feedback signals trying to hold the position. The rod, however, still has a lot of energy and therefore keeps oscillating. In this phase, MC_W increases. These results are similar on all levels of the control hierarchy (Fig. 6.8). Interestingly, MC_W^{acc} actually becomes zero on the lower hierarchy levels in the resonance oscillating movements between $2 \leq t \leq 4$s. This means that muscle fiber force $\mathbf{F}^{CE}$, muscle-tendon unit force $\mathbf{F}^{MTU}$, and joint torques $\mathbf{T}$ contain the same information as the mechanical state of the system $\mathbf{q}$.

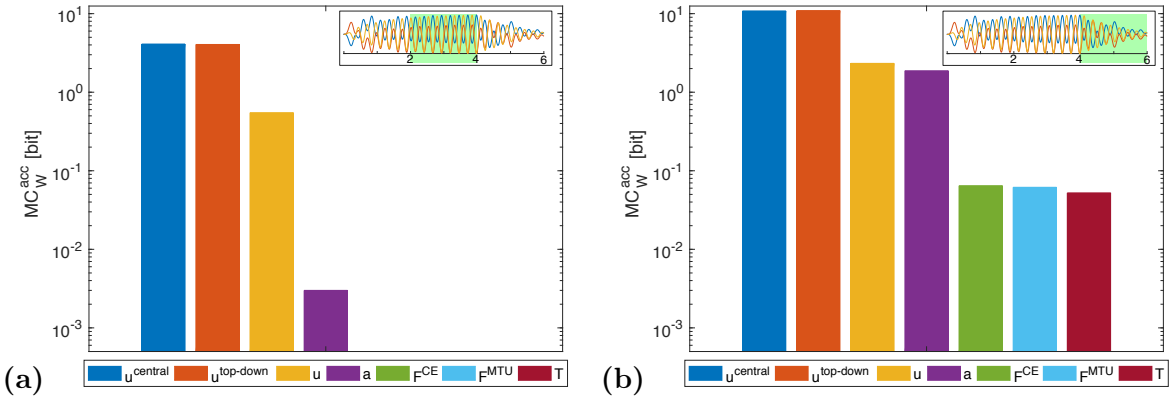

Figure 6.8: **Dynamic oscillation movement:** Morphological computation is higher for the last movement phase where the central pattern stimulation is deactivated and the movement continues due to the passive dynamics of the arm-rod system. **(a)** $\mathrm{MC}_\mathrm{W}^\mathrm{acc}$ evaluated for the time span between 2 and 4s **(b)** for the time span between 4 and 6s, as indicated by the insets, which show the oscillation of the joints and the rod (cf. Fig. 6.9). In the first time span, the control signals are sinusoidal muscle stimulations exciting the rod at its resonance frequency ($f^\mathrm{CPG} = 3.8\mathrm{Hz}$). In the second time span **(b)**, the sinusoidal stimulation is zero and the oscillation is only driven by the dynamics of the rod. The limit of the y-axis is set to the maximum MC value that would result from having a constant signal as input. Note that a logarithmic scale is used for the y-axis.

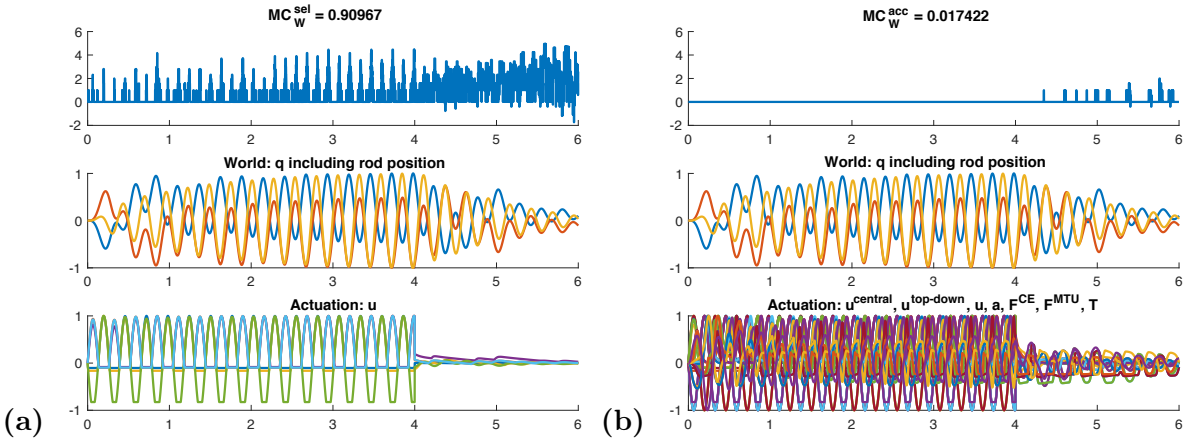

Figure 6.9: **Time evolution of morphological computation MC_W, world state W and actuator state A for the dynamic oscillation movement.** The oscillation is exited for $0 \leq t \leq 4\mathrm{s}$ by a sinusoidal CPG stimulation signal. After this, $\mathbf{u}^\mathrm{CPG} = 0$ and the oscillation is then only a result of the dynamics of the system and not of the controller anymore. Shown here is exemplary **(a)** the case of $\mathrm{MC}_\mathrm{W}^\mathrm{sel}$ of the muscle stimulation level $\mathbf{u}$ (yellow bar in Figure 6.7 (a)) and **(b)** the case of $\mathrm{MC}_\mathrm{W}^\mathrm{acc}$ including only the joint angles and rod position as world state (dark red bar in Figure 6.7 (b)).

6.4 Discussion

The meaning of morphological computation can be seen quite well in the example of the dynamic oscillations. In the initial phase, the controller enforces a dynamic oscillation at the system's resonance. In resonance, the morphological computation is then quite low, as most—or even all—information on the system state is already contained in the stimulation, activity, and muscle force signals (Fig. 6.8a) and (Fig. 6.9). This is similar to a robotic model, driven by complex control signals (Ghazi-Zahedi et al., 2016). However, if the sinusoidal excitation is switched off, the rod dynamics take over and generate a rich dynamic behavior at almost no information input on the control/actuation levels. Hence, morphological computation is high (Fig. 6.8b). This case is similar to e.g., mechanical toys such as passive dynamic walkers which generate the entire behavior based on their mechanical properties. This example confirms that the measure of MC_W captures what we would expect as morphological computation.

By measuring morphological computation in a hierarchical control system, we can—for the first time—quantify the contribution of different hierarchy-levels to the control. The increase of morphological computation for higher-levels of the control hierarchy in the accumulative evaluation (MC_W^{acc}) means that the lower control levels actually contribute quite significantly. To be able to test whether the differences between the hierarchy-levels are significant, we introduced variations based on experimental data. Not all MC data generated in this way fulfills the ANOVA assumption of equal distribution for each group represented by a hierachy level. Still, the results found by the ANOVA and post-hoc test match what can be seen in Figure 6.5 and Figure 6.7. Literature suggests this contribution of muscles to dynamic movements (Bayer et al., 2017; Eriten and Dankowicz, 2009; Gerritsen et al., 1998; Haeufle et al., 2020b, 2012b, 2010b; John et al., 2013; Kambara et al., 2013; Pinter et al., 2012; Stollenmaier et al., 2020b; van der Krogt et al., 2009; van Soest et al., 1993a; Wagner and Blickhan, 1999). In this sense, the MC_W^{acc} quantifies the "importance" of each hierarchical level in the sense of influence on the behavior (world state evolution) of the system. This approach shows that the muscle-driven arm movements can be initiated with very little information on the top control levels while the lower control levels and also the biochemical and muscular dynamics generate a smooth information-rich signal and ultimately dynamic behavior out of these reduced signals (Kistemaker et al., 2006; Stollenmaier et al., 2020b). This is reflected in the large differences in MC_W^{acc} (please note that the plots use a logarithmic scale).

We expect similar results for robotic arm systems that employ muscle-like actuation, e.g., fluidic muscles (Boblan et al., 2004; Driess et al., 2018). Fluidic muscles show muscle-like force-length-velocity characteristics (Klute et al., 2002) and by antagonistic co-contraction allow for variable joint stiffness (Wolfen et al., 2018). This way, even simple piecewise constant control signals will result in smooth dynamic movements (Driess et al., 2018), very similar to what is known from simulation results (Kistemaker et al., 2007a; Stollenmaier et al., 2020b,d; Wochner et al., 2020), and are hypothesized to be a control principle of goal-directed arm movements (Feldman and Levin, 2009). Furthermore, as mechanical (visco-)elastic morphological characteristics are also known to benefit robotic locomotion (Hubicki et al., 2016; Hutter et al., 2013; Iida et al., 2009; Manfredi et al., 2013; Niiyama et al., 2012; Nurzaman et al., 2015; Ruppert and Badri-Spröwitz, 2019; Shepherd et al., 2011; Sprowitz et al., 2013), we expect that such a hierarchy in morphological control may be present in such systems too. This will become especially interesting if hierarchical control systems learn to exploit these morphological contributions

to efficiently generate movements (e.g., Büchler et al., 2020; Driess et al., 2018; Manoonpong et al., 2007).

Difference between the two approaches to calculate MC: The MC_W^{acc} approach is particularly of value for the evaluation of hierarchical computational models of motor control, where all system states are observable. The calculation of morphological computation only based on selected actuation signals MC_W^{sel}, however, better represent the experimenters' reality, where most of the system states are not or hardly observable. While the general trend is the same, we observed that for the joint torques the morphological computation increases again. This can be attributed to the fact that the two joint torque signals contain less information than the six muscle force signals. Furthermore, MC_W^{sel} is influenced by noise. Increasing noise increases the apparent information content of the signals and thus reduces morphological MC_W^{sel} (yellow bar in Fig. 6.6). Interestingly, this additional noise is basically filtered by the low-pass filter characteristics of the muscles' activation and contraction dynamics resulting in quite similar output behavior. Therefore, MC_W^{sel} increases for the lower hierarchy levels. The consequence of this is, that one has to be careful if applying MC_W^{sel} to experimental data, as noise on the signals may alter the result.

Model considerations: The model used in this study was chosen as it resembles the coarse organ-level dynamics of the neuro-musculoskeletal system that leads to goal-directed movements. However, it does not consider that in reality, each muscle-tendon unit consists of many motor units that have to be and can be controlled separately by higher control levels. We cannot rule out that these principles of the biological system will have a significant effect on the overall morphological computation and its distribution among the hierarchy levels. In principle, this could be investigated in more detailed models (e.g., Heidlauf and Röhrle, 2013; Mordhorst et al., 2015). However, our model represents the basic functional unit (Schmitt et al., 2019a) considering the main dynamic properties relevant for the passive contribution of muscles to control (Pinter et al., 2012). Furthermore, the two movements investigated here represent primitives that could potentially be combined to generate more complex arm movements (Sternad et al., 2000; Wei et al., 2003). Therefore, we expect that our findings represent a fundamental concept in biology. We further expect that it extends to other movements too, e.g., locomotion, for which it is known that muscles significantly contribute to the movement generation (Daley et al., 2009; Gerritsen et al., 1998; Haeufle et al., 2010b; John et al., 2013; van Soest et al., 1993a) and allow to simplify higher-level control (Ghazi-Zahedi et al., 2016; Haeufle et al., 2014b, 2020b).

Overall, we here provide evidence that the systems' design in the mechanical as well neurological structure facilitates the control task by providing an appropriate integration of signals at different levels of the control hierarchy.

7 | Combining computer simulations with a bio-inspired robot and human experiments

Human experiments, numerical computer simulations as well as biorobotic systems have proven to be valuable tools for the investigation of motor control principles. Combining all three methods into one coherent framework requires a reasonable similarity between the numerical and the biorobotic model and the human subject. This is especially relevant for motor control concepts that explicitly rely on the muscles' non-linear viscoelastic characteristics. For the investigation of such concepts, linear torque or impedance models on the joint level and electric motor actuation are not sufficient. Rather, both the numerical and the biorobotic model need to provide the necessary level of physiological detail and include the relevant muscle characteristics. In this study, we developed such an integrated framework of data measured in human experiments, a numerical musculoskeletal model, and a bio-inspired robotic system with pneumatic muscles. The framework was designed for the investigation of two-degree-of-freedom point-to-point arm movements, a setup commonly used in motor control studies. We demonstrate the relevance of this framework using the example of a bio-inspired intermittent hybrid equilibrium posture control scheme, which has previously been demonstrated to reproduce human arm movements in computer simulation. The results show that the same controller (with different parameters) can be used to reproduce four different goal-directed human movements in the sagittal plane in both the numerical simulation and the biorobotic system. This is possible because the necessary characteristics of biological muscles (force-length relation and activation dynamics) are considered in both models. The successful transfer to the robotic system indicates that the controller is robust against changes in the system dynamics, friction, and natural variance. This demonstrates that our framework is relevant especially for studying control concepts that consider muscle dynamics and/or investigate the interaction with the environment where passive mechanical forces contribute to the behavior.

Note that large parts of the content of this chapter are part of a manuscript that was written in collaboration with other authors. For details on this manuscript, including a list of authors, see Manuscript 4 in Chapter 2.

7.1 Introduction

It is known that the well-tuned integration of neuronal and muscular dynamics is the physiological basis for human goal-directed arm movements. However, it is still under investigation, which motor control principles underlay this interaction. To investigate such concepts of motor

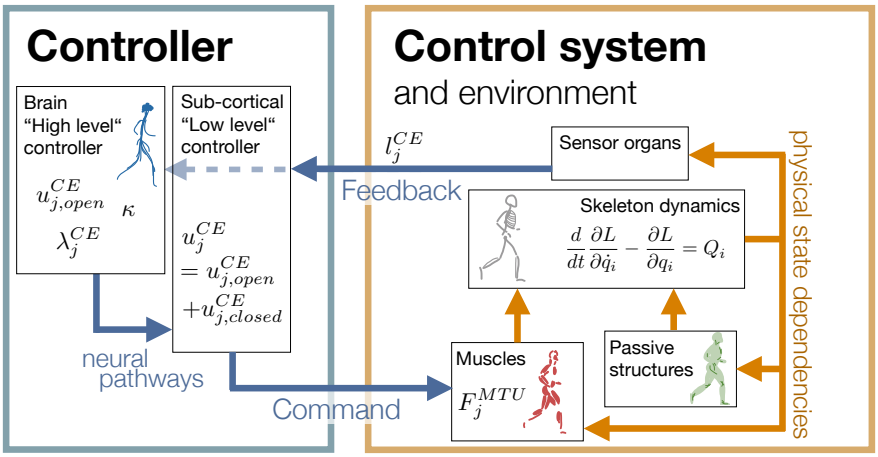

Figure 7.1: **Motion generation in biological systems from a system biophysics perspective.** The system can be divided into a controller and a control system. Herein, the controller represents the part of the nervous system that processes information (blue arrows) and generates a motor command. It may include high-level movement planning or low-level generation of commands. These commands represent the activity of α-motor neurons and actuate the control system by changing the activity of the muscles. The muscle forces drive the skeletal system, leading to a movement and a resulting change of the system's state. Consequently - due to the physical state dependencies (orange arrows) - the muscle and passive tissue forces and the sensor signals are changed. The loop is closed by feeding back the sensor signals to the controller. This biophysical concept can be transferred to both, mathematical and bio-inspired, robotic models of the musculoskeletal system (Picture reproduced and adapted with permission from Schmitt et al. (2019b)).

control, human experiments are usually the first choice. While this method allows gaining insights by analyzing behavioral data in different experimental setups, the deductions about the underlying motor control concept are limited due to the practical and ethical limitations of human experiments. For example, it is not possible to remove or add dedicated neuronal circuits and sensors to study their respective contribution and relevance. For this purpose, both numerical simulations (e.g., Bayer et al., 2017; Kistemaker et al., 2006; Valero-Cuevas et al., 2009) and biorobotic models (e.g., Casellato et al. (2012); Rosendo et al. (2015), see Vitiello et al. (2015) for an overview) provide a valuable methodological extension to human experiments. The advantage of numerical simulations is that they provide more variation possibilities than physical models as the parameters can be adjusted more freely. On the other hand, due to their physical nature, biorobotic models can reveal the practicability of a control model under real-world conditions, e.g., friction or impact dynamics, which are difficult to model. Moreover, the physical nature of such biorobotic models results in random (noise) or systematic (hysteresis) variability which reveals whether a control concept is robust under such conditions. Hence, from this standpoint, it seems desirable to combine human experiments with computer simulations and biorobotic approaches into one research paradigm. Such a combination has previously

been proposed and termed *test trilogy* (Kalveram and Seyfarth, 2009): (1) human experiments providing the data for informed model development and validation, (2) computer simulation for the confirmation of the mathematical consistency of the derived model, and (3) biorobotic hardware experiments as a test of the real-world feasibility of the control model. Combining all three methods promises to overcome the limitations of each of the approaches and provide a platform to investigate neuro-mechanical interaction in goal-directed arm movements. To implement this test trilogy, it is necessary to develop a coherent framework of experiment, numerical model, and biorobotic testbed.

To formally introduce this test trilogy, Kalveram and Seyfarth (2009) investigated a motor control concept for single-joint human arm movements relying on the assumption that the joint is actuated directly by a joint torque. This assumption has often been made in computational models, as it allows a simplified calculation of the required motor control signals for a desired trajectory (inverse model) (e.g., Bhanpuri et al., 2014; Kalveram and Seyfarth, 2009). Furthermore, the assumption of ideal torque generators in the joints can, at least to some extent, be implemented by a current-controlled DC motor in a robotic system. Thus, the link between computational motor control and biorobotics is often approached via this unifying assumption of torque-based controllers in the joint (Buschmann et al., 2007; Casellato et al., 2012; He et al., 2017).

However, in biology, motor control is a dynamic interplay of the neuronal and biomechanical system (Figure 7.1). Joint torques are generated by muscle-tendon units with non-linear state-dependent lever arms (Murray et al., 1995), series elasticity (Roberts and Azizi, 2011), force-length-velocity characteristics (Günther et al., 2007; Nishikawa, 2016; Rassier et al., 1999), and activation dynamics (biochemistry) (van Zandwijk et al., 1996). The antagonistic setup of such muscle-tendon units with tuneable viscoelastic characteristics in the joint allows the emergence of equilibrium positions (Feldman and Levin, 2009; Kistemaker et al., 2007b). This means, that—in contrast to the torque assumption—a stable position can be achieved without any neuronal control, simply by the passive characteristics of the muscle-tendon unit. These characteristics are a necessary requirement to study joint stiffness (Gribble et al., 1998; Kistemaker et al., 2007b) and several motor control theories like impedance control (Hogan, 1984) or equilibrium trajectory control (Feldman and Levin, 2009; Flash, 1987; Gribble and Ostry, 2000; Gribble et al., 1998). Moreover, in intermittent control concepts, where the entire movement is generated by the combination of a few time-discrete signals, a smooth trajectory emerges from the dynamics of the musculoskeletal system (Bayer et al., 2017; Brändle et al., 2020; Günther and Ruder, 2003; Kistemaker et al., 2006; Koike et al., 2011; Stollenmaier et al., 2020b; Wochner et al., 2020). For such control concepts, the assumption of ideal torque generators fails as they rely on the muscles' non-linear viscoelastic characteristics to explain the dynamic interplay of neuronal control and musculoskeletal system (Pinter et al., 2012; Stollenmaier et al., 2020b) (Figure 7.1).

To apply the test trilogy to such control concepts, the muscle characteristics listed above need to be considered. In computer simulations, this is realized by a muscle-tendon-unit model (e.g., Haeufle et al., 2014a), activation dynamics (e.g., Rockenfeller et al., 2015), and anatomical routing (e.g., Hammer et al., 2019). In robotics, muscle routing can be implemented using cables as tendons (Haegele et al., 2015; Shin et al., 2011), variable joint impedance by serial elastic actuators with tuneable stiffness (Albu-Schäffer et al., 2008), and muscle-like force-length-velocity characteristics e.g., by pneumatic muscles (Boblan et al., 2004; Klute et al.,

2002, 1999; Shin et al., 2011; Wolfen et al., 2018).

Both numerical (e.g., Kistemaker et al., 2006; Stollenmaier et al., 2020b) and biorobotical (e.g., Boblan et al., 2004; Lenzi et al., 2011) models that provide the necessary level of physiological detail have been used to investigate such motor control concepts by the comparison with data from human experiments. However, an integrated, coherent framework of human experiments, computer simulation, and biorobotic testbed allowing a systematic comparison of all three methodological approaches has not yet been published. The purpose of this study was to develop such a framework for testing human motor control concepts that explicitly rely on muscle dynamics. We demonstrate the relevance of this framework by applying it to a bio-inspired intermittent control scheme exploiting the natural dynamic of the musculoskeletal system to generate point-to-point arm movements. This requires our novel framework to consider the relevant natural dynamics, i.e, the muscular force-length characteristics, series elasticity, physiological lever arms, activation dynamics, and proprioceptive feedback signals. These natural dynamics are realized by a musculoskeletal model in the computer simulation and pneumatic muscles in the biorobotic system, thus allowing the same controller to generate goal-directed arm movements with acting gravity resembling human arm movements in both models. The combination of all three methodological approaches promises to establish realistic models of motor control and, at the same time, may seed translation into (bio-)robotic applications.

7.2 Methods

As stated in the introduction, we developed a framework of human experiment, computer simulation, and biorobotic testbed. Its purpose is to test motor control hypotheses that explicitly consider and rely on the passive viscoelastic properties of muscles and tendons. Therefore, we exemplarily apply the proposed test trilogy to a bio-inspired intermittent hybrid equilibrium point controller (Kistemaker et al., 2006; Stollenmaier et al., 2020d). We chose this control scheme because it exploits the viscoelastic properties of the muscle-tendon units as it generates smooth trajectories by an intermittent control signal representing a sequence of a limited number of equilibrium points. Hence, the control scheme exploits the muscles' force-length relation to achieve stable equilibrium positions (see Figure 7.2) and their activation dynamics (biochemistry) to generate a smooth movement from a piecewise constant control input (Bayer et al., 2017; Stollenmaier et al., 2020b). Therefore, these characteristics were considered in both the numerical model and the biorobotic hardware.

The investigated movement is a point-to-point arm movement. The task is to point to different targets appearing on a screen, all in one vertical line. In the human experiment, this resulted in a movement predominantly in the sagittal plane, with flexion and extension movements in the shoulder and elbow joint. As subjects were not allowed to touch the screen, going from the start to the target position required to slightly retract, and afterward extend the arm (typically by elbow flexion) to avoid collision with the screen. This is important, as each movement thus requires at least three equilibrium points, one initial position, one retraction, and one final position. The numerical musculoskeletal model and the biorobotic system were implemented to reflect this level of movement complexity and the operating range of the robot was tuned to achieve the range of motion in each joint as observed in the experiments.

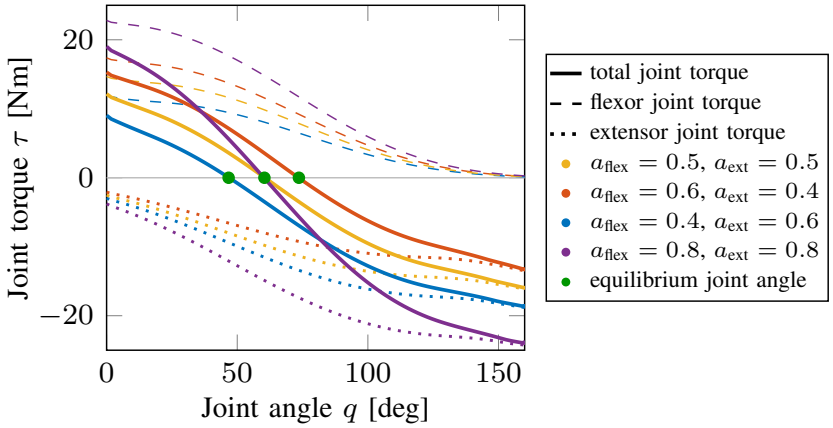

Figure 7.2: **Emergence of equilibrium states (green) in relation to the static muscle activity a for an exemplary model with one joint and two antagonistic muscles (flexor and extensor).** The torques that the muscles generate depend non-linearly on the joint angle q. This force-length relation of muscles is dependent on the muscle activity a. In case of an external perturbation, the passive viscoelastic properties of the muscles generate a torque opposing the perturbation. Therefore, if the sum of both torques (total joint torque) is equal to zero, an equilibrium point is reached. The joint angle in this equilibrium depends on the muscle activities a. Simultaneously increasing a in both muscles increases the muscle co-contraction and, as a consequence, the joint stiffness (see difference in slope at the middle green point for orange and violet line), while maintaining the equilibrium angle (Picture re-used, with permission, from Driess et al. (2018) ©2018 IEEE).

7.2.1 Human Experiment

Eight healthy subjects (age 46 (±5) years) participated in the study. The experimental procedure was approved by the local ethics committee (886/2018BO2). All participants gave their informed consent prior to participation.

The participants were seated in front of a vertical canvas at a distance of 50 % of their arm length (see Figure 7.3a). Four different targets appeared randomly on a vertical line on the canvas and the subjects were instructed to follow the targets fast, but precisely with their dominant hand. The vertical distance between the target positions varied between approximately 15 cm for small movements and 45 cm for large movements (distance between circle centers).

The movements were recorded with a 12-camera motion capturing system (Vicon Motion Systems Ltd, UK) with 120 Hz using a marker set with 29 retro-reflecting markers (see marker position table in Appendix A4.2). Using the recorded marker positions over time, shoulder and elbow angles were reconstructed (Rettig et al., 2009). The reconstructed joint angle trajectories were smoothed with a Savitzky-Golay polynomial filter (of order 4 and with a window size of 41 sampling points). For the comparison with robotic and simulated movements, we chose one representative movement.

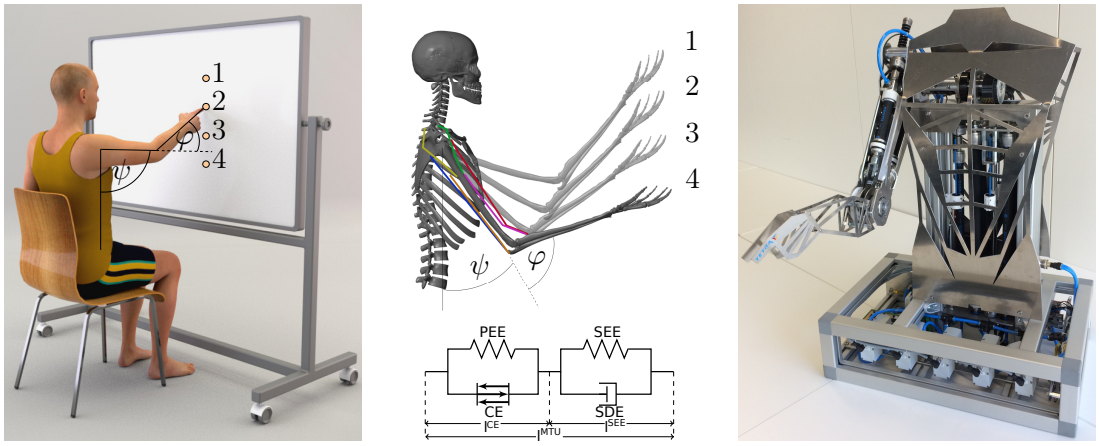

(a) (b) (c)

Figure 7.3: **Trilogy of human experiment, computer simulation, and biorobotic testbed.** (a) Sketch of the human experimental setup. Using a motion capture system, elbow and shoulder angles of fast goal-directed pointing movements have been captured. (b) Numerical musculoskeletal model that was used for the computer simulations of the arm movements. The colored lines represent the six muscles that are modeled using an extended Hill-type muscle model (Haeufle et al., 2014b). (c) Robotic experimental setup. The robot is actuated by pneumatic muscles (Festo AG & Co. KG). Linear sensors in parallel to the muscles (small blue tubes visible in the trunk) mimic muscle spindles.

7.2.2 Numerical musculoskeletal model

For the computer simulation of human arm movements, we used a musculoskeletal model of the human arm with six muscles and two degrees of freedom (Stollenmaier et al. (2020b), see Figure 7.3b and Section 3.2.4). A vertical arm movement in the presence of gravity is simulated in accordance with the experimental setup described above.

The skeletal structure of the arm is modeled using two rigid bodies (lower and upper arm) that are connected via two one-degree-of-freedom revolute joints that represent the shoulder and elbow joint. Movement is generated by active forces that are applied to the skeleton by six muscle-tendon units (MTUs, four monoarticular (shoulder flexor (anteversion), shoulder extensor (retroversion), elbow flexor, elbow extensor) and two biarticular muscles (biarticular flexor, biarticular extensor)). The force of each MTU is calculated using an extended Hill-type muscle model including force-length-velocity characteristics, tendon and parallel tissue elasticity, and damping in the tendon (Haeufle et al. (2014b)). The activity of the muscles is determined by a model of the activation dynamics that considers the fiber length dependency of the activity as described by (Hatze, 1977).

The geometry of the muscle path is implemented using a via-ellipse approach that uses ellipses attached to the bones to limit the muscle path, matching experimental lever arm data (Hammer et al., 2019).

All parameters used in the musculoskeletal model represent a generic man (collected from

different sources, among others: Bhanpuri et al. (2014); Kistemaker et al. (2006); Mörl et al. (2012); van Soest et al. (1993a), see Section 3.2.4 for a detailed list). Hence, the parameters are not subject-specific.

The input to the model is the vector of muscle stimulation signals $\mathbf{u}(t)$ with $\mathbf{u} \in \mathbb{R}^6$ including one signal for each of the six muscles. The output of the model is proprioceptive feedback describing the muscle fiber length $\mathbf{l}^{\mathrm{CE}}(t)$ (with $\mathbf{l}^{\mathrm{CE}} \in \mathbb{R}^6$) and the movement $\mathbf{q}(t) = [\varphi(t), \psi(t)]$ (with $\mathbf{q} \in \mathbb{R}^2$, including elbow and shoulder joint angles, respectively).

Implementation The arm model was implemented using Matlab®/Simulink® version 2018a with the Simscape Multibody™environment. For all simulations, the variable-step Matlab ODE solver *ode15s* with relative solver tolerance 1×10^{-5} has been used. The absolute tolerance and the minimum/maximum/initial step size are set to be determined automatically.

7.2.3 Biorobotic model

To implement the hardware test, we used a biorobotic model that resembles the characteristics of the numerical musculoskeletal model as closely as possible in hardware (see also Appendix A5 and (Driess et al., 2018, 2019)). Its key characteristic—in analogy to the numerical model—is that for a given constant feed-forward set of muscle stimulations, i.e., pressures in its pneumatic artificial muscles, the arm will reach a static equilibrium posture (EP) which is passively stable against external perturbations (Driess et al., 2018, 2019; Wolfen et al., 2018).

Similar to the numerical model, the biorobotic model represents the right human arm. It can perform movements in two degrees of freedom in the sagittal plane. Two hinge joints represent the shoulder and the elbow joint. It is actuated by five muscle-spring units (four monoarticular (shoulder flexor (anteversion), shoulder extensor (retroversion), elbow flexor, elbow extensor), and one biarticular (biarticular flexor)). Due to spatial restrictions, the robotic model has only one biarticular muscle compared to the numerical model which has two biarticular muscles (six muscles in total). Each muscle-spring unit consists of a pneumatic artificial muscle (DMSP, Festo AG & Co. KG) and a spring in series which provides compliance over the entire range of motion (Wolfen et al., 2018). Similar to the biological muscle, pneumatic artificial muscles show a force-length relationship with decreasing muscle force for shorter muscle lengths (Festo AG and Co. KG, 2016; Klute et al., 2002; Wolfen et al., 2018). The force of the muscle-spring units is transmitted to the arm segments via integrated pulleys in the joints. The lever arm determines how much force is transmitted to the corresponding segment. In biology (Murray et al., 1995) and in the numerical model, the muscle lever arm depends non-linearly on the joint angle. Therefore, we developed a non-linear pulley for the elbow joint which makes it possible to mimic the biological lever arm (for more details see Appendix A5). Linear sensors (Temposonics C-Series analog sensor, MTS Sensor Technologie GmbH & Co. KG) in parallel to the pneumatic muscles provide length feedback similar to proprioceptive muscle spindle feedback. The joint positions of the arm are measured by magnetic incremental encoders (LM13IC2D0BA10F00, MR050E040A080B00; cpr:144000, ppr:36000; RLS Merilna tehnika d.o.o).

The key differences to the numerical model are the following: Firstly, the range of motion is limited as the pneumatic artificial muscles can contract only by about 20% of their rest length. The numerical muscle model resembles a biological contraction range of about 50% resulting in a higher range of motion with similar lever arms. Secondly, the elasticity of the series elastic

elements is linear in the biorobotic muscle-spring units and non-linear in the numerical model. Finally, the force levels and inertia properties are not completely matched, but the robotic arm is powerful enough to through a juggling ball more than two meters up in the air.

The input to the biorobotic model is a vector of muscle stimulation signals $\mathbf{u}(t)$ with $\mathbf{u} \in \mathbb{R}^5$ including one signal for each of the five pneumatic muscles. These signals are given as set values to 3-way proportional valves (VPPX-8L-L-1-G14-0L10H-S1, Festo AG & Co. KG) which then ensure the desired pressure in the pneumatic artificial muscles. The output of the biorobotic model is proprioceptive feedback describing the muscle length $\mathbf{l}^{\mathrm{CE}}(t)$ (with $\mathbf{l}^{\mathrm{CE}} \in \mathbb{R}^5$) and the movement $\mathbf{q}(t) = [\varphi(t), \psi(t)]$ (with $\mathbf{q} \in \mathbb{R}^2$, including elbow and shoulder joint angles, respectively). While the length feedback is used for the controller, the joint angles are only used to record the movement.

Implementation The investigated motor control hypothesis is described below and implemented as a *hardware-in-the-loop* framework using Matlab®/Simulink® version 2016a with the Simulink Desktop Real-Time™environment and a Sensoray 626 i/o board. This allowed us to use the same control scheme and simply apply it to the numerical model and the biorobotic model replacing the virtual physics engine with real-world hardware.

A few additional measures were taken in the hardware model: To match the muscle activation dynamics of the numerical model as closely as possible, we used the same model of activation dynamics (Hatze, 1977). This model acts like a non-linear low-pass filter of the control signals, which considers biochemical processes that are not present in the pneumatic artificial muscles. However, design limitations of the muscle-spring units and sensor noise required us to neglect the muscle fiber length dependence of the activation dynamics, i.e., we used a constant muscle length as input for the activation dynamics ($l^{\mathrm{CE}} = l^{\mathrm{CE,opt}}$). In addition, it was necessary to lower the time constant of the activation dynamics to $m_{\mathrm{biorobotic}} = 0.1 \cdot m$ to reduce unwanted oscillations in the system. The drawback of the slower reaction of the system to changes in stimulation is only visible in one movement (movement 1→4), where the slower deflation of the shoulder muscles led to a lower acceleration. We expect that this trade-off between oscillations and reaction speed could be improved by higher stiffness of the series elastic element.

7.2.4 Motor control model

The bio-inspired hybrid equilibrium point controller that we used to demonstrate our framework (Bayer et al., 2017; Haeufle et al., 2020a; Kistemaker et al., 2006; Stollenmaier et al., 2020d) exploits the muscles' force-length relation to achieve stable equilibrium positions (see Figure 7.2) and their activation dynamics (biochemistry) to generate a smooth movement from a piece-wise constant control input.

The controller combines a feed-forward command $\mathbf{u}^{\mathrm{open}}(t)$ with a feedback signal $\mathbf{u}^{\mathrm{closed}}(t)$ that incorporates proprioceptive spinal feedback. This feedback represents a simplified version of the mono-synaptic muscle spindle reflex, assuming that the muscle spindles provide accurate time-delayed information about the muscle fiber lengths $\mathbf{l}^{\mathrm{CE}}(t)$ (Kistemaker et al., 2006).

The total motor command $\mathbf{u}(t)$ is a sum of those components and represents α-motor neuron activity. For each muscle i, it is calculated as

$$u_i(t) = \left\{ u_i^{\mathrm{open}}(t) + u_i^{\mathrm{closed}}(t) \right\}_0^1 = \left\{ u_i^{\mathrm{open}}(t) + k_p \left(l_i^{\mathrm{CE}}(t-\delta) - \lambda_i(t) \right) \right\}_0^1, \tag{7.1}$$

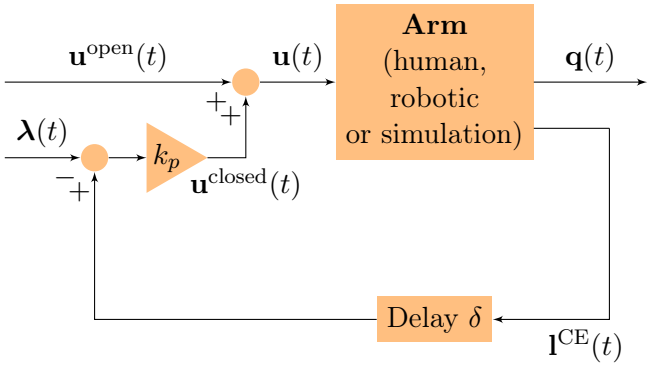

Figure 7.4: **Schematic diagram of the bio-inspired motor control model.** The motor command $\mathbf{u}(t)$ is a sum of an open-loop and a closed-loop signal. The time-delayed feedback loop incorporates proprioceptive feedback (mono-synaptic reflexes) by comparing the actual muscle fiber lengths $\mathbf{l}^{\text{CE}}(t)$ to desired values $\boldsymbol{\lambda}(t)$. Here, the observable state $\mathbf{q}(t) = [\varphi(t), \psi(t)]$ contains the elbow and shoulder angle, respectively.

where k_p is a feedback gain and the time delay δ is set to 10 ms representing a short-latency reflex delay which is in a physiologically plausible range for arm muscles (Houk and Rymer, 1981; More et al., 2010). The operation $\{u_i\}_0^1$ sets values $u_i < 0$ to 0 and $u_i > 1$ to 1.

In our model, the open-loop part $u_i^{\text{open}}(t)$ and the desired muscle fiber lengths $\lambda_i(t)$ represent an intermittent control approach, because they are piecewise constant functions over time (for more details see Stollenmaier et al. (2020b) and Haeufle et al. (2020a)). Herein, each constant value represents an *equilibrium posture* (EP), i.e. the system is in a stable equilibrium in these positions:

$$\dot{\mathbf{q}} = 0 \quad \text{and} \quad \ddot{\mathbf{q}} = 0\,, \tag{7.2}$$

leading to the condition that the net joint moment vanishes in these postures. This condition allows for the calculation of the open-loop muscle stimulations $u_i^{\text{open}}(t)$ and the corresponding desired muscle fiber lengths $\lambda_i(t)$: For each EP, the muscle stimulations $u_i^{\text{open}}(t)$ can be determined by minimizing the difference between the muscle stimulation u_i^{open} and the desired level of co-contraction $u^{\text{des.}}$:

$$\sum_{i=1}^{6}(u_i^{\text{open}} - u^{\text{des.}}) \to \min\,, \tag{7.3}$$

subject to the constraint that the sum of all torques acting on the joint is zero, i.e. the system is in a stable equilibrium position. The corresponding desired muscle fiber lengths λ_i are set by measuring the length l_i^{CE} of the muscle fibers in the equilibrium positions.

For all considered movements along a vertical screen (see Figure 7.3a), the human movement can be reconstructed by selecting only three equilibrium postures (EPs) both in the computer simulation and using the biorobotic model. The first EP represents the initial posture, the last

the target posture. The intermediate EP is necessary to retract the elbow – otherwise, the finger would penetrate the screen.

Note that in this framework, the steady states of the EPs are not necessarily reached. In particular, the third EP is triggered (i.e. the control parameters are switched to the third EP) before the arm reaches the position that corresponds to the second EP.

7.2.4.1 Implementation of the controller in the computer simulation

In the computer simulation, we optimized some of the control parameters to follow the experimental trajectories. The parameters in this optimization are: the shoulder and elbow angle for the second EP, the desired level of co-contraction for the second and the third EP, the starting times for the second and the third EP and the feedback gain $\bar{k}_p$. Using the pattern search algorithm in Matlab®, the quadratic difference between the simulated and the experimental trajectory was minimized. The resulting parameters can be found in Table A4.3. Note that - in contrast to the robotic experiments - the feedback gain in the computer simulation is calculated as

$$k_p = \frac{\bar{k}_p}{l_i^{\mathrm{CE,opt}}}\,, \tag{7.4}$$

where $\bar{k}_p$ is the optimized constant gain for every movement and $l_i^{\mathrm{CE,opt}}$ is the optimal muscle fiber length of the muscle i in consideration.

Using the resulting parameters, the muscle stimulations u_i^{open} were then optimized in order to fulfill the conditions for equilibrium points (see Equation (7.3)) using the Matlab® optimizer *fmincon* which is suitable for finding the minimum of a constraint function.

7.2.4.2 Implementation of the controller in the bio-inspired robot

To match the experimental trajectory, three EPs were defined for each movement: The first EP was determined by an online search procedure that holds the desired position and finds the minimal stimulation of the muscles to do so. The second and the third EP were found manually by adjusting the pressure in the pneumatic muscle such that the respective shoulder and elbow angle trajectories correspond to the experimental data. The switching times between the EPs were also set manually to achieve the movement speed of the experimental data.

This semi-manual tuning lead to a movement that is not as close to the experiment as the simulated trajectories but shows the same qualitative behavior. Computationally optimizing all necessary control parameters, as it was done in the computer simulation, may lead to better results, but would come with the cost of high material stress in the mechanical robot and extensive time effort. This seemed not appropriate here, as the purpose is not to exactly reproduce one trajectory (trajectory optimization) but rather to demonstrate that the same intermittent controller can generate similar smooth trajectories as observed in the friction- and noise-free simulation.

The feedback gain k_p was set to $0.18\,\frac{1}{\mathrm{m}}$.

7.2.5 Data processing

All data from human experiments, numerical model, and biorobotic model were aligned such that $t = 0$ is defined as the point where the difference quotient of the shoulder angle over time is greater or equal to 15 °/s. To correct for offsets in the angle definitions, the robotic angle data are shifted by the mean difference to the human experimental reference movement. This mean difference is calculated by averaging the difference to the reference movement at the start and the end of the movement over all trials of each case.

7.3 Results

The numerical simulation and the biorobot can reproduce the kinematics of human goal-directed arm movements with the same control concept by exploiting the viscoelastic properties of the muscles (numerical muscle model and pneumatic artificial muscles). Both were tuned to reproduce a selected trajectory from the human experiments (one subject, one trial, orange lines in Figure 7.5 and Figure 7.6), which is reproduced for all four considered movements. Both rely on three EPs to generate the movement. The EPs are defined by open-loop control signals resulting in stable starting and end positions by exploiting the force-length characteristics of the muscle. Furthermore, both models generate a smooth dynamic behavior from an intermittent control due to the low-pass filter characteristics of the activation dynamics, the viscoelastic properties of the muscles, and the inertia of the segments.

The optimization of the control parameters, which was only possible in the numerical simulation, lead to a closer reproduction of the experimental data in the simulation than the manual tuning in the robot (Figure 7.5 and Figure 7.6). Especially the case from the highest to the lowest position (1→4) was more difficult to match in the biorobotic system, as here the forces of the pneumatic artificial flexor muscles did not decrease fast enough to achieve the acceleration observed in the experiment (and simulation). Furthermore, the dynamics of the muscle-spring units in the robot caused a significant oscillation towards the end of this movement, which can be attributed to the fact that the robot operated at the extremes of its range of motion, which is obviously not true for humans and also not for the simulation (which is parameterized to roughly match the human range of motion). Despite these limitations, the core characteristics of the movement are preserved.

Although the maximum forces and contraction ranges differ—and therefore also the values of the control parameters—the general characteristics of the control remain identical. In both the computer simulation and the robot, the open-loop muscle stimulation level is dependent on the position of the arm. For example, for a big upward movement, the mean open-loop muscle stimulation is low for the starting position and increases for the second and third EP (Table 7.1). The reason for this is that the muscle lengths change with the position of the arm and - due to the force-length relationship implemented in the muscle models - the muscles need to be stimulated differently to produce the same amount of force. In addition to that, the lever arm of the gravitational force is higher for the more elevated arm positions requiring higher muscle stimulations to hold the arm.

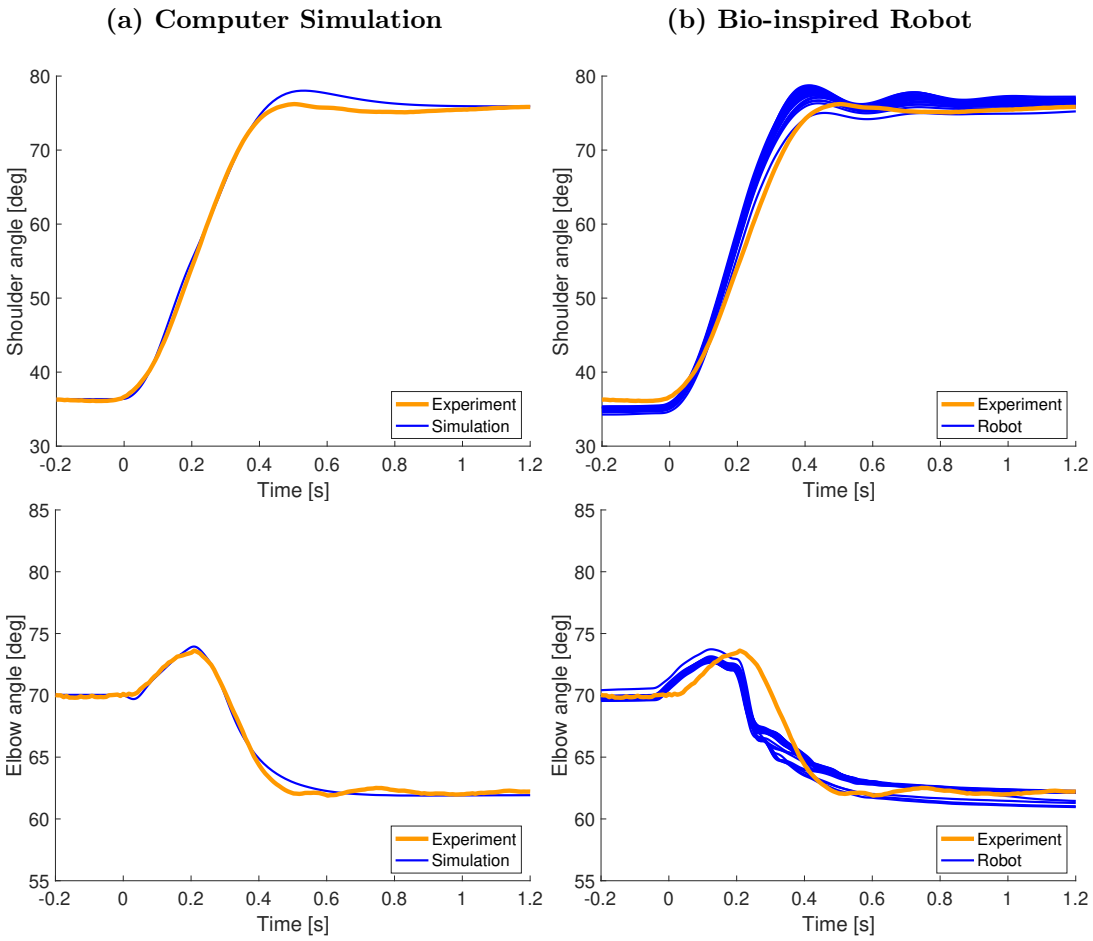

Figure 7.5: **Results for a big upward movement from position 4 to position 1 ($4 \rightarrow 1$) using (a) the computer simulation and (b) the bio-inspired robot.** The two rows show the shoulder and the elbow joint trajectory, respectively. The blue lines depict the robot and simulation trajectories, the orange lines show one movement of one typical control subject in the experiment.

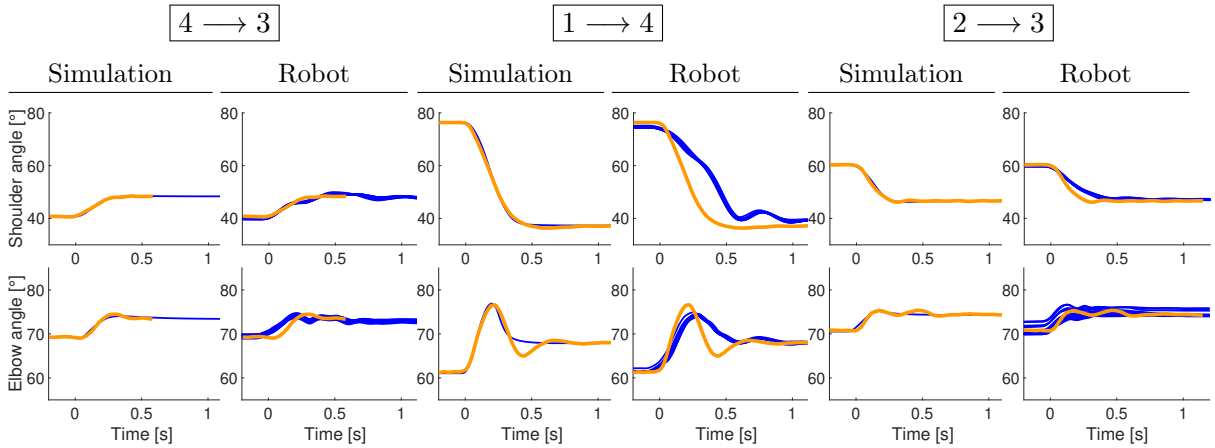

Figure 7.6: **Resulting trajectories for the other evaluated movements between the four target positions.** For more details see Appendix A5. The blue lines depict the robot and simulation trajectories, the orange lines show one movement of one typical control subject in the experiment.

	EP 1	EP 2	EP 3
Simulation	0.11	0.37	0.46
Robot	0.04	0.09	0.08

Table 7.1: **Mean open-loop muscle stimulations for every EP (average over all muscles), exemplary for a big upward movement from position 4 to position 1** ($4 \rightarrow 1$). For more detailed results on the muscle stimulations, see bar diagrams in Appendix A5.

7.4 Discussion

Using the musculoskeletal numerical model and the biorobotic system in combination with measurements from human experiments, we set up a framework that allows investigating motor control concepts that rely on muscular dynamics for two-degree-of-freedom arm movements. The major novelty is the approach to implement a control hypothesis that relies on the muscular dynamics in the computer simulation and then develop a biorobotic testbed with dynamics that are close enough to the numerical model such that the control law can be transferred directly. The key to this are two characteristics of the biological muscles which are considered in both models: the force-length relation and the activation dynamics. In our opinion, the complexity of this setup with two degrees of freedom is a sweet spot as it is complex enough to reproduce typical motor control experiments and at the same time not too complex to realize as a biorobotic model.

We tested this framework using the example of an equilibrium point control approach. Our results show that this control concept can be used to reproduce human two-degree-of-freedom point-to-point arm movements in both the computer simulation and the biorobot with only three constant EPs. The bio-inspired control law explicitly uses the non-linear viscoelastic properties of the muscles, so that the controller does not need a model of the actuator to execute soft movements. As we consider the required muscle properties in both the computer simulation and the biorobot, our framework can be used to test the real-world feasibility of this control concept. Despite several differences between the biorobot and the numerical simulation, it is possible to reproduce the human experiment with the same controller (using different control parameters). Hence, combining human experiments, computer simulation, and the biorobotic testbed into one framework, we showed that EP control can be well-performing in real-world physical conditions and produce stable movements and positions.

7.4.1 Comparison to other approaches in bio-robotics

Robotic systems are used as tools to study the principles of biological movement generation. This includes biomechanical principles in locomotion (Ijspeert, 2014; Kashiri et al., 2018), motor control principles (Lenzi et al., 2011), or even principles of motor learning (Aguirre et al., 2017; Driess et al., 2018, 2019). We refer the reader to Vitiello et al. (2015) for an overview on neuro-robotics and the potential mutual benefits of the combination of motor-control neuroscience and robotics.

As the viscoelastic and variable stiffness joint characteristics of the antagonistic muscle-setup may also be beneficial for other purposes, e.g., for safe human-robot interaction (Albu-Schäffer et al., 2008), they have also been implemented on more classical robotic systems with current-controlled DC motors. Since an electric motor has no innate viscoelastic properties, additional control policies are required to emulate these. This is possible to some extend (Dietrich et al., 2011; Wang and Kheddar, 2019) by real-time control with high control frequency (10 kHz or more) but comes at the cost of increased control complexity.

On the other hand, using pneumatic muscle-driven robots for the purpose of classical control approaches (e.g., torque control) requires an exact model of the pneumatic actuator forces. These model-based approaches are based on complex characterization using geometric (Boblan et al., 2007; Martens et al., 2018), empirical (Wickramatunge and Leephakpreeda, 2013), phe-

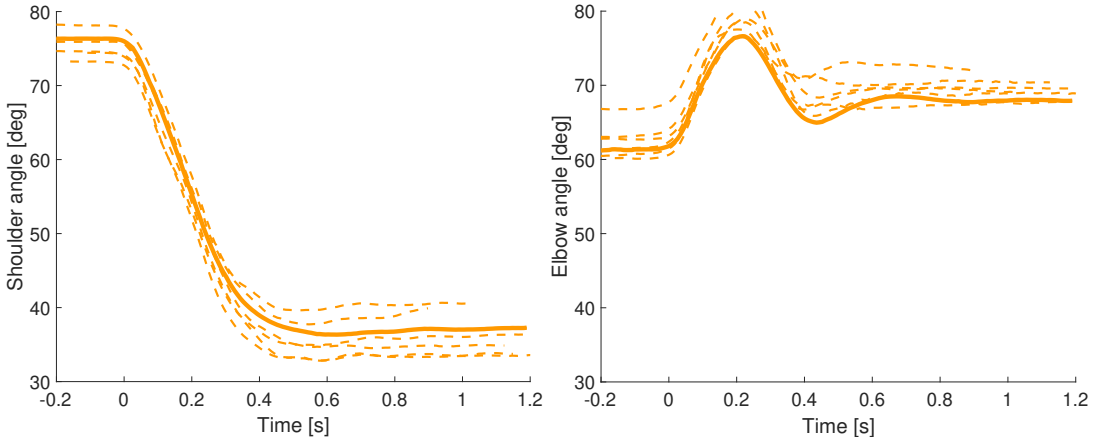

Figure 7.7: **Several trials of one subject for a big downward movements from position 1 to position 4 ($1 \rightarrow 4$).** The dashed lines show the trials, the solid line shows the trial that has been used as reference for this movement in our investigations.

nomenological (Tsagarakis and Caldwell, 2000), or FEM models (Tu et al., 2020). Controllers for robotic systems with pneumatic muscles often do not have to deal with non-linear lever arms, different muscle lengths, biarticular muscles, or series elastic tendons (Anh and Ahn, 2011; Shin et al., 2011), all of which are present in the biological system. Here, we show that a relatively simple bio-inspired control concept allows for the generation of goal-directed arm movements despite these complications by exploiting the muscles' properties.

7.4.2 Outlook and relevance for motor control research

To study how humans achieve the variety and incredible performance in motor control, different classes and aspects of movements are investigated in isolation and combination. Hogan and Sternad proposed that three classes of dynamic primitives are used to encode motor commands: *submovements, oscillations, and impedance* (Hogan and Sternad, 2013). The impedance class of dynamic primitives is relevant when interacting with the environment and may physically emerge from the antagonistic setup of muscles and be tuned by their co-contraction (Hogan, 1984). Especially for this class, the passive characteristics of the musculoskeletal system play an important role, as already described in detail in the introduction. One important research field in this direction is the control of goal-directed movements facing perturbations (Kurtzer et al., 2009). In the last years, there is emerging evidence that such control strategies consist of a fine-tuned interaction of musculoskeletal system characteristics, short- and long-term reflexes, and voluntary error feedback correction, with a strong interaction of the different mechanism levels in terms of adaptation and optimization. Regarding movement adaptation, control strategies do not only have to be adjusted in respect to external changes like abrupt perturbations or handheld objects changing arm dynamics, but also in respect to internal changes, e.g. changes in musculoskeletal system characteristics caused by muscle fatigue (Dube and Roy, 2019) or even neuro-muscular diseases (Dunkelberger et al., 2020; Kurtzer et al., 2013). In order to investigate the described interaction between mechanisms for the control (Kistemaker et al., 2013; Kurtzer et al., 2008; Weiler et al., 2019) and adaptation (Maeda et al., 2020) of movements, the explicit

modeling of the neuro-muscular system and its characteristics in interaction with the higher control levels delivers specific insights (Cheng and Loeb, 2008; Tytell et al., 2011).

Moreover, the natural variability in motor control, as e.g., visible in the human data shown in Figure 7.7, provides insights into control strategies (Latash et al., 2002), motor learning (Herzfeld and Shadmehr, 2014), and motor control impairments (Markanday et al., 2018; Sanger, 2006). Furthermore, the reaction to small variations may reveal the stability and robustness of a controller (Kalveram and Seyfarth, 2009). One drawback of deterministic motor control models is the lack of any natural variance and hysteresis of the data, if not explicitly introduced. The implementation on a suitable biorobotic system introduces noise, hysteresis, and variance by physical processes and has therefore not only the potential to reveal inconsistencies and instabilities in the controller, but may also provide a means to distinguish between physical and neuronal sources of motor control variability. At least, we find that in general, the variability in our robotic setup is smaller than found in the human experimental data. This may become especially relevant for building testbeds in two fields: (1) learning strategies like reward-based trial-and-error learning (Codol et al., 2020) which exploit variability as a means of exploration for increased robustness and (2) motor control impairments, when consequences of specific dysfunctional mechanisms can be examined without the system inherent motor variability of the human motor control system.

8 | Investigating the reflex contribution in repositioning processes

In the closed-loop interaction of humans and technical devices, it can become necessary that the artificial system manipulates the human by imposing a movement without exactly knowing the human's intention. In this chapter, we investigated the interactive dynamics of such a repositioning by combining a whole-body musculoskeletal model (Section 3.2.5) with a model of low-level proprioceptive feedback (Section 3.3). The core questions are: 1) How much differs the muscle force prediction when including feedback? 2) Does this depend on the externally imposed movement speed? 3) How much is the muscle force affected by the human's cognitive state? We investigated both the passive reaction forces of the musculoskeletal system as well as the contribution of a long-latency stretch reflex to the muscular forces for a large range of movement velocities. We found that in our setting, the predicted relative force contribution of the feedback mechanism is not negligible, especially for high movement velocities. The force increases when modeling an unprepared cognitive state and decreases for the prepared case.

Note that large parts of the content of this chapter were submitted to *Computer Methods in Biomechanics and Biomedical Engineering*. For details on this manuscript, including a list of authors, see Manuscript 5 in Chapter 2.

8.1 Introduction

Pervasive augmentation of human capabilities, that is, closed-loop interactions of humans and technical devices seem to become part of almost every aspect of our lives in the future. Starting from already established augmentation of motorized hospital beds and robots for walking rehabilitation, new devices will emerge, for example, exoskeletons for standing, walking and running or repositioning devices in future mobility vehicles. In this regard, it becomes more and more relevant to investigate the interplay of humans with such systems that can be autonomous and intelligent for their part. This interplay can be seen as an interaction of two autonomous intelligent systems: (a) a natural autonomous intelligent system, the human which we consider as a neuro-mechanical, senso-motorical system and (b) an autonomous artificial intelligent system. In this interaction, it can become necessary that the artificial system manipulates the movement of the human by imposing a movement without exactly knowing the human's movement intention. Such a repositioning process can happen on different time scales (Figure 8.1): slow movements like in motorized hospital beds or rehabilitation robotics or faster movements in exoskeletons as human power amplifiers or active seats as they might, for example, occur in

cars as an active safety system (Adient Ltd. & Co. KG, 2018). One interesting example is the repositioning of a driver to a safe position in the event of an anticipated crash (Adient Ltd. & Co. KG, 2015). In this interaction, the behavior of the artificial system can depend on the current state of the human (e.g. position, velocity, relaxed vs. tensed state) and the movement of the human is partially prescribed/imposed by the artificial system. To investigate this interaction and how it affects the human, the interactive dynamics between the human and the artificial system need to be considered.

Computer simulations using neuro-musculoskeletal models provide a useful tool to investigate this interaction and to predict the consequences for the human in these repositioning movements. Internal muscle forces can be calculated, reflexes can be modeled and their contribution can be investigated (Stollenmaier et al., 2020b). Another advantage of musculoskeletal modeling is that different levels of co-contraction can be investigated. As a result, different levels of attention can be investigated by testing different levels of co-contraction. Also, a change in the level of attention or preparedness (e.g. when the human notices that they are moved by the artificial system or when they are warned by a signal shortly before movement) can be considered. More and more complex models of both, the neuronal control and the musculoskeletal system, are being developed (Kapelner et al., 2020). More physiologically valid models consider more effects and are hence expected to yield better results. However, these models are also more complex and usually need more sophisticated tuning of parameters and are computationally more expensive. So the question is: how much do the predictions differ when different levels of modeling detail are included? Previous work indicates that the resulting movement mostly depends on the controller and the pre-activation of the muscles and not on the biophysical model components (Bayer et al., 2017). Therefore, the two core questions of this contribution are: 1) How much differs the internal muscle force prediction for an increased level of neuronal control modeling detail? 2) Does this depend on the externally imposed movement speed?

We exemplary look at a device that moves the human from a lying to a seated position and investigate the consequences on the hip muscle forces. To this end, we combine a whole-body musculoskeletal model with a model of low-level proprioceptive feedback. This allows us to investigate both the passive reaction forces of the musculoskeletal system as well as the contribution of a (long-latency) stretch reflex to the resulting muscular forces for a large range of movement velocities.

The prediction of muscle forces can be relevant for different applications as it can allow for the calculation of joint stiffness, the prediction of possible injuries, and the estimation of the required torque to move the system. For example for exoskeletons, the estimation of the system's stiffness is important for the choice of actuators, materials, and the design in both the normal application velocity and fast emergency actions, e.g. to prevent the user from falling. In the case of an active car seat, the prediction of the hip joint stiffness can help to predict whether the passenger will stay in the seat. The predicted muscle force itself can be compared to soft tissue material data to assess the potential injury risk of this biological part (Noelle et al., 2020).

In a previous study (Stollenmaier et al., 2020b), we investigated the neuro-muscular response to external perturbations using a musculoskeletal model of the arm in combination with the same control concept as used here. On a full-body scale, however, the investigation of the dynamic interplay between the somatosensory system and the musculoskeletal system in the presence of external perturbations is a novelty. In particular, the systematic analysis for differ-

ent movement velocities allows for new insights into the influence of different levels of neuronal model detail in the interplay with a musculoskeletal model.

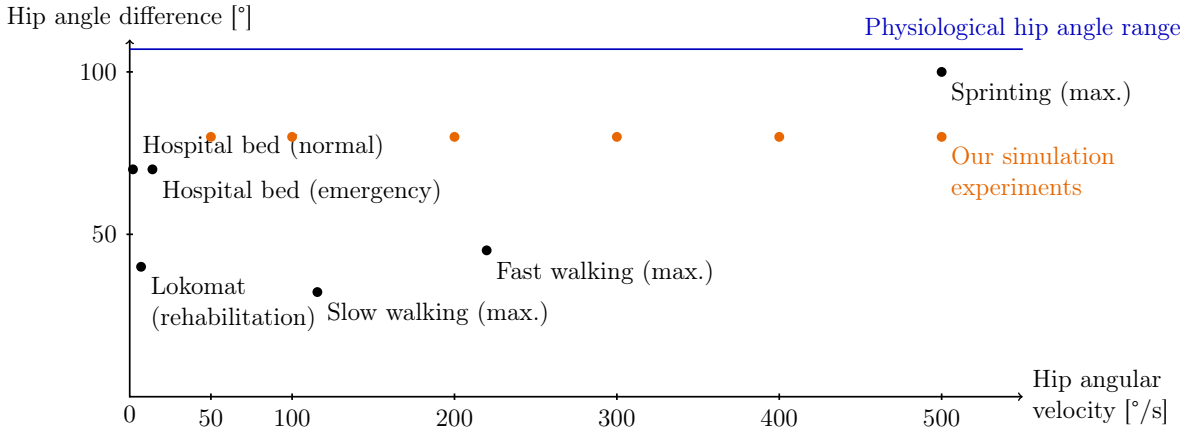

Figure 8.1: **Hip angle difference in relation to the angular velocity of the repositioning process in different applications where an artificial systems interacts with a human.** The orange dots show our simulation experiments. The black dots show other potential devices. Automatic hospital beds can move the patients from a lying to a seating position (Griswold, Lee F; Edward A. and Beckstrom, 2014; Hermann Bock GmbH, 2018; Lacasse et al., 2016). Exoskeletons can support walking movements by prescribing typical walking speeds to the lower limb joints: maximal hip angle differences and angular velocities for different walking speeds (Mentiplay et al., 2018) and sprinting (Belli et al., 2002; Higashihara et al., 2018; Hunter et al., 2005; Slawinski et al., 2010) are shown here. One example of such an exoskeleton is the Lokomat (Hocoma AG, Volketswil, Switzerland, Jezernik et al. (2003)) that is used for gait rehabilitation (Domingo and Lam, 2014). The shown values are examples and do not represent the whole working range of these applications. The horizontal blue line shows the maximal physiological hip angle difference averaged over a group of 200 people of different ages and genders (Elson and Aspinall, 2008).

8.2 Methods

8.2.1 Full-body musculoskeletal model

For the investigations presented here, we used a three-dimensional musculoskeletal model of the full human body representing a generic, 50th percentile male. A detailed description of the musculoskeletal model can be found in Section 3.2.5.

The model of the skeletal structure consists of 15 rigid bodies, connected via 14 joints including 20 mechanical degrees of freedom. This multibody system is actuated by 36 muscle-tendon units that produce active forces. These muscle-tendon units are modeled using an extended Hill-type muscle model as described by Haeufle et al. (2014b), which accounts for force-length-velocity characteristics, tendon and parallel tissue elasticity, and damping in the tendon (see Figure 8.2). The activity of the muscles is determined using a model of biochemical muscle activation dynamics (Rockenfeller and Günther, 2018) as introduced by Hatze (1977), which considers the fiber length dependency. The muscle and activation dynamics parameters are taken from the literature (see Section 3.2.5). The muscle-tendon unit forces are internal forces that act on the skeleton. External forces that act on the system are gravity and contact forces (see below).

8.2.2 Controller

The bio-inspired control model combines a feed-forward motor command with a feedback loop based on muscle fiber lengths and contraction velocities (Figure 8.2). The total stimulation $\mathbf{u}$ represents α-motor neuron firing rate and is calculated for each muscle i as

$$u_i(t) = \left\{ u_i^{\text{open}}(t) + u_i^{\text{closed}}(t) \right\}_0^1 , \tag{8.1}$$

where the operation $\{u_i\}_0^1$ sets values $u_i < 0$ to 0 and $u_i > 1$ to 1.

Herein, the feed-forward (open-loop) command $\mathbf{u}^{\text{open}}(t)$ represents a constant basis muscle tone which is set to the same value for all muscles i:

$$u_i^{\text{open}}(t) = \bar{u}^{\text{open}} . \tag{8.2}$$

With $\bar{u}^{\text{open}}$ it is possible to regulate the level of muscle co-contraction. It can hence be related to the level of attention or tenseness of the human: A higher value of $\bar{u}^{\text{open}}$ leads to higher muscle tensions and hence a higher stiffness of the system.

The closed-loop signal $\mathbf{u}^{\text{closed}}(t)$ incorporates proprioceptive feedback since it represents a simplified version of the muscle spindle reflex by comparing the actual lengths and contraction velocities $(\mathbf{l}^{\text{CE}}(t), \dot{\mathbf{l}}^{\text{CE}}(t))$ of the muscle fibers (contractile elements (CEs)) to desired values $(\boldsymbol{\lambda}(t), \dot{\boldsymbol{\lambda}}(t))$. As the information about the current state of the muscle only becomes available with a neuronal delay, a time lag δ is introduced. Since experimental findings indicate that the long-latency stretch reflex plays an important role in the reaction to mechanical perturbations in goal-directed reaching movements (e.g., Kurtzer et al., 2014; Weiler et al., 2016), we implemented a long-latency feedback loop by setting the time delay to 50 ms (R2 response (Pruszynski et al., 2011; Scott, 2016)). This model approach is based on the assumption that the muscle spindles provide accurate time-delayed information about the muscle fiber lengths $\mathbf{l}^{\text{CE}}(t)$ (Kistemaker et al., 2006).

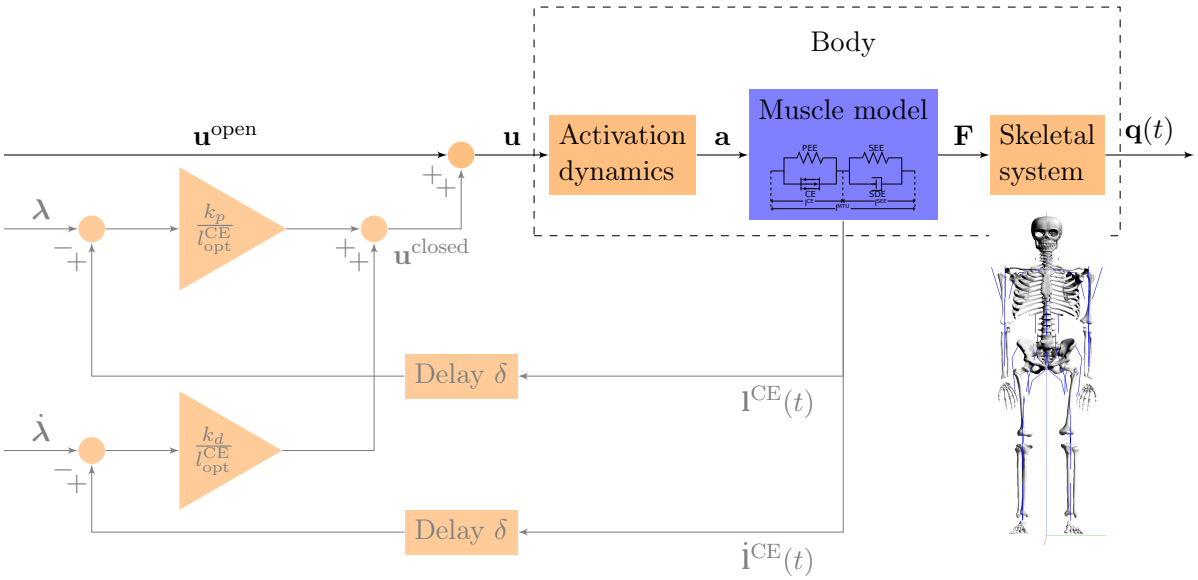

Figure 8.2: **Schematic diagram of the neuro-musculoskeletal model.** In the feed-forward version of the model (black lines), the total motor command $\mathbf{u}$ contains only the open-loop signal $\mathbf{u}^{\text{open}}$. The motor command $\mathbf{u}$ is fed into the model of the activation dynamics of muscles which relates the neuronal stimulation to muscular activity $\mathbf{a}$ that drives the muscle model. The muscles produce forces $\mathbf{F}$ that act on the skeletal system resulting in a simulated movement $\mathbf{q}(t)$ of the body. In the time-delayed feedback loop (gray lines), the sensory system, which represents a simplified version of the muscle spindles, measures the current lengths and contraction velocities of the muscle fibers ($\mathbf{l}^{\text{CE}}(t), \dot{\mathbf{l}}^{\text{CE}}(t)$). They are compared to the desired values ($\boldsymbol{\lambda}$, $\dot{\boldsymbol{\lambda}}$) and the resulting feedback error is multiplied by the feedback gains k_d and k_p, normalized by the muscle's optimal fiber length $l_{\text{opt}}^{\text{CE}}$ (see Equation (8.3)). To include feedback, the total motor command $\mathbf{u}$ is a sum of the open-loop signal $\mathbf{u}^{\text{open}}$ and the time-delayed feedback signal $\mathbf{u}^{\text{closed}}$.

The closed-loop signal $\mathbf{u}^{\text{closed}}(t)$ for each muscle i is calculated as

$$\begin{aligned} u_i^{\text{closed}}(t) &= u_i^{\text{closed,l}}(t) + u_i^{\text{closed,v}}(t) \\ &= \frac{k_p}{l_i^{\text{CE,opt}}} \left(l_i^{\text{CE}}(t-\delta) - \lambda_i(t) \right) + \frac{k_d}{l_i^{\text{CE,opt}}} \left(\dot{l}_i^{\text{CE}}(t-\delta) - \dot{\lambda}_i(t) \right), \end{aligned} \tag{8.3}$$

where k_p and k_d are the feedback gains and $l_i^{\text{CE,opt}}$ stands for the optimal length of the contractile element (Kistemaker et al., 2007a).

The desired muscle fiber lengths $\boldsymbol{\lambda}$ are set depending on the considered scenario, see Section 8.2.4. Since the human is assumed to target a resting position at all times, the desired muscle fiber contraction velocity $\dot{\lambda}_i$ is set to zero for all muscles i. The feedback gains k_p and k_d are set as:

$$k_p = 0.1, k_d = 0.01\,.$$

The components of the input parameter vectors to the controller ($\mathbf{u}^{\text{open}}(t)$, $\boldsymbol{\lambda}(t)$, $\dot{\boldsymbol{\lambda}}(t)$) are piecewise constant functions over time where each constant set of parameters represents a stable *equilibrium posture* or *equilibrium point* (EP). Therefore, this control model can be classified as a hybrid equilibrium point controller (Bayer et al., 2017; Kistemaker et al., 2006).

8.2.3 Seat and contact points

To investigate different repositioning velocities in the hip joint, the human model is placed on a model seat (Figure 8.3). To achieve a stable lying position, the initial position of the human is above the seat and the human falls into the seat before the repositioning movement starts (Figure 8.3a). After a short resting phase (1.1 s), the seat is moved from a lying position (0°, $t = 0$ s, Figure 8.3c) to a seated position (80°, Figure 8.3d). The movement of the seat is implemented by prescribing the angle between seat and seatback as a linear function over time between the starting and the target angle. The contact between the seat and the human is implemented using 11 viscoelastic contact points (Figures 8.3a and 8.3b, Table 8.1). In addition to the contact points between the seat and the human, there are contact points between the feet and the floor.

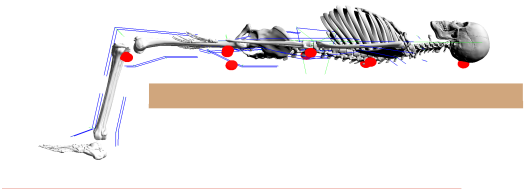

(a) Initial position

Human	Seat	Position
Knee	Seat	left, right
Pelvis	Seat	left, right
Back	Seatback	left, right
Head	Seatback	middle
Elbow	Seatback	left, right
Wrist	Seatback	left, right

(b) List of contact points

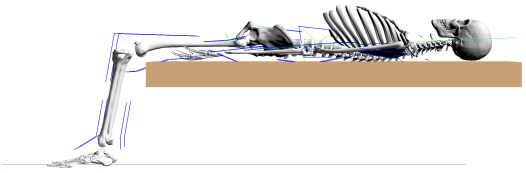

(c) Movement start ($t = 0$ s)

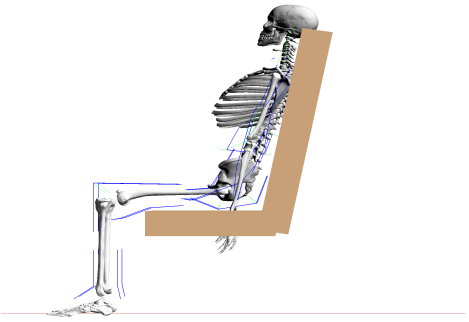

(d) Movement end

Figure 8.3: **Investigated repositioning movement.** (a) Initial position before the start of the movement. The red spheres visualize the positions of the contact points between the human and the seat. (b) List of all contacts between the human and the seat. (c) Lying position at the beginning ($t = 0$ s, 0° seat angle) and (d) sitting position (80° seat angle) at the end of the repositioning movement.

The contacts between the human and the seat are described using linear contact elements with stip-slick transitions. However, the contacts were parametrized such that only stick occurs. The contact algorithm describes the contact between a point and a surface. The point and the surface are in contact if the perpendicular distance between is negative. The contact force is calculated as

$$\mathbf{F} = \begin{pmatrix} f_\perp \\ \mathbf{f}_\parallel \end{pmatrix} = \begin{cases} \begin{pmatrix} \kappa_\perp r_\perp + \rho_\perp^{01} v_\perp + \rho_\perp^{11} r_\perp v_\perp \\ \sigma \mathbf{v}_\parallel + \mu |f_\perp| \frac{\mathbf{v}_\parallel}{|\mathbf{v}_\parallel|} \end{pmatrix} & : \text{if} \quad f_\perp < 0 \\ \mathbf{0} & : \text{otherwise,} \end{cases} \tag{8.4}$$

$$\tau_\perp = \mu_\sigma |f_\perp| \omega_\perp \,, \tag{8.5}$$

with $(\cdot)_\perp$: perpendicular component and $(\cdot)_\parallel$: parallel component. r: distance v: velocity ω: angular velocity.

Body part	$\kappa_\perp$	$\rho_\perp^{01}$	$\rho_\perp^{11}$	σ	μ	v_c	μ_σ	ω_c
Knee	1.0e5	1.0e2	0.0	0.0	1.5	1.0e−3	0.0	9.9e1
Pelvis	1.0e5	1.0e2	0.0	0.0	1.5	1.0e−3	0.0	9.9e1
Back	2.0e7	5.0e3	0.0	0.0	1.5	1.0e−3	0.0	9.9e1
Head	2.0e7	5.0e3	0.0	0.0	1.5	1.0e−3	0.0	9.9e1
Elbow	5.0e6	5.0e3	0.0	0.0	1.5	1.0e−3	0.0	9.9e1
Wrist	5.0e6	5.0e3	0.0	0.0	1.5	1.0e−3	0.0	9.9e1

Body part	$\kappa_\parallel$	$\rho_\parallel$	μ_0	κ_σ	ρ_σ	$\mu_{0\sigma}$
Knee	2.0e4	2.0e3	2.0	2.0e2	2.0e1	9.9e1
Pelvis	2.0e4	2.0e3	2.0	2.0e2	2.0e1	9.9e1
Back	2.0e4	2.0e3	2.0	2.0e2	2.0e1	9.9e1
Head	2.0e4	2.0e3	2.0	2.0e2	2.0e1	9.9e1
Elbow	2.0e4	2.0e3	2.0	2.0e2	2.0e1	9.9e1
Wrist	2.0e4	2.0e3	2.0	2.0e2	2.0e1	9.9e1

Table 8.1: List of contact points with their parameters.

8.2.4 Simulation Experiments

We changed the angle between the seat and the seatback with different angular velocities. The changes in angle shall represent a repositioning from a lying position (0° seat angle) to a seated position (80° seat angle, see Figure 8.3). We varied the velocity of this repositioning process from 50 °/s to 500 °/s to investigate the effect of the movement velocity on the resulting internal forces. In addition to that, we varied the level of basic muscle stimulation $\bar{u}^{\text{open}}$ from 1% to 10% to investigate the influence of muscle co-contraction.

Using these variations of velocity and co-contraction level, we investigated three different levels of control model detail:

Level 1: Without feedback To investigate the contribution of the properties of the musculoskeletal system to the resulting movements and forces, we ran purely open-loop controlled simulations by switching off the feedback mechanisms ($k_p, k_d = 0$, see Figure 8.2). This means that the stimulation of every muscle is constant throughout the simulation experiment: $u_i(t) = \bar{u}^{\text{open}}$.

Level 2a: With feedback, unprepared Introducing feedback requires setting desired muscle fiber lengths $\boldsymbol{\lambda}(t)$. This tuning of the control target variable $\boldsymbol{\lambda}$ can be associated with setting the threshold of the stretch reflex.

The unprepared cognitive state is modeled by setting the desired muscle fiber lengths $\boldsymbol{\lambda}$ to the lengths corresponding to the position at the beginning of the repositioning movement ($t = 0\,\text{s}$). Due to the closed-loop part of the controller $\mathbf{u}^{\text{closed}}$, the muscles are then stimulated with the goal to maintain the starting position. Hence, this choice of desired values represents that the human is at rest and strives to maintain this resting position.

Experimental findings indicate that early voluntary activities start at around 100 ms after a perturbation (Kurtzer, 2015; Pruszynski and Scott, 2012; Weiler et al., 2016). Therefore, we assume that the human reacts to the imposed movement and adapts the reflex threshold lengths anticipating the repositioning. At 100 ms after the beginning of the movement, we set the desired muscle fiber lengths $\boldsymbol{\lambda}$ to the lengths corresponding to the position at the end of the movement. This can be seen as a switch of desired equilibrium positions from the starting to the target position once a human may become aware of the repositioning.

$$\boldsymbol{\lambda}(t) = \begin{cases} \mathbf{l}^{\text{CE,start}} & \text{for t} \leq 0.1\,\text{s} \\ \mathbf{l}^{\text{CE,end}} & \text{for t} > 0.1\,\text{s} \end{cases} .$$

Level 2b: With feedback, prepared The prepared cognitive state is modeled by using the muscle fiber lengths of the target position as desired values $\boldsymbol{\lambda}$ in the controller already at the beginning of the movement. So, the human is assumed to be aware of the upcoming repositioning process and adapts the reflex thresholds in accordance with the target position.

$$\boldsymbol{\lambda}(t) = \begin{cases} \mathbf{l}^{\text{CE,start}} & \text{for t} \leq 0\,\text{s} \\ \mathbf{l}^{\text{CE,end}} & \text{for t} > 0\,\text{s} \end{cases} .$$

All in all, the investigated variations are 6 different repositioning velocities, 3 levels of co-contraction, and 3 control model variants. We ran simulations for all of the 54 combinations of these variations and analyzed them below.

8.2.5 Data analysis

To investigate the influence of the repositioning velocity and model detail, we evaluate the internal muscle forces exemplary for the left hip extensor muscle at 100 ms after the beginning of the movement (Figure 8.4). We focus on this first part of the movement, because at a later point in time, voluntary reactions and higher-level feedback mechanisms come into play that are

not considered in our model. The hip extensor muscle is of particular interest in this movement as it is stretched with different velocities and is possibly overburdened.

8.2.6 Sensitivity analysis

The resulting muscle forces are influenced by the chosen model parameters, in particular the feedback gains in the control model (Equation (8.3)) and the parameters that describe the passive properties of the muscle are expected to have a big influence. To quantify this influence, we performed a local, first order differential sensitivity analysis (e.g., Dickinson and Gelinas, 1976; Morio, 2011; Rockenfeller, 2016, see also Stollenmaier et al. (2020b)).

To this end, both the feedback gains k_p and k_d, as well as the parameters describing the passive viscoelastic behavior of the muscle $l^{\mathrm{SEE},0}$,$\mathcal{L}^{\mathrm{PEE},0}$, D^{SDE}, and R^{SDE}, are varied one-at-a-time and the sensitivity of a scalar state variable to the chosen parameters is quantified.

We define the relative sensitivity coefficient as

$$S_{\mathrm{rel.}} \coloneqq \frac{\frac{f(x+\Delta)-f(x)}{f(x)}}{\frac{\Delta}{x}}\,, \tag{8.6}$$

a normalized formulation of the difference quotient of the state variable $f(x)$. The difference quotient is an approximation of the derivative of $f(x)$ in the direction of the parameter x for Δ small enough (e.g., Lehman and Stark, 1982). We set the relative change of a parameter x to $\Delta = 1 \times 10^{-3} \cdot x$, i.e. we perform a local sensitivity analysis without taking into account the physiological range of the parameters (Rockenfeller et al., 2015). The relative sensitivity is sometimes referred to as *elasticity* (ten Broeke, 2017). The advantage of the normalization is that the resulting sensitivity indicator is easier to interpret and more comparable between different cases or even across models (Rockenfeller et al., 2015; Scovil and Ronsky, 2006). Using this definition, the relative sensitivity indicates the percentage change in the state variable per percentage change in the parameter value. For example, a relative sensitivity $S_{\mathrm{rel.}} = 2$ indicates that a $m\%$ change of the input parameter x results in a $2m\%$ change of the output $f(x)$.

As scalar state variables f that describe the behavior, we chose two quantities that are also evaluated in Figures 8.4a and 8.4b: (a) To investigate the influence on the absolute muscle force, the muscle force of the left hip extensor in the closed-loop controlled movement is chosen. (b) The influence on the contribution of the feedback mechanism can be quantified by choosing the relative difference between the open- and closed-loop forces as state variable. For example when the force increases by 20% when including a feedback mechanism, the relative difference would be 0.2. In both cases, we look at the unprepared case with $\bar{u}^{\mathrm{open}} = 0.1$ at 100 ms after the beginning of the movement.

8.3 Results

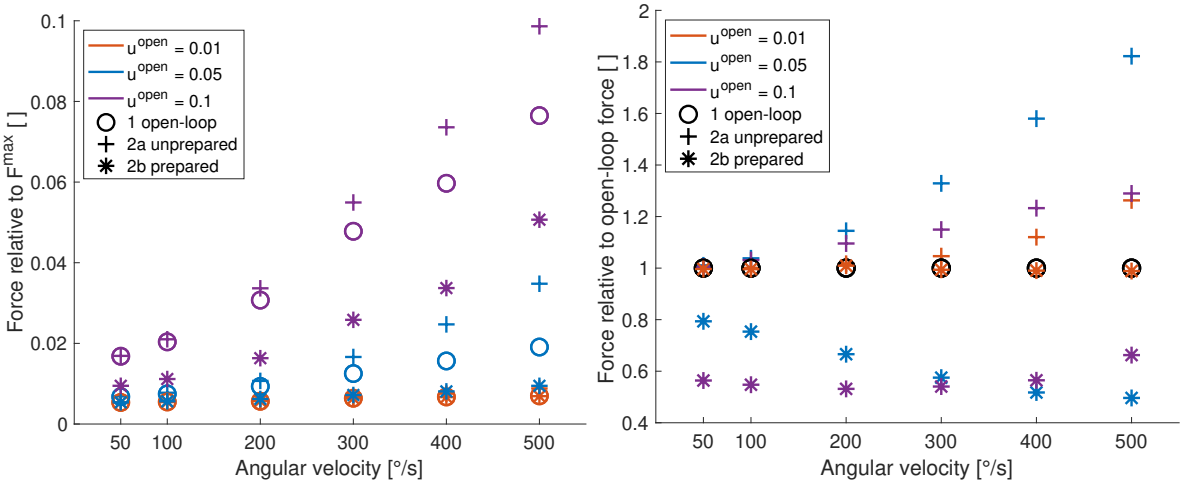

(a) Normalized muscle force

(b) Muscle force relative to the open-loop force

Figure 8.4: **Resulting internal muscle forces for the left hip extensor muscle for different repositioning velocities and modelling details at $t = 0.1\,\mathrm{s}$.** (a) Muscle force normalized by the muscle's maximal isometric force $F^{\max}$. (b) Muscle force relative to the open-loop force. This depiction emphasizes the feedback contribution to the muscle forces and shows that the unprepared case (2a) results in increased muscle forces, while the prepared case (2b) results in reduced muscle forces.

We evaluated the muscle forces normalized to their maximal isometric force and relative to the force that results from an open-loop controller and compared different levels of control model detail (Figures 8.4a and 8.4b). Our main result is that, at this evaluation time point, the muscle force increases when including feedback that represents an unprepared cognitive state (+) and decreases when the feedback parameters correspond to a prepared cognitive state (∗). The influence of these feedback representations becomes clearer when looking at the resulting forces relative to the open-loop forces (Figure 8.4b). For the lowest investigated co-contraction level ($\bar{u}^{\mathrm{open}} = 0.01$), the difference between the models with and without feedback is comparatively small. For the higher muscle tones, including feedback can increase or decrease the muscle forces compared to the open-loop case by a factor of approximately two for the unprepared and prepared cases, respectively. However, the relative force contribution of the feedback does not necessarily depend on the movement velocity, in particular for the prepared cases.

Looking at different repositioning velocities, the absolute force after 100 ms increases with the angular velocity of the movement for all cases (Figure 8.4a). Note that we look at the muscle forces at a fixed time for different movement velocities. Hence, the body is in different positions depending on the angular velocity. Consequently, the muscle fiber lengths and therefore the resulting forces differ both due to the force-length relationship of the muscles and the length-dependency of the feedback mechanism. As a result, the velocity dependence of the muscle force that is observed here is a combined consequence of both the length and the velocity dependency of both the muscle forces and the feedback mechanism. Evaluating the components of the muscle

stimulations (Figures 8.5a and 8.5b) and the muscle forces (Figures 8.5c and 8.5d) allows gaining further insight into the processes that are involved in the dependencies that can be observed in the muscle forces. With the chosen feedback gains, the contribution of the closed-loop part is rather small in the unprepared case (Figure 8.5a), while the contribution in the prepared case (Figure 8.5b) is larger. This difference can be attributed to the higher length-dependent feedback contribution in the prepared setting due to the higher discrepancy between the current and the desired muscle fiber lengths at the beginning of the movement. In the unprepared cases, the length-dependent feedback contribution $u^{\text{closed,l}}$ increases with the angular velocity of the prescribed movement while it decreases in the prepared case. The contribution of the velocity-dependent feedback $u^{\text{closed,v}}$ relative to the length-dependent feedback $u^{\text{closed,l}}$ increases with the angular velocity. The muscle output force F^{MTU} is a sum of the force acting in the serial elastic element F^{SEE} and the serial damping element force F^{SDE} (Figure 8.5c). The latter represents the passive damping force of the muscles. It is small and does not have a significant influence on the velocity dependency of the muscle forces. For the considered hip extensor muscle, the investigated movement is an eccentric movement as it is passively stretched during the repositioning process. Therefore, the muscle force depends only little on the velocity as the slope of the force-velocity curve in the eccentric area is comparatively small for fast velocities (see Haeufle et al. (2014b)).

Another relation that can be observed is that the resulting muscle force increases with the desired level of co-contraction $\bar{u}^{\text{open}}$ (Figure 8.4a).

8.3.1 Sensitivity analysis

Calculating the relative sensitivity, allows to quantify the influence of control and muscle parameters on the resulting muscle force (Figure 8.6a) and the contribution of the feedback mechanism (Figure 8.6b) . While the influence of the feedback parameters (k_p and k_d) is relatively small at this early stage of the movement, the predicted muscle force is more sensitive to the muscle parameters, in particular the parameters describing the damping properties of the muscle-tendon unit (D^{SDE} and R^{SDE}). Due to the velocity dependence of the damping force F^{SDE}, the sensitivity of the muscle force to the damping parameters increases with the angular velocity of the repositioning process. The parameter that determines the rest length of the parallel elastic element ($\mathcal{L}^{\text{PEE,0}}$) has zero influence on the result, as $l^{\text{CE}} < l^{\text{PEE,0}}$ and therefore $F^{\text{PEE}} = 0$ in the considered movement.

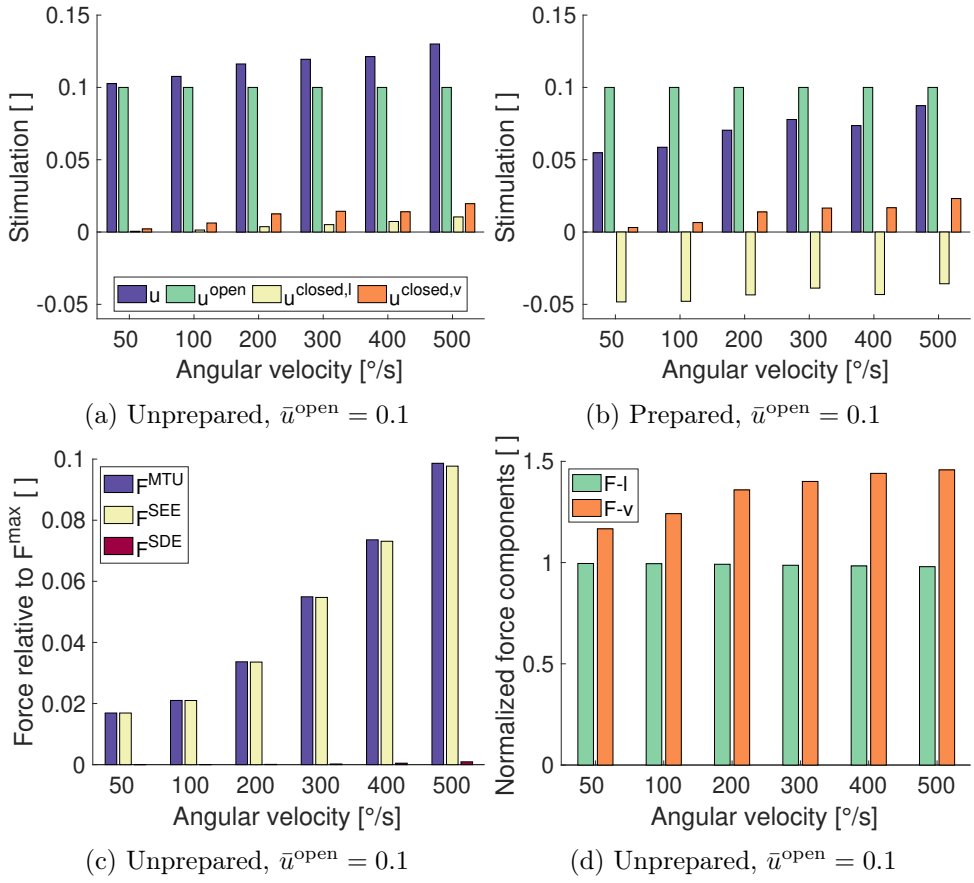

(a) Unprepared, $\bar{u}^{\text{open}} = 0.1$

(b) Prepared, $\bar{u}^{\text{open}} = 0.1$

(c) Unprepared, $\bar{u}^{\text{open}} = 0.1$

(d) Unprepared, $\bar{u}^{\text{open}} = 0.1$

Figure 8.5: **Components of the muscle stimulations and muscle forces for the left hip extensor muscle for different repositioning velocities and modelling details at $t = 0.1\,\text{s}$.** (a) and (b) Muscle stimulations for the unprepared and prepared cognitive state exemplary for $\bar{u}^{\text{open}} = 0.1$. (c) Components of the muscle forces and (d) normalized force-length (F-l) and force-velocity (F-v) components of the muscle force for the unprepared cognitive state exemplary for $\bar{u}^{\text{open}} = 0.1$. The F-l component is equivalent to F^{isom} in the muscle model. The normalized F-v component is calculated by setting $F^{\max}$, q and F^{isom} to 1 in the calculation of the F^{CE} force.

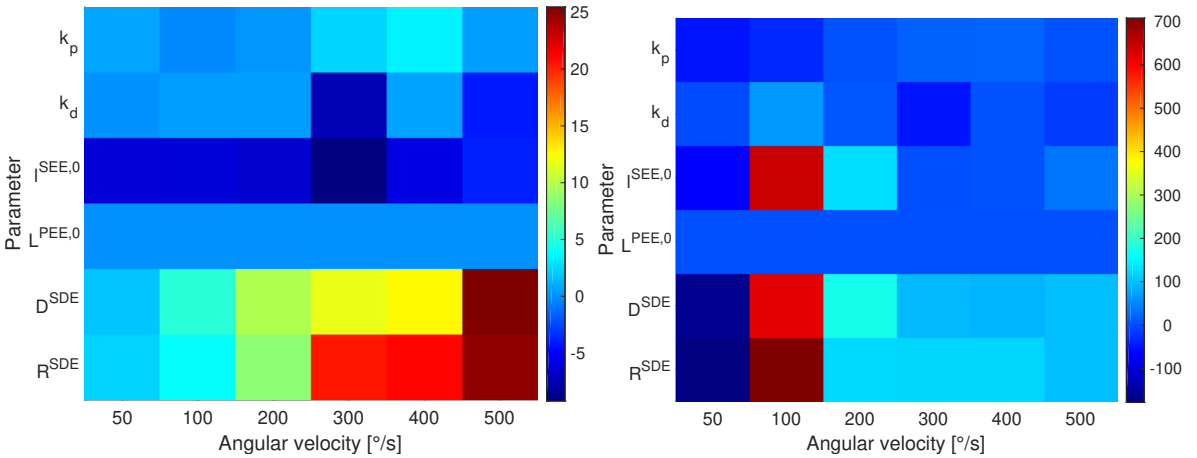

(a) Relative sensitivity of the muscle force

(b) Relative sensitivity of the contribution of the feedback mechanism to the muscle force

Figure 8.6: **Relative sensitivity** $S_{\text{rel.}}$ of (a) the left hip extensor muscle force and (b) the contribution of the feedback mechanism to the muscle force at $t = 0.1\,\text{s}$ with respect to changes of the feedback gains and the free parameters describing the viscoelastic properties of the muscle for different repositioning velocities. Each line represents one of the varied parameters.

8.4 Discussion

The main question we want to address is whether adding simple cognitive state modeling and how much the level of detail of neuronal modeling influence the predicted internal muscle forces dependent on the movement velocity in a repositioning process. To address this question, we looked at an exemplary, daily movement over a wide range of movement velocities. We compared the resulting muscle forces in the hip extensor muscle when neglecting proprioceptive feedback (case 1 open loop) with the results that include feedback with two different parameter sets representing different cognitive states (cases 2a unprepared and 2b prepared). Reflexes are a well-documented part of the neuro-muscular interaction in the generation of movement in the human body (e.g., Kurtzer et al., 2008; Schmit and Benz, 2002). However, for certain scenarios, they may not play a significant role and it may be justifiable to neglect them in model representations. Neglecting feedback in the model can have various advantages. For example, modeling the prepared feedback state as described above, requires knowledge about the target pose and configuration, even when investigating only the beginning of the movement. This also means that the model includes more parameters. For a multi-body model as used here, this is a manageable problem. For more complex models like finite element models, including more parameters and simulating the target position may be a considerable additional effort (Martynenko et al., 2017).

Our results show that the hip extensor muscle force including the reflex is higher when the human works against the movement, because of unforeseen repositioning, i.e. when the starting position is used as reference length for the muscle spindle reflex. When the human anticipates the repositioning and sets the reflex threshold towards the upcoming movement, e. g. forward bending, the reflex contribution to the muscle forces acts in the direction of movement and, as a result, the muscle forces are smaller than without the reflex contribution. Therefore, at the beginning of the movement, the hip extensor muscle forces decrease when including feedback (Figure 8.4a). This means that if the human is prepared and can tune its reflex thresholds accordingly, the resulting muscle forces might be smaller. So, our results indicate that a warning signal (e.g. sound or haptic signal) could decrease the injury risk in this particular muscle before the beginning of the movement. However, at the same time, the muscle forces increase with higher muscle co-contraction. Hence, when the human gets tenser and increases the muscular co-contraction due to a warning signal, this warning might have the opposite effect.

The cognitive state of the human depends on the device and the situation of the repositioning process. For example, when using a rehabilitation robot, the subject is aware of the process and can adapt their neuronal state accordingly, given that the respective neuronal function is intact. However, for the feedback parameters chosen here, the difference in muscle force due to altering repositioning velocities (and resulting positions) exceeds the difference due to changes in the reflex modeling.

In the case of high to very high repositioning velocities, for example in emergency situations in which the human has no time to prepare for the upcoming external perturbation, potential injury risk can be studied using a digital human model. One exemplary scenario could be a sleeping driver of a future autonomous car in a close-to-lying position. In this scenario, i. e. the autonomous intelligent artificial system *car* realizes a potential, upcoming crash within the next several milliseconds, the artificial system has to decide which next action is best to mitigate

injury risk of its occupants. Repositioning of the occupants to a more upright position might be one solution in this case. This contribution shows that only including the highest level of detail for the neuronal modeling allows for an appropriate assessment of the potential injury risk imposed by the interaction of the artificial and natural system. In our case, a muscle force criterion could be defined to evaluate whether the repositioning could be potentially harmful, for example, the ratio of actual muscle force and physiological maximum muscle force (Noelle et al., 2020).

As with most digital engineering approaches, using the presented modeling approach, not only muscle forces and muscle-related criteria can be investigated. It is further possible to assess other internal quantities like for example the kinematics for assessing typical movement ranges in collaborative workspaces with robots or kinetics to develop appropriate active exoskeletons on all body parts. This approach opens up the possibility towards integrating a human-centered design approach of many future artificial systems, which we foresee coming as pervasive augmentation in our daily life, very soon.

8.4.1 Limitations and assumptions

The control concept that we use is based on the assumption that the reflex threshold parameters are changed only once during the movement. However, especially for the slower movements, it is likely that the human adapts these parameters more often (potentially at about 5-9 Hz, (Gross et al., 2002)). In addition to that, for the reflex model, we assume that the human targets a resting position at all time ($\dot{\lambda}_i = 0$) and that the state at the target position (in particular muscle fiber lengths) are known such that the muscle spindle sensitivity can be tuned accordingly. Due to the chosen neuronal delay time of 50 ms, the model represents a long-latency proprioceptive feedback (R2 response (Scott, 2016)) that reacts to both stretch and shortening of the muscle. However, our formulation only includes the muscle-fiber-length- and contraction-velocity-dependent contribution to the long-latency feedback while neglecting other aspects. All considered movements have a duration that is longer than the reflex delay threshold of long-latency reflexes, so in a holistic investigation, also feedback mechanisms with longer time delay should be considered (e.g. visual feedback). This is of particular importance when the investigation is focused on the late parts of the movement.

In a previous study (Stollenmaier et al., 2020b), we investigated the neuro-muscular response to external perturbations using a musculoskeletal model of the arm in combination with the same control concept as used here. The resulting trajectories were in good agreement with results from human experiments. In this work, we transfer the same control concept to a full-body model in a different scenario. Since there are no experimental data available for this setting, we can not validate this control concept for the hip muscle in the considered scenario. For this reason, it is difficult to choose adequate feedback gain parameters. The choice in this contribution was therefore for a generic set of parameters. These parameters do affect the magnitude of the influence of the feedback loop (Figure 8.6b), but compared to the other parameters, their influence is small. Nonetheless, without validation of our model, we can not make absolute statements about the influence of proprioceptive reflexes on the internal forces in such a scenario. However, a comparison of the contribution for different velocities and cognitive states allows for insights into the relevant processes that are not experimentally accessible.

In addition to the feedback parameters, also other model parameters and assumptions in-

fluence the results. The choice of contact model between human and device and its model parameters change the system's behavior. Also, in the model, a multitude of muscles is represented by a smaller number of lumped substitute muscles (see Section 3.2.5) and the model of the skeleton is reduced to a limited number of necessary degrees of freedom. This method has the advantage that many cases can be investigated with little computing effort. However, the results are sensitive to the parametrization of these substitute muscles. For example, the maximum isometric force $F^{\max}$ scales the resulting muscle force and thus both $F^{\max}$ of the muscle in consideration and of its antagonist influence the behavior.

Due to the complexity of the system, we restricted the analysis presented here to one muscle (left hip extensor) at a fixed time. The result for the right hip extensor muscle is identical, because of the system's symmetry. Due to the evaluation at a fixed time, the body is in a different mechanical state depending on the movement velocity. However, in comparison with a time-based evaluation, this method has the advantage that the time-based controller is in the same state for all data points.

For the considered scenario, the hip extensor muscle is stretched and thus loaded eccentrically. The contraction dynamics are considered in the muscle model we use (Haeufle et al., 2014b), but recent findings on the behavior of muscles under eccentric loading conditions (Tomalka et al., 2017) as well as the possible role of short-range stiffness (De Groote et al., 2017; Nichols and Houk, 1976), or the effect of transversal loading (Siebert et al., 2014) are not considered. These new findings may influence the response originating from the muscles' passive characteristics.

9 | Transferring the control parameters of a multibody model to a finite element model

The hybrid equilibrium point control approach that we used in the chapters above has proven to be efficient for predicting human movements in combination with a multibody musculoskeletal model. However, for certain applications, the use of finite element (FE) models is more suitable. These applications include car crash simulations were the dynamics and deformation of the soft tissues play a significant role due to the fast movements. Therefore, a transfer of the same control approach to FE models would be beneficial. For the determination of the control parameters, however, the optimization paradigms that were proposed for multibody models are not feasible in finite element models due to the high computational cost of every simulation run. Hence, in this chapter, we describe an approach to transferring control parameters that were optimized for a multibody model to a finite element model.

Note that this chapter describes work in progress and parts of the content of this chapter have been published in Proceedings in Applied Mathematics and Mechanics (PAMM) (Martynenko et al., 2019).

9.1 Introduction

Finite element active human body models (FE aHBMs) are used for the design and testing of vehicle safety systems as they allow for the analysis of an occupant's voluntary motion during different phases of crash simulation. Primarily, they are used for simulations of the pre-crash phase of an accident where the influence of the active movements of occupants is significant. Such models are capable of accounting for dynamic human behavior and reflexes by incorporating bio-inspired muscle controllers. For this forward-dynamic modeling of active behavior, the stimulations of hundreds of muscles need to be determined for every time step before running the simulation. The determination of these muscle stimulations is, however, nontrivial due to the highly nonlinear relationship between muscle stimulations and body motion and the redundant assembly of the muscles. Tuning these parameters using an optimization algorithm that requires multiple runs of the FE model is computationally expensive and requires a tremendous amount of run time. As run time is an essential element in the research and development process of a new vehicle, we instead propose a method to perform all calculations that are required to determine the controller parameters on a reduced multibody model and to then transfer these parameters to the fully deformable FE model.

9.2 Methods

9.2.1 Musculoskeletal model

To demonstrate the applicability of the proposed approach, the right upper extremity from the 50th percentile male THUMS v.5 FE model (Iwamoto et al., 2015) was extracted, simplified and transformed into a multibody model in LS-DYNA® (Figure 9.1). This multibody model was then actuated by six lumped muscles modeled with an extended Hill-type material (Haeufle et al., 2014a; Kleinbach et al., 2017) and activation dynamics as introduced by Hatze (1977). The resulting arm model is very similar to the *Arm26* model described in Section 3.2.4. Therefore, the muscle parameters from *Arm26* were used. However, unlike *Arm26*, the THUMS model represents a 50th percentile male. Therefore, we scaled all length-dependent quantities to the segment lengths of the THUMS model.

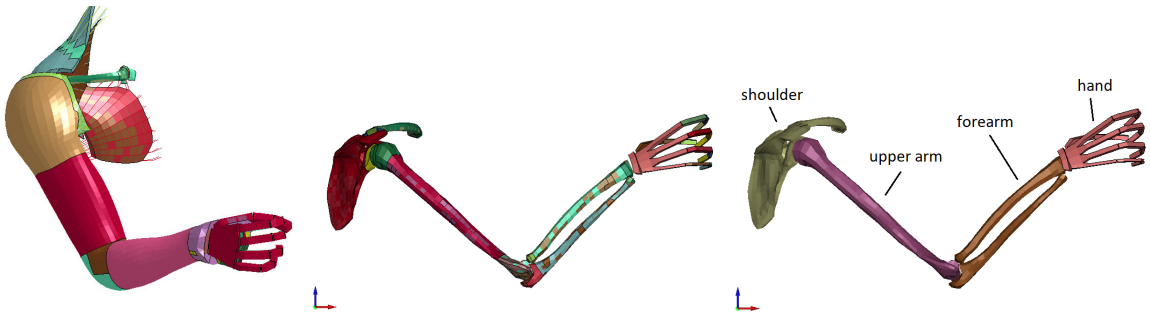

(a) Full FE model with soft tissue (b) FE model with deformable bones (c) Multibody model with rigid bones

Figure 9.1: **The upper extremity model from the THUMS v.5 active human body model (Iwamoto et al., 2015): transformation steps from the full finite element model to a multibody model.** (a) Isolated FE arm model with soft tissues, (b) FE model with deformable bones consisting of various materials after removing the soft tissues and (c) multibody model with bones made from rigid material.

9.2.2 Hybrid equilibrium point controller

The same control approach as described in Section 3.3 was used to determine the muscle stimulations. It is based on the hypothesis that voluntary movements are generated by switching between stable equilibrium points. The stimulation $u_i(t)$ for each muscle i is calculated as

$$\begin{aligned} u_i(t) &= \left\{ u_i^{\text{open}}(t) + u_i^{\text{closed}}(t) \right\}_0^1 \\ &= \left\{ u_i^{\text{open}}(t) + \frac{k_p}{l_i^{\text{CE,opt}}} \left(l_i^{\text{CE}}(t-\delta) - \lambda_i(t) \right) + \frac{k_d}{l_i^{\text{CE,opt}}} \left(\dot{l}_i^{\text{CE}}(t-\delta) \right) \right\}_0^1 , \end{aligned} \tag{9.1}$$

Note that in comparison with the general formulation in Section 3.3, the desired contraction velocity was set to $\dot{\lambda}_i(t) \equiv 0$ for all i to model point-to-point movements between two EPs.

The desired muscle fiber lengths λ_i are set to the muscle fiber lengths l_i^{CE} in the equilibrium positions.

9.2.3 Determination of the control parameters

Optimization algorithms Using the multibody model, the open-loop muscle stimulations for each equilibrium position (EP) can be optimized such that the net joint torques are equal to zero, meaning the system is in stable equilibrium in this position. An optimal set of muscle stimulations can then be determined by minimizing the sum of all muscle stimulations. Once all control parameters are determined using the multibody model, they can be transferred to the FE model with the goal to obtain the same equilibrium points.

Machine learning approaches An alternative to optimizing the muscle stimulations using the aforementioned optimization paradigm is to use machine learning approaches as, for example, reinforcement learning (Iwamoto et al., 2012). Additionally, previous work showed that an approach based on a combination of neural networks and sequential quadratic programming (SQP) can be used to learn the relationship between muscle stimulations and resulting equilibrium positions (Driess et al., 2018). They used an arm model that was implemented in the C/C++ multibody simulation code *demoa* that is very similar to *Arm26* and found that the dynamics of the musculoskeletal structure simplify the learning task if treated properly. As part of a student project, the scalability of this neural network approach to the 50th percentile model (Figure 9.1), to a model with two additional muscles and one additional degree of freedom and to a finite element model was explored (Endler, 2019). These investigations are part of a manuscript that is being worked on at the moment.

9.3 First results and discussion

To investigate the transferability of the muscle stimulations optimized or learned for a multibody model to the FE model, three target positions were chosen on a horizontal line. Using the multibody model in combination with a neural network, the muscle stimulations required for the multibody model to reach these positions are optimized and then applied to the FE model. In doing so, the comparability of these models and the influence of the soft tissue on the movement can be assessed.

The results indicate that given the constant muscle stimuli, the finite element model reaches stable equilibrium positions (Figure 9.2). However, the reached end positions differ between the multibody and the FE model (Table 9.1). Also, the end positions in z-direction differ between the movements to the three target points which should not be the case as positions on a horizontal line are targeted (the different end position of the multibody model in z-direction for the left position in comparison to the other two positions originates from an error in the neural network). These results show that in the current state of the models, the control parameters optimized or trained on the multibody model can not be used to reach the same positions with the finite element model. Therefore, further adaptations of the multibody model to the more complex finite element model are necessary. The differences might originate in differences in joint modeling as the multibody model, for example, does not consider damping effects due

to friction or tissue deformation. Also, the oscillations that have been observed in the first simulation seconds of the FE model need to be addressed (Figure 9.2b).

	FE results, x [mm]	FE results, z [mm]	MB prediction, x [mm]	MB prediction, z [mm]
left	373.9665	-27.2872	330.5659	-29.7908
mid	403.3229	-60.0191	385.4500	-11.1599
right	421.2955	-72.3742	435.8158	-11.1910

Table 9.1: **Actual positions that are reached by the FE arm model and predictions by the multibody model for the three targeted positions (left, middle, right).** This table was taken from Endler (2019) with kind permission from the author.

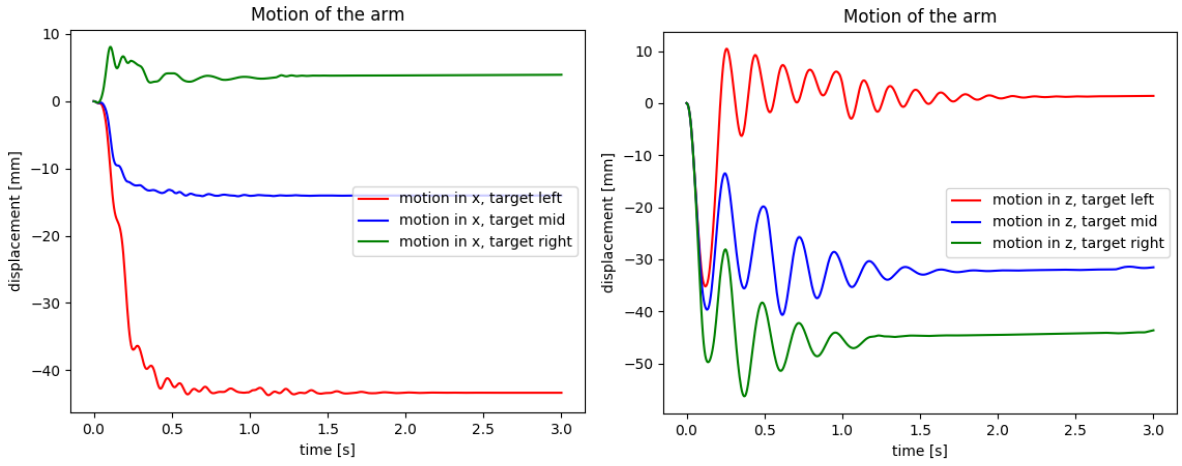

(a) Displacement in x-direction.

(b) Displacement in z-direction (axis of gravitiy).

Figure 9.2: **Displacement from the initial position of the FE model that uses muscle stimulations that were optimized using the multibody model.** Three positions are targeted (left, middle, right). These figures were taken from Endler (2019) with kind permission from the author.

10 | Conclusions and future work

10.1 Summary of the results

The goal of the projects described in this thesis was to use neuro-musculoskeletal models as a tool to study concepts of biological motor control and the role of the muscles therein. In Chapter 4, we showed that our musculoskeletal arm model is capable of validly predicting the response to both static and dynamic mechanical perturbations with one set of basic parameters (Figures 4.5 and 4.7). The considered single-joint point-to-point movement was controlled by a bio-inspired hybrid equilibrium point controller that considers muscle-tendon based stretch reflexes. This implemented feedback mechanism, however, had only little influence as the mechanical zero-time delay response elicited by the muscle characteristics compensated for the perturbations to a large extend (Figures 4.6 and 4.8). While being a useful tool to test motor control theories, this model provides the necessary level of detail to allow for the investigation of internal forces, including muscle-bone contact forces and joint loadings (Figure 4.9). Therefore, we consider this model to be a good starting point for further investigations of research questions where motor control and ergonomics issues overlap, for example for the development of assistive devices.

The study described in Chapter 5 took a first step in this direction. It used the same arm model and control approach as in the study described above, however, in this case, two-degree-of-freedom movements were investigated. A neuronal perturbation was introduced in the control scheme, leading to an overshooting behavior (hypermetria) as it can be observed in the movements of patients with cerebellar ataxia or other neurological movement disorders (Figure 5.3). This perturbation is implemented as a mismatch between the motor command and the initial conditions. In the same study, we simulated an assistive torque, as it could be applied by a simple wearable assistive device, to compensate for the overshooting behavior. Our results indicate that simple mechanical or low-level controlled devices might be sufficient to reduce unwanted hypermetria (Figures 5.4 and 5.5). Such simple devices might be relevant in particular in the early phase of clinical symptoms where the movement coordination may be improved by relatively small assistive forces. We performed this simulation using our musculoskeletal model and an equivalent torque-driven arm model. We found that the predicted torques and powers that are necessary to compensate for the overshoot can differ by a factor of more than 10 between the musculoskeletal model and the torque-driven model. Therefore, the magnitude of torque and power required to reduce hypermetria by simple wearable assistive devices may be significantly underestimated if muscle-tendon characteristics are not considered in the model that is used for the design of the device.

Both the results in Chapter 4 (Figures 4.6 and 4.8) and Chapter 5 (Figures 5.4 and 5.5) indicated that the musculoskeletal structure and thus the morphology majorly contribute to

the resulting movement. Therefore, in Chapter 6, the concept of quantifying morphological computation allowed us to characterize this contribution using an information entropy-based approach. We applied this concept on different levels on the neuronal control hierarchy for goal-directed and oscillatory arm movements with two degrees of freedom. We found that morphological computation is highest for the most central level of modeled control hierarchy (movement initiation and timing) and decreases for the lower levels (Figure 6.5). These results indicate that the lower levels of control (including the model of muscle and activation dynamics) make important contributions to the control. In particular, the muscle stimulation input exploits the muscles' biochemical and biophysical characteristics to generate smooth dynamic movements. Hence, these results confirm our observations in the other studies, where a simple control signal that contains only little information was sufficient to generate a smooth movement and the muscle characteristics stabilized the movement in the presence of external perturbations.

As we were interested in the further investigation and testing of our control concept, in Chapter 7, we developed a framework that combines three methods that all have their assets and drawbacks: measuring kinematic data in human experiments and reproducing these movements in both numeric computer simulations and a biologically inspired robotic system. We proposed a mathematical model and a biorobot that include the necessary level of physiological detail to investigate control concepts that explicitly rely on the muscular non-linear viscoelastic characteristics. Our results showed that the same bio-inspired hybrid equilibrium point controller can be used to reproduce goal-directed human movements in both the robot and the computer simulations (Figure 7.5). Only three equilibrium positions were necessary to reproduce the dynamic human movement in the shoulder and elbow joints. This successful transfer to the robotic system shows that our controller is robust against changes in the system dynamics, friction, and natural variance and can be well-performing in real-world physical conditions.

In Chapter 8, we applied the same control concept to a more complex, whole-body musculoskeletal model with much more muscles and degrees of freedom. As in the other studies, we were interested in the contribution of the musculoskeletal system to the control. Here, we looked at the contribution of the stretch reflex to the muscle forces during an active external repositioning of the hip joint for a large range of movement velocities and different cognitive states. We found that in the presented setting, the predicted relative force contribution of the feedback mechanism is not negligible, especially for high movement velocities (Figure 8.4). Also, we found that the muscular force increases when modeling feedback representing an unprepared cognitive state and decreases for the prepared case. So, the cognitive state might have an influence on the muscle-force related injury risk.

Applying our control model to a finite element (FE) model, in Chapter 9, we discussed the possibility to use control parameters that were optimized for a multibody model for the control of a more complex FE model. First results indicated that our models were not similar enough for a direct transfer of the control parameters (Table 9.1). However, the emergence of equilibrium positions in the FE model (Figure 9.2) promises that our control approach is applicable to the FE model and it might be possible to transfer the control parameters if the multibody model is further adapted to the FE model.

In summary, our results show that the biochemical and biophysical properties of the musculoskeletal system significantly contribute to the resulting movements as the muscle-tendon structures compensate for external perturbations to a large extent, stabilizing the movement.

Additionally, a piecewise constant feed-forward signal that contains only little information is sufficient to generate information-rich smooth movement trajectories. This observation has been confirmed when we quantified this contribution using the concept of quantifying morphological computation. Therefore, it is important to take into account the intrinsic properties of the muscles when modeling human movements, in particular in the presence of external perturbations as, for example, for the design of technical assistive devices. Nevertheless, not only the open-loop muscle stimulations determine the movement. While including a model of proprioceptive feedback had only little influence for small perturbations, it significantly affected the results for high externally imposed movement velocities.

10.2 Future work and first steps in these directions

In my point of view, future work following this project would include further steps in the direction of reproducing and understanding the impaired movements of patients with neurodegenerative movement disorders or other pathological conditions. To this end, it is necessary to reproduce these impaired movements in computer simulations. A first step could be to try to use the existing optimization paradigms to optimize the control parameters in order to reproduce the impaired trajectories. The resulting parameters for healthy and diseased movements could then be compared to try to draw conclusions about possible causes for dysmetria or other impairments. The necessary next step would then be to find a systematic way to perturb the neuronal controller to reproduce the impaired movements and also the variability observed in many patients' movements (Topka et al., 1998a). We tested one approach to this in Chapter 5 where we generated hypermetria in the computer simulation by introducing a mismatch between the motor command and the initial conditions. This mismatch can be interpreted as a misestimation of the current state of the system by the neurological structures that are responsible for the generation of the motor command. In this study, the initial co-contraction was increased after the optimization of the control parameters, leading to a discrepancy between the motor command and the actual conditions. Testing other kinds of perturbations of the initial conditions was the task in a student project that I co-supervised (Rist, 2020). Both an increase and decrease of the initial muscular co-contraction and of a simulated weight in the hand were tested, representing a misestimation of the muscle co-contraction at the beginning of the movement or lifting an unknown weight with the hand. Since these settings led to impaired movements similar to observations in patients (Figure 10.1), it could be the basis of further investigations of the causes of their movement disorders.

One hypothesis for the physiological processes involved here would be that the cerebellum finetunes the descending motor command based on its current estimation of the system's state (e.g., initial muscle co-contraction, the weight of the arm and manipulated objects, fatigue, interaction with the environment). Therefore, a false estimation of the state would lead to an impaired motor command and, consequently, an impaired movement. Since the system's state changes constantly, this misestimation might also be the origin of the observed variability. As mentioned before, internal models in the cerebellum might be involved in the generation of the motor commands, for example for the selection and timing of EPs (see Section 3.3). Herein, the choice of the internal model that is appropriate for the current setting might be based on an estimate of the current state, leading to a flawed selection of motor commands if the estimate

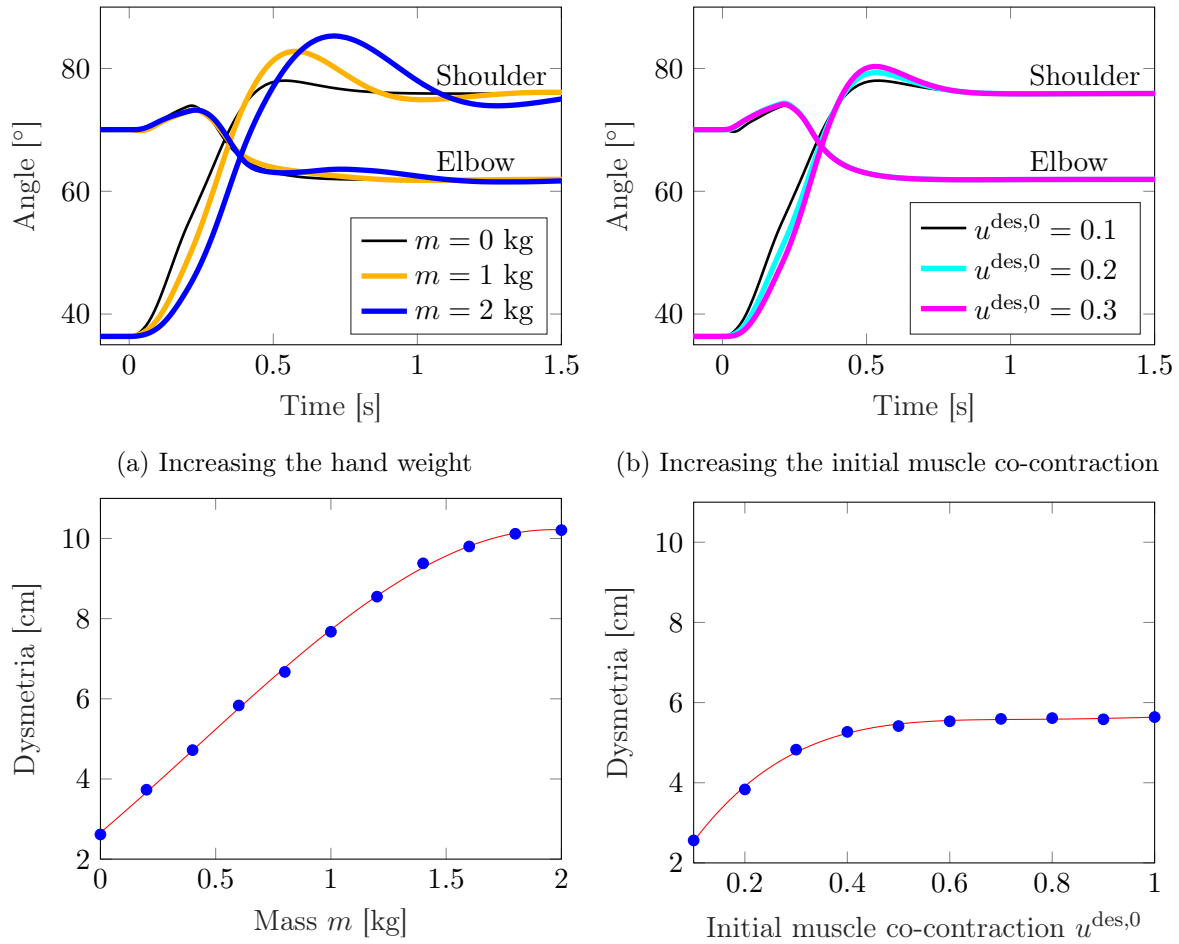

(a) Increasing the hand weight

(b) Increasing the initial muscle co-contraction

(c) Increasing the hand weight

(d) Increasing the initial muscle co-contraction

Figure 10.1: **Joint angle trajectories for different perturbations of the initial conditions after optimizing the control parameters.** Both (a) increasing the hand mass, representing lifting an unknown weight, and (b) increasing the initial muscle co-contraction leads to an overshooting behavior. This dysmetria is measured for a large range of perturbations in (c) and (d), showing that there seems to be an asymptotic behavior for large changes. The control parameters for all of these perturbations were optimized for a co-contraction level of 0.1 with 0 kg weight in the hand. These figures were taken and adapted from the student thesis of Ilka Rist (Rist, 2020) with kind permission from the author.

is not correct (see Figure 10.2).

Another aspect that can be observed in humans is the adaptation to perturbations (Albert and Shadmehr, 2017; Shadmehr et al., 2010; Yang et al., 2007). Therefore, when modeling the reaction to external perturbations or unforeseen physical conditions (e.g., the weight of a manipulated object), these adaptation processes need to be taken into account, in particular, when longer-term effects are studied. For example, an iterative optimization approach could

be used to represent adaptation in a mathematical model. These adaptation processes are of particular interest for the investigation of neurological disorders, as either the adaptation itself or the signals it is based on might be disturbed in the patients' nervous system (Maschke et al., 2004). A flawed adaptation process might be another reason for the variability that is observed in patients.

Besides investigating possible origins and pathological processes that are involved in movement disorders, another important advance to help the patients is the development of technical assistive devices for the compensation of their disorders or rehabilitation devices that can help them to re-gain or improve physical or cognitive function (Siciliano and Khatib, 2016). For example, our first tests in computer simulation showed that simple mechanical devices might be capable of reducing hypermetria to an extent that is present in unimpaired movements (Chapter 5). Implementing such a device as a prototype in the real-world and testing it in experimental studies with humans might give further insights into the usability of such a simple appliance. For example, simple springs or dampers could be tested or a corrective torque might be applied by an electric motor based on the measured initial velocity.

For all of these investigations, it would be helpful to extend the existing arm model to more degrees of freedom, such that more movements that are relevant in everyday life can be reproduced. Alternatively, one could resort to other existing models and adapt them such that they fulfill the criteria that we pose on our models. In addition, the physiological accuracy of the control model could be improved. In its current formulation, our control model includes proprioceptive feedback based on the assumption that the muscle spindles provide direct feedback on the muscle fiber lengths and contraction velocities. However, as our model reacts to both stretch and shortening of the muscle fibers, it does not seem to be an accurate representation of the natural muscle spindle feedback which is only sensitive to the muscle's local stretch (Kurtzer et al., 2014). Additionally, recent findings indicate that the muscle spindle afferents are rather force-dependent than directly encoding muscle fiber lengths and velocities (Blum et al., 2017). Furthermore, more detailed representations of the underlying processes in muscle spindle feedback (Mileusnic et al., 2006) would, for example, allow for the analysis of α-γ co-activation (Lan and Zhu, 2007; Lan and He, 2012; Li et al., 2015). In addition to that, our models neglect other types of proprioceptive feedback, for example from the tension-sensitive Golgi tendon organs (Kistemaker et al., 2013; Mileusnic and Loeb, 2006). Another critical assumption in the control model is the neuronal time delay. The choice of this time delay influences the interpretation of the feedback mechanism on the neuronal control hierarchy. We tested both short- and long-latency versions of the implemented stretch reflex. The short-latency implementation (25 ms delay) represents a simplified model of the spinal, mono-synaptic muscle spindle reflex (Pruszynski and Scott, 2012; Weiler et al., 2019). However, as mentioned above, our model does not accurately reflect the natural muscle spindle feedback. Therefore, modeling a long-latency reflex (50 ms delay) that includes supraspinal influences seemed more appropriate. However, we consider only the muscle-fiber-length- and contraction-velocity-dependent part of the long-latency feedback and neglect other aspects and longer-latency feedback mechanisms as, for example, visual feedback. Including visual feedback, the impaired eye-hand coordination that was observed in patients with cerebellar ataxia (Hemmers, 2018) could be investigated. In a student project, our arm model was used with an open-loop controller in combination with a model of visual feedback (Inoue, 2019). With six EPs, it was possible to simulate a scenario where a ball is thrown and caught in the sagittal plane. Also, the influence of motor noise was

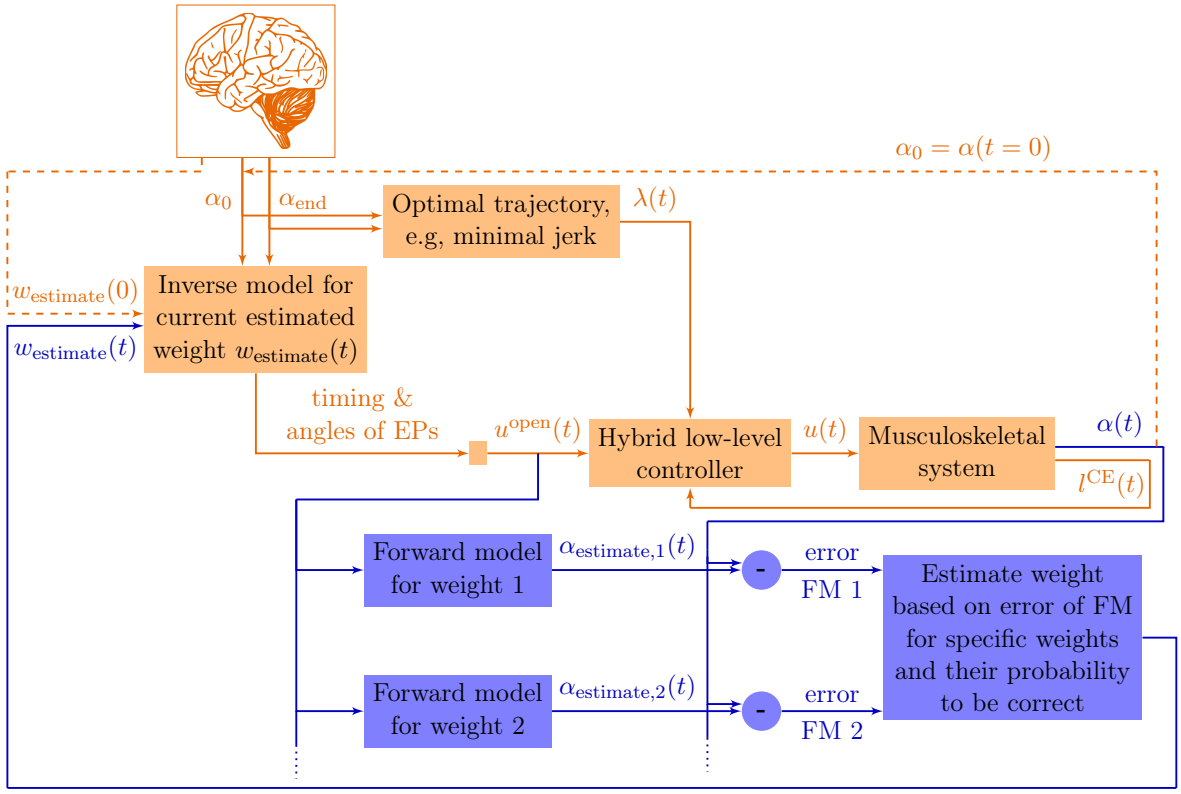

Figure 10.2: **One hypothesis how the cerebellum could be involved in the generation of movement in our control model formulation, shown with the example of lifting an unknown weight on a desired trajectory.** Based on the information about the current position α_0, the desired end position α_{end} and an initial estimate of the weight $w_{\text{estimate}}(0)$, an inverse model is selected. This inverse model is possibly located in the cerebellum. The outputs of this inverse model are desired EP angles and the timing of these EPs. Based on this information, muscle stimulation signals over time $u^{\text{open}}(t)$ can be composed. Using the starting and end position α_0 and α_{end}, an optimal trajectory is determined as part of the movement planning and is used as reference values $\lambda(t)$ in the feedback part of the hybrid low-level controller. At the same time, various forward models (FMs) use an efference copy of the open-loop motor command to predict the movement for different weights. This parallel execution of several internal models is inspired by the work of Haruno et al. (2001); Wolpert and Kawato (1998). Based on the errors between these estimated trajectories $\alpha_{\text{estimate}}(t)$ and the actual trajectory $\alpha(t)$ and the probability for each forward model to be correct, an updated guess for the estimated weight $w_{\text{estimate}}(t)$ is used to update the choice of inverse model. Note that this figure is a visualization of our thoughts with the purpose of being a possible basis for future work.

investigated with the result that the catching performance decreased with higher noise levels. Based on this work, both the inclusion of visual feedback and motor noise could be further investigated, also for different kinds of movements and in combination with other feedback mechanisms.

In their current state, the aforementioned musculoskeletal and control models are based on assumptions and have their limitations that are discussed in detail in the chapters above. In addition to the limitations named in the last section, for example, the so far neglected dynamics of soft tissues could be included in form of wobbling masses (Gruber et al., 1998) as they have a damping effect for high velocities (Denoth et al., 1985; Schmitt and Günther, 2011) and, therefore, without them unphysiologically high forces might occur. Also, multi-scale models that include more details of the microscopic processes in the relevant neuronal structures would be preferable (Elias et al., 2018; Kandel et al., 2013). However, computer simulations using mathematical models are always a trade-off between modeling and computational effort and scientific benefit. Reducing the models to the most relevant processes can even have the advantage that it is easier to investigate the causal relations between the structures. Also, not all of the limitations of the models limit the conclusions one can draw from the studies.

For the determination of motor commands for a large range of desired movements, an alternative to the computationally expensive optimization algorithms that we used above could be to optimize the control parameters only for selected trajectories and then "interpolate" movements in between (or even "extrapolate" outlying movements) using a support vector regression model or a similar machine learning approach. First tests of applying support vector regression in the prediction of motor commands were performed in form of a student project for one-degree-of-freedom arm movements (Li, 2019). The successful prediction of the timing and amplitude of motor commands for some unlearned movements (different start/end position or different weight of the arm) based on previously optimized, learned movements indicates that this approach could be used as an efficient alternative to the optimization paradigms. One could even hypothesize that an internal model in the nervous system might use a similar approach. An alternative approach to determining muscle stimulations for desired movements (or at least a first guess) might be to approximate the inverse of a multibody musculoskeletal model by approximating the inverse of single functional units, for example the activation dynamics or parts of the muscle model. The feasibility of this approach, however, would need to be tested.

10.3 My conclusion

I consider the work that is presented in this thesis an important step towards the comprehension of the processes underlying the generation of healthy and pathologically impaired human movements. Our results showed that it is important to take into account the properties of the musculoskeletal system when modeling human movement as they significantly contribute to the movement. Therefore, computer simulations using a combination of a physiologically well-founded biomechanical and biochemical model of the musculoskeletal system with biologically inspired concepts of motor control have proven to be a useful tool. Complemented with human experiments and biorobotic systems, this approach promises to allow for the formulation and investigation of all sorts of hypotheses, hopefully leading to new insights from which people suffering from motor disorders can benefit.

References

Adient Ltd. & Co. KG. Autonomous driving in the car seat of the future / IAA 2015: Johnson Controls reveals response to the autonomous driving megatrend. Technical report, Adient Ltd. & Co. KG, 2015.

Adient Ltd. & Co. KG. Adient showcases passenger protection for autonomous-driving vehicles, 2018.

Aguirre, A., Tejera, G., and Baliosian, J. Imitation for motor learning on humanoid robots. In *2017 Latin American Robotics Symposium (LARS) and 2017 Brazilian Symposium on Robotics (SBR)*, pages 1–6. IEEE, 2017.

Aisen, M. L., Arnold, A., Baiges, I., Maxwell, S., and Rosen, M. The effect of mechanical damping loads on disabling action tremor. *Neurology*, 43(7):1346–1346, 1993.

Al Borno, M., Hicks, J. L., and Delp, S. L. The effects of motor modularity on performance, learning and generalizability in upper-extremity reaching: a computational analysis. *Journal of the Royal Society, Interface*, 17(167):20200011, 2020.

Albert, S. T. and Shadmehr, R. Estimating properties of the fast and slow adaptive processes during sensorimotor adaptation. *Journal of Neurophysiology*, 119:jn.00197.2017, 2017.

Albu-Schäffer, A., Eiberger, O., Grebenstein, M., Haddadin, S., Ott, C., Wimbock, T., Wolf, S., and Hirzinger, G. Soft robotics. *IEEE Robotics & Automation Magazine*, 15(3):20–30, 2008.

Alexander, R. M. N. A minimum energy cost hypothesis for human arm trajectories. *Biological Cybernetics*, 76(2):97–105, 1997.

Anderson, F. C. and Pandy, M. G. Dynamic Optimization of Human Walking. *Journal of Biomechanical Engineering*, 123(5):381, 2001.

Anh, H. P. H. and Ahn, K. K. Hybrid control of a pneumatic artificial muscle (pam) robot arm using an inverse narx fuzzy model. *Engineering Applications of Artificial Intelligence*, 24(4): 697–716, 2011.

Aumüller, G., Aust, G., Engele, J., Kirsch, J., Maio, G., and Mayerhofer, A. *Duale Reihe Anatomie*. Thieme-Verlag, 2017.

Ay, N. and Löhr, W. The umwelt of an embodied agent—a measure-theoretic definition. *Theory in Biosciences*, 134(3):105–116, 2015.

Ay, N. and Zahedi, K. On the causal structure of the sensorimotor loop. In Prokopenko, M., editor, *Guided Self-Organization: Inception*, volume 9 of *Emergence, Complexity and Computation*. Springer, 2014.

Bayer, A., Schmitt, S., Günther, M., and Haeufle, D. F. The influence of biophysical muscle properties on simulating fast human arm movements. *Computer Methods in Biomechanics and Biomedical Engineering*, 20(8):803–821, 2017.

Belli, A., Kyröläinen, H., and Komi, P. V. Moment and power of lower limb joints in running. *International Journal of Sports Medicine*, 23(2):136–141, 2002.

Berniker, M., Jarc, A., Bizzi, E., and Tresch, M. C. Simplified and effective motor control based on muscle synergies to exploit musculoskeletal dynamics. *Proceedings of the National Academy of Sciences*, 106(18):7601–7606, 2009.

Bernstein, N. A. *The Coordination and Regulation of Movements*. Oxford, New York, Pergamon Press, 1967.

Berret, B., Chiovetto, E., Nori, F., and Pozzo, T. Evidence for composite cost functions in arm movement planning: An inverse optimal control approach. *PLoS Computational Biology*, 7 (10), 2011.

Bhanpuri, N. H., Okamura, A. M., and Bastian, A. J. Predicting and correcting ataxia using a model of cerebellar function. *Brain*, 137(7):1931–1944, 2014.

Biewener, A. A. and Roberts, T. J. Muscle and tendon contributions to force, work, and elastic energy savings: a comparative perspective. *Exercise and sport sciences reviews*, 28(3):99–107, 2000.

Bizzi, E., Hogan, N., Mussa-Ivaldi, F. A., and Giszter, S. Does the nervous system use equilibrium-point control to guide single and multiple joint movements? *Behavioral and Brain Sciences*, 15(04):603–613, 1992.

Blickhan, R., Seyfarth, A., Geyer, H., Grimmer, S., Wagner, H., and Günther, M. Intelligence by mechanics. *Philosophical Transactions of the Royal Society of London, Series A*, 365 (1850):199–220, 2007.

Blum, K. P., Lamotte D'Incamps, B., Zytnicki, D., and Ting, L. H. Force encoding in muscle spindles during stretch of passive muscle. *PLoS Computational Biology*, 13(9), 2017.

Boblan, I., Bannasch, R., Schwenk, H., Prietzel, F., Miertsch, L., and Schulz, A. A Human-Like Robot Hand and Arm with Fluidic Muscles: Biologically Inspired Construction and Functionality. In *Embodied Artificial Intelligence*, pages 160–179. Springer, Berlin, Heidelberg, 2004.

Boblan, I., Bannasch, R., Schulz, A., and Schwenk, H. *A Human-like Robot Torso ZAR5 with Fluidic Muscles: Toward a Common Platform for Embodied AI*, pages 347–357. Springer-Verlag, Berlin, Heidelberg, 2007.

Bossomaier, T., Barnett, L., Harré, M., and Lizier, J. T. *An Introduction to Transfer Entropy.* Springer, 2016.

Brändle, S., Schmitt, S., and Müller, M. A. A systems-theoretic analysis of low-level human motor control: application to a single-joint arm model. *Journal of Mathematical Biology*, 2020.

Brochu, E., Cora, V. M., and de Freitas, N. A Tutorial on Bayesian Optimization of Expensive Cost Functions, with Application to Active User Modeling and Hierarchical Reinforcement Learning. *arXiv preprint arXiv:1012.2599*, 2010.

Brown, I. E., Scott, S. H., and Loeb, G. E. Preflexes—programmable high-gain zero-delay intrinsic responses of perturbed musculoskeletal systems. *Society of Neuroscience, Abstracts*, 21:562, 1995.

Brown, I. E., Scott, S. H., and Loeb, G. E. Mechanics of feline soleus: II. Design and validation of a mathematical model. *Journal of muscle research and cell motility*, 17(2):221–33, 1996.

Büchler, D., Guist, S., Calandra, R., Berenz, V., Schölkopf, B., and Peters, J. Learning to Play Table Tennis From Scratch using Muscular Robots. *arXiv preprint arXiv:2006.05935*, 2020.

Burdet, E., Tee, K. P., Mareels, I., Milner, T. E., Chew, C. M., Franklin, D. W., Osu, ·. R., and Kawato, ·. M. Stability and motor adaptation in human arm movements. *Biological Cybernetics*, 94(1):20–32, 2006.

Buschmann, T., Lohmeier, S., Kühnlenz, K., Buss, M., Ulbrich, H., and Pfeiffer, F. LOLA - a Performance Enhanced Humanoid Robot (LOLA - ein leistungsgesteigerter humanoider Roboter). *IT - Information Technology*, 49(4):218–223, 2007.

Campos, F. and Calado, J. Approaches to human arm movement control—A review. *Annual Reviews in Control*, 33(1):69–77, 2009.

Casellato, C., Pedrocchi, A., Garrido, J., Luque, N., Ferrigno, G., D'Angelo, E., and Ros, E. An integrated motor control loop of a human-like robotic arm: feedforward, feedback and cerebellum-based learning. In *2012 4th IEEE RAS & EMBS International Conference on Biomedical Robotics and Biomechatronics (BioRob)*, pages 562–567. IEEE, 2012.

Chadwick, E. K., Blana, D., van den Bogert, A. J. T., and Kirsch, R. F. A real-time, 3-D musculoskeletal model for dynamic simulation of arm movements. *IEEE transactions on bio-medical engineering*, 56(4):941–8, 2009.

Cheng, E. J. and Loeb, G. E. On the use of musculoskeletal models to interpret motor control strategies from performance data. *Journal of neural engineering*, 5(2):232, 2008.

Clark, A. *Being There: Putting Brain, Body, and World Together Again.* MIT Press, Cambridge, MA, USA, 1996.

Codol, O., Holland, P. J., Manohar, S. G., and Galea, J. M. Reward-based improvements in motor control are driven by multiple error-reducing mechanisms. *Journal of Neuroscience*, 40(18):3604–3620, 2020.

Collins, S., Ruina, A., Tedrake, R., and Wisse, M. Efficient bipedal robots based on passive-dynamic walkers. *Science*, 307(5712):1082–1085, 2005.

Cover, T. M. and Thomas, J. A. *Elements of Information Theory*, volume 2nd. Wiley, Hoboken, New Jersey, USA, 2006.

Daley, M. A., Voloshina, A., and Biewener, A. A. The role of intrinsic muscle mechanics in the neuromuscular control of stable running in the guinea fowl. *The Journal of Physiology*, 587 (Pt 11):2693–707, 2009.

De Groote, F., Allen, J. L., and Ting, L. H. Contribution of muscle short-range stiffness to initial changes in joint kinetics and kinematics during perturbations to standing balance: A simulation study. *Journal of Biomechanics*, 55:71–77, 2017.

Deimel, R. and Brock, O. A novel type of compliant and underactuated robotic hand for dexterous grasping. *The International Journal of Robotics Research*, 35(1-3):161–185, 2016.

Denoth, J., Gruber, K., Ruder, H., and Keppler, M. Forces and torques during sports activities with high accelerations. In *Biomechanics: Current interdisciplinary research*, pages 663–668. Springer, 1985.

Desmurget, M. and Grafton, S. Forward modeling allows feedback control for fast reaching movements. *Trends in Cognitive Sciences*, 4(11):423–431, 2000.

Dickinson, R. P. and Gelinas, R. J. Sensitivity analysis of ordinary differential equation systems - a direct method. *Journal of Computational Physics*, 21(2):123–143, 1976.

Dietrich, A., Wimböck, T., and Albu-Schäffer, A. Dynamic whole-body mobile manipulation with a torque controlled humanoid robot via impedance control laws. In *2011 IEEE/RSJ International Conference on Intelligent Robots and Systems*, pages 3199–3206. IEEE, 2011.

Domingo, A. and Lam, T. Reliability and validity of using the Lokomat to assess lower limb joint position sense in people with incomplete spinal cord injury. *Journal of NeuroEngineering and Rehabilitation*, 11(1), 2014.

Driess, D., Zimmermann, H., Wolfen, S., Suissa, D., Haeufle, D., Hennes, D., Toussaint, M., and Schmitt, S. Learning to Control Redundant Musculoskeletal Systems with Neural Networks and SQP: Exploiting Muscle Properties. In *2018 IEEE International Conference on Robotics and Automation (ICRA)*, pages 6461–6468, Brisbane, 2018. IEEE.

Driess, D., Schmitt, S., and Toussaint, M. Active inverse model learning with error and reachable set estimates. In *2019 IEEE/RSJ International Conference on Intelligent Robots and Systems (IROS)*, pages 1826–1833, 2019.

Dube, M.-O. and Roy, J.-S. Effect of fatigue and the absence of visual feedback on shoulder motor control in an healthy population during a reaching task. *Gait & posture*, 74:135–141, 2019.

Dunkelberger, N., Schearer, E. M., and O'Malley, M. K. A review of methods for achieving upper limb movement following spinal cord injury through hybrid muscle stimulation and robotic assistance. *Experimental Neurology*, 2020.

Durães, F., Pinto, M., and Sousa, E. Old drugs as new treatments for neurodegenerative diseases. *Pharmaceuticals*, 11(2):44, 2018.

Elias, L. A., Matoso, D. E. d. C., Watanabe, R. N., and Kohn, A. F. Perspectives on the modeling of the neuromusculoskeletal system to investigate the influence of neurodegenerative diseases on sensorimotor control. *Research on Biomedical Engineering*, 34(2):176–186, 2018.

Elson, R. A. and Aspinall, G. R. Measurement of hip range of flexion-extension and straight-leg raising. *Clinical Orthopaedics and Related Research*, 466(2):281–286, 2008.

Endler, C. Numerical Simulation of musculoskeletal movement with LS-DYNA: On the scalability of learning-based muscle stimulation. Master's thesis, University of Stuttgart, 2019.

Eriten, M. and Dankowicz, H. A rigorous dynamical-systems-based analysis of the self-stabilizing influence of muscle. *Journal of Biomechanical Engineering*, 131(1):011011–1–9, 2009.

Feldman, A. G. Once More on the Equilibrium-Point Hypothesis (λ Model) for Motor Control. *Journal of Motor Behavior*, 18(1):17–54, 1986.

Feldman, A. G. and Levin, M. F. The equilibrium-point hypothesis–past, present and future. *Advances in Experimental Medicine and Biology*, 629:699–726, 2009.

Festo AG and Co. KG. Fluidic muscle DMSP/MAS, 2016.

Flash, T. The control of hand equilibrium trajectories in multi-joint arm movements. *Biological Cybernetics*, 57(4-5):257–274, 1987.

Flash, T. and Hogan, N. The coordination of arm movements: an experimentally confirmed mathematical model. *The Journal of neuroscience*, 5(7):1688–1703, 1985.

Franklin, D. W. and Wolpert, D. M. Computational mechanisms of sensorimotor control. *Neuron*, 72(3):425–442, 2011.

Frenzel, S. and Pompe, B. Partial mutual information for coupling analysis of multivariate time series. *Phys. Rev. Lett.*, 99:204101, 2007.

Frisoli, A. Exoskeletons for upper limb rehabilitation. In *Rehabilitation Robotics*, pages 75–87. Elsevier, 2018.

Fromme, N. P., Camenzind, M., Riener, R., and Rossi, R. M. Need for mechanically and ergonomically enhanced tremor-suppression orthoses for the upper limb: a systematic review. *Journal of NeuroEngineering and Rehabilitation*, 16(1):93, 2019.

Gerritsen, K. G., van den Bogert, A. J., Hulliger, M., and Zernicke, R. F. Intrinsic Muscle Properties Facilitate Locomotor Control—A Computer Simulation Study. *Motor Control*, 2 (3):206–220, 1998.

Geyer, H. and Herr, H. A Muscle-Reflex Model That Encodes Principles of Legged Mechanics Produces Human Walking Dynamics and Muscle Activities. *IEEE Transactions on Neural Systems and Rehabilitation Engineering*, 18(3):263–73, 2010.

Ghazi-Zahedi, K. *Morphological Intelligence: Measuring the Body's Contribution to Intelligence*. Springer London, 2019a.

Ghazi-Zahedi, K. Gomi github repository. http://github.com/kzahedi/gomi, 2019b.

Ghazi-Zahedi, K., Haeufle, D. F. B., Montúfar, G., Schmitt, S., and Ay, N. Evaluating Morphological Computation in Muscle and DC-motor Driven Models of Human Hopping. *Frontiers in Robotics and AI*, 3(July):1–10, 2016.

Glenday, J. D., Steinhilber, B., Jung, F., and Haeufle, D. F. B. Development of a subject-specific musculoskeletal model of the wrist to predict frictional work dissipated due to tendon gliding resistance in the carpal tunnel. *Computer Methods in Biomechanics and Biomedical Engineering*, 2020.

Glenday, J., Kontaxis, A., Roche, S., and Sivarasu, S. Effect of humeral tray placement on impingement-free range of motion and muscle moment arms in reverse shoulder arthroplasty. *Clinical Biomechanics*, 62:136–143, 2019.

Gribble, P. L. and Ostry, D. J. Compensation for loads during arm movements using equilibrium-point control. *Experimental Brain Research*, 135(4):474–482, 2000.

Gribble, P. L., Ostry, D. J., Sanguineti, V., and Laboissiere, R. Are complex control signals required for human arm movement? *Journal of Neurophysiology*, 79:1409–1424, 1998.

Griswold, Lee F; Edward A., G. B. E. and Beckstrom, D. Patient Transfer System, 2014.

Gross, J., Timmermann, L., Kujala, J., Dirks, M., Schmitz, F., Salmelin, R., and Schnitzler, A. The neural basis of intermittent motor control in humans. *Proceedings of the National Academy of Sciences of the United States of America*, 99(4):2299–2302, 2002.

Gruber, K., Ruder, H., Denoth, J., and Schneider, K. A comparative study of impact dynamics: Wobbling mass model versus rigid body models. *Journal of Biomechanics*, 31:439–444, 1998.

Guess, T. M., Thiagarajan, G., Kia, M., and Mishra, M. A subject specific multibody model of the knee with menisci. *Medical Engineering and Physics*, 32(5):505–515, 2010.

Günther, M., Schmitt, S., and Wank, V. High-frequency oscillations as a consequence of neglected serial damping in Hill-type muscle models. *Biological Cybernetics*, 97(1):63–79, 2007.

Günther, M. *Computersimulationen zur Synthetisierung des muskulär erzeugten menschlichen Gehens unter Verwendung eines biomechanischen Mehrkörpermodells*. PhD thesis, Eberhard-Karls-Universität zu Tübingen, 1997.

Günther, M. and Ruder, H. Synthesis of two-dimensional human walking: a test of the lambda-model. *Biological Cybernetics*, 89(2):89–106, 2003.

Haegele, M., Maufroy, C., Kraus, W., Siee, M., and Breuninger, J. Musculoskeletal Robots and Wearable Devices on the Basis of Cable-driven Actuators. In *Soft Robotics*, pages 42–53. Springer Berlin Heidelberg, Berlin, Heidelberg, 2015.

Haeufle, D. F. B., Grimmer, S., Kalveram, K.-T., and Seyfarth, A. Integration of intrinsic muscle properties, feed-forward and feedback signals for generating and stabilizing hopping. *Journal of The Royal Society Interface*, 9(72):1458–1469, 2012a.

Haeufle, D. F. B., Günther, M., Bayer, A., and Schmitt, S. Hill-type muscle model with serial damping and eccentric force-velocity relation. *Journal of Biomechanics*, 47(6):1531–6, 2014a.

Haeufle, D. F. B., Günther, M., Wunner, G., and Schmitt, S. Quantifying control effort of biological and technical movements: An information-entropy-based approach. *Physical Review E*, 89(1):012716, 2014b.

Haeufle, D. F., Grimmer, S., and Seyfarth, A. The role of intrinsic muscle properties for stable hopping - Stability is achieved by the force-velocity relation. *Bioinspiration and Biomimetics*, 5(1):16004–16015, 2010a.

Haeufle, D. F. B., Stollenmaier, K., Heinrich, I., Schmitt, S., and Ghazi-Zahedi, K. Morphological computation increases from lower- to higher-level of biological motor control hierarchy. *Frontiers in Robotics and AI - Soft Robotics, Research topic: Recent Trends in Morphological Computation*, 2020a.

Haeufle, D. F. B., Wochner, I., Holzmüller, D., Driess, D., Günther, M., and Schmitt, S. Muscles reduce neuronal information load: quantification of control effort in biological vs robotic pointing and walking. *Frontiers in Robotics and AI - Soft Robotics, Research topic: Recent Trends in Morphological Computation*, 2020b.

Haeufle, D., Günther, M., Blickhan, R., and Schmitt, S. Can Quick Release Experiments Reveal the Muscle Structure? A Bionic Approach. *Journal of Bionic Engineering*, 9(2): 211–223, 2012b.

Haeufle, D. F. B., Grimmer, S., and Seyfarth, A. The role of intrinsic muscle properties for stable hopping - stability is achieved by the force-velocity relation. *Bioinspiration & Biomimetics*, 5(1):016004, 2010b.

Hammer, M., Günther, M., Haeufle, D., and Schmitt, S. Tailoring anatomical muscle paths: a sheath-like solution for muscle routing in musculoskeletal computer models. *Mathematical Biosciences*, 311:68–81, 2019.

Haruno, M., Wolpert, D. M., and Kawato, M. MOSAIC Model for Sensorimotor Learning and Control. *Neural Computation*, 13(10):2201–2220, 2001.

Hatze, H. A Myocybernetic Control Model of Skeletal Muscle. *Biol. Cybernetics*, 25:103–119, 1977.

He, W., Ge, W., Li, Y., Liu, Y. J., Yang, C., and Sun, C. Model Identification and Control Design for a Humanoid Robot. *IEEE Transactions on Systems, Man, and Cybernetics: Systems*, 47(1):45–57, 2017.

Heidlauf, T. and Röhrle, O. Modeling the chemoelectromechanical behavior of skeletal muscle using the parallel open-source software library openCMISS. *Computational and Mathematical Methods in Medicine*, 2013, 2013.

Heinrich, I. M. Bioinspirierte Regelung in einem neuromuskulären Modell: Ausnutzung von Resonanzeigenschaften externer Feder-Masse-Dynamik durch Central Pattern Generators. Studienarbeit, University of Stuttgart, 2019.

Hemmers, S. Eye-Hand-Coordination during upper limb pointing movements in patients with cerebellar ataxia. Master's thesis, University of Stuttgart, 2018.

Henze, A. *Dreidimensionale biomechanische Modellierung und die Entwicklung eines Reglers zur Simulation zweibeinigen Gehens*. PhD, Eberhard-Karls-Universität zu Tübingen, 2002.

Hermann Bock GmbH. Assembly and operation manual Nursing care beds. Technical report, Hermann Bock GmbH, 2018.

Herzfeld, D. J. and Shadmehr, R. Cerebellum estimates the sensory state of the body. *Trends in Cognitive Science*, 18(2):66–67, 2014.

Higashihara, A., Nagano, Y., Ono, T., and Fukubayashi, T. Differences in hamstring activation characteristics between the acceleration and maximum-speed phases of sprinting. *Journal of Sports Sciences*, 36(12):1313–1318, 2018.

Hirose, M. and Ogawa, K. Honda humanoid robots development. *Philosophical Transactions of the Royal Society of London, Series A*, 365(1850):11–9, 2007.

Hoffmann, M. and Pfeifer, R. The implications of embodiment for behavior and cognition: animal and robotic case studies. In Tschacher, W. and Bergomi, C., editors, *The Implications of Embodiment: Cognition and Communication*, pages 31–58. Imprint Academic, 1 edition, 2011.

Hogan, N. Adaptive Control of Mechanical Impedance by Coactivation of Antagonist Muscles. *IEEE Transactions on Automatic Control*, 29(8):681–690, 1984.

Hogan, N. and Sternad, D. Dynamic primitives in the control of locomotion. *Frontiers in Computational Neuroscience*, 7(May):1–16, 2013.

Holzbaur, K. R. S., Murray, W. M., and Delp, S. L. A model of the upper extremity for simulating musculoskeletal surgery and analyzing neuromuscular control. *Annals of Biomedical Engineering*, 33(6):829–840, 2005.

Houk, J. and Rymer, W. Neural control of muscle length and tension. In *Supplement 2. Handbook of Physiology, The Nervous System, Motor Control*. American Physiological Society, 1981.

Huang, J., Huo, W., Xu, W., Mohammed, S., and Amirat, Y. Control of upper-limb power-assist exoskeleton using a human-robot interface based on motion intention recognition. *IEEE Transactions on Automation Science and Engineering*, 12(4):1257–1270, 2015.

Hubicki, C., Grimes, J., Jones, M., Renjewski, D., Spröwitz, A., Abate, A., and Hurst, J. ATRIAS: Design and Validation of a Tether-Free 3D-Capable Spring-Mass Bipedal Robot. *The International Journal of Robotics Research*, 35(12):1497–1521, 2016.

Huh, D. H. D. and Todorov, E. Real-time motor control using recurrent neural networks. *2009 IEEE Symposium on Adaptive Dynamic Programming and Reinforcement Learning*, pages 42–49, 2009.

Hunter, J. P., Marshall, R. N., and McNair, P. J. Relationships between ground reaction force impulse and kinematics of sprint-running acceleration. *Journal of Applied Biomechanics*, 21 (1):31–43, 2005.

Hutter, M., Remy, C. D., Hoepflinger, M. A., and Siegwart, R. Efficient and Versatile Locomotion With Highly Compliant Legs. *IEEE/ASME Transactions on Mechatronics*, 18(2): 449–458, 2013.

Iida, F., Pfeifer, R., Steels, L., and Kuniyoshi, Y. *Embodied Artificial Intelligence*, volume 3139 of *Lecture Notes in Computer Science*. Springer Berlin Heidelberg, Berlin, Heidelberg, 2004.

Iida, F., Minekawa, Y., Rummel, J., and Seyfarth, A. Toward a human-like biped robot with compliant legs. *Robotics and Autonomous Systems*, 57(2):139–144, 2009.

Ijspeert, A. Biorobotics: Using robots to emulate and investigate agile locomotion. *Science (New York, N.Y.)*, 346:196–203, 2014.

Inoue, J. Neuro-muscular control of dynamic movements: juggling and the influence of motor noise. Lab rotation report, University of Tübingen, 2019.

Iwamoto, M., Nakahira, Y., Kimpara, H., Sugiyama, T., and Min, K. Development of a human body finite element model with multiple muscles and their controller for estimating occupant motions and impact responses in frontal crash situations. Technical report, SAE Technical Paper, 2012.

Iwamoto, M., Nakahira, Y., and Kimpara, H. Development and validation of the Total HUman Model for Safety (thums) toward further understanding of occupant injury mechanisms in precrash and during crash. *Traffic injury prevention*, 16(sup1):S36–S48, 2015.

Jezernik, S., Colombo, G., Keller, T., Frueh, H., and Morari, M. Robotic Orthosis Lokomat: A Rehabilitation and Research Tool. *Neuromodulation*, 6(2):108–115, 2003.

John, C. T., Anderson, F. C., Higginson, J. S., and Delp, S. L. Stabilisation of walking by intrinsic muscle properties revealed in a three-dimensional muscle-driven simulation. *Computer Methods in Biomechanics and Biomedical Engineering*, 16(4):451–462, 2013.

Kalveram, K. T. and Seyfarth, A. Inverse biomimetics: How robots can help to verify concepts concerning sensorimotor control of human arm and leg movements. *Journal of Physiology Paris*, 103(3-5):232–243, 2009.

Kalveram, K. T., Schinauer, T., Beirle, S., Richter, S., and Jansen-Osmann, P. Threading neural feedforward into a mechanical spring: how biology exploits physics in limb control. *Biological Cybernetics*, 92(4):229–40, 2005.

Kalveram, K. T., Haeufle, D. F. B., and Seyfarth, A. From Hopping to Walking - how the Biped Jena-Walker can Learn from the Single-Leg Marco-Hopper. In Marques, L., De Almeida, A., and Tokhi, M. O., editors, *CLAWAR-Advances in Mobile Robotics*, pages 638–645, Coimbra, 2008. World Scientific.

Kalveram, K. T., Haeufle, D. F. B., Seyfarth, A., and Grimmer, S. Energy management that generates terrain following versus apex-preserving hopping in man and machine. *Biological Cybernetics*, 106(1):1–13, 2012.

Kambara, H., Kim, K., Shin, D., Sato, M., and Koike, Y. Learning and generation of goal-directed arm reaching from scratch. *Neural Networks*, 22(4):348–361, 2009.

Kambara, H., Shin, D., and Koike, Y. A computational model for optimal muscle activity considering muscle viscoelasticity in wrist movements. *Journal of Neurophysiology*, 109(8): 2145–2160, 2013.

Kandel, E. R., Schwartz, J. H., Jessell, T. M., Jessell, T., Siegelbaum, S., and Hudspeth, A. *Principles of neural science*, volume 5. McGraw-hill New York, 2013.

Kapelner, T., Sartori, M., Negro, F., and Farina, D. Neuro-musculoskeletal mapping for man-machine interfacing. *Scientific Reports*, 10(1):5834, 2020.

Karniel, A. Open questions in computational motor control. *Journal of Integrative Neuroscience*, 10(3):385–411, 2011.

Kashiri, N., Abate, A., Abram, S. J., Albu-Schaffer, A., Clary, P. J., Daley, M., Faraji, S., Furnemont, R., Garabini, M., Geyer, H., et al. An overview on principles for energy efficient robot locomotion. *Frontiers in Robotics and AI*, 5:129, 2018.

Kawato, M. Internal models for motor control and trajectory planning. *Current Opinion in Neurobiology*, 9(6):718–27, 1999.

Kim, S., Laschi, C., and Trimmer, B. Soft robotics: a bioinspired evolution in robotics. *Trends in biotechnology*, 31(5):287–94, 2013.

Kistemaker, D. A., Van Soest, A. J., and Bobbert, M. F. Length-dependent [Ca2+] sensitivity adds stiffness to muscle. *Journal of Biomechanics*, 38(9):1816–1821, 2005.

Kistemaker, D. A., Van Soest, A. J., and Bobbert, M. F. Is equilibrium point control feasible for fast goal-directed single-joint movements? *Journal of Neurophysiology*, 95(5):2898–912, 2006.

Kistemaker, D. A., Van Soest, A. J., and Bobbert, M. F. Equilibrium Point Control Cannot be Refuted by Experimental Reconstruction of Equilibrium Point Trajectories. *Journal of Neurophysiology*, 98(3):1075–1082, 2007a.

Kistemaker, D. A., Van Soest, A. J., and Bobbert, M. F. A model of open-loop control of equilibrium position and stiffness of the human elbow joint. *Biological Cybernetics*, 96(3): 341–350, 2007b.

Kistemaker, D. A., Wong, J. D., and Gribble, P. L. The central nervous system does not minimize energy cost in arm movements. *Journal of neurophysiology*, 104:2985–2994, 2010.

Kistemaker, D. A., Van Soest, A. J. K., Wong, J. D., Kurtzer, I., and Gribble, P. L. Control of position and movement is simplified by combined muscle spindle and Golgi tendon organ feedback. *Journal of Neurophysiology*, 109(4):1126–1139, 2013.

Kistemaker, D. A., Wong, J. D., and Gribble, P. L. The cost of moving optimally : kinematic path selection. *Journal of Neurophysiology*, 112(8):1815–1824, 2014.

Kitazaki, S. and Griffin, M. A modal analysis of whole-body vertical vibration, using a finite element model of the human body. *Journal of Sound and Vibration*, 200(1):83 – 103, 1997.

Kleinbach, C., Martynenko, O., Promies, J., Haeufle, D. D. F. B., Fehr, J., and Schmitt, S. Implementation and validation of the extended Hill-type muscle model with robust routing capabilities in LS-DYNA for active human body models. *BioMedical Engineering OnLine*, 16(1):109, 2017.

Klute, G. K., Czerniecki, J. M., and Hannaford, B. Artificial Muscles: Actuators for Biorobotic Systems. *The International Journal of Robotics Research*, 21(4):295–309, 2002.

Klute, G., Czerniecki, J., and Hannaford, B. McKibben artificial muscles: pneumatic actuators with biomechanical intelligence. In *1999 IEEE/ASME International Conference on Advanced Intelligent Mechatronics*, volume pp, pages 221–226. IEEE, 1999.

Koch, M., Mostert, J., Heersema, D., and De Keyser, J. Tremor in multiple sclerosis. *Journal of Neurology*, 254(2):133–145, 2007.

Koditschek, D. E., Full, R. J., and Buehler, M. Mechanical aspects of legged locomotion control. *Arthropod Structure & Development*, 33(3):251–72, 2004.

Koike, Y., Kambara, H., Yoshimura, N., and Shin, D. Brain–Machine Interfaces Based on Computational Model. In Kansaku, K. and Cohen, L. G., editors, *Systems Neuroscience and Rehabilitation*, pages 35–57. Springer Japan, Tokyo, 2011.

Krakauer, J. W. and Shadmehr, R. Towards a computational neuropsychology of action. *Progress in Brain Research*, 165:383–394, 2007.

Kraskov, Alexander and Stögbauer, Harald and Grassberger, Peter. Estimating mutual information. *Phys. Rev. E*, 69:066138, 2004.

Kukillaya, R., Proctor, J., and Holmes, P. Neuromechanical models for insect locomotion: Stability, maneuverability, and proprioceptive feedback. *Chaos*, 19(2):26107, 2009.

Kurtzer, I., Pruszynski, J. A., and Scott, S. H. Long-latency responses during reaching account for the mechanical interaction between the shoulder and elbow joints. *Journal of neurophysiology*, 102(5):3004–3015, 2009.

Kurtzer, I., Trautman, P., Rasquinha, R. J., Bhanpuri, N. H., Scott, S. H., and Bastian, A. J. Cerebellar damage diminishes long-latency responses to multijoint perturbations. *Journal of neurophysiology*, 109(8):2228–2241, 2013.

Kurtzer, I., Crevecoeur, F., and Scott, S. H. Fast feedback control involves two independent processes utilizing knowledge of limb dynamics. *Journal of Neurophysiology*, 111(8):1631–1645, 2014.

Kurtzer, I. L. Long-latency reflexes account for limb biomechanics through several supraspinal pathways. *Frontiers in Integrative Neuroscience*, 8(JAN):1–19, 2015.

Kurtzer, I. L., Pruszynski, J. A., and Scott, S. H. Long-latency reflexes of the human arm reflect an internal model of limb dynamics. *Current Biology*, 18(6):449–453, 2008.

Lacasse, S., Bolduc, S., Laflamme, J., Lemire, G., Beaudet, J.-P., Mercier, G., and Berthelot, E. Systems for patient support surface orientation and displacement, 2016.

Lan, L. and Zhu, K. Y. Biomechanical stability analysis of the lambda-model controlling one joint. *International journal of neural systems*, 17(3):193–206, 2007.

Lan, N. and He, X. Fusimotor control of spindle sensitivity regulates central and peripheral coding of joint angles. *Frontiers in Computational Neuroscience*, 6(August):1–13, 2012.

Latash, M. L. Motor Control: In Search of Physics of the Living Systems. *Journal of Human Kinetics*, 24(-1):7–18, 2010.

Latash, M. L. *Fundamentals of motor control*. Academic Press, 2012.

Latash, M. L., Scholz, J. P., and Schöner, G. Motor Control Strategies Revealed in the Structure of Motor Variability. *Exercise and Sport Sciences Reviews*, 30(1):26–31, 2002.

Latash, M. M. L., Levin, M. M. F., Scholz, J. P., and Schöner, G. Motor Control Theories and Their Applications. *Medicina*, 46(6):382–92, 2010.

Legnani, G., Casolo, F., Righettini, P., and Zappa, B. A homogeneous matrix approach to 3d kinematics and dynamics - i. theory. *Mechanism and Machine Theory*, 31(5):573 – 587, 1996.

Lehman, S. and Stark, L. Three algorithms for interpreting models consisting of ordinary differential equations: Sensitivity coefficients, sensitivity functions, global optimization. *Mathematical Biosciences*, 62(1):107–122, 1982.

Lenzi, T., Vitiello, N., McIntyre, J., Roccella, S., and Carrozza, M. C. A robotic model to investigate human motor control. *Biological Cybernetics*, 105(1):1–19, 2011.

Li, C.-Y. Neural muscular control learning: an application of support vector regression in predicting motor commands. Lab rotation report, University of Tübingen, 2019.

Li, S., Zhuang, C., Hao, M., He, X., Marquez, J. C., Niu, C. M., and Lan, N. Coordinated alpha and gamma control of muscles and spindles in movement and posture. *Frontiers in Computational Neuroscience*, 9(October):1–15, 2015.

Lin, H.-T., Leisk, G. G., and Trimmer, B. GoQBot: a caterpillar-inspired soft-bodied rolling robot. *Bioinspiration & Biomimetics*, 6(2):026007, 2011.

Lloyd, D. G. and Besier, T. F. An EMG-driven musculoskeletal model to estimate muscle forces and knee joint moments in vivo. *Journal of Biomechanics*, 36(6):765–776, 2003.

Lloyd, J. E., Stavness, I., and Fels, S. ArtiSynth: A Fast Interactive Biomechanical Modeling Toolkit Combining Multibody and Finite Element Simulation. In *Studies in Mechanobiology, Tissue Engineering and Biomaterials*, volume 11, pages 355–394. Springer, 2012.

Loeb, G. E., Brown, I. E., and Cheng, E. J. A hierarchical foundation for models of sensorimotor control. *Experimental Brain Research*, 126(1):1–18, 1999.

Loeb, G. and Mileusnic, M. Proprioceptors and Models of Transduction. In *Scholarpedia of Touch*, volume 10. Springer, 2016.

Loeb, G. E. Optimal isn't good enough. *Biological Cybernetics*, 106(11-12):757–765, 2012.

Logroscino, G., Piccininni, M., Marin, B., Nichols, E., Abd-Allah, F., Abdelalim, A., Alahdab, F., Asgedom, S. W., Awasthi, A., Chaiah, Y., et al. Global, regional, and national burden of motor neuron diseases 1990–2016: a systematic analysis for the global burden of disease study 2016. *The Lancet Neurology*, 17(12):1083–1097, 2018.

MacKay, D. J. *Information Theory, Inference and Learning Algorithms*. Cambridge University Press, 2003.

Maeda, R. S., Gribble, P. L., and Pruszynski, J. A. Learning new feedforward motor commands based on feedback responses. *Current Biology*, 30(10):1941 – 1948.e3, 2020.

Manfredi, L., Assaf, T., Mintchev, S., Marrazza, S., Capantini, L., Orofino, S., Ascari, L., Grillner, S., Wallén, P., Ekeberg, Ö., Stefanini, C., and Dario, P. A bioinspired autonomous swimming robot as a tool for studying goal-directed locomotion. *Biological Cybernetics*, 107 (5):513–527, 2013.

Manoonpong, P., Geng, T., Kulvicius, T., Porr, B., and Wörgötter, F. Adaptive, fast walking in a biped robot under neuronal control and learning. *PLoS Computational Biology*, 3(7): 1305–1320, 2007.

Markanday, A., Messner, J., and Thier, P. A loss of a velocity-duration trade-off impairs movement precision in patients with cerebellar degeneration. *European Journal of Neuroscience*, 48(4):1976–1989, 2018.

Martens, M., Seel, T., Zawatzki, J., and Boblan, I. A novel framework for a systematic integration of pneumatic-muscle-actuator-driven joints into robotic systems via a torque control interface. *Actuators*, 7, 2018.

Martynenko, O., Schmitt, S., Bayer, A., Blaschke, J., and Mayer, C. A movement generation algorithm for FE Human Body Models. *Proceedings in Applied Mathematics and Mechanics*, 17(May):201–202, 2017.

Martynenko, O. V., Stollenmaier, K., Endler, C. A., Neininger, F. T., Schmitt, S., and Haeufle, D. F. Towards overcoming the bottleneck of optimizing control parameters in finite element active human body models. *PAMM*, 19(1), 2019.

Maschke, M., Gomez, C. M., Ebner, T. J., and Konczak, J. Hereditary cerebellar ataxia progressively impairs force adaptation during goal-directed arm movements. *Journal of neurophysiology*, 91(1):230–238, 2004.

McGeer, T. Passive walking with knees. In *In Robotics and Automation*, pages 1640–1645, 1990.

McIntyre, J. and Bizzi, E. Servo Hypotheses for the Biological Control of Movement. *Journal of Motor Behavior*, 25(3):193–202, 1993.

McMahan, W., Chitrakaran, V., Csencsits, M., Dawson, D., Walker, I. D., Jones, B. A., Pritts, M., Dienno, D., Grissom, M., and Rahn, C. D. Field trials and testing of the OctArm continuum manipulator. In *Proceedings - IEEE International Conference on Robotics and Automation*, volume 2006, pages 2336–2341, 2006.

Mentiplay, B. F., Banky, M., Clark, R. A., Kahn, M. B., and Williams, G. Lower limb angular velocity during walking at various speeds. *Gait and Posture*, 65(June):190–196, 2018.

Mergner, T., Huethe, F., Maurer, C., and Ament, C. Human Equilibrium Control Principles Implemented into a Biped Humanoid Robot. In Zielinska, T. and Zielinski, C., editors, *Robot Design, Dynamics, and Control, CISM Courses and Lectures 487*, pages 271–279. Springer, 2006.

Micheau, P., Kron, A., and Bourassa, P. Evaluation of the lambda model for human postural control during ankle strategy. *Biological Cybernetics*, 89(3):227–236, 2003.

Mileusnic, M. P. and Loeb, G. E. Mathematical Models of Proprioceptors. II. Structure and Function of the Golgi Tendon Organ. *Journal of Neurophysiology*, 96(4):1789–1802, 2006.

Mileusnic, M. P., Brown, I. E., Lan, N., and Loeb, G. E. Mathematical models of proprioceptors. I. Control and transduction in the muscle spindle. *Journal of neurophysiology*, 96(4):1772–88, 2006.

Millard, M., Uchida, T., Seth, A., and Delp, S. L. Flexing Computational Muscle: Modeling and Simulation of Musculotendon Dynamics. *Journal of Biomechanical Engineering*, 135(2): 021005, 2013.

Mordhorst, M., Heidlauf, T., and Rohrle, O. Predicting electromyographic signals under realistic conditions using a multiscale chemo-electro-mechanical finite element model. *Interface Focus*, 5(2):20140076–20140076, 2015.

More, H. L., Hutchinson, J. R., Collins, D. F., Weber, D. J., Aung, S. K., and Donelan, J. M. Scaling of sensorimotor control in terrestrial mammals. *Proceedings of the Royal Society B: Biological Sciences*, 277(1700):3563–3568, 2010.

Morio, J. Global and local sensitivity analysis methods for a physical system. *European Journal of Physics*, 32(6):1577–1583, 2011.

Mörl, F., Siebert, T., Schmitt, S., Blickhan, R., and Günther, M. Electro-Mechanical Delay in Hill-Type Muscle Models. *Journal of Mechanics in Medicine and Biology*, 12(05):1250085, 2012.

Mugge, W., Munts, A. G., Schouten, A. C., and van der Helm, F. C. Modeling movement disorders—CRPS-related dystonia explained by abnormal proprioceptive reflexes. *Journal of Biomechanics*, 45(1):90 – 98, 2012.

Murray, W. M., Delp, S. L., and Buchanan, T. S. Variation of muscle moment arms with elbow and forearm position. *Journal of Biomechanics*, 28(5):513–525, 1995.

NASA. *Anthropometric source book. A handbook of anthropometric data (NASA RP-1024).* National Aeronautics and Space Administration, NTIS No. N79-13711, Texas, 2 edition, 1978.

Navacchia, A., Hume, D. R., Rullkoetter, P. J., and Shelburne, K. B. A computationally efficient strategy to estimate muscle forces in a finite element musculoskeletal model of the lower limb. *Journal of Biomechanics*, 84:94–102, 2019.

Nichols, T. R. and Houk, J. C. Improvement in linearity and regulation of stiffness that results from actions of stretch reflex. *Journal of Neurophysiology*, 39(1):119–142, 1976.

Niiyama, R., Nishikawa, S., and Kuniyoshi, Y. Biomechanical Approach to Open-Loop Bipedal Running with a Musculoskeletal Athlete Robot. *Advanced Robotics*, 26(3-4):383–398, 2012.

Niku, S. B. *Introduction to robotics: analysis, control, applications.* John Wiley & Sons, 2020.

Nishikawa, K. Eccentric contraction: unraveling mechanisms of force enhancement and energy conservation. *The Journal of Experimental Biology*, 219(2):189–196, 2016.

Nishikawa, K., Biewener, A. A., Aerts, P., Ahn, A. N., Chiel, H. J., Daley, M. A., Daniel, T. L., Full, R. J., Hale, M. E., Hedrick, T. L., Lappin, A. K., Nichols, T. R., Quinn, R. D., Satterlie, R. A., and Szymik, B. Neuromechanics: An integrative approach for understanding motor control. *Integrative and Comparative Biology*, 47(1):16–54, 2007.

Noelle, L. V., Schmitt, S., and Martynenko, O. V. Defining Injury Criteria for the Muscle-Tendon-Unit. In *International Research Council on Biomechanics of Injury (IRCOBI)*, 2020.

Nordin, A. D., Rymer, W. Z., Biewener, A. A., Schwartz, A. B., Chen, D., and Horak, F. B. Biomechanics and neural control of movement, 20 years later: What have we learned and what has changed? *Journal of NeuroEngineering and Rehabilitation*, 14(1):1–11, 2017.

Nurzaman, S. G., Yu, X., Kim, Y., and Iida, F. Goal-directed multimodal locomotion through coupling between mechanical and attractor selection dynamics. *Bioinspiration and Biomimetics*, 10(2):1–13, 2015.

Östh, J., Brolin, K., Ólafsdóttir, J. M., Davidsson, J., Pipkorn, B., Jakobsson, L., Törnvall, F., and Lindkvist, M. Muscle activation strategies in human body models for the development of integrated safety. In *Proceedings of the 24th International Techical Conference on the Enhanced Safety of Vehicles (ESV), Gothenburg, Sweden*, pages 8–11. Citeseer, 2015.

Ostry, D. J. and Feldman, A. G. A critical evaluation of the force control hypothesis in motor control, 2003.

Pandy, M. G. Computer Modeling and simulation of human movement. *Annual review of biomedical engineering*, 3(1):245–273, 2001.

Pandy, M. G., Zajac, F. E., Sim, E., and Levine, W. S. An optimal control model for maximum-height human jumping. *Journal of Biomechanics*, 23(12):1185–1198, 1990.

Paninski, L. Estimation of entropy and mutual information. *Neural Comput.*, 15(6):1191–1253, 2003.

Papachrysostomou, C. Predicting the relation of joint-angle, muscle activity and contact force of tendons in the carpal tunnel by computer simulation. Master's thesis, University of Tübingen, 2018.

Paul, C. Morphological computation: A basis for the analysis of morphology and control requirements. *Robotics and Autonomous Systems*, 54(8):619–630, 2006.

Pennestrì, E., Stefanelli, R., Valentini, P. P., and Vita, L. Virtual musculo-skeletal model for the biomechanical analysis of the upper limb. *Journal of Biomechanics*, 40(6):1350–1361, 2007.

Petrič, T., Peternel, L., Morimoto, J., and Babič, J. Assistive arm-exoskeleton control based on human muscular manipulability. *Frontiers in Neurorobotics*, 13(May), 2019.

Pfeifer, R. and Iida, F. Morphological computation: Connecting body, brain and environment. *Japanese Scientific Monthly*, 58(2):48–54, 2005.

Pfeifer, R., Lungarella, M., and Iida, F. Self-organization, embodiment, and biologically inspired robotics. *Science*, 318(5853):1088–93, 2007.

Pfeifer, R. and Bongard, J. *How the body shapes the way we think: a new view of intelligence.* MIT press, 2006.

Pigeon, P., Yahia, L., and Feldman, A. G. Moment arms and lengths of human upper limb muscles as functions of joint angles. *Journal of Biomechanics*, 29(10):1365–1370, 1996.

Pinter, I. J., Van Soest, A. J., Bobbert, M. F., and Smeets, J. B. J. Conclusions on motor control depend on the type of model used to represent the periphery. *Biological Cybernetics*, 106(8-9):441–451, 2012.

Polygerinos, P., Correll, N., Morin, S. A., Mosadegh, B., Onal, C. D., Petersen, K., Cianchetti, M., Tolley, M. T., and Shepherd, R. F. Soft Robotics: Review of Fluid-Driven Intrinsically Soft Devices; Manufacturing, Sensing, Control, and Applications in Human-Robot Interaction. *Advanced Engineering Materials*, 19(12), 2017.

Prilutsky, B. I. and Edwards, D. H. *Neuromechanical modeling of posture and locomotion.* Springer, 2015.

Proctor, J. and Holmes, P. Reflexes and preflexes: on the role of sensory feedback on rhythmic patterns in insect locomotion. *Biological Cybernetics*, 102(6):513–531, 2010.

Pruszynski, J. A. and Scott, S. H. Optimal feedback control and the long-latency stretch response. *Experimental Brain Research*, 218(3):341–359, 2012.

Pruszynski, J. A., Kurtzer, I., and Scott, S. H. The long-latency reflex is composed of at least two functionally independent processes. *Journal of Neurophysiology*, 106(1):449–459, 2011.

Radkhah, K., Maufroy, C., Maus, M., Scholz, D., Seyfarth, A., and von Stryk, O. Concept and design of the BioBiped1 robot for human-like walking and running. *International Journal of Humanoid Robotics*, 08(03):439, 2011.

Rassier, D. E., MacIntosh, B. R., and Herzog, W. Length dependence of active force production in skeletal muscle. *Journal of Applied Physiology*, 86(5):1445–57, 1999.

Renjewski, D. and Seyfarth, A. Robots in human biomechanics-a study on ankle push-off in walking. *Bioinspiration & Biomimetics*, 7(3):036005, 2012.

Rettig, O., Fradet, L., Kasten, P., Raiss, P., and Wolf, S. I. A new kinematic model of the upper extremity based on functional joint parameter determination for shoulder and elbow. *Gait and Posture*, 30(4):469–476, 2009.

Rieffel, J. A., Valero-Cuevas, F. J., and Lipson, H. Morphological communication: exploiting coupled dynamics in a complex mechanical structure to achieve locomotion. *Journal of the royal society interface*, 7(45):613–621, 2010.

Riener, R. and Straube, A. Inverse dynamics as a tool for motion analysis: Arm tracking movements in cerebellar patients. *Journal of Neuroscience Methods*, 72(1):87–96, 1997.

Rist, I. S. Simulation von motorischen Defiziten im neuro-muskuloskelettalen Modell zur Abschätzung von korrektiven Kräften in Assistenzsystemen. Studienarbeit, University of Stuttgart, 2020.

Roberts, T. J. and Azizi, E. Flexible mechanisms: the diverse roles of biological springs in vertebrate movement. *The Journal of experimental biology*, 214(Pt 3):353–61, 2011.

Rockenfeller, R. *On the Application of Mathematical Methods in Hill – Type Muscle Modeling : Stability , Sensitivity and Optimal Control.* PhD thesis, Universitaet Koblenz-Landau, 2016.

Rockenfeller, R. and Günther, M. Inter-filament spacing mediates calcium binding to troponin: A simple geometric-mechanistic model explains the shift of force-length maxima with muscle activation. *Journal of Theoretical Biology*, 454:240 – 252, 2018.

Rockenfeller, R., Günther, M., Schmitt, S., and Götz, T. Comparing different muscle activation dynamics using sensitivity analysis. *CoRR*, 2014.

Rockenfeller, R., Günther, M., Schmitt, S., and Götz, T. Comparative sensitivity analysis of muscle activation dynamics. *Computational and Mathematical Methods in Medicine*, 2015: 585409, 2015.

Röhrle, O., Sprenger, M., and Schmitt, S. A two-muscle, continuum-mechanical forward simulation of the upper limb. *Biomechanics and Modeling in Mechanobiology*, 2016.

Rosendo, A., Liu, X., Shimizu, M., and Hosoda, K. Stretch reflex improves rolling stability during hopping of a decerebrate biped system. *Bioinspiration & Biomimetics*, 10(1):016008, 2015.

Ruppert, F. and Badri-Spröwitz, A. Series elastic behavior of biarticular muscle-tendon structure in a robotic leg. *Frontiers in Neurorobotics*, 13(August):1–13, 2019.

Rus, D. and Tolley, M. T. Design, fabrication and control of soft robots. *Nature*, 521(7553): 467–475, 2015.

Rutishauser, S., Sprowitz, A., Righetti, L., and Ijspeert, A. J. Passive compliant quadruped robot using Central Pattern Generators for locomotion control. In *IEEE RAS & EMBS International Conference on Biomedical Robotics and Biomechatronics*, pages 710–715. IEEE, 2008.

Sanger, T. D. Arm trajectories in dyskinetic cerebral palsy have increased random variability. *Journal of Child Neurology*, 21(7):551–557, 2006.

Sartori, M., Reggiani, M., Lloyd, D. G., and Pagello, E. A neuromusculoskeletal model of the human lower limb: Towards EMG-driven actuation of multiple joints in powered orthoses. In *2011 IEEE International Conference on Rehabilitation Robotics*, pages 1–6. IEEE, 2011.

Schmit, B. D. and Benz, E. N. Extensor reflexes in human spinal cord injury: Activation by hip proprioceptors. *Experimental Brain Research*, 145(4):520–527, 2002.

Schmitt, S. and Günther, M. Human leg impact: energy dissipation of wobbling masses. *Archive of Applied Mechanics*, 81(7):887–897, 2011.

Schmitt, S., Günther, M., and Häufle, D. F. B. The dynamics of the skeletal muscle: A systems biophysics perspective on muscle modeling with the focus on Hill-type muscle models. *GAMM-Mitteilungen*, page e201900013, 2019a.

Schmitt, S., Günther, M., and Häufle, D. F. The dynamics of the skeletal muscle: A systems biophysics perspective on muscle modeling with the focus on Hill-type muscle models. *GAMM Mitteilungen*, 42(October), 2019b.

Schreiber, T. Measuring information transfer. *Physical Review Letters*, 85(2), 2000.

Scott, S. H. Optimal feedback control and the neural basis of volitional motor control. *Nature reviews. Neuroscience*, 5(7):532–46, 2004.

Scott, S. H. A Functional Taxonomy of Bottom-Up Sensory Feedback Processing for Motor Actions. *Trends in Neurosciences*, 39(8):512–526, 2016.

Scott, S. H. and Norman, K. E. Computational approaches to motor control and their potential role for interpreting motor dysfunction. *Current Opinion in Neurology*, 16(6):693–698, 2003.

Scovil, C. Y. and Ronsky, J. L. Sensitivity of a Hill-based muscle model to perturbations in model parameters. *Journal of biomechanics*, 39(11):2055–2063, 2006.

Shadmehr, R. Actuator and Kinematic Redundancy in Biological Motor Control. In *Visual structures and integrated functions*, pages 239–254. Springer, 1991.

Shadmehr, R. Distinct neural circuits for control of movement vs. holding still. *Journal of Neurophysiology*, 117(4):1431–1460, 2017.

Shadmehr, R., Smith, M. A., and Krakauer, J. W. Error Correction, Sensory Prediction, and Adaptation in Motor Control. *Annual Review of Neuroscience*, 33(1):89–108, 2010.

Sharifi, M., Salarieh, H., and Behzadipour, S. Nonlinear Optimal Control of Planar Musculoskeletal Arm Model With Minimum Muscles Stress Criterion. *Journal of Computational and Nonlinear Dynamics*, 12(1):011014, 2016.

Shelburne, K. B. and Pandy, M. G. A dynamic model of the knee and lower limb for simulating rising movements. *Computer Methods in Biomechanics and Biomedical Engineering*, 5(2): 149–159, 2002.

Shemmell, J., Krutky, M. A., and Perreault, E. J. Stretch sensitive reflexes as an adaptive mechanism for maintaining limb stability. *Clinical Neurophysiology*, 121(10):1680–1689, 2010.

Shepherd, R. F., Ilievski, F., Choi, W., Morin, S. a., Stokes, A. a., Mazzeo, A. D., Chen, X., Wang, M., and Whitesides, G. M. Multigait soft robot. *Proceedings of the National Academy of Sciences of the United States of America*, 108(51):20400–3, 2011.

Shin, D., Yeh, X., and Khatib, O. Variable radius pulley design methodology for pneumatic artificial muscle-based antagonistic actuation systems. In *2011 IEEE/RSJ International Conference on Intelligent Robots and Systems*, pages 1830–1835. IEEE, 2011.

Siciliano, B. and Khatib, O. *Springer handbook of robotics*. Springer, 2016.

Siebert, T. and Rode, C. Computational modeling of muscle biomechanics. In Jin, Z., editor, *Computational Modelling of Biomechanics and Biotribology in the Musculoskeletal System*, chapter 6, pages 173–204. Woodhead Publishing, Elsevier, 1 edition, 2014.

Siebert, T., Till, O., Stutzig, N., Günther, M., and Blickhan, R. Muscle force depends on the amount of transversal muscle loading. *Journal of Biomechanics*, 47(8):1822–1828, 2014.

Slawinski, J., Bonnefoy, A., Ontanon, G., Leveque, J. M., Miller, C., Riquet, A., Chèze, L., and Dumas, R. Segment-interaction in sprint start: Analysis of 3D angular velocity and kinetic energy in elite sprinters. *Journal of Biomechanics*, 43(8):1494–1502, 2010.

Smeets, C. J. and Verbeek, D. S. Cerebellar ataxia and functional genomics: Identifying the routes to cerebellar neurodegeneration. *Biochimica et Biophysica Acta - Molecular Basis of Disease*, 1842(10):2030–2038, 2014.

Sobotta, J. *Atlas der Anatomie des Menschen*, volume 3. Elsevier Health Sciences, 2010.

Soekadar, S. R., Birbaumer, N., Slutzky, M. W., and Cohen, L. G. Brain-machine interfaces in neurorehabilitation of stroke. *Neurobiology of Disease*, 83:172–179, 2015.

Song, D., Lan, N., Loeb, G. E., and Gordon, J. Model-based sensorimotor integration for multi-joint control: Development of a virtual arm model. *Annals of Biomedical Engineering*, 36(6):1033–1048, 2008.

Sproewitz, A., Moeckel, R., Maye, J., and Ijspeert, A. J. Learning to Move in Modular Robots using Central Pattern Generators and Online Optimization. *The International Journal of Robotics Research*, 27(3-4):423–443, 2008.

Sprowitz, A., Tuleu, A., Vespignani, M., Ajallooeian, M., Badri, E., and Ijspeert, A. J. Towards dynamic trot gait locomotion: Design, control, and experiments with Cheetah-cub, a compliant quadruped robot. *The International Journal of Robotics Research*, 32(8):932–950, 2013.

Stadelmann, C. Multiple sclerosis as a neurodegenerative disease: Pathology, mechanisms and therapeutic implications. *Current Opinion in Neurology*, 24(3):224–229, 2011.

Sternad, D., Dean, W. J., and Schaal, S. Interaction of rhythmic and discrete pattern generators in single-joint movements. *Human Movement Science*, 19(4):627–664, 2000.

Stollenmaier, K., Haeufle, D. F. B., and Schmitt, S. Active external propulsion of the hip activates internal reflex-based resistance forces depending on movement speed and neuronal preparedness: a full-body computer simulation study. *Computer Methods in Biomechanics and Biomedical Engineering (submitted)*, 2020a.

Stollenmaier, K., Ilg, W., and Haeufle, D. F. B. Predicting Perturbed Human Arm Movements in a Neuro-Musculoskeletal Model to Investigate the Muscular Force Response. *Frontiers in Bioengineering and Biotechnology*, 2020b.

Stollenmaier, K., Nadler, T., Pley, C., Ilg, W., Wolfen, S., Schmitt, S., and Haeufle, D. F. B. A coherent numerical and biorobotic framework to investigate neuro-muscular interaction in goal-directed arm movements. 2020c.

Stollenmaier, K., Rist, I. S., Izzi, F., and Haeufle, D. F. B. Simulating the response of a neuro-musculoskeletal model to assistive forces: implications for the design of wearables compensating for motor control deficits. In *IEEE International Conference on Biomedical Robotics & Biomechatronics, © 2020 IEEE*, New York, 2020d.

Stops, A., Wilcox, R., and Jin, Z. Computational modelling of the natural hip: A review of finite element and multibody simulations, 2012.

Suissa, D. R. Modeling, Control and Optimization in Human Motor Control: A Simulation Study of a Physiological Human Arm. Master's thesis, University of Stuttgart, 2017.

Sutton, R. S. and Barto, A. G. *Reinforcement Learning: An Introduction*. MIT Press, 1998.

Teka, W. W., Hamade, K. C., Barnett, W. H., Kim, T., Markin, S. N., Rybak, I. A., and Molkov, Y. I. From the motor cortex to the movement and back again. *PloS one*, 12(6), 2017.

ten Broeke, G. *Sensitivity analysis methodologies for analysing emergence using agent-based models*. PhD thesis, Wageningen University, 2017.

Ting, L. H. and Macpherson, J. M. A limited set of muscle synergies for force control during a postural task. *Journal of Neurophysiology*, 93(1):609–613, 2005.

Tishby, N., Pereira, F. C., and Bialek, W. The information bottleneck method. In *37th Annual Allerton Conference on Communication, Control and Computing*, Illinois, 1999. Urbana-Champaign.

Todorov, E. Optimality principles in sensorimotor control. *Nature Neuroscience*, 7(9):907–915, 2004.

Todorov, E. and Jordan, M. I. Optimal feedback control as a theory of motor coordination. *Nature Neuroscience*, 5(11):1226–1235, 2002.

Tomalka, A., Rode, C., Schumacher, J., and Siebert, T. The active force-length relationship is invisible during extensive eccentric contractions in skinned skeletal muscle fibres. *Proceedings of the Royal Society B: Biological Sciences*, 284(1854), 2017.

Topka, H., Konczak, J., and Dichgans, J. Coordination of multi-joint arm movements in cerebellar ataxia: Analysis of hand and angular kinematics. *Experimental Brain Research*, 119(4):483–492, 1998a.

Topka, H., Konczak, J., Schneider, K., Boose, A., and Dichgans, J. Multijoint arm movements in cerebellar ataxia: Abnormal control of movement dynamics. *Experimental Brain Research*, 119(4):493–503, 1998b.

Tsagarakis, N. and Caldwell, D. G. Improved modelling and assessment of pneumatic muscle actuators. In *Proceedings 2000 ICRA. Millennium Conference. IEEE International Conference on Robotics and Automation. Symposia Proceedings (Cat. No. 00CH37065)*, volume 4, pages 3641–3646. IEEE, 2000.

Tu, Q., Wang, Y., Yue, D., and Dwomoh, F. Analysis on the impact factors for the pulling force of the mckibben pneumatic artificial muscle by a fem model. *Journal of Robotics*, 2020: 1–11, 2020.

Tytell, E. D., Holmes, P., and Cohen, a. H. Spikes alone do not behavior make: why neuroscience needs biomechanics. *Current opinion in neurobiology*, 21(5):816–22, 2011.

Uno, Y., Kawato, M., and Suzuki, R. Formation and control of optimal trajectory in human multijoint arm movement. *Biological Cybernetics*, 61(2):89–101, 1989.

Valero-Cuevas, F. J., Hoffmann, H., Kurse, M. U., Kutch, J. J., and Theodorou, E. A. Computational models for neuromuscular function. *IEEE Reviews in Biomedical Engineering*, 2: 110–135, 2009.

van der Krogt, M. M., de Graaf, W. W., Farley, C. T., Moritz, C. T., Richard Casius, L. J., and Bobbert, M. F. Robust passive dynamics of the musculoskeletal system compensate for unexpected surface changes during human hopping. *Journal of Applied Physiology*, 107(3): 801–808, 2009.

van Soest, A., Bobbert, M., Iijima, T., Shimizu, K., and Asanuma, N. The Contribution of Muscle Properties in the Control of Explosive Movements. *Biological Cybernetics*, 69(3): 195–204, 1993a.

van Soest, A. J., Schwab, A. L., Bobbert, M. F., and van Ingen Schenau, G. J. The influence of the biarticularity of the gastrocnemius muscle on vertical-jumping achievement. *Journal of Biomechanics*, 26(1):1–8, 1993b.

van Zandwijk, J. P., Bobbert, M. F., Baan, G. C., and Huijing, P. A. From twitch to tetanus: performance of excitation dynamics optimized for a twitch in predicting tetanic muscle forces. *Biological Cybernetics*, 75(5):409–417, 1996.

Varghese, R. J., Freer, D., Deligianni, F., Liu, J., and Yang, G.-Z. Wearable Robotics for Upper-Limb Rehabilitation and Assistance. In *Wearable Technology in Medicine and Health Care*, pages 23–69. Elsevier, 2018.

Vitiello, N., Oddo, C. M., Lenzi, T., Roccella, S., Beccai, L., Vecchi, F., Carrozza, M. C., and Dario, P. Neuro-robotics paradigm for intelligent assistive technologies. In *Intelligent Assistive Robots*, pages 1–40. Springer, 2015.

von Förster, H. *Understanding Understanding - Essays on Cybernetics and Cognition*. Springer Verlag, New York, 2003.

von Uexkuell, J. A stroll through the worlds of animals and men. In Schiller, C. H., editor, *Instinctive Behavior*, pages 5–80. International Universities Press, New York, 1957.

Wachholder, K. and Altenburger, H. Beiträge zur Physiologie der willkürlichen Bewegung. *Pflügers Archiv European Journal of Physiology*, 214(1):642–661, 1926.

Wagner, H. and Blickhan, R. Stabilizing function of skeletal muscles: an analytical investigation. *Journal of Theoretical Biology*, 199(2):163–79, 1999.

Wagner, H., Giesl, P., and Blickhan, R. Musculoskeletal Stabilization of the Elbow - Complex or Real. *Journal of Mechanics in Medicine and Biology*, 07(03):275, 2007.

Walter, J. R., Günther, M., Haeufle, D. F. B., and Schmitt, S. A geometry- and muscle-based control architecture for synthesising biological movement. *Biological Cybernetics*, 2021.

Wang, Y. and Kheddar, A. Impact-Friendly Robust Control Design with Task-Space Quadratic Optimization. In *Proceedings of the 2019 IEEE Robotics: Science and Systems (RSS), Freiburg im Breisgau, Germany*, 2019.

Wei, K., Wertman, G., and Sternad, D. Interactions between rhythmic and discrete components in a bimanual task. *Motor control*, 7(2):134–154, 2003.

Weiler, J., Saravanamuttu, J., Gribble, P. L., and Pruszynski, J. A. Coordinating long-latency stretch responses across the shoulder, elbow, and wrist during goal-directed reaching. *Journal of Neurophysiology*, 116(5):2236–2249, 2016.

Weiler, J., Gribble, P. L., and Pruszynski, J. A. Rapid feedback responses are flexibly coordinated across arm muscles to support goal-directed reaching. *Journal of Neurophysiology*, 119 (2):537–547, 2018.

Weiler, J., Gribble, P. L., and Pruszynski, J. A. Spinal stretch reflexes support efficient hand control. *Nature neuroscience*, 22(4):529–533, 2019.

Wickramatunge, K. C. and Leephakpreeda, T. Empirical modeling of dynamic behaviors of pneumatic artificial muscle actuators. *ISA Transactions*, 52(6):825–834, 2013.

Wierzbicka, M. M., Wiegner, A. W., and Shahani, B. T. Role of agonist and antagonist muscles in fast arm movements in man. *Experimental Brain Research*, 63(2):331–340, 1986.

Wise, S. P. and Shadmehr, R. Motor Control. *Encyclopedia of the Human Brain*, 3(1):1–21, 2002.

Wochner, I., Driess, D., Zimmermann, H., Haeufle, D. F. B., Toussaint, M., and Schmitt, S. Optimality Principles in Human Point-to-Manifold Reaching Accounting for Muscle Dynamics. *Frontiers in Computational Neuroscience*, 14:38, 2020.

Wolfen, S., Walter, J., Günther, M., Haeufle, D. F., and Schmitt, S. Bioinspired pneumatic muscle spring units mimicking the human motion apparatus: benefits for passive motion range and joint stiffness variation in antagonistic setups. In *2018 25th International Conference on Mechatronics and Machine Vision in Practice (M2VIP)*, pages 1–6. IEEE, 2018.

Wolpert, D. M. Computational Approaches to Motor Control. *Trends in Cognitive Sciences*, 1 (6):1–15, 1997.

Wolpert, D. M. and Ghahramani, Z. Computational principles of movement neuroscience. *Nature Neuroscience*, 3:1212–1217, 2000.

Wolpert, D. M. and Kawato, M. Multiple paried forward and inverse models for motor control. *Neural Networks*, 11:1317–1329, 1998.

Wolpert, D. M., Miall, R. C., and Kawato, M. Internal models in the cerebellum. *Trends in Cognitive Sciences*, 2(9):338–347, 1998.

Wolpert, D. M., Diedrichsen, J., and Flanagan, J. R. Principles of sensorimotor learning. *Nature Reviews Neuroscience*, 12(12), 2011.

Yang, J. F., Scholz, J. P., and Latash, M. L. The role of kinematic redundancy in adaptation of reaching. *Experimental Brain Research*, 176(1):54–69, 2007.

Zahedi, K. and Ay, N. Quantifying morphological computation. *Entropy*, 15:1887–1915, 2013.

Appendix: Supplementary results and additional information

A1 Model parameters of *Arm26*

Note that the following tables were published/submitted as electronic supplementary material accompanying Haeufle et al. (2020a); Stollenmaier et al. (2020b,c,d).

	Length [m]	d [m]	Mass [kg]	I [kgm^2]	I with exoskeleton [kgms^2]
Upper arm	0.335	0.146	2.10	0.024	0.024
Lower arm	0.263	0.179	1.65	0.025	0.1118

Table A1.1: **Mechanical parameters of the skeletal structure (Kistemaker et al. (2006)).** With d: distance from proximal joint to center of mass and I: moment of inertia with respect to the center of mass. Last column: when comparing to experiments, the inertia properties of the lower arm can be adapted according to an arm that is attached to an exoskeleton robot that was used by Bhanpuri et al. (2014).

	Parameter	Unit	Value	Source	Description
CE	ΔW^{des}	[ ]	0.45	similar to Bayer et al. (2017); Kistemaker et al. (2006)	width of normalized bell curve in descending branch, adapted to match observed force-length curves
	ΔW^{asc}	[ ]	0.45	similar to Bayer et al. (2017); Kistemaker et al. (2006)	width of normalized bell curve in ascending branch, adapted to match observed force-length curve
	$\nu^{\text{CE,des}}$	[ ]	1.5	Mörl et al. (2012)	exponent for descending branch
	$\nu^{\text{CE,asc}}$	[ ]	3.0	Mörl et al. (2012)	exponent for ascending branch
	$A^{\text{rel},0}$	[ ]	0.2	Günther (1997)	parameter for contraction dynamics: maximum value of A^{rel}
	$B^{\text{rel},0}$	[1/s]	2.0	Günther (1997)	parameter for contraction dynamics: maximum value of B^{rel}

	$\mathcal{S}^{\text{ecc}}$	[ ]	2.0	van Soest et al. (1993a)	relation between $F(v)$ slopes at $v^{\text{CE}} = 0$
	$\mathcal{F}^{\text{ecc}}$	[ ]	1.5	van Soest et al. (1993a)	factor by which the force can exceed F^{isom} for large eccentric velocities
PEE	$\mathcal{L}^{\text{PEE},0}$	[ ]	0.95	Günther (1997)	rest length of PEE normalized to optimal length of CE
	ν^{PEE}	[ ]	2.5	Mörl et al. (2012)	exponent of F^{PEE}
	$\mathcal{F}^{\text{PEE}}$	[ ]	2.0	Mörl et al. (2012)	force of PEE if l^{CE} is stretched to ΔW^{des}
SDE	D^{SDE}	[ ]	0.3	Mörl et al. (2012)	dimensionless factor to scale $d^{\text{SDE,max}}$
	R^{SDE}	[ ]	0.01	Mörl et al. (2012)	minimum value of d^{SDE} (at $F^{MTU} = 0$), normalized to $d^{\text{SDE,max}}$
SEE	$\Delta U^{\text{SEE,nll}}$	[ ]	0.0425	Mörl et al. (2012)	relative stretch at non-linear linear transition
	$\Delta U^{\text{SEE,l}}$	[ ]	0.017	Mörl et al. (2012)	relative additional stretch in the linear part providing a force increase of $\Delta F^{\text{SEE},0}$
	$\Delta F^{\text{SEE},0}$	[N]	$0.4\,F^{\max}$		both force at the transition and force increase in the linear part
Hatze	m	[1/s]	11.3	Kistemaker et al. (2006)	time constant for the activation dynamics
	c	[mol/l]	1.37e-4	Kistemaker et al. (2006)	constant for the activation dynamics
	η	[l/mol]	5.27e4	Kistemaker et al. (2006)	constant for the activation dynamics
	k	[ ]	2.9	Kistemaker et al. (2006)	constant for the activation dynamics
	q_0	[ ]	0.005	Günther (1997)	resting active state for all activated muscle fibers
	ν	[ ]	3	Kistemaker et al. (2006)	constant for the activation dynamics

Table A1.2: **Muscle non-specific actuation parameters for the muscles and the activation dynamics.**

	$F^{\max}$ [N]	$l^{\text{CE,opt}}$ [m]	$l^{\text{SEE,0}}$ [m]
Monarticular Elbow Flexion (MEF)	1420	0.092	0.182
Monarticular Elbow Extension (MEE)	1550	0.093	0.187
Monoarticular Shoulder Anteversion (MSA)	838	0.134	0.039
Monoarticular Shoulder Retroversion (MSR)	1207	0.140	0.066
Biarticular Elbow Flexion Shoulder Anteversion (BEFSA)	414	0.151	0.245
Biarticular Elbow Extension Shoulder Retroversion (BEESR)	603	0.152	0.260

Table A1.3: **Muscle-specific actuation parameters (Kistemaker et al. (2006) and Kistemaker et al. (2013)).** With $F^{\max}$: maximum isometric force, $l^{\text{CE,opt}}$: optimal length of the contractile element, $l^{\text{SEE,0}}$ rest length of the serial elastic element. The lengths of $l^{\text{CE,opt}}$ and $l^{\text{SEE,0}}$ were adapted to match the muscle path routed through the ellipses in order to allow for a big range of motion. For this parameter adaptation method see Suissa (2017).

Mechanics parameters defining the geometry and the mechanical properties

```
% Gravity
PM.Gravity = [0 0 -9.80665];

%% %%%%%%%%%%%%%%%%%%%
% Segment parameters %
%%%%%%%%%%%%%%%%%%%%%%%
PM.SegShoulder.p_Bone_CoM           = [0 0 0]; %[m] position of Bone CoM relative to proximal joint
PM.SegShoulder.p_joint_distal       = [0 -.1816 0]; %[m] position of distal joint relative to CoM

PM.SegShoulder.m_Bone               = 16.895560; %[kg] m
PM.SegShoulder.MomInert_Bone        = [0.096243 0.0811621 0.159251]; %[kg*m^2] Diagonal elements of the inertia tensor
PM.SegShoulder.ProdInert_Bone       = [0 0 0]; %[kg*m^2] Non-diagonal elements of the intertia tensor in the order [I_yz I_zx I_xy]
PM.SegUparm.p_Bone_CoM              = [0 0 0.146]*(-1); %[m] position of Bone CoM relative to proximal joint, source: Kistemaker2007
PM.SegUparm.p_joint_distal          = [0 0 -0.189]; %[m] position of distal joint relative to CoM

PM.SegUparm.m_Bone                  = 2.10; %[kg] mass, source: Kistemaker2007
PM.SegUparm.MomInert_Bone           = [0.0154388 0.024 0.00278951]; %[kg*m^2] Diagonal elements of the inertia tensor
PM.SegUparm.ProdInert_Bone          = [0 0 0]; %[kg*m^2] Non-diagonal elements of the intertia tensor in the order [I_yz I_zx I_xy]
PM.SegForearm.p_Bone_CoM            = [0 0 0.179]*(-1); %[m] position of Bone CoM relative to proximal joint, source: Kistemaker2007
PM.SegForearm.p_joint_distal        = [0 0 -0.084]; %[m] position of distal joint relative to CoM

PM.SegForearm.m_Bone                = 1.65; %[kg] mass, source: Kistemaker2007
PM.SegForearm.MomInert_Bone         = [0.009824518 0.025 0.001500813]; %[kg*m^2] Diagonal elements of the inertia tensor
PM.SegForearm.ProdInert_Bone        = [0 0 0]; %[kg*m^2] Non-diagonal elements of the intertia tensor in the order [I_yz I_zx I_xy]
PM.SegHand.p_Bone_CoM               = [0 0 0.07]*(-1); %[m] position of Bone CoM relative to proximal joint
PM.SegHand.p_fingertip              = [0 0 -0.084]; %[m] position of distal joint relative to CoM

PM.SegHand.m_Bone                   = 0; %[kg] m
PM.SegHand.MomInert_Bone            = [0 0 0]; %[kg*m^2] Diagonal elements of the inertia tensor
PM.SegHand.ProdInert_Bone           = [0 0 0]; %[kg*m^2] Non-diagonal elements of the intertia tensor in the order [I_yz I_zx I_xy]

%%%%%%%%%%%%%%%%%%%%%
% Deflection parameters %
%%%%%%%%%%%%%%%%%%%%%

PM.Deflection.biart_flexor.rO                       = [0.03 -0.1816 0.02]; % Origin of the muscle relative to the center of mass of the parent
      body %Parent: Shoulder
PM.Deflection.biart_flexor.rI                       = [0.012, 0.0000, 0.12]; % Insertion of the muscle %Parent: Forearm
PM.Deflection.biart_flexor.Ellipse1.r               = [0.018, 0.0000, -0.1425]; % Coordinates of the reference point of deflection ellipse 1
      relative to the parent body %Parent:Uparm
PM.Deflection.biart_flexor.Ellipse1.G               = [0 1 0]*0.0001; % Length of the half-axis of ellipse 1 in y direction
PM.Deflection.biart_flexor.Ellipse1.H               = [0 0 1]*0.0001; % % Length of the half-axis of ellipse 1 in z direction
PM.Deflection.biart_flexor.Ellipse1.angle           = [0,90,0]; % Angle [deg] of rotation of the ellipse triade around y-axis to orient the
      ellipse correctly
PM.Deflection.biart_flexor.Ellipse2.r               = [0.012, 0.0000, 0.125]; %Parent: Forearm
```

```
PM.Deflection.biart_flexor.Ellipse2.G               = [0 1 0]*0.0001;
PM.Deflection.biart_flexor.Ellipse2.H               = [0 0 1]*0.0001;
PM.Deflection.biart_flexor.Ellipse2.angle           = [0,0,0];

PM.Deflection.biart_extensor.rO                     = [-0.02 -0.1816 -0.03]; %Parent: Shoulder
PM.Deflection.biart_extensor.rI                     = [-0.0225, 0.0000, 0.1925]; %Parent: Forearm
PM.Deflection.biart_extensor.Ellipse1.r             = [-0.0225, 0.0000, -0.165]; %Parent:Uparm
PM.Deflection.biart_extensor.Ellipse1.G             = [0 1 0]*0.0001;
PM.Deflection.biart_extensor.Ellipse1.H             = [0 0 1]*0.00001;
PM.Deflection.biart_extensor.Ellipse1.angle         = [0,-90,0];
PM.Deflection.biart_extensor.Ellipse2.r             = [-0.0, 0.0000, 0.1975]; %Parent: Forearm
PM.Deflection.biart_extensor.Ellipse2.G             = [0 1 0]*0.0001;
PM.Deflection.biart_extensor.Ellipse2.H             = [0 0 1]*0.03;
PM.Deflection.biart_extensor.Ellipse2.angle         = [0,-60,0];

PM.Deflection.Shoulder_Anteversion.rO               = [0.00, -0.1816, 0.05]; %Parent: Shoulder
PM.Deflection.Shoulder_Anteversion.rI               = [0.01, 0.0000, 0.045];  %Parent:Uparm
PM.Deflection.Shoulder_Anteversion.Ellipse1.r       = [0.025, -0.1816, 0.04]; %Parent: Shoulder
PM.Deflection.Shoulder_Anteversion.Ellipse1.G       = [0 1 0]*0.0001;
PM.Deflection.Shoulder_Anteversion.Ellipse1.H       = [0 0 1]*0.0001;
PM.Deflection.Shoulder_Anteversion.Ellipse1.angle   = [0,0,0];
PM.Deflection.Shoulder_Anteversion.Ellipse2.r       = [0.02, 0.0000, 0.1];  %Parent:Uparm
PM.Deflection.Shoulder_Anteversion.Ellipse2.G       = [0 1 0]*0.0001;
PM.Deflection.Shoulder_Anteversion.Ellipse2.H       = [0 0 1]*0.0001;
PM.Deflection.Shoulder_Anteversion.Ellipse2.angle   = [0,90,0];

PM.Deflection.Shoulder_Retroversion.rO              = [-0.035, -0.1816, 0.045]; %Parent: Shoulder
PM.Deflection.Shoulder_Retroversion.rI              = [-0.01, 0.0000, 0.045];  %Parent:Uparm
PM.Deflection.Shoulder_Retroversion.Ellipse1.r      = [-0.04, -0.1816, -0.01]; %Parent: Shoulder
PM.Deflection.Shoulder_Retroversion.Ellipse1.G      = [0 1 0]*0.0001;
PM.Deflection.Shoulder_Retroversion.Ellipse1.H      = [0 0 1]*0.0001;
PM.Deflection.Shoulder_Retroversion.Ellipse1.angle  = [0,0,0];
PM.Deflection.Shoulder_Retroversion.Ellipse2.r      = [-0.02, 0.0000, 0.1];  %Parent:Uparm
PM.Deflection.Shoulder_Retroversion.Ellipse2.G      = [0 1 0]*0.0001;
PM.Deflection.Shoulder_Retroversion.Ellipse2.H      = [0 0 1]*0.0001;
PM.Deflection.Shoulder_Retroversion.Ellipse2.angle  = [0,90,0];

PM.Deflection.Elbow_flexor.rO                       = [0.01, 0.0000, 0.038]; %Parent:Uparm
PM.Deflection.Elbow_flexor.rI                       = [0.01, 0.0000, 0.12]; %Parent: Forearm
PM.Deflection.Elbow_flexor.Ellipse1.r               = [0.0, 0.0000, -0.132]; %Parent:Uparm
PM.Deflection.Elbow_flexor.Ellipse1.G               = [0 1 0]*0.0001;
PM.Deflection.Elbow_flexor.Ellipse1.H               = [0 0 1]*0.005;
PM.Deflection.Elbow_flexor.Ellipse1.angle           = [0,90,0];
PM.Deflection.Elbow_flexor.Ellipse2.r               = [0.01, 0.0000, 0.135]; %Parent: Forearm
PM.Deflection.Elbow_flexor.Ellipse2.G               = [0 1 0]*0.0001;
PM.Deflection.Elbow_flexor.Ellipse2.H               = [0 0 1]*0.003;
PM.Deflection.Elbow_flexor.Ellipse2.angle           = [0,90,0];

PM.Deflection.Elbow_extensor.rO                     = [-0.022, 0.0000, 0.0605]; %Parent:Uparm
PM.Deflection.Elbow_extensor.rI                     = [-0.0225, 0.0000, 0.1925]; %Parent: Forearm
PM.Deflection.Elbow_extensor.Ellipse1.r             = [-0.0225, 0.0000, -0.165]; %Parent:Uparm
PM.Deflection.Elbow_extensor.Ellipse1.G             = [0 1 0]*0.0001;
PM.Deflection.Elbow_extensor.Ellipse1.H             = [0 0 1]*0.00005;
PM.Deflection.Elbow_extensor.Ellipse1.angle         = [0,-90,0];
PM.Deflection.Elbow_extensor.Ellipse2.r             = [-0.0, 0.0000, 0.1975]; %Parent: Forearm
PM.Deflection.Elbow_extensor.Ellipse2.G             = [0 1 0]*0.0001;
PM.Deflection.Elbow_extensor.Ellipse2.H             = [0 0 1]*0.03;
PM.Deflection.Elbow_extensor.Ellipse2.angle         = [0,-60,0];
```

A2 Model parameters of *allmin*

Note that the following tables were published as electronic supplementary material accompanying Stollenmaier et al. (2020a). See this reference for the list of authors.

Name	Type	Movement	RoM [°]
Lumbar spine	Universal	left/right	$[-30 \dots 30]$
Lumbar spine	Universal	flexion/extension	$[0 \dots 30]$
Cervival spine	Universal	left/right	$[-30 \dots 30]$
Cervival spine	Universal	flexion/extension	$[-30 \dots 30]$
Shoulder (Right)	Universal	abduction/adduction	$[-10 \dots 60]$
Shoulder (Right)	Universal	flexion/extension	$[-100 \dots 10]$
Ellbow (Right)	Revolute	flexion/extension	$[-120 \dots 10]$
Wrist (Right)	Revolute	flexion/extension	$[0 \dots 0]$
Shoulder (Left)	Universal	abduction/adduction	$[-10 \dots 60]$
Shoulder (Left)	Universal	flexion/extension	$[-100 \dots 10]$
Ellbow (Left)	Revolute	flexion/extension	$[-120 \dots 10]$
Wrist (Left)	Revolute	flexion/extension	$[0 \dots 0]$
Hip (Right)	Universal	flexion/extension	$[-120 \cdots -10]$
Hip (Right)	Universal	abduction/adduction	$[-10 \dots 70]$
Knee (Right)	Revolute	flexion/extension	$[-1 \dots 120]$
Ankle (Right)	Revolute	flexion/extension	$[-20 \dots 40]$
Hip (Left)	Universal	flexion/extension	$[-120 \dots 10]$
Hip (Left)	Universal	abduction/adduction	$[-10 \dots 70]$
Knee (Left)	Revolute	flexion/extension	$[-1 \dots 120]$
Ankle (Left)	Revolute	flexion/extension	$[-20 \dots 40]$

Table A2.1: **List of all joints included in the model.**

	Parameter	Unit	Value	Source	Description
CE	ΔW^{des}	[ ]	0.45	similar to Bayer et al. (2017); Kistemaker et al. (2006)	width of normalized bell curve in descending branch, adapted to match observed force-length curves
	$\nu^{\mathrm{CE,des}}$	[ ]	1.5	Mörl et al. (2012)	exponent for descending branch
	$\nu^{\mathrm{CE,asc}}$	[ ]	3.0	Mörl et al. (2012)	exponent for ascending branch
	$A^{\mathrm{rel,0}}$	[ ]	0.2	Günther (1997)	parameter for contraction dynamics: maximum value of A^{rel}
	$B^{\mathrm{rel,0}}$	[1/s]	2.0	Günther (1997)	parameter for contraction dynamics: maximum value of B^{rel}
	$\mathcal{S}^{\mathrm{ecc}}$	[ ]	2.0	van Soest et al. (1993a)	relation between $F(v)$ slopes at $v^{\mathrm{CE}} = 0$

	$\mathcal{F}^{\text{ecc}}$	[ ]	1.5	van Soest et al. (1993a)	factor by which the force can exceed F^{isom} for large eccentric velocities
PEE	$\mathcal{L}^{\text{PEE},0}$	[ ]	0.95	Günther (1997)	rest length of PEE normalized to optimal length of CE
	ν^{PEE}	[ ]	2.5	Mörl et al. (2012)	exponent of F^{PEE}
	$\mathcal{F}^{\text{PEE}}$	[ ]	2.0	Mörl et al. (2012)	force of PEE if l^{CE} is stretched to ΔW^{des}
SDE	D^{SDE}	[ ]	0.3	Mörl et al. (2012)	dimensionless factor to scale $d^{\text{SDE,max}}$
	R^{SDE}	[ ]	0.01	Mörl et al. (2012)	minimum value of d^{SDE} (at $F^{MTU} = 0$), normalized to $d^{\text{SDE,max}}$
SEE	$\Delta U^{\text{SEE,nll}}$	[ ]	0.0425	Mörl et al. (2012)	relative stretch at non-linear linear transition
	$\Delta U^{\text{SEE,l}}$	[ ]	0.017	Mörl et al. (2012)	relative additional stretch in the linear part providing a force increase of $\Delta F^{\text{SEE},0}$
	$\Delta F^{\text{SEE},0}$	[N]	$0.4\,F^{\text{max}}$		both force at the transition and force increase in the linear part
activation dynamics	M_H	[1/s]	11.3	Kistemaker et al. (2006)	time constant for the activation dynamics
	γ_c	[mol/l]	1.37e-4	Kistemaker et al. (2006)	constant for the activation dynamics
	ρ_0	[l/mol]	5.27e4	Kistemaker et al. (2006)	constant for the activation dynamics
	a_0	[ ]	0.005	Günther (1997)	resting active state for all activated muscle fibers
	ν	[ ]	3	Kistemaker et al. (2006)	constant for the activation dynamics

Table A2.5: **Muscle non-specific actuation parameters for the muscles and the activation dynamics**.

Body Name	m [kg]	r_x [m]	r_y [m]	h_z [m]	$\mathbf{d}_1$ [m]	Child	$\mathbf{d}_2$ [m]
Pelvis (world)	10.2516	0.1224	0.1643	0.18783	[0,0,0]	Spine	[0.000557293, 0.0000, 0.12213]
						Thigh (l/r)	$[0.0147, \pm 0.0796, -0.0657]$
Spine	33.2397	0.1224	0.1643	0.4166	[-0.00055, 0.0000, -0.2083]	Head	[0.00055, 0.0000, 0.2083]
						Uparm (l/r)	$[0.00677703, \pm 0.1816, 0.10507988]$
Head	4.8869	0.0993	0.0778	0.278194	[-0.0092, 0.0000, -0.11]	-	-
Uparm (l/r)	2.1631	0.0495	–	0.3065	[0.0000, 0.0000, 0.1456]	Forearm (l/r)	[0.0000, 0.0000, -0.1609]
Forearm (l/r)	1.3389	0.0477	–	0.2725	[0.0000, 0.0000, 0.1117]	Hand (l/r)	[0.0000, 0.0000, -0.1608]
Hand (l/r)	0.5252	0.028	0.089	0.192	[0.0000, 0.0000, 0.0574]	-	-
Thigh (l/r)	8.1719	0.0947	–	0.4347	$[0.0000, \mp 0.0188, 0.1782]$	Shank (l/r)	[0.0000, 0.0000, -0.2565]
Shank (l/r)	3.3541	0.0597	–	0.4239	$[0.0000, \mp 0.0059, 0.1865]$	Foot (l/r)	[0.0000, 0.0000, -0.2374]
Foot (l/r) $*$	1.0172	0.0398	–	0.272	[-0.0656, 0.0000, 0.0402]	-	-

Table A2.2: **List of all bodies included in the model with their mechanical properties.** With m: mass, r_x,r_y: radius in x and y direction, h_z: height in z direction, $\mathbf{d}_1$: distance proximal joint to the body's center of mass and $\mathbf{d}_2$: distance center of mass to distal joint. The spine body has an underlying curvature based on Kitazaki and Griffin (1997). The allover body dimensons are based on data describing a 50th percentile male from NASA (1978).

Name	R_O [m]			Parent	R_{DF1} [m]			Parent	R_{DF2} [m]			Parent	R_I [m]			Parent
LSE	−0.0283	0.0000	0.1082	Pelvis	−0.0399	0.0000	0.1101	Pelvis	−0.0416	0.0000	−0.1310	Spine	−0.0315	0.0000	−0.1288	Spine
LSF	0.0181	0.0000	0.1006	Pelvis	0.0878	0.0000	0.0891	Pelvis	0.0693	0.0000	−0.1059	Spine	0.0089	0.0000	−0.1196	Spine
LSSBL	−0.0051	0.0500	0.1044	Pelvis	−0.0051	0.0500	0.1044	Pelvis	−0.0113	0.0500	−0.1242	Spine	−0.0113	0.0500	−0.1242	Spine
LSSBR	−0.0051	−0.0500	0.1044	Pelvis	−0.0051	−0.0500	0.1044	Pelvis	−0.0113	−0.0500	−0.1242	Spine	−0.0113	−0.0500	−0.1242	Spine
CSE	−0.0544	0.0000	0.1990	Spine	−0.0544	0.0000	0.1990	Spine	−0.0560	0.0000	−0.0701	Head	−0.0560	0.0000	−0.0701	Head
CSF	0.0427	0.0000	0.1752	Spine	0.0427	0.0000	0.1752	Spine	0.0436	0.0000	−0.0796	Head	0.0436	0.0000	−0.0796	Head
CSSBL	−0.0059	0.0500	0.1871	Spine	−0.0059	0.0500	0.1871	Spine	−0.0062	0.0500	−0.0748	Head	−0.0062	0.0500	−0.0748	Head
CSSBR	−0.0059	−0.0500	0.1871	Spine	−0.0059	−0.0500	0.1871	Spine	−0.0062	−0.0500	−0.0748	Head	−0.0062	−0.0500	−0.0748	Head
HE (l/r)	−0.0750	±0.0796	0.0253	Pelvis	−0.0750	±0.0896	−0.0947	Pelvis	−0.0750	∓0.0188	0.1209	Thigh	−0.0200	∓0.0088	0.0309	Thigh
HF (l/r)	0.0650	±0.0396	0.1008	Pelvis	0.0750	±0.0396	0.0208	Pelvis	0.0150	∓0.0188	0.1011	Thigh	0.0150	∓0.0188	0.0200	Thigh
HAbd (l/r)	−0.0250	±0.1200	0.0500	Pelvis	0.0000	±0.1519	−0.0300	Pelvis	−0.0300	±0.0400	0.0354	Thigh	−0.0200	±0.0300	0.0050	Thigh
HAdd (l/r)	0.0000	0.0000	0.0000	Pelvis	−0.0100	±0.0100	−0.1000	Pelvis	−0.0050	∓0.0351	0.0902	Thigh	0.0000	∓0.0201	0.0102	Thigh
KF (l/r)	−0.0500	0.0000	0.0000	Thigh	−0.0500	0.0000	−0.1075	Thigh	−0.0594	0.0000	0.1060	Shank	−0.0297	0.0000	0.1000	Shank
KE (l/r)	0.0400	0.0000	0.0000	Thigh	0.0299	0.0000	0.2527	Thigh	0.0300	0.0000	0.0500	Shank	0.0300	0.0000	0.0500	Shank
FE (l/r)	−0.0500	0.0000	−0.0250	Shank	−0.0500	0.0000	−0.1750	Shank	−0.1250	0.0000	0.0500	Foot	−0.1250	0.0000	0.0500	Foot
FF (l/r)	0.0300	0.0000	−0.0250	Shank	0.0300	0.0000	−0.1750	Shank	0.0300	0.0000	0.0500	Foot	0.0300	0.0000	0.0500	Foot
SE (l/r)	−0.0688	±0.1816	0.1128	Spine	−0.0500	0.0000	0.1250	Uparm	−0.0172	0.0000	0.0000	Uparm	−0.0172	0.0000	0.0000	Uparm
SF (l/r)	0.0216	±0.1816	0.1387	Spine	0.0216	±0.1816	0.1387	Spine	0.0172	0.0000	0.0000	Uparm	0.0172	0.0000	0.0000	Uparm
SAbd (l/r)	−0.0263	±0.2422	0.1353	Spine	−0.0263	±0.2422	0.1353	Spine	0.0000	±0.0172	0.0000	Uparm	0.0000	±0.0172	0.0000	Uparm
SAdd (l/r)	−0.0236	0.0000	0.1257	Spine	0.0073	±0.1250	0.1033	Spine	0.0000	∓0.0400	0.1250	Uparm	0.0000	∓0.0172	0.0000	Uparm
EF (l/r)	0.0246	0.0000	0.0000	Uparm	0.0300	0.0000	−0.0500	Uparm	0.0300	0.0000	0.0136	Forearm	0.0238	0.0000	−0.1000	Forearm
EE (l/r)	−0.0246	0.0000	0.0000	Uparm	−0.0493	0.0000	−0.1603	Uparm	−0.0476	0.0000	0.1002	Forearm	−0.0238	0.0000	0.0000	Forearm

Table A2.3: **Muscle routing parameters.** Origin R_O, Deflection Point 1 R_{DF1} and 2 R_{DF2} and Insertion R_I relative to their parent body. All numbers in this table are rounded to four decimal digits. Muscle names: EF, EE, Foot Flexion (FF), Foot Extension (FE), Hip Abduction (HAbd), Hip Adduction (HAdd), Hip Flexion (HF), Hip Extension (HE), Cervical Spine Flexion (CSF), Cervical Spine Side Bend Left (CSSBL), Cervical Spine Side Bend Right (CSSBR), Cervical Spine Extension (CSE), Knee Flexion (KF), Knee Extension (KE), Lumbar Spine Flexion (LSF), Lumbar Spine Side Bend Left (LSSBL), Lumbar Spine Side Bend Right (LSSBR), Lumbar Spine Extension (LSE), Shoulder Abduction (SAbd), Shoulder Adduction (SAdd), SF, SE.

	$F^{\max}$ [N]	$l^{\text{CE,opt}}$ [m]	ΔW^{asc}	$l^{\text{SEE,0}}$ [m]
EF	1420.0	0.1885	1.0	0.1845
EE	1550.0	0.171	0.525	0.18
FF	3000.0	0.15	1.0	0.133
FE	3000.0	0.13	1.0	0.115
HAbd	2000.0	0.18	1.0	0.121
HAdd	2000.0	0.204	0.75	0.136
HF	5000.0	0.195	1.0	0.135
HE	5000.0	0.192	1.0	0.191
CSF	5000.0	0.07	1.5	0.01
CSSBL	5000.0	0.05	1.5	0.01
CSSBR	5000.0	0.046	1.5	0.01
CSE	5000.0	0.062	1.5	0.01
KF	6000.0	0.258	0.525	0.112
KE	6000.0	0.264	1.0	0.28
LSF	15000.0	0.2	1.5	0.11
LSSBL	15000.0	0.09	1.5	0.02
LSSBR	15000.0	0.09	1.5	0.02
LSE	15000.0	0.075	1.5	0.04
SAbd	6000.0	0.12	1.0	0.08
SAdd	6000.0	0.225	1.0	0.12
SF	10000.0	0.1	1.0	0.073
SE	6000.0	0.165	1.0	0.105

Table A2.4: **Muscle-specific actuation parameters.** With $F^{\max}$: maximum isometric force, $l^{\text{CE,opt}}$: optimal length of the CE, ΔW^{asc}: width of normalized bell curve in ascending branch of the force-length relationship, $l^{\text{SEE,0}}$ rest length of the SEE, $l^{\text{CE,init}}$: initial length of the CE. Muscle names: Elbow Flexion (EF), Elbow Extension (EE), Foot Flexion (FF), Foot Extension (FE), Hip Abduction (HAbd), Hip Adduction (HAdd), Hip Flexion (HF), Hip Extension (HE), Cervical Spine Flexion (CSF), Cervical Spine Side Bend Left (CSSBL), Cervical Spine Side Bend Right (CSSBR), Cervical Spine Extension (CSE), Knee Flexion (KF), Knee Extension (KE), Lumbar Spine Flexion (LSF), Lumbar Spine Side Bend Left (LSSBL), Lumbar Spine Side Bend Right (LSSBR), Lumbar Spine Extension (LSE), Shoulder Abduction (SAbd), Shoulder Adduction (SAdd), Shoulder Flexion (SF), Shoulder Extension (SE).

A3 Additional information and results to Chapter 4

Note that the following tables and plots were published as electronic supplementary material accompanying Stollenmaier et al. (2020b). See this reference for the list of authors.

A3.1 Control parameters

			① without external torque	② with external torque, flexion	② with external torque, extension
initial position	$u^{\text{des.},0}$		0^{*}	0^{*}	0^{*}
	u_i^0	Elbow flexor	$0.0100^{\#}$	$0.0704^{\#}$	$0.198^{\#}$
		Elbow extensor	$0.0295^{\#}$	$0.0101^{\#}$	$0.0165^{\#}$
		biart. flexor	$0.0101^{\#}$	$0.0101^{\#}$	$0.0539^{\#}$
		biart. extensor	$0.0101^{\#}$	$0.0101^{\#}$	$0.0286^{\#}$
acceleration	$u^{\text{min.}}$		0.005^{*}	0.005^{*}	0.005^{*}
	$u^{\text{acc.}}$		$0.116^{\triangle}$	$0.140^{\triangle}$	$4.46 \times 10^{-4\triangle}$
	t_1		$0.410\,\text{s}^{\triangle}$	$0.509\,\text{s}^{\triangle}$	$0.382\,\text{s}^{\triangle}$
deceleration	$u^{\text{des.,dec.}}$		$0.240^{\diamondsuit}$	$0.240^{\diamondsuit}$	$0.240^{\diamondsuit}$
	$u_i^{\text{dec.}}$	Elbow flexor	$0.267^{\#}$	$0.267^{\#}$	$0.204^{\#}$
		Elbow extensor	$0.0898^{\#}$	$0.0898^{\#}$	$0.259^{\#}$
		biart. flexor	$0.261^{\#}$	$0.261^{\#}$	$0.221^{\#}$
		biart. extensor	$0.229^{\#}$	$0.229^{\#}$	$0.243^{\#}$
	t_2		$0.7\,\text{s}^{*}$	$0.7\,\text{s}^{*}$	$0.7\,\text{s}^{*}$
final position	$u^{\text{des.,final}}$		0.3^{*}	0.3^{*}	0.3^{*}
	u_i^{final}	Elbow flexor	$0.330^{\#}$	$0.334^{\#}$	$0.221^{\#}$
		Elbow extensor	$0.104^{\#}$	$0.0928^{\#}$	$0.325^{\#}$
		biart. flexor	$0.324^{\#}$	$0.326^{\#}$	$0.266^{\#}$
		biart. extensor	$0.284^{\#}$	$0.283^{\#}$	$0.307^{\#}$
	k_p		$0.2^{\diamondsuit}$	$0.2^{\diamondsuit}$	$0.2^{\diamondsuit}$
	k_d		$0.15^{\diamondsuit}$	$0.15^{\diamondsuit}$	$0.15^{\diamondsuit}$
	δ		0.05^{*}	0.05^{*}	0.05^{*}

Table A3.1: **Control parameters used in the computer simulation of external perturbations during point-to-point movements in a horizontal plane.** For a better understanding of the abbreviations see Figure 4.3. Gray values indicate that the same values as for ① have been used. Meaning of the symbols: $*$: quantities that we set to a fixed value, #: optimized such that there is an equilibrium point at this position given the desired level of co-contraction, $\triangle$: optimized to match the unperturbed trajectory for case ①, $\diamondsuit$: optimized to match the perturbed trajectories for case ①.

A3.2 Additional results using time delay $\delta = 25\,\mathrm{ms}$

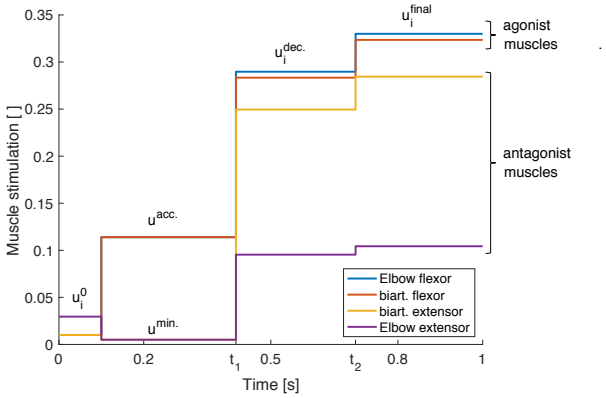

Figure A3.1: **Triphasic stimulation pattern for a flexion movement.** Starting from the initial position at $t = 0.1\,\mathrm{s}$, during the acceleration phase, mainly the agonist muscles are active. In the second phase between $t = t_1$ and $t = t_2$, both muscle groups are active, braking the movement. In the last phase for $t > t_2$, again both muscle groups are active in order to reach the final position and hold it with a desired level of co-contraction.

A3.2.1 Static perturbation of inertia and viscosity

	Closed-loop	Open-loop
Increased damping	0.53	3.47
Decreased damping	0.03	0.70
Increased inertia	0.54	0.84
Decreased inertia	2.99	2.94
Sum of all cases	4.09	7.94

Table A3.2: **Quantification of the difference between simulation and experiment for case (1) by evaluating the cost function that was used in the optimization of the closed-loop control parameters and splitting it into the contributions of the different perturbations.** Hence, for the single cases, a value smaller than one means that the result lies within the experimental standard deviation area (taking the maximum standard deviation in each direction).

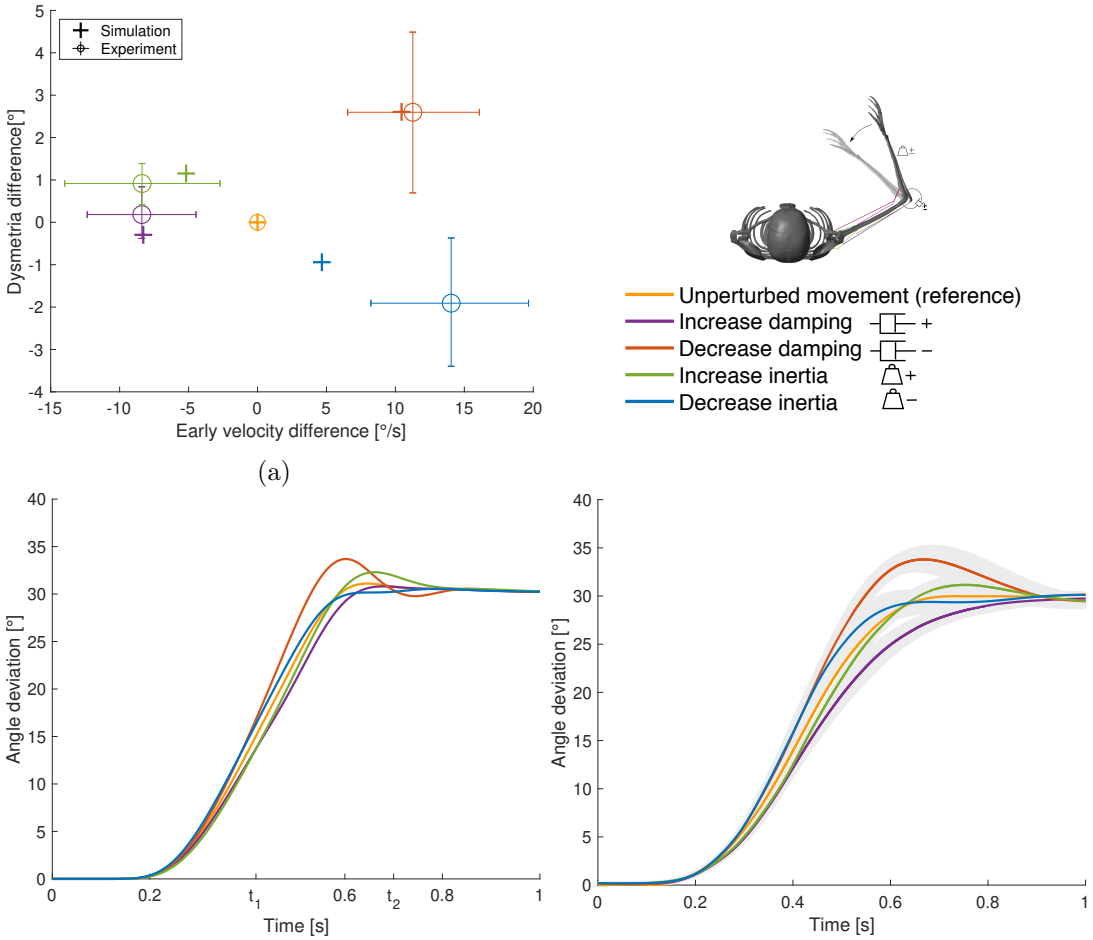

(a)

(b) Simulation

(c) Experiment (Bhanpuri et al. (2014))

Figure A3.2: **Results for case** ①. (a) Evaluation criterion for the static perturbations: Early velocity difference in relation to the dysmetria difference (both calculated as the early velocity/dysmetria of the perturbed movement minus the early velocity/dysmetria of the reference movement) shown for both, simulation and experiment. The experimental results are digitized from Bhanpuri et al. (2014), the control group averages (n=11) are shown and the error bars indicate standard deviation. (b) our simulation results and (c) experimental results digitized from Bhanpuri et al. (2014) for one typical control subject in null condition (reference) and with perturbations (shaded areas indicate standard deviation).

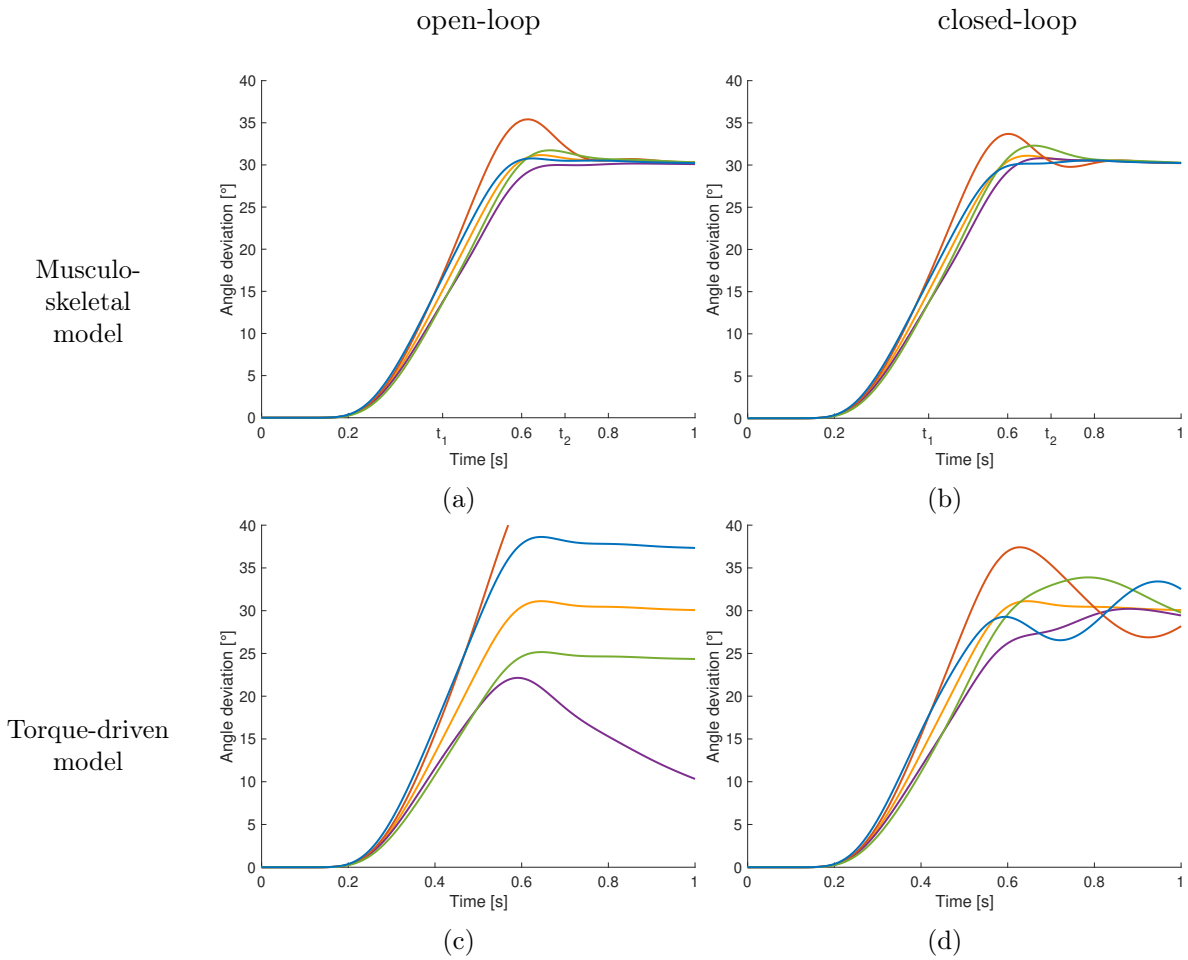

Figure A3.3: **Comparison to open-loop and torque-driven model for case** ①. (a) Resulting trajectories when controlling the musculoskeletal model open-loop, (b) trajectories when controlling the musculoskeletal model closed-loop, (c) trajectories when controlling a purely torque-driven model open-loop and (d) trajectories when controlling a purely torque-driven model closed-loop.

A3.2.2 Dynamic torque perturbation

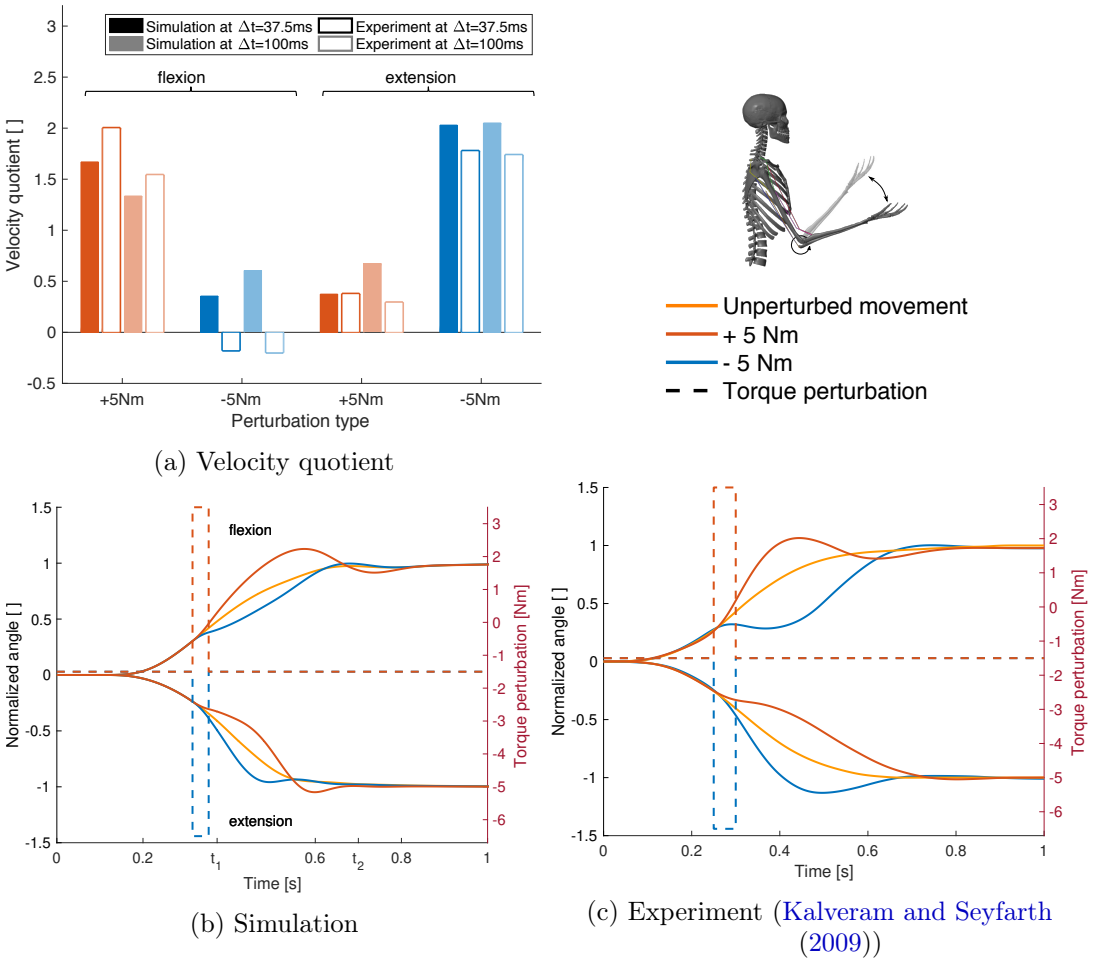

(a) Velocity quotient

(b) Simulation

(c) Experiment (Kalveram and Seyfarth (2009))

Figure A3.4: **Results for case** ②. (a) Evaluation criterion for the dynamic perturbations: The quotient of the angular velocity at the beginning of the perturbation and after Δt (37.5 ms and 100 ms, see Equation (4.6)) shown for both, the simulation results (filled bars) and the experimental results (empty bars) for all four perturbation types (experimental results are digitized from Kalveram and Seyfarth (2009)). (b) Joint angle trajectories for the four different perturbation types in our simulation and (c) in the experiment (digitized from Kalveram and Seyfarth (2009)). Note that the experimental results show the trajectory for one typical control subject. The upper curves show flexion movements, the lower curves show extension movements. The dashed lines visualize the applied torque perturbations.

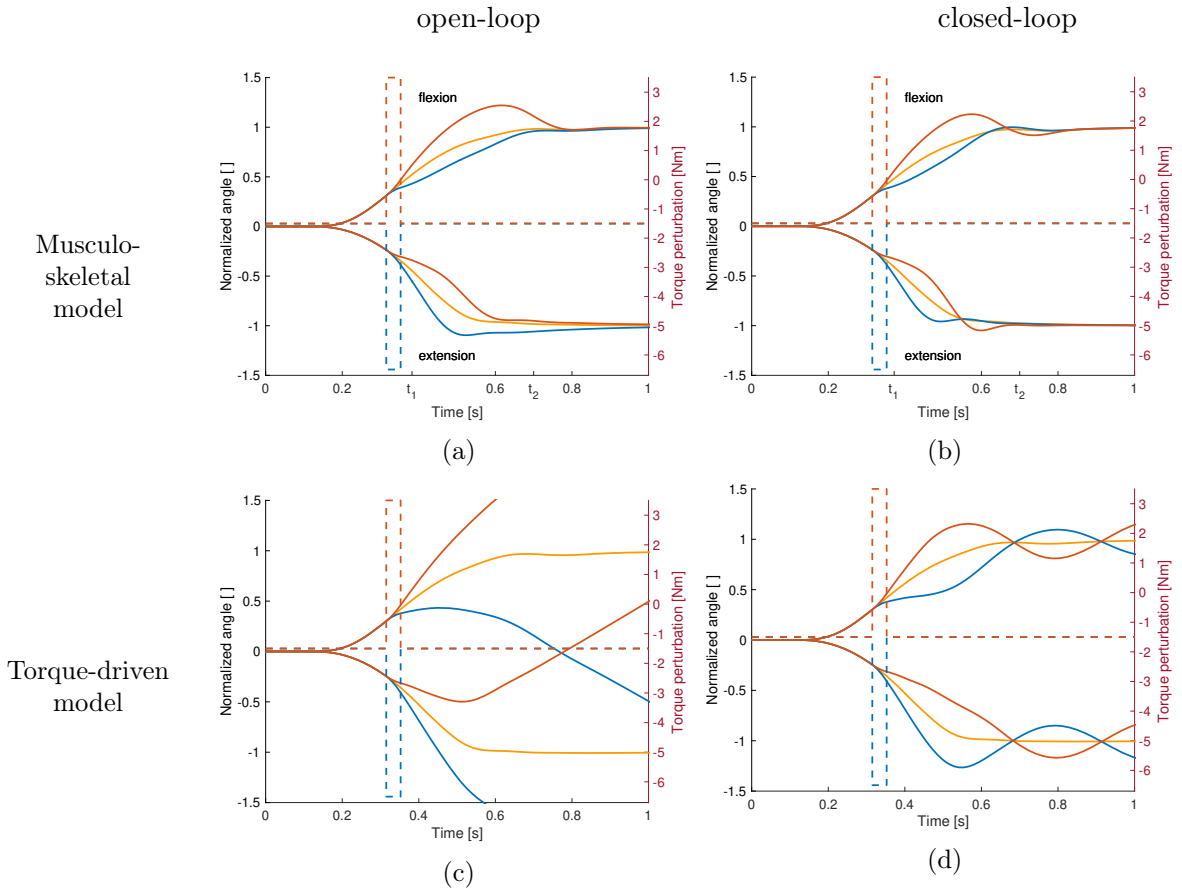

Figure A3.5: **Comparison to open-loop and torque-driven model for case ②.** (a) Resulting trajectories when controlling the musculoskeletal model open-loop, (b) trajectories when controlling the musculoskeletal model closed-loop, (c) trajectories when controlling a purely torque-driven model open-loop and (d) trajectories when controlling a purely torque-driven model closed-loop with the same controller as described above.

A3.2.3 Internal force responses

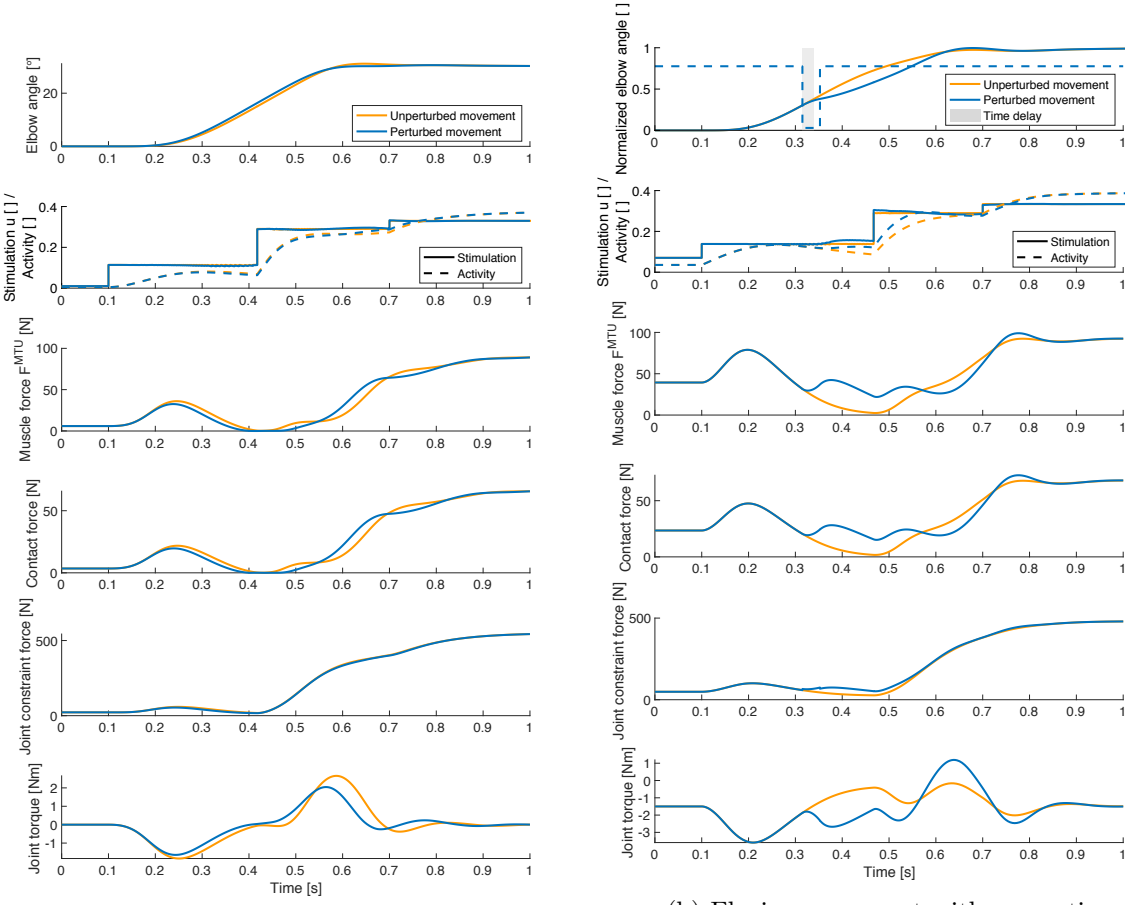

(a) Increased inertia

(b) Flexion movement with a negative torque impulse perturbation

Figure A3.6: **Selection of quantities that can be investigated using our model.** Elbow joint angle, muscle stimulation and activity, muscle force, muscle-bone contact force, joint constraint force and active joint torque for the unperturbed trajectory (orange) and for a perturbed movement (blue). These results are exemplary shown for the elbow flexor muscle and (a) for an increase in inertia and (b) for a flexion movement with a negative torque impulse perturbation. Here, the gray area visualizes the length of the time delay in the controller (50 ms), i.e. the time after the perturbation before the feedback mechanism is activated. Note that the total muscle stimulation in the unperturbed case is equal to the open-loop contribution in the perturbed case. For all forces, the resultant force is shown.The contact force is the force at the first deflection ellipse. The active joint torque represents the torque acting on the joint that is a consequence of the muscle forces.

A3.2.4 Control parameters

			① without external torque	② with external torque, flexion	② with external torque, extension
initial position	$u^{\text{des.},0}$		0^{*}	0^{*}	0^{*}
	u_i^0	Elbow flexor	$0.0100^{\#}$	$0.0704^{\#}$	$0.198^{\#}$
		Elbow extensor	$0.0295^{\#}$	$0.0101^{\#}$	$0.0165^{\#}$
		biart. flexor	$0.0101^{\#}$	$0.0101^{\#}$	$0.0539^{\#}$
		biart. extensor	$0.0101^{\#}$	$0.0101^{\#}$	$0.0286^{\#}$
acceleration	$u^{\text{min.}}$		0.005^{*}	0.005^{*}	0.005^{*}
	$u^{\text{acc.}}$		$0.114^{\triangle}$	$0.138^{\triangle}$	$2.51 \times 10^{-6\triangle}$
	t_1		$0.418\,\text{s}^{\triangle}$	$0.467\,\text{s}^{\triangle}$	$0.372\,\text{s}^{\triangle}$
deceleration	$u^{\text{des.,dec.}}$		$0.262^{\diamondsuit}$	$0.262^{\diamondsuit}$	$0.262^{\diamondsuit}$
	$u_i^{\text{dec.}}$	Elbow flexor	$0.290^{\#}$	$0.290^{\#}$	$0.212^{\#}$
		Elbow extensor	$0.0954^{\#}$	$0.0954^{\#}$	$0.283^{\#}$
		biart. flexor	$0.283^{\#}$	$0.283^{\#}$	$0.237^{\#}$
		biart. extensor	$0.249^{\#}$	$0.249^{\#}$	$0.266^{\#}$
	t_2		$0.7\,\text{s}^{*}$	$0.7\,\text{s}^{*}$	$0.7\,\text{s}^{*}$
final position	$u^{\text{des.,final}}$		0.3^{*}	0.3^{*}	0.3^{*}
	u_i^{final}	Elbow flexor	$0.330^{\#}$	$0.334^{\#}$	$0.221^{\#}$
		Elbow extensor	$0.104^{\#}$	$0.0928^{\#}$	$0.325^{\#}$
		biart. flexor	$0.324^{\#}$	$0.326^{\#}$	$0.266^{\#}$
		biart. extensor	$0.284^{\#}$	$0.283^{\#}$	$0.307^{\#}$
	k_p		$0.503^{\diamondsuit}$	$0.503^{\diamondsuit}$	$0.503^{\diamondsuit}$
	k_d		$0.0484^{\diamondsuit}$	$0.0484^{\diamondsuit}$	$0.0484^{\diamondsuit}$
	δ		0.025^{*}	0.025^{*}	0.025^{*}

Table A3.3: **Control parameters used in the computer simulation of external perturbations during point-to-point movements in a horizontal plane.** For a better understanding of the abbreviations see Figure 4.3. Gray values indicate that the same values as for ① have been used. Meaning of the symbols: $*$: quantities that we set to a fixed value, #: optimized such that there is an equilibrium point at this position given the desired level of co-contraction, $\triangle$: optimized to match the unperturbed trajectory for case ①, $\diamondsuit$: optimized to match the perturbed trajectories for case ①.

A4 Additional information and results to Chapter 6

Note that large parts of this chapter were submitted as electronic supplementary material accompanying Haeufle et al. (2020a). See this reference for the list of authors.

A4.1 More details on quantifying morphological computation

This section discusses one concept of quantifying morphological computation. For a full discussion, the reader is referred to Ghazi-Zahedi (2019a).

A4.1.1 Causal Model of the Sensorimotor Loop

We assume that there is a canonical way to separate a cognitive system into four parts, namely brain, sensors, actuators, and body. We are fully aware that the system–environment separation is a very difficult and yet unsolved question for biological systems (see e.g., von Förster (2003) for a discussion). In fact, one question of this paper is to investigate different levels of hierarchy with respect to quantifying morphological computation.

In our concept of the sensorimotor loop, which is derived from Pfeifer et al. (2007), the brain or controller sends signals to the actuators that influence the environment (see Figure A4.1). We prefer the notion of the system's *Umwelt* (Ay and Löhr, 2015; Clark, 1996; von Uexkuell, 1957), which is the part of the system's environment that can be affected by the system and itself affects the system. The state of the actuators and the *Umwelt* are not directly accessible to the cognitive system, but the loop is closed as information about both the *Umwelt* and the actuators are provided to the controller by the system's sensors. In addition to this general concept, which is widely used in the embodied artificial intelligence community (see e.g., (Pfeifer et al., 2007)), we introduce the notion of *world* to the sensorimotor loop, that is, the system's morphology and the system's *Umwelt*. This differentiation between body and world is analogous to the agent–environment distinction made in the context of reinforcement learning (Sutton and Barto, 1998), where the environment is defined as everything that cannot be changed arbitrarily by the agent.

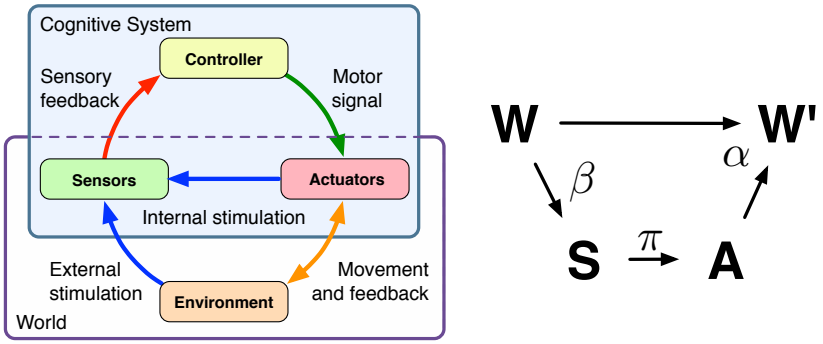

Figure A4.1: **Sensorimotor Loop.** Left-hand side: schematics of the sensorimotor loop (redrawn from Pfeifer et al. (2007)), Right-hand side: causal diagram of a reactive system.

Arm movements, and actually most behaviours that are interesting in the context of morphological computation, can be modelled sufficiently as reactive behaviours. Hence, for the remainder of this work, we will omit the controller and assume that the sensors are directly connected to the actuators. For a discussion of the causal diagram for non-reactive systems, the reader is referred to Ay and Zahedi (2014). Quantifications of morphological computation for non-reactive systems are discussed in Zahedi and Ay (2013).

The causal diagram of the sensorimotor loop is shown on the right-hand side of Figure A4.1. The random variables A, S, W, and W' refer to actuator signals, sensor signals, and the current and next world state. Directed edges reflect causal dependencies between the random variables. The random variables S and A are not to be mistaken with the sensors and actuators. The variable S is the output of the sensors, which is available to the controller or brain, and the action A is the input that the actuators take. Consider an artificial robotic system as an example. Then the sensor state S could be the pixel matrix delivered by a camera sensor and the action A could be a numerical value that is taken by a motor controller and converted in currents to drive a motor.

We use capital letters (A, W, ...) to denote random variables, non-capital letters (a, w, ...) to denote a specific value that a random variable can take, and calligraphic letters ($\mathcal{A}$, $\mathcal{W}$, ...) to denote the alphabet for the random variables. This means that a_t is the specific value that the random variable A can take at time $t \in \mathbb{N}$, and it is from the set $a_t \in \mathcal{A}$. Greek letters refer to generative kernels, i.e., kernels that describe an actual underlying mechanism or a causal relation between two random variables. In the causal graphs throughout this paper, these kernels are represented by direct connections between corresponding nodes. This notation is used to distinguish generative kernels from others, such as the conditional probability of a given that w was previously seen, denoted by $p(a|w)$, which can be calculated or sampled but that does not reflect a direct causal relation between the two random variables A and W (see Figure A4.1).

We abbreviate the random variables for better comprehension in the remainder of this work, as all measures consider random variables of consecutive time indices. Therefore, we use the following notation. Random variables without any time index refer to time index t and hyphened variables to time index $t+1$. The two variables W and W' refer to W_t and W_{t+1}, respectively.

A4.1.2 Quantifying Morphological Computation

We can now restate the two original concepts of quantifying morphological computation (Ghazi-Zahedi, 2019a; Zahedi and Ay, 2013) (see Figure A4.2).

The basis for both original concepts $\mathrm{MC_A}$ and $\mathrm{MC_W}$ is the world dynamics kernel $\alpha(w'|w,a)$, which describes how the next world states W' depends on the current world state W and the current action A (see Figure A4.1, right-hand side, and Figure A4.2, left-hand side, respectively). For the first concept $\mathrm{MC_A}$, let us assume that there is no dependence of the next world state W' on the current action A. In this case, the world dynamics kernel $\alpha(w'|w,a)$ reduces to $\hat{\alpha}(w'|w)$ (which is given by $\hat{\alpha}(w'|w) = \sum_a {}^{p(w',w,a)}\!/_{p(w)}$, see also Figure A4.2, centre). As a result, we would state that we have maximal morphological computation, as the system's behaviour is not controlled by the brain at all. An example of such a system is the Passive Dynamic Walker (Collins et al., 2005; McGeer, 1990). We can measure how much the

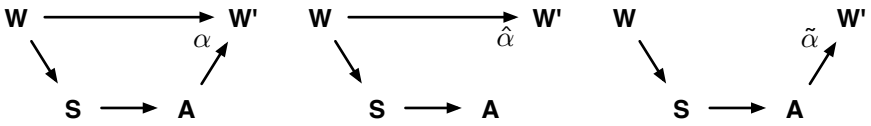

Figure A4.2: **Visualization of the two concepts** $\mathrm{MC_A}$ **and** $\mathrm{MC_W}$. Left-hand side: causal diagram for a reactive system. Centre: causal diagram assuming no effect of the action A on the next world state W'. Right-hand side: causal diagram assuming no effect of the previous world state W on the next world state W'.

observed behaviour differs from this assumption with the Kullback-Leibler divergence (Cover and Thomas, 2006). This leads to the following formalisation:

$$\mathrm{MC_A} := \sum_{w',w,a} p(w',w,a) \log_2 \frac{\alpha(w'|w,a)}{\hat{\alpha}(w'|w)} \tag{A4.1}$$

$$= I(W';A|W) \tag{A4.2}$$

Unfortunately, Equation (A4.1) is zero for maximal morphological computation, which is why we initially chose to normalise and invert it, leading to the following definition:

$$\mathrm{MC_A} := 1 - \frac{1}{\log_2 |\mathcal{W}|} \sum_{w',w,a} p(w',w,a) \log_2 \frac{\alpha(w'|w,a)}{\hat{\alpha}(w'|w)} \tag{A4.3}$$

The second concept, $\mathrm{MC_W}$ starts with the opposite assumption, namely, that the current world state W does not have any influence on the next world state W' (see Figure A4.2, right-hand side). In this case, the world dynamics kernel $\alpha(w'|w,a)$ reduces to $\tilde{\alpha}(w'|a)$ (which is given by $\tilde{\alpha}(w'|a) = \sum_w {}^{p(w',w,a)}/_{p(a)}$, see also Figure A4.2) and analogously to the following definition for $\mathrm{MC_W}$:

$$\mathrm{MC_W} := \sum_{w',w,a} p(w',w,a) \log_2 \frac{\alpha(w'|w,a)}{\tilde{\alpha}(w'|a)} \tag{A4.4}$$

$$= I(W';W|A) \tag{A4.5}$$

The relation of the measures to transfer entropy (Bossomaier et al., 2016; Schreiber, 2000) and the information bottleneck (Tishby et al., 1999) are discussed in Ghazi-Zahedi (2019a); Zahedi and Ay (2013).

Next, we briefly describe, how the quantification can be calculated from data.

A4.1.3 Estimating Quantifications of Morphological Computation

We will explain how to estimate information-theoretic quantities based on an estimation of entropy. A more detailed discussion about the topic can be found in (Paninski, 2003) and a more detailed discussion with respect to quantifying morphological intelligence can be found in (Ghazi-Zahedi, 2019a).

The general concepts will be discussed along the example of estimation entropy:

$$\hat{H}(X) = -\int_x \mu(x) \ln \mu(x) dx. \tag{A4.6}$$

Estimating the entropy $H(X)$ requires knowledge about the underlying probability distribution $\mu(x)$. In real-world scenarios, $\mu(x)$ cannot be accessed directly, but only via observations x_i. The task is to estimate $p(x_i)$ such that the estimated entropy $H(X) = -\sum_x p(x) \ln p(x)$ approximates $\hat{H}(X)$. The most common technique is known as binning of frequency estimation. This method uses a discrimination of the state space X and estimates $p(x_i)$ by the number of samples that fall into each bin. Hence, the entropy of X is given by:

$$H(X) = -\sum_x \frac{c_i}{N} \ln \frac{c_i}{N}, \tag{A4.7}$$

where c_i are the number of samples that fall into bin i and N is the total number of samples.

The second method is only discussed conceptually. For a full discussion, please read (Frenzel and Pompe, 2007; Ghazi-Zahedi, 2019a; Kraskov, Alexander and Stögbauer, Harald and Grassberger, Peter, 2004). The general idea is to estimate $p(x_i)$ without the intermediate step of binning the state space. Instead, the probability density is estimated by the distance to the k-nearest neighbour of each sample x_i. The distance to the k-nearest neighbour is small if the sample x_i is an area of the state space that has a high concentration of samples, and hence, the probability mass for x_i should be large. The distance to the k-nearest neighbour is large if the sample x_i is in a sparsly populated area of the state space. These assumptions are used to shape locally constant or Gaussian functions around each sample x_i.

Both methods can be used in *gomi* (Ghazi-Zahedi, 2019b) to estimate MC_W and MC_A.

A4.2 Description of the human experiments

The sole purpose of the experiments was to get a quantitative basis for the variations of the simulated movements. These variations allowed us to statistically test the main hypothesis of this paper: that there is a difference in morphological computation between different hierarchy levels.

A4.2.1 Experimental setup: general description

A quantitative movement analysis by a VICON motion capture system with 12 cameras was used to quantify the participants' movements. The system captures three-dimensional movement trajectories of the subjects. The spatial resolution of the system was approximately 1 mm. All trials were recorded at a sampling rate of 120 Hz, using 29 retro-reflecting markers that were positioned based on the Heidelberger Upper Extremity (HUX) model (Rettig et al., 2009).

The HUX model consists of seven segments and determines the individual's joint center of the shoulder and elbow joint with one static and three dynamic calibrations per subject. The calibration movements include shoulder abduction and adduction, shoulder anteversion and retroversion (both performed with zero elbow flexion) and elbow flexion and extension, all with the participant's maximal range of motion. Additional to the HUX marker set, further markers were added to evaluate the finger position (point-to-point movements) and to the swing rod (oscillating movements). All markers are listed in Table A4.1.

Marker	Anatomical Position
HUX model:	
HEAD	central forehead
R/L MAS	above mastoids (right/left)
CLAV	jugular notch
C7	thoracic vertebrae cervicalis 7
T10	thoracic vertebrae thoracalis 10
SACR	mid-way between posteriorsuperior iliac spines
R/L ASI	anterior superior iliac spines (right/left)
R/L SHO	acromio-clavicular joint (right/left)
R/L HUMS	tuberositas deltoidea (right/left)
R/L ELB	twin-marker ulna 2 cm distally to the olecranon (right/left)
R/L ELBW	twin-marker ulna 2 cm distally to the olecranon (right/left)
R/L ULN	processus styloideus ulnae (right/left)
R/L RAD	processus styloideus radii (right/left)
additional markers:	
R 1PD	1st distal interphalangeal
R 2MCP	2nd articulationes metacarpophalangeae
R 2PD	2nd phalanx distalis
R 5MCP	5th articulationes metacarpophalangeae

Table A4.1: **Marker placement according to the HUX model with additional markers to determine the finger position.**

A4.2.2 Experimental setup: Point-to-point movements

For the point-to-point movements, the participant was seated in front of a vertical canvas at a distance of 50 % of their arm length (see Figure A4.3). Four different targets appeared randomly on a vertical line on the canvas and the subjects were instructed to follow the targets fast, but precisely with their dominant hand. The vertical distance between the target positions varied between approximately 15 cm for small movements and 45 cm for large movements (distance between circle centers).

A4.2.3 Experimental setup: Oscillation movements

For the oscillation movements, the participant was standing upright, holding the swing rod in their dominant hand and instructed to get the swing rod in resonance. We used the therapy rod called "Propriomed 1" that is produced by the company *Haider Bioswing*. Here, we additionally

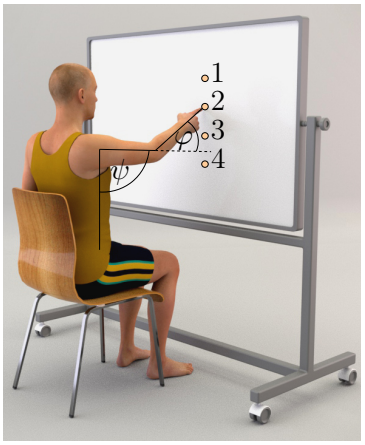

Figure A4.3: **Sketch of the experimental setup.** Using a motion capture system, elbow and shoulder angles of fast goal-directed pointing movements have been captured.

recorded the muscle surface electromyograms (EMG) of the m.bisceps and m.triceps muscle.

A4.2.4 Experimental results: Point-to-point movements

The point-to-point movement of interest was repeated seven times. We extracted the different initial and target angles, as well as one intermittent posture which represents the point of maximal elbow angle (Table A4.2). These joint configurations were assumed to represent the equilibrium points for the neuronal controller in the simulation. See Chapter 6 for more details. The resulting trajectories in comparison to the experimental trajectories are shown in Figure A4.4.

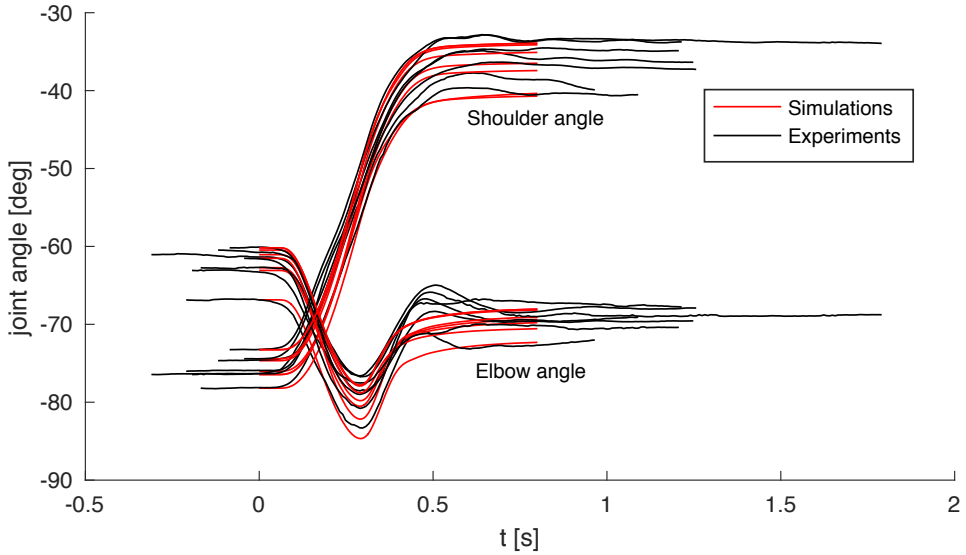

Figure A4.4: **Variability of experimental data (black) and simulated data (red).** These variations are the source of the error bars in Chapter 6.

Initial angle		Intermittant angle		Target angle	
Elbow	Shoulder	Elbow	Shoulder	Elbow	Shoulder
66,86°	76,03°	83,30°	76,03°	72,02°	39,91°
62,73°	78,20°	78,54°	78,26°	69,08°	40,52°
63,08°	76,44°	78,99°	76,45°	69,56°	36,36°
61,06°	76,44°	76,61°	76,45°	67,92°	37,28°
60,47°	74,67°	77,53°	74,67°	70,39°	34,88°
61,53°	74,42°	80,79°	74,43°	68,77°	33,94°
60,18°	73,26°	76,74°	73,26°	67,79°	33,75°

Table A4.2: **Equilibrium point angles extracted from the experimental data.**

A4.2.5 Experimental results: Oscillation movements

The experimental data of the joint angles and EMG was analyzed with a fast Fourier analysis (Figure A4.5). This data indicates that the range of oscillation frequencies occurring in the movement is about ±0.2Hz. This was used as the variance of randomly selected frequencies to introduce a "natural" variation in the movements in the simulation.

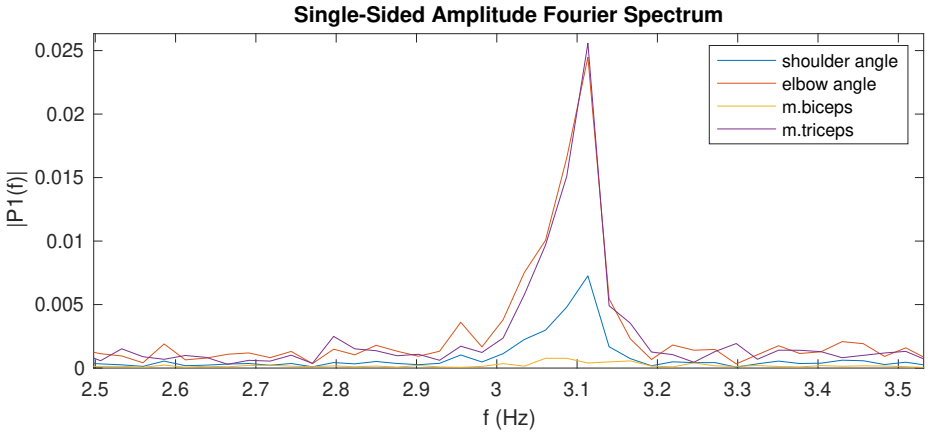

Figure A4.5: **Fourier transformation of the experimental data on a swing rod exercise.** Shown are the frequency spectra for two muscles (EMG of m. biceps and m.triceps) as well as the two joints (shoulder and elbow). This data indicates that the range of oscillation frequencies occurring in the movement is about ±0.2Hz. This was used as the variance of randomly selected frequencies to introduce a "natural" variation into the movements in the simulation.

A4.3 More detailed description of the computer simulation

A4.3.1 Equilibrium Point Controller

The bio-inspired hybrid equilibrium point controller exploits muscle characteristics by combining a feed-forward command ($\mathbf{u}^{\text{open}}(t)$) with spinal feedback on muscle fiber lengths ($\mathbf{u}^{\text{closed}}(t)$). This feedback represents a simplified version of the mono-synaptic muscle spindle reflex, assuming that the muscle spindles provide accurate time-delayed information about the muscle fiber lengths $\mathbf{l}^{\text{CE}}(t)$ (Kistemaker et al., 2006). The total motor command u_i for each muscle i is a sum of those components and is calculated as

$$\begin{aligned} u_i(t) &= \left\{ u_i^{\text{open}}(t) + u_i^{\text{closed}}(t) + u_i^{\text{CPG}}(t) \right\}_0^1 \\ &= \left\{ u_i^{\text{open}}(t) + \frac{k_p}{l^{\text{CE,opt}}} \left(\lambda_i(t) - l_i^{\text{CE}}(t-\delta) \right) + u_i^{\text{CPG}}(t) \right\}_0^1 , \end{aligned} \tag{A4.8}$$

where k_p is a feedback gain and the time delay δ is set to 10 ms representing a short-latency reflex delay which is in a physiologically plausible range (Houk and Rymer, 1981; More et al.,

2010). $l^{\mathrm{CE,opt}}$ stands for the optimal length of the contractile element. The operation $\{x\}_0^1$ sets values $x < 0$ to 0 and $x > 1$ to 1. The signal u_i^{CPG} represents a central pattern generator (CPG).

The low-level controller gets two top-down input signals: The open-loop muscle stimulation $u_i^{\mathrm{open}}(t)$ and the desired muscle fiber lengths $\lambda_i(t)$. Here, they represent an intermittent control approach, because they are piecewise constant functions over time. Herein, each constant value represents an *equilibrium posture* (EP), i.e. the system is in a stable equilibrium in these positions:

$$\dot{\mathbf{q}} = 0 \quad \text{and} \quad \ddot{\mathbf{q}} = 0\,, \tag{A4.9}$$

leading to the condition that the net joint moment vanishes in these postures (given enough time for the system to settle). This allows for the calculation of the muscle stimulations $u_i^{\mathrm{open}}(t)$ and the corresponding desired muscle fiber lengths $\lambda_i(t)$: For each EP, the muscle stimulations $u_i^{\mathrm{open}}(t)$ can be determined by minimizing the difference between the muscle stimulation u_i^{open} and the desired level of co-contraction $u^{\mathrm{des.}}$:

$$\sum_{i=1}^{4}(u_i^{\mathrm{open}} - u^{\mathrm{des.}}) \rightarrow \min\,, \tag{A4.10}$$

subject to the constraint that the sum of all torques acting on the joint is zero, i.e. the system is in a stable equilibrium position. The corresponding desired muscle fiber lengths λ_i are set by measuring the length of the muscle fiber lengths l_i^{CE} in the equilibrium positions.

A4.3.2 Optimization of the control parameters for a point-to-point movement

For the goal-directed point-to-point movements, three EPs were used per movement. To follow experimental trajectories, we optimized some of the control parameters: the shoulder and elbow angle for the second EP, the desired level of co-contraction for the second and the third EP, the starting times for the second and the third EP and the feedback gain k_p. Using the pattern search algorithm in Matlab®, the quadratic difference between the simulated and the experimental trajectory was minimized. The resulting parameters can be found in Table A4.3.

Using the resulting parameters, the muscle stimulations u_i^{open} were then optimized in order to fulfill the conditions for equilibrium points (see Equation (A4.10)) using the Matlab® optimizer *fmincon* which is suitable for finding the minimum of a constraint function.

A4.3.3 Dynamic oscillation movements with vibrating rod

The dynamic oscillation movements were inspired by the training and rehabilitation exercises performed with a vibrating rod. When we experienced such a training, we noticed how, after some training, we were able to excite the resonance frequency of the rod. This seems an interesting task in the sense of morphological computation, as the dynamic interaction with the "umwelt" with its specific resonance characteristics, is surprisingly not that difficult to learn.

A concept for modeling rhythmic excitement of the processes is the concept of the central pattern generator (CPG). Central pattern generators are neural networks with the ability to produce rhythmic patterns without receiving rhythmic input signals from higher control centers

		$1 \rightarrow 4$	$2 \rightarrow 3$	$4 \rightarrow 1$	$4 \rightarrow 3$
Shoulder Angle	EP 1	76.4°	60.4°	36.4°	40.8°
	EP 2	42.3°	37.5°	54.3°	47.1°
	EP 3	37.3°	46.7°	75.9°	48.4°
Elbow Angle	EP 1	61.1°	70.5°	70.0°	69.2°
	EP 2	74.3°	77.5°	76.0°	75.9°
	EP 3	67.9°	74.3°	61.9°	73.4°
Level of co-contraction	EP 1	0.10	0.10	0.10	0.10
	EP 2	0.077	0.094	0.38	0.33
	EP 3	0.28	0.20	0.5	0.44
Switching times	EP 1	0.00s	0.00s	0.00s	0.00s
	EP 2	0.35s	0.43s	0.37s	0.19s
	EP 3	0.57s	0.63s	0.57	0.41s
k_p		0.27	0.09	0.92	0.39

Table A4.3: **Resulting control parameters for the computer simulation of point-to-point movements.** Some simulation parameters resulted from the optimization that was performed to match the corresponding experimental trajectories: the shoulder and elbow angle for the second EP, the desired level of co-contraction for the second and the third EP, the starting times for the second and the third EP and the feedback gain k_p. The other parameters were set according to the experimental data.

or sensory feedback. The control concept of CPG implemented here is a simple sinusoidal pattern with a defined phase-shift between the stimultations to the extensor and flexor muscles. This was inspired by the work of Sproewitz et al. (2008).

The vibrating rod was modeled based on a therapy rod called "Propriomed 1" that is produced by the company *Haider Bioswing*. To implement the vibrating rod in Simulink the mechanical parameters of the spring-mass damper system are determinded experimentally including the mass m, the spring constant k and the damping constant d. For this purpose the vibrating rod was fixed and equipped with reflecting markers at both ends of the rod. The vibrating rod is then deflected evenly on both sides and the resulting vibration is recorded using a motion capture system (VICON motus). The resulting oscillation is analyzed and the mechanical properties are calculated with the formula of the quasiharmonic oscillation. Resulting in a damping constant of $d = 0,405\,\mathrm{kg/s}$ and a spring stiffness of $k = 300,523\,\mathrm{kg/s^2}$.

In order to verify the values for the spring and damper constant calculated from the experimental excitation the calculated parameters are fed into the Simulink model and a bilateral deflection is simulated.

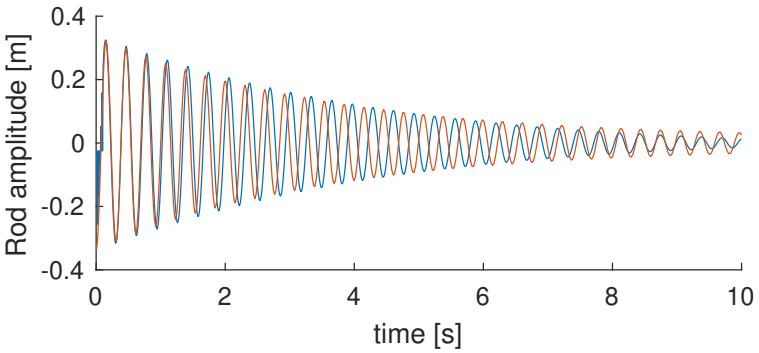

Figure A4.6: **Rod amplitude over time.** The oscillation generated in the simulation (in orange) corresponds to a large extent to the experimentally generated oscillation (in blue) at the beginning. Only after a few oscillations a deviation in amplitude and frequency can be observed.

The Simulink model of the vibrating rod is connected to the wrist and consists of a prismatic joint as well as the mass of the vibrating rod. The prismatic joint is actuated by a viscoelastic force element, which contains the spring and damper constants. The is guided by a virtual rail to limit the movement to horizontal forward movement, compensating for the influence of gravity.

The control of rhythmic movements is performed based on the general controller described in the main text

$$u_i(t) = \left\{ u_i^{\text{open}}(t) + \frac{k_p}{l^{\text{CE,opt}}} \left(\lambda_i(t) - l_i^{\text{CE}}(t-\delta) \right) + u_i^{\text{CPG}}(t) \right\}_0^1 , \tag{A4.11}$$

The first two terms are parameterized such that, in the absence of a CPG signal, the hand holds the rod in front of the body at rest.

To excite the rod, as done in training and rehabilitation exercises, a sinusoidal signal $\mathbf{u}^{\text{CPG}}$ mimicking the output of a central pattern generator (CPG) is added to the motor command $\mathbf{u}$:

$$\mathbf{u}^{\text{CPG}}(t) = \hat{u} \cdot \sin(\omega \cdot t + \phi_0) , \tag{A4.12}$$

with $\hat{u} = 0.1$: amplitude, ω: angular frequency, ϕ_0: phase. The muscles are synchronized by setting $\phi_0 = 0$ for flexing muscles and $\phi_0 = \pi$ for extending muscles.

The oscillation is exited for $0 \leq t \leq 4$s. After this, $\mathbf{u}^{\text{CPG}} = 0$ and the oscillation is then only a result of the dynamics of the system and not of the controller anymore.

A4.4 Supplementary simulation results point-to-point movements

We further quantified the other three pointing movements, which have quite a different amplitude (and direction) than the point-to-point movement reported in Chapter 6. Despite these differences in movement, the main trend of the results is similar: morphological computation is highest for the highest level in the control hierarchy.

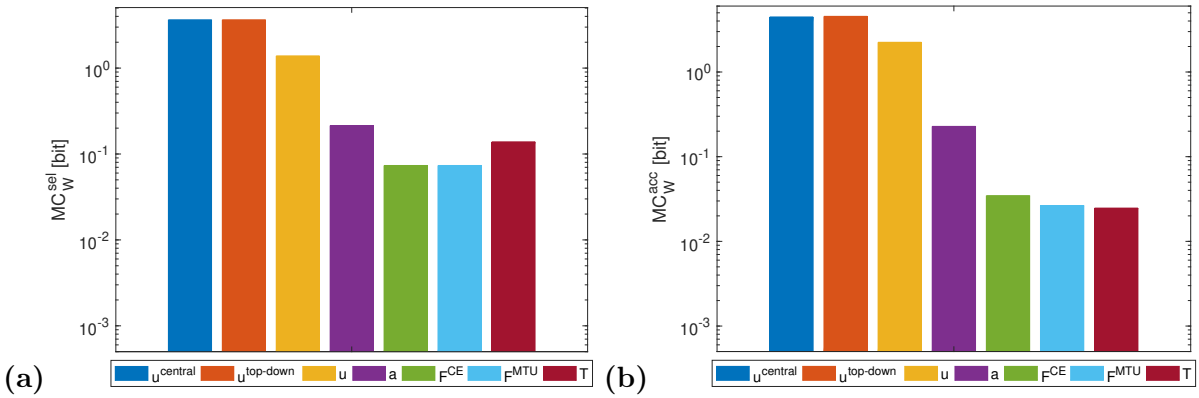

Figure A4.7: **Morphological computation MC_W on different hierarchy levels for an exemplary point-to-point movement ($2 \rightarrow 3$).** Morphological computation was evaluated using **(a)** selected (MC_W^{sel}) and **(b)** accumulated hierarchy levels (MC_W^{acc}). Note that a logarithmic scale is used for the y-axis. The limit of the y-axis is set to the maximum MC value that would result from having a constant signal as input.

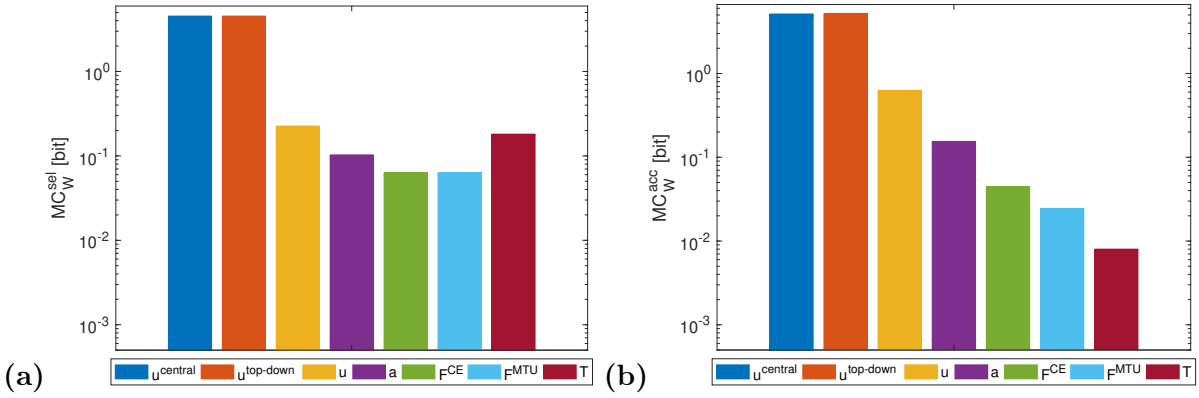

Figure A4.8: **Morphological computation MC_W on different hierarchy levels for an exemplary point-to-point movement ($4 \rightarrow 1$).** Morphological computation was evaluated using **(a)** selected (MC_W^{sel}) and **(b)** accumulated hierarchy levels (MC_W^{acc}). Note that a logarithmic scale is used for the y-axis. The limit of the y-axis is set to the maximum MC value that would result from having a constant signal as input.

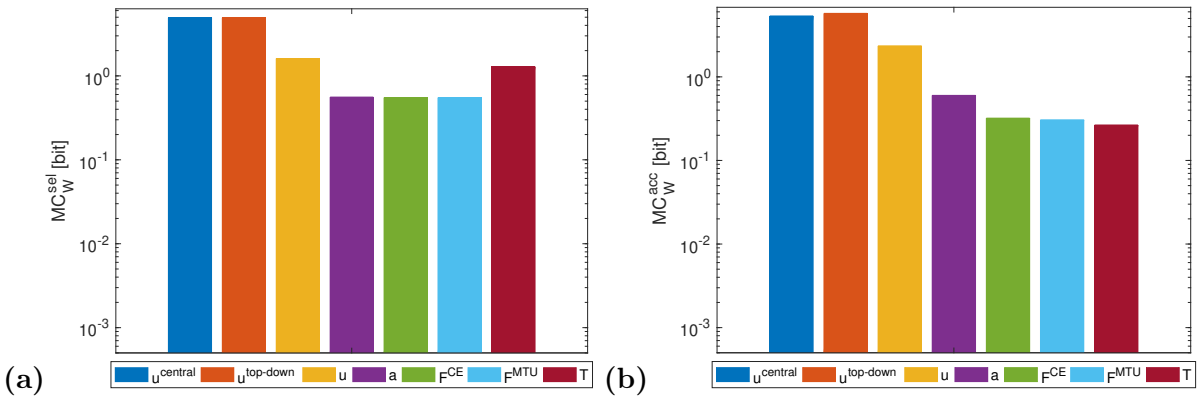

Figure A4.9: **Morphological computation MC_W on different hierarchy levels for an exemplary point-to-point movement** ($4 \rightarrow 3$)**.** Morphological computation was evaluated using **(a)** selected (MC_W^{sel}) and **(b)** accumulated hierarchy levels (MC_W^{acc}). Note that a logarithmic scale is used for the y-axis. The limit of the y-axis is set to the maximum MC value that would result from having a constant signal as input.

A5 Additional information and results to Chapter 7

A5.1 More detailed description of the human experiments

For more details on the setup of the human experiments see sections A4.2.1 and A4.2.2.

A5.2 The bio-inspired robot *Ataro*

Note that the following model description was submitted as electronic supplementary material accompanying Stollenmaier et al. (2020c). It was written by Tobias Nadler, Simon Wolfen, and Syn Schmitt.

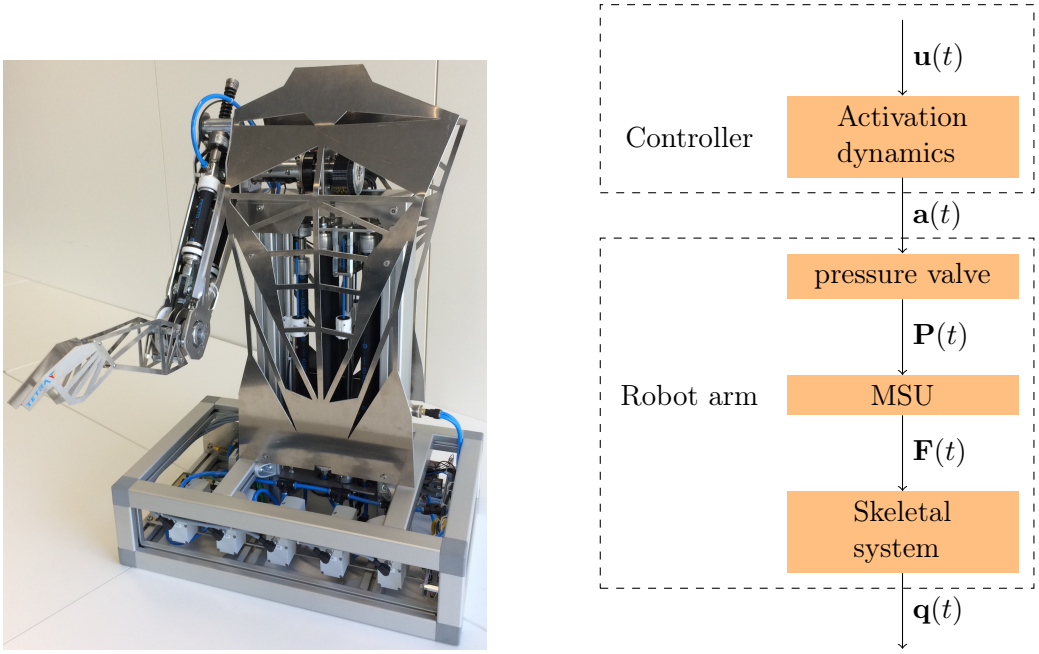

(a) (b)

Figure A5.1: **Visualization of the bio-inspired arm robot *ATARO*.** (a) Picture of the arm robot with pneumatically actuated MSUs and (b) Schematic representation of the actuation of the robot arm: the stimulation $\mathbf{u}(t)$ is fed into the model of the activation dynamics of muscles which relates the neuronal stimulation to the muscular activation $\mathbf{a}(t)$. The activation is converted into an electrical control signal which controls the pressure valves. The output pressure $\mathbf{P}(t)$ of the valves causes the pneumatic muscles to contract and exert a force $\mathbf{F}(t)$. This force acts on the arm segments of the robot and leads to a movement $\mathbf{q}(t)$ of the arm.

ATARO is a bio-inspired arm robot with two degrees of freedom. The physical model is based on the musculoskeletal model *Arm26*. Five artificial muscle-spring units (MSUs) (Wolfen et al., 2018) are used for actuation. The MSUs, each consisting of a pneumatic artificial muscle (PAM) and a spring in series, mimic the characteristics of the human muscle-tendon complex. Five proportional control valves actuate the PAMs. To mimic biological proprioception, a

force sensor and a length sensor in each muscle, and an angle sensor in each joint are used. A computer with an I/O board is used to control the arm robot in a real-time hardware-in-the-loop setup. The controller is implemented using Matlab 2016b®/Simulink®.

A5.2.1 Structure of the Biorobot (ATARO): Mechanics and Actuation

Mechanics The dimensions of the segments, as well as the position of the joints, are based on the anthropometric data of the numerical simulation model *Arm26*.

The robot consists of the following segments:

1. Torso: Rigid profile rail construction
2. Upper arm: Rigid sheet metal construction
3. Forearm and hand: Rigid sheet metal construction

The two degrees of freedom of the robot are realized by two mechanical hinge joints (shaft guided by two radial bearings), which represent the shoulder and the elbow joint. Usually, linear pulleys are used for force transmission. A linear pulley means that the lever arm has the same length at each joint angle. Since this does not correspond to biology, we developed a non-linear pulley exemplary for the elbow joint (Figure A5.3). This non-linear pulley is based on the lever arm profile of the numerical model *Arm26* (see Section 3.2.4). A comparison of the moment arm trajectory is depicted in Figure A5.4.

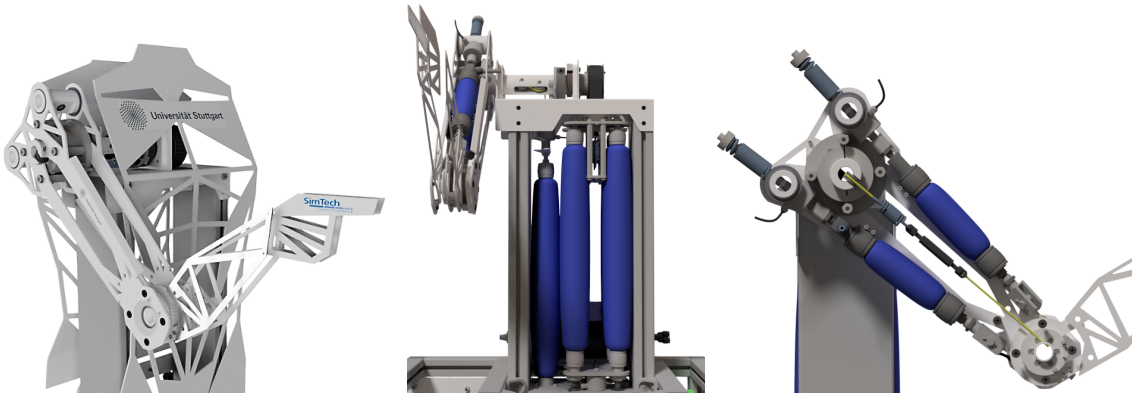

Figure A5.2: **CAD sketch of the bio-inspired arm robot *ATARO*.**

Actuation The biorobot is actuated by five muscle-spring units (MSUs) (Wolfen et al., 2018), which are implemented in a bio-inspired agonistic-antagonistic setup. Four of them are monoarticular muscles and one is a biarticular muscle. The muscles represent a multitude of anatomical muscles:

1. Elbow Flexor (EF):
   m. brachioradialis, m. brachialis, m. pronator teres, m. extensor carpi radialis

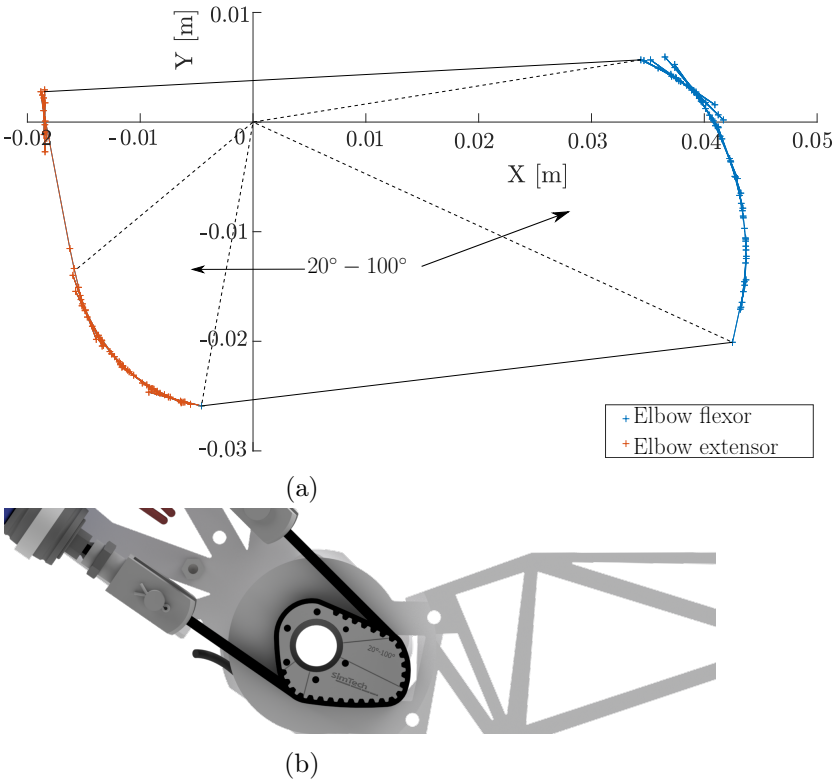

(a)

(b)

Figure A5.3: **Muscle lever arm trajectory.** (a) Geometric projection of the lever arm trajectory. The dotted lines representing the angle range from 20° to 100°, starting with an elongated arm (0°). (b) The 3D model of the nonlinear pulley derived from the geometry of (a).

2. Elbow Extensor (EE):
   m. triceps lateralis, m.triceps medialis, m. an-coneus, m. extensor carpi ulnaris

3. Biarticular muscle: Elbow Flexor Shoulder Anteversion (BF):
   m. biceps brachii caput longum and caput breve

4. Shoulder Anteversion (SF):
   m. deltoideus (pars clavicularis, anterior,lateral), m. superior pectoralis major, m. coracobrachialis

5. Shoulder Retroversion (SE):
   m. deltoideus (pars spinalis, posterior), m. latissimus dorsi

Each muscle-tendon-unit (MSU) consists of a pneumatic artificial muscle (PAM) and a spring in series, mimicking the characteristics of the biological muscle-tendon complex.

1. Elbow Flexor (EF): Actuator: Festo DMSP-20-100N-RM-CM; Spring: Gutekunst D-339R-01

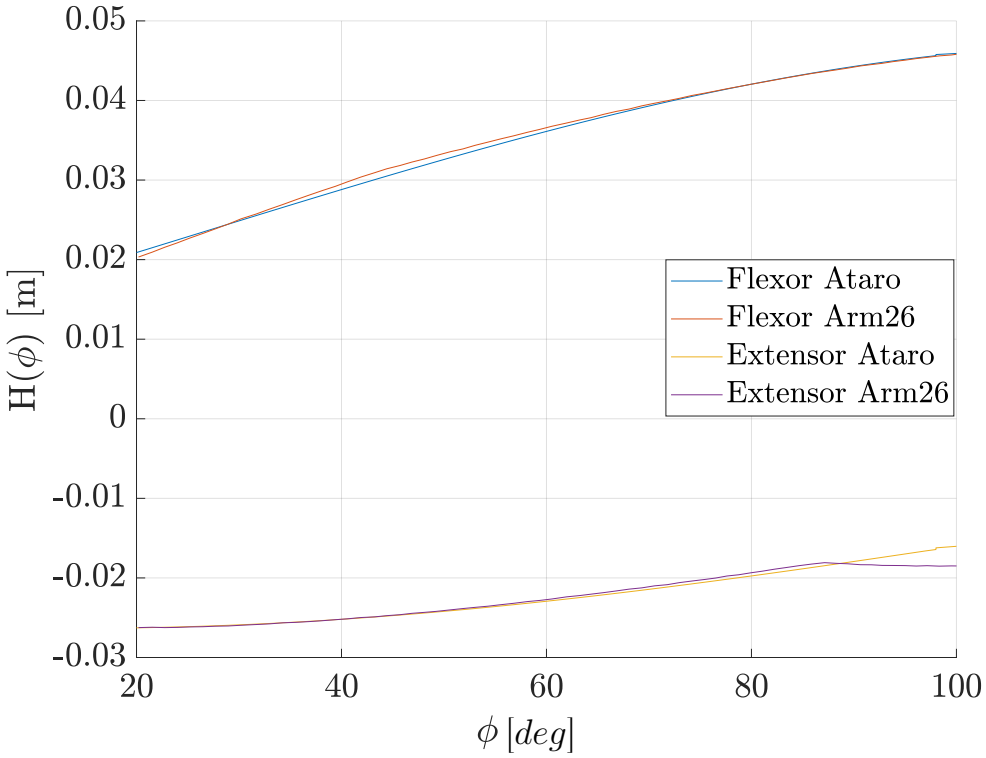

Figure A5.4: **Comparison of the moment arm trajectory of the monoarticular elbow flexor between *ATARO* and the *Arm26* Model.** The trajectory of the moment arm of *ATARO* was measured with the CAD software Autodesk Inventor 2017.

2. Elbow Extensor (EE): Actuator: Festo DMSP-20-100N-RM-CM; Spring: Gutekunst D-339R-01

3. Biarticular muscle: Elbow Flexor and Shoulder Anteversion (BF): Actuator DMSP-20-400N-AM-CM

4. Shoulder Anteversion (SF): Actuator: 2x in parallel Festo DMSP-20-400N-AM-CM; Spring: Gutekunst Z-117QL

5. Shoulder Retroversion (SE): Actuator: 2x in parallel Festo DMSP-20-400N-AM-CM; Spring: Gutekunst Z-117QL

Due to reasons of comparability between the robot *ATARO* and the numerical model *Arm26*, all MSUs act in parallel to the sagittal plane. Elbow flexor and elbow extensor are located in the lower arm. The shoulder flexor and the shoulder extensor as well as the biarticular shoulder anteversion and elbow flexor are located in the torso. The force of the shoulder flexor and extensor is transmitted through a mechanical shaft extended into the torso. The force of the biarticular muscle is applied via a rope acting on the shoulder shaft and the elbow shaft.

The contraction of each PAM depends on the output pressure of a 3-way proportional pressure control valve (Festo VPPX-8L-L-1-G14-0L10H-S1). The valves (five in total, one per muscle) have an internal PID controller. The following parameterization for the external control loop of the VPPX-PID controller is used:

- Amplification of the reference variable: $F = 45$
- Amplification of the proportional component: $P = 16.87$
- Amplification of the integral component: $I = 5$
- Amplification of the differential component: $D = 0$
- Input filter for limiting the dynamics of the setpoint: $\tau = 3.2$ms

Due to the working pressure range of the pneumatic muscle, the pressure is limited to a maximum of 6 bar. To compare the activation (0-1) values with the numerical model (*Arm26*) the output of the robot controller is multiplied by the factor 6 (6 Volts results in 6 bar).

Sensors To mimic biological proprioception, the following sensors are used for each muscle:

- Force sensors in the muscles: A Lorenz K-1563 (0 N to 2000 N) + DMS-Sensor-Interface LCV-U10_kompl is used to mimic the Golgi tendon organ.
- Length sensors in the muscles: A non-contact position sensor of the company MTS Sensor Technologie (Temposonics C-Serie Analogsensor) is used to represent the muscle spindles.
- Angle encoders in the joints: To measure the current movement, the robot has an angle sensor (LM13IC2D0BA10F00 + LM13 magnetic ring encoder system MR050E040A080B00 Magnetring MR050).

Runtime environment To connect the sensors with a PC, a Sensoray Model 626 I/O Board is used. A bio-inspired hybrid equilibrium point controller is used to control the muscles of the arm robot. The controller is described in detail in Chapter 7.

This controller is implemented in Matlab 2016b®/Simulink®. The Desktop Real-Time System is used for code generation (Target file: sldrt.tlc, Solver: ode4 (Runge-Kutta), fixed-step size, fundamental sample time: 500Hz).

	Length$[m]$	Weight$[kg]$	I$[kgm^2]$ $[\mathsf{I_{yz}I_{zx}I_{xy}}]$
Upper arm	0.335	$\sim$ 6.540	$\sim$ [0.000145 0.052369 0.000041]
Forearm	0.260	$\sim$ 0.367	$\sim$ [0.000003 0.003655 0.000001]

Table A5.1: **Skeletal parameters of the arm segments of the single arm robot.** The weight and the moments of inertia $I_{yz,zx,xy}$ were calculated approximately using the CAD system Autodesk Inventor 2017.

Muscle	$F_{max}[N]$	$l[m]$	$l_{Spring}[m]$	Origin point	Insertion point
EF	6000	0.1	0.04	Upper arm	Forearm
EE	6000	0.1	0.04	Upper arm	Forearm
BI	6000	0.4	0.04	Shoulder	Forearm
SF	6000	0.4	0.04	Shoulder	Upper arm
SE	6000	0.4	0.04	Shoulder	Upper arm

Table A5.2: **Technical data of the pneumatic muscles installed in the single arm robot.** The monoarticular muscles of the shoulder joint for anteversion and retroversion as well as the biarticular muscle are shifted into the torso. Since this does not alter the force application, the muscle origin points can still be regarded as originating from the shoulder.

A5.3 Additional results for all movements

Note that the following plots were submitted as electronic supplementary material accompanying Stollenmaier et al. (2020c). See this reference for the list of authors.

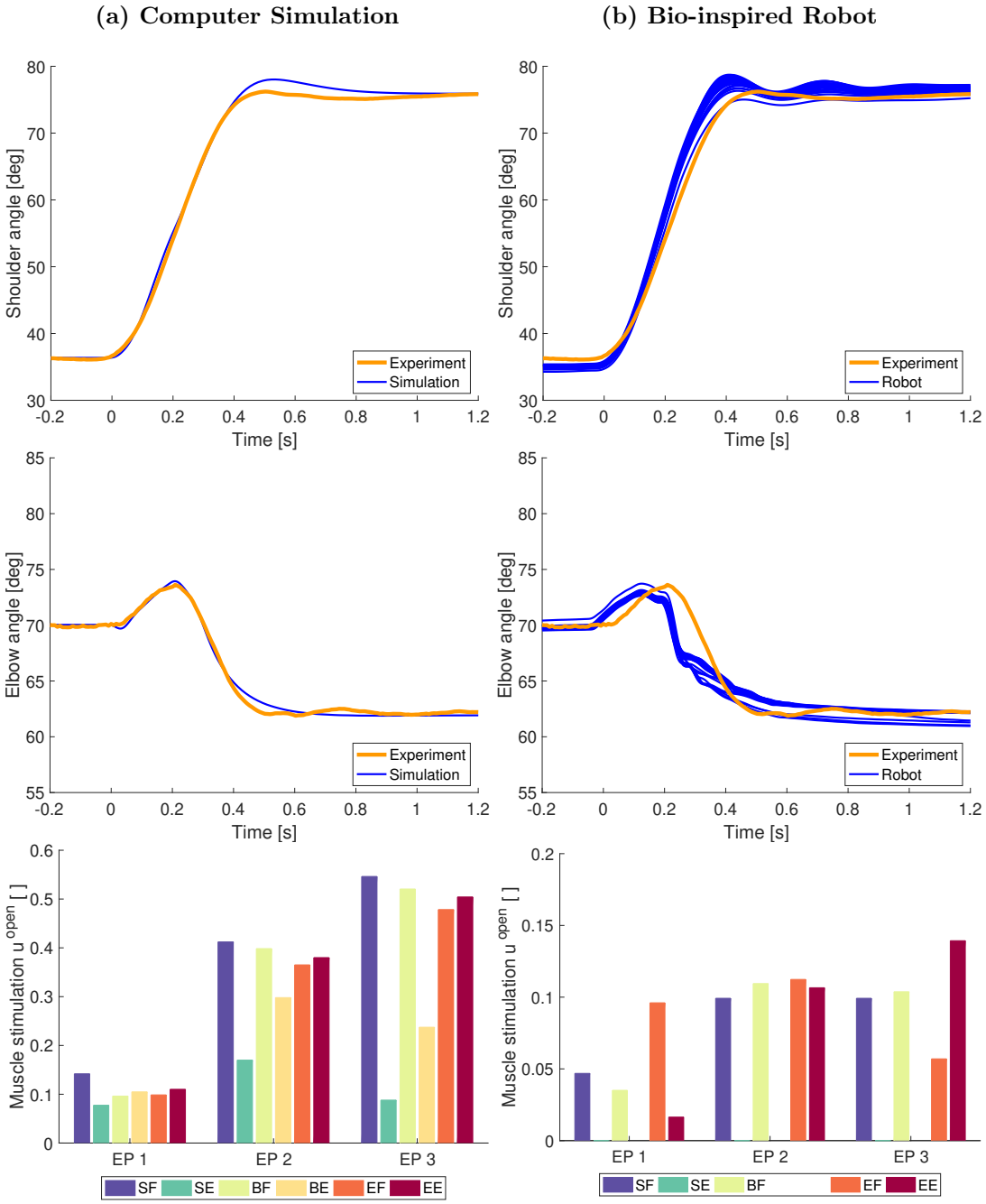

Figure A5.5: **Results for a big upward movement from position 4 to position 1 ($4 \rightarrow 1$) using (a) the computer simulation and (b) the bio-inspired robot.** The two rows show the shoulder and the elbow joint trajectory, respectively. The blue lines depict the robot and simulation trajectories, the orange lines show one movement of one typical control subject in the experiment.

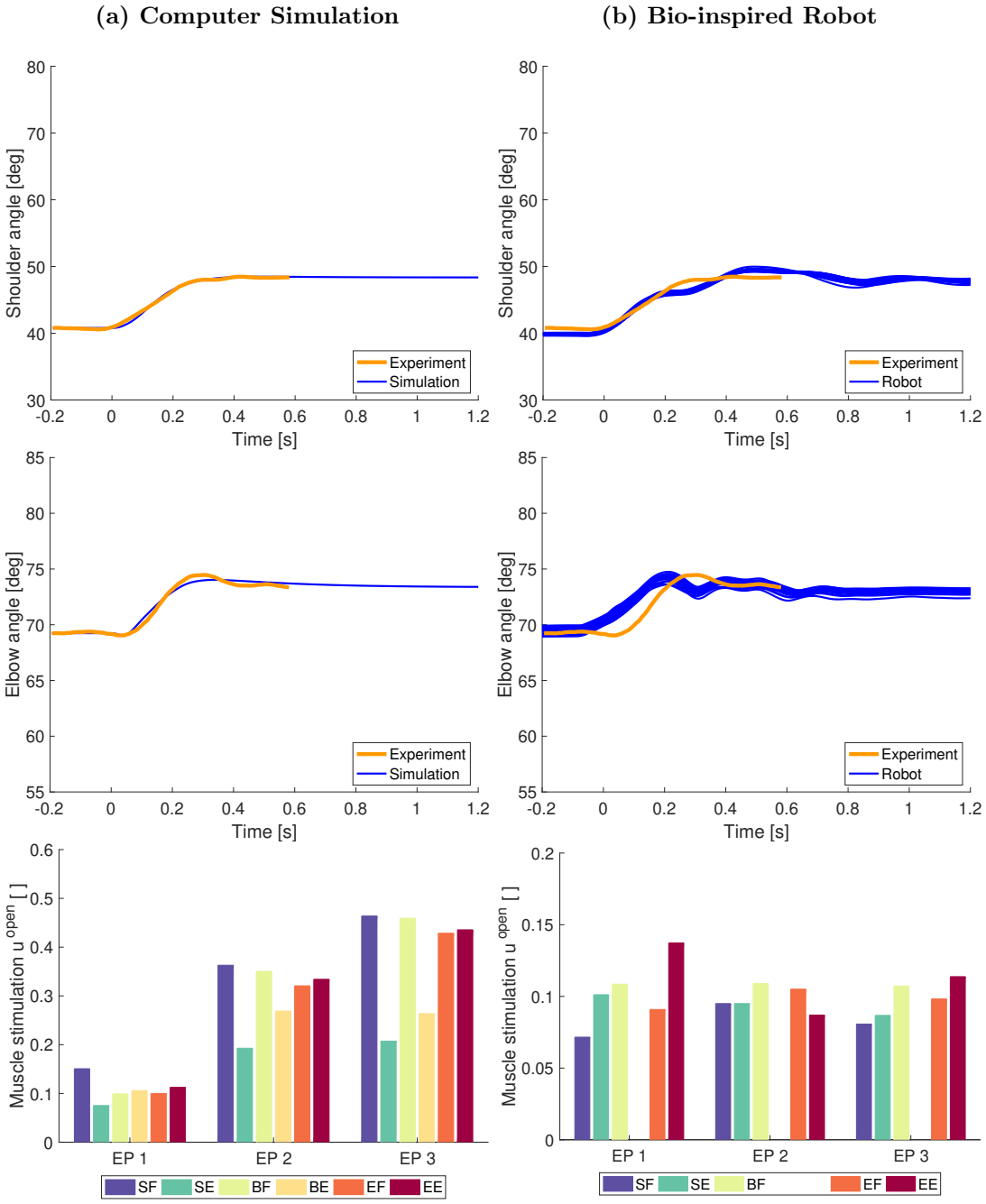

Figure A5.6: **Results for a small upward movement from position 4 to position 3 (4 → 3) using (a) the computer simulation and (b) the bio-inspired robot.** The two rows show the shoulder and the elbow joint trajectory, respectively. The blue lines depict the robot and simulation trajectories, the orange lines show one movement of one typical control subject in the experiment.

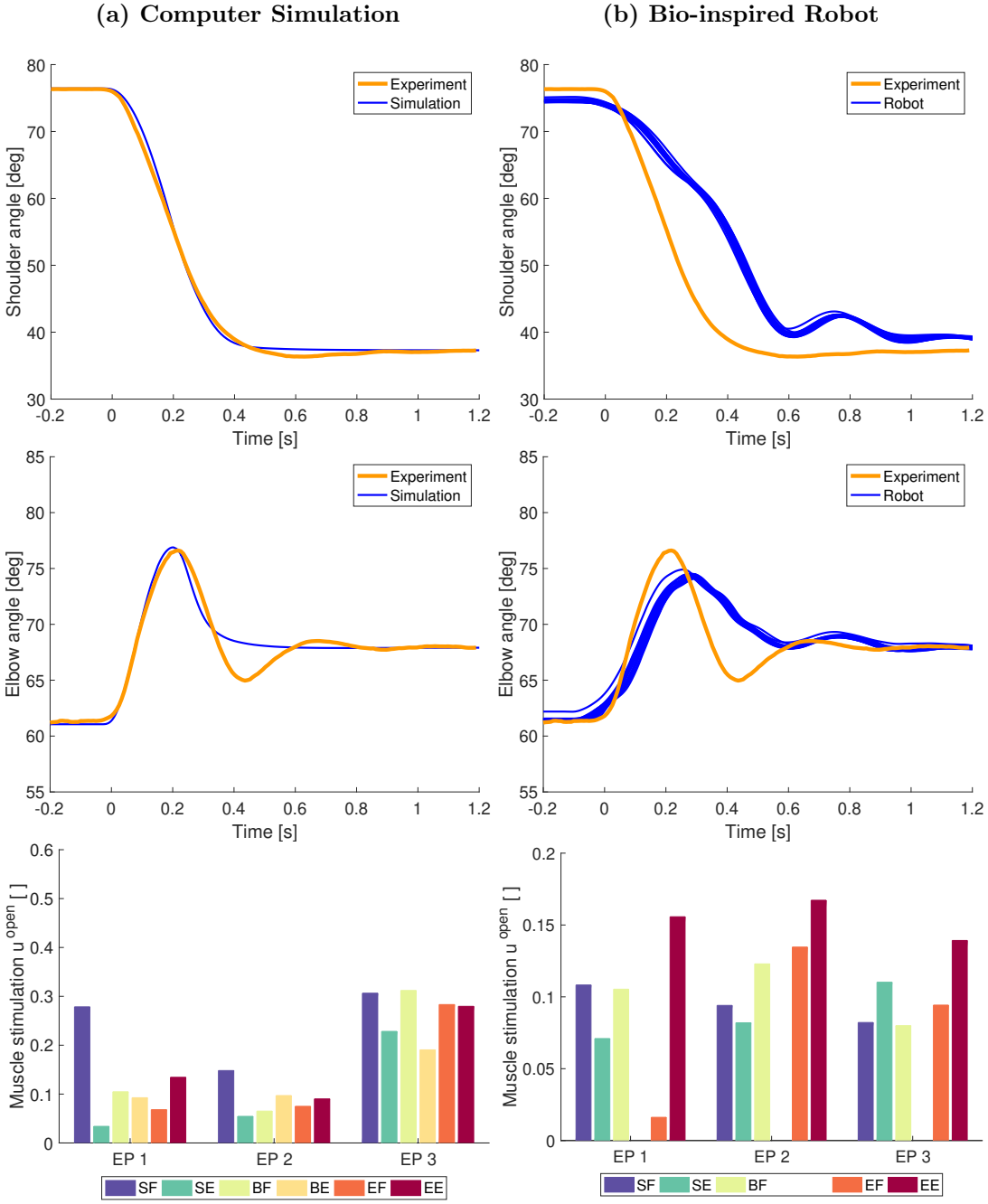

Figure A5.7: **Results for a big downward movement from position 1 to position 4 (1 → 4) using (a) the computer simulation and (b) the bio-inspired robot.** The two rows show the shoulder and the elbow joint trajectory, respectively. The blue lines depict the robot and simulation trajectories, the orange lines show one movement of one typical control subject in the experiment.

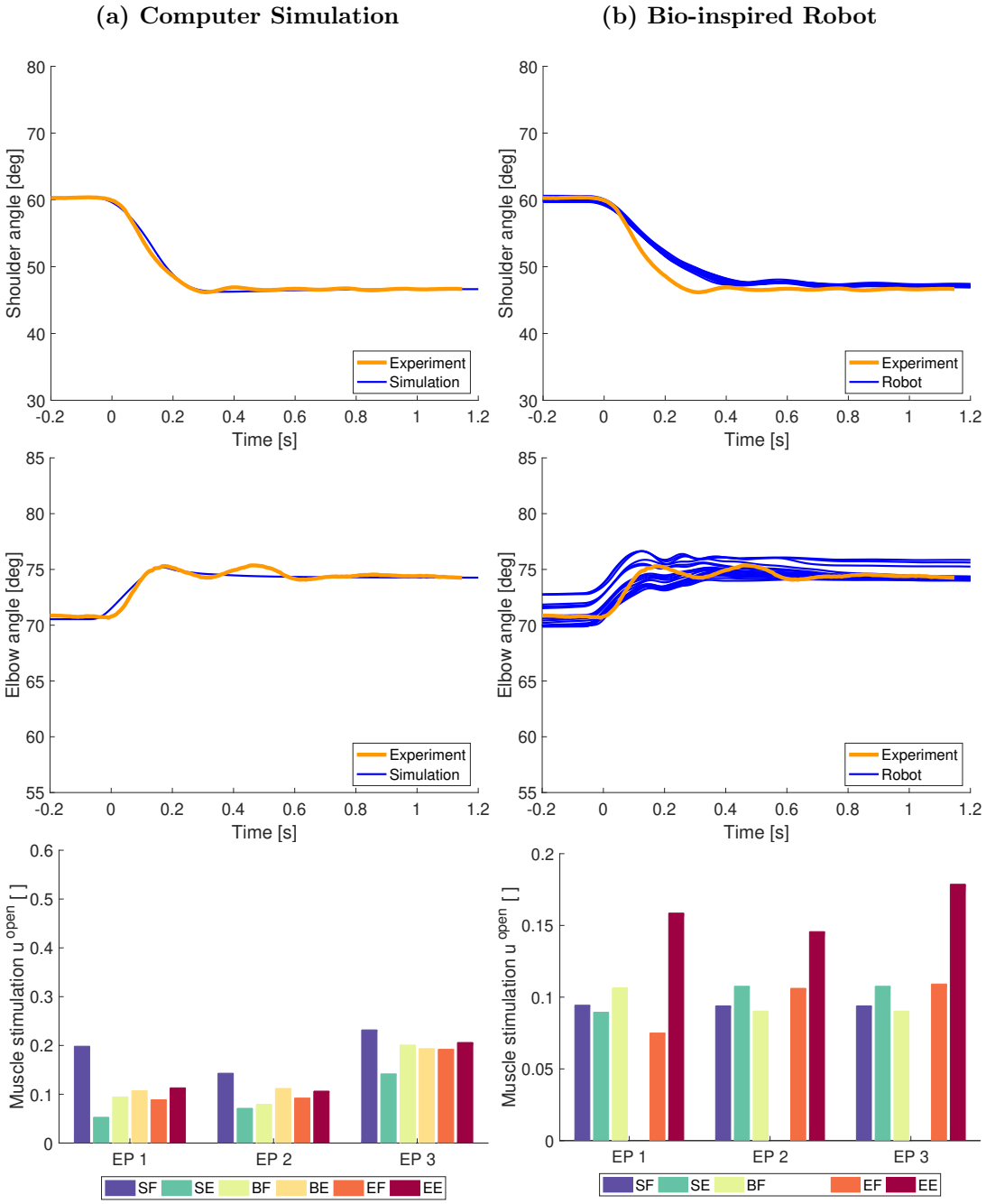

Figure A5.8: **Results for a small upward movement from position 2 to position 3 (2 → 3) using (a) the computer simulation and (b) the bio-inspired robot.** The two rows show the shoulder and the elbow joint trajectory, respectively. The blue lines depict the robot and simulation trajectories, the orange lines show one movement of one typical control subject in the experiment.